

FMH606 Master's Thesis 2022

Process Technology

Enhanced sulfate removal- and deaeration package performance at Ivar Aasen

Espen Nilsen

Faculty of Technology, Natural sciences and Maritime Sciences
Campus Porsgrunn

Course: FMH606 Master's Thesis, 2022

Title: Enhanced sulfate removal- and deaeration package performance at Ivar Aasen

Number of pages: 186, including title page and appendices.

Keywords: Sulfate removal, Nanofiltration, Membrane transport mechanisms, Solution-diffusion, Oxygen deaeration, Theoretical mechanical deaeration performance, Henry's law, Henry-Setchenov model, Valve flow calculations, Process optimization and Trend-analysis.

Student: Espen Nilsen

Supervisor: Britt Margrethe Emilie Moldestad

External partner: **Aker BP**

Summary:

Ivar Aasen is an oil and gas field situated in the northern part of the Norwegian continental shelf. A part of their operational strategy is to maintain reservoir pressure at a desirable level by injecting a combination of produced water and treated seawater into the reservoir. The seawater used for this purpose must be pretreated to remove both sulfate ions and dissolved oxygen to certain concentration levels. This is to prevent reservoir souring, scaling and corrosion damage in the topside process equipment and injection wells. At Ivar Aasen the sulfate and oxygen in the seawater to be injected are removed by nanofiltration and vacuum/chemical deaeration in two separate unit operations. The combination of the two is referred to as the Sulfate Removal Deaeration Package (SRDP).

The overall project objective was to evaluate and optimize the SRDP performance. The method to do so was to initially study the plant to set the frames for the subsequent literature review intended to theoretically evaluate unit performance and to understand the detailed mechanisms of the different unit operations. This was in turn utilized for the plant tests during the projects practical phase to assess the performance and optimization potentials.

The theoretical study made it clear that it was not possible to establish a theoretical performance model for the SRUs due to lack of publicly available information on the specific membranes in use. As a compromise a systematic overview of the expected SRU response upon parameter changes was established. During the plant specific SRDP study it was found that the SRUs are likely operated at too high total recovery relative to the manufacturer's recommendations. In addition, assessment of historical data indicates that the deaerator vacuum ejector underperforms. This hypothesis that was strengthened during the practical phase of the project.

The practical phase of the project suffered from time constraints and process issues due to an unforeseen power loss at Ivar Aasen. This disabled the ability to elevate the seawater temperature to the SRDP for the remainder of the project period. In addition, Aker BP decided to start early on their planned maintenance shutdown while the plant was already without main power. This restricted the available resources for testing significantly during a large portion of the planned test period. The plant tests that were initiated (but not completed) involved increasing the seawater temperature, validation of a mathematical permeate flow model, and changes to stage recoveries by altering the permeate backpressure. The temperature test ended abruptly due to the mentioned power loss which made evaluating the test data difficult. Increasing the seawater temperature showed promising results regarding optimizing the sulfate removal system but could not conclude on how the rate of biofouling responds. The deaerator response was not significant, but the test yielded strong indications of underperformance. The data indicates the vacuum ejector as the reason for this underperformance. The theoretical performance model derived for the deaerator was not possible to validate with the little data available from this test. However, this derived model relative to the performance model made by the manufacturer, seems to predict the deaerator temperature response better. The next test involving validation of a permeate flow model was not completed but it proved that the model could be corrected to different levels of permeate production. The ability to deal with membrane fouling for this flow model was not tested, but the test data retrieved seems to indicate that it will fail to do so. The last test indicates that increasing the 1st stage recovery above a certain, unknown, level can increase the rate of membrane fouling. Thus, it is important with explicit control over the recoveries if these are to be altered to optimize the system. The temperature test and flow model validation should be resumed when possible.

The University of South-Eastern Norway takes no responsibility for the results and conclusions in this student report.

Preface

This master thesis is a theoretical optimization study with practical plant tests on the sulfate- and oxygen removal plant at Ivar Aasen. It has been conducted during the spring of 2022 via the University of South-Eastern Norway (USN), Department of Process technology in collaboration with Aker BP.

Some of the sources used to write about the specific plant at Ivar Aasen in this report are not available for the public and is therefore not cited. Most of these sources are used in Chapter 2 and are documents such as P&IDs, system descriptions, datasheets technical- and engineering manuals, and so forth. These sources are retrieved from Aker BPs database and can both be Aker BP- and subcontractor documents. It should be mentioned that I (the author) work on Ivar Aasen in the position as Operation- and Maintenance supervisor. For this reason, some of the theory on Ivar Aasen are written based on my own experience. Software like SeeQ, GeoGebra and Excel is used for trend plotting and calculations in this report.

The task given by Aker BP has given me the opportunity get in-depth knowledge in sulfate removal by nanofiltration and mechanical oxygen removal by vacuum deaeration. I am very grateful to my colleagues and Aker BP for making it possible to do this master study alongside work. I am also very grateful to USN with professors for a very interesting and well-structured online master study.

I would like to thank both the USN- and Aker BP supervisor, Britt Margrethe Emile Moldestad and Halvor Damslora for great support and assistance throughout the project. And finally, I would like to thank my daughter and fiancé, Luna and Kathrine, for their support through these four years as a master student. I could not have done this without you!

Halden, 16.05.2022



Espen Nilsen

Contents

Preface	4
Contents.....	5
Nomenclature	7
Abbreviations	10
1 Introduction	11
1.1 Background	11
1.2 Method and Objectives.....	12
1.3 Scope	13
1.4 Thesis outline	13
2 Ivar Aasen study – the SRDP	14
2.1 The seawater system – an overview	14
2.2 Seawater characteristics.....	20
2.3 Sulfate Removal Units	21
2.3.1 <i>FilmTec™ SR90-440i</i> membrane elements	21
2.3.2 <i>SRU staging</i>	25
2.3.3 <i>Membrane pressure vessels</i>	26
2.3.4 <i>Overall operating limits and feedwater requirements</i>	27
2.3.5 <i>Dimensions, design basis and performance guarantee</i>	28
2.3.6 <i>Control loops and adjustable parameters</i>	28
2.3.7 <i>Performance Normalization</i>	31
2.3.8 <i>Membrane autopsy by Avista Technology</i>	31
2.3.9 <i>Historical performance</i>	34
2.3.10 <i>Typical operational problems</i>	34
2.4 Deaeration package	36
2.4.1 <i>Technical build-up and functionality</i>	36
2.4.2 <i>Dimensions, design basis and performance guarantee</i>	44
2.4.3 <i>Control loops and adjustable parameters</i>	46
2.4.4 <i>Historical performance</i>	46
2.4.5 <i>Typical operational problems</i>	47
3 Literature review	50
3.1 Membrane separation.....	50
3.1.1 <i>Overview and terminology</i>	50
3.1.2 <i>Osmotic pressure and reverse osmosis</i>	54
3.1.3 <i>Transport mechanisms</i>	55
3.1.4 <i>Solution-Diffusion</i>	57
3.1.5 <i>Concentration polarization</i>	69
3.1.6 <i>Fouling and membrane degradation</i>	76
3.2 Vacuum deaeration.....	81
3.2.1 <i>Henry’s law</i>	81
3.2.2 <i>Temperature and salinity dependency for Henry’s constant</i>	84
4 Method	88
4.1 Models and SRU parameter dependencies.....	88
4.1.1 <i>Parameter dependencies for the SRUs</i>	88
4.1.2 <i>The old permeate flow model</i>	90

4.1.3 <i>Theoretical mechanical deaeration performance</i>	93
4.2 Plant tests	96
4.2.1 <i>Test 1 - Increased feedwater temperature</i>	96
4.2.2 <i>Test 2 - Validate permeate flow model</i>	98
4.2.3 <i>Test 3 – Recovery and backpressure adjustments</i>	100
5 Results and discussion	102
5.1 Theoretical assessments	102
5.1.1 <i>The new permeate flow model and stage recoveries in the SRUs</i>	103
5.1.2 <i>Theoretical mechanical deaeration performance versus the Eta Process Plant performance model</i>	108
5.2 Plant tests	110
5.2.1 <i>Test 1 – Increasing feedwater temperature</i>	110
5.2.2 <i>Test 2 – Validate permeate flow model</i>	141
5.2.3 <i>Test 3 – Recovery and backpressure adjustments</i>	147
6 Conclusion	154
6.1 Further work	156
References	157
Appendices	162

Nomenclature

Symbols	Description	Units
a, b	Stoichiometric coefficients	$[-]$
A_m	Active membrane area	m^2
c	Mass concentration	kg/m^3
C_c	Model constant	$[-]$
C_f	Orifice coefficient	$[-]$
C_v	Valve coefficient	$[-]$
D	Diffusion coefficient	m^2/s
D_∞	Diffusion coefficient at infinite time	m^2/s
E_a	Activation energy	J/mol
$f(u_{\%})$	Valve opening function	$[-]$
H_s	Henry solubility constant	$mbar^{-1}$
H_v	Henry volatility constant	$mbar$
I	Ionic strength	mol/kg
J	Mass flux	$kg/(m^2s)$
J_V	Permeate volume flux	$m^3/(m^2s)$
K	Sorption coefficient	$[-]$
k_B	Boltzmann's constant	$m^2kg/(s^2K)$
K_{IP}	Ion product	$[mol/kg]^{a+b}$
K_{sp}	Solubility product	$[mol/kg]^{a+b}$
L	Coefficient of proportionality	$[-]$
l	Membrane thickness	m
L_w	Permeation coefficient pure water	m^2s/kg
M	Molar mass	$kg/kmol$
\dot{m}	Mass flow	kg/s
N	Molality	mol/kg
n	Mol	mol
P	Permeability	m^2/s
p	Pressure	Pa

Δp	Differential pressure	Pa
\dot{Q}	Volumetric flowrate	m^3/s
R	Universal gas constant	$J/(mol \cdot K)$
\mathcal{R}	Recovery	%
r_s	Solute radius	m
S	Salinity	%
SG	Specific gravity (ρ/ρ_{water})	[–]
T	Absolute temperature	K
$u_{\%}$	Valve position	%
w	Permeation coefficient solute	s/m
X	mole fraction	[–]
x	Spatial coordinate	m
z	Ionic charge of an ion	[–]

Greek letters	Description	Units
γ	Activity coefficient	[–]
δ	Laminar boundary layer thickness	m
η	Dynamic viscosity	$Pa \cdot s$
μ	Chemical potential	J/mol
$\Delta\pi$	Osmotic pressure difference	Pa
ρ	Mass density	kg/m^3
$\tilde{\rho}$	Molar density	mol/m^3
σ	Reflection coefficient	[–]
v	Molar volume	m^3/mol
φ	Conductivity	mS/cm
ω	Acentric factor	[–]

Subscripts	Description
0	Spatial x position indicating membrane origin relative to direction of thickness (feed side surface, feed/membrane)
b	Bulk (well mixed feed/concentration)
c	Concentrate (or retentate)

f	Feed
i	Species (solvent, seawater)
j	Species (Solutes, e.g. sulfate, ionic specie, oxygen, etc.)
l	Spatial x position indicating end of membrane relative to direction of thickness (permeate side interface, membrane/permeate)
p	Permeate
(m)	Inside active membrane layer

Superscripts	Description
$^{\circ}$	Reference condition
$-$	Average
$*$	Pure substance

Abbreviations

CIP	Clean In Place
FAC	Free Available Chlorine
ICP	Internal Concentration Polarization
LBL	Laminar Boundary Layer
MF	Microfiltration
MOC	Management of Change
NCS	Norwegian Continental Shelf
NF	Nanofiltration
NOV	National Oilwell Varco
P&ID	Piping and Instrumentation Diagram
PV	Pressure Valve
RO	Reverse Osmosis
SRDP	Sulfate Removal and Deaeration Package
SRU	Sulfate Removal Unit
TCF	Temperature Correction Factor
TDS	Total Dissolved Salt
UF	Ultrafiltration
USN	University of South-Eastern Norway

1 Introduction

This chapter describes the context, objectives, method, thesis outline and the scope of the project.

1.1 Background

Aker BP is an independent exploration and production company of oil and gas operating in the Norwegian continental shelf (NCS). They operate five fields in the North Sea, Ivar Aasen is one of these. In 2020 Aker BP delivered a daily net production of 210.7 thousand barrels per day with a production efficiency of 92 % [1]. They have high focus on both low cost and low carbon production with safety and environment at the top of their priority. [2]

Ivar Aasen is situated at the Utsira height in the northern part of the NCS. It was discovered in 2008 and first oil production was established late 2016. Estimated retrievable reserves from the reservoir are roughly 200-million-barrel oil equivalent [2]. Due to its vicinity to Lundins Edvard Grieg field the project and operation between them are coordinated. Thus, oil and gas from Ivar Aasen is, after single stage oil-, water-, and gas separation, exported to Edvard Grieg for final processing. Thereafter, oil and gas are exported via pipelines to the Sture terminal and British sector for further refinement. [3] Ivar Aasen process, treat and reinject the produced water back into the reservoir. Produced water is water associated with the oil and gas in a reservoir [4].

Produced water poses an environmental threat due to traces of substances like dispersed oil, aromatic hydrocarbons, heavy metals, and hazardous metals like barium ions. This is one of the reasons for why Aker BP mainly re-injects all produced water back into the reservoir at Ivar Aasen. This reinjection acts both as an environmental- and production optimizing measure as it prevents emission and functions as pressure recovery in the depleting oil and gas reservoir.

To maintain the desired pressure recovery more water than the available produced water is required. To achieve this seawater is introduced as a supplement. This supplement of seawater is what yields the need for the Sulfate Removal and Deaeration Package (SRDP) package that is to be assessed in this master thesis. The main reasons for the SRDP are:

- Seawater contains sulfate (SO_4^{2-}) and other anions like chloride and nitrate (Cl^- and NO_3^- , respectively). While produced water contains barium and other cations. Mixing these will form scaling like barium sulfate. This scaling can cause serious safety- and operability problems as it can accumulate a solid scale deposit layer inside emergency valves, process valves/pipe/equipment preventing them from closing sufficiently and increasing pressure drop within the plant, respectively. It can also reduce heat transfer in heat exchangers and so forth. Reducing the sulfate content in the seawater period to mixing it with the produced water will minimize these effects. Removal of sulfate also have a positive effect on H_2S generation in the reservoir as less molecular Sulfur is introduced [5, p. 63]. H_2S will sour the reservoir and cause problems/other demands for the production plant as it is highly poisonous and corrosive. Therefore, souring of the reservoir is unwanted as it can potentially require top side modification so that the plant can handle it.

- Seawater contains dissolved oxygen which can cause corrosion and set the conditions for bio growth in top side piping and wells, the latter can cause bacteria-plugging in the injection wells [6]

To sum up, the main reasons for SRDP are to reduce scaling, reservoir souring, top-side corrosion and bio growth when mixing sea- and produced water for reservoir pressure recovery.

1.2 Method and Objectives

The overall objective of this project is to evaluate and potentially optimize the Sulfate Removal Deaerator Package (SRDP) performance on Ivar Aasen. The method is to do an initial plant study with a following literature review to be able to evaluate the expected system performance theoretically. And to be able to understand the detailed mechanisms of the unit operations to understand the functional relations between system response and parameter/process variable changes. The subsequent phase is a practical phase where the theoretical performance models will be validated, the system performance assessed, and the process attempted optimized through different practical plant tests based on the initial theoretical study.

The evaluation and optimization part of the project will focus on system availability and performance. For the SRUs this means to reduce the frequency of chemical membrane cleaning and keeping the target sulfate content in the permeate. For the Deaerator the focus is on assessing the mechanical deaeration performance which in turn can reduce the need for chemicals for chemical deaeration of residual dissolved oxygen.

The specified objectives of this master thesis are as follows:

1. Literature study of SRU design and which parameters affect the SRU performance.
2. Evaluate SRU performance with respect to mass balance, seawater temperature, algae season, chemical treatment, and clean-in-place (CIP) frequency based on available data.
3. Elaborate and test means of enhanced SRU performance (e.g. mass distribution with existing instrumentation, elevated seawater temperature).
4. Theoretical assessment of deaerator efficiency i.e. expected dissolved O₂-content as function of pressure, flow, and temperature on the incoming seawater.
5. Recommend further work for SRDP optimisation

The complete task description for this thesis is attached in Appendix A.

1.3 Scope

The scope of this project is narrowed down to how the SRDP installed on Ivar Aasen is operated today and how it can be optimized to deliver the desired flow and quality of seawater for reservoir pressure recovery with highest possible regularity. This means that:

- No plant modifications are considered or suggested. Suggesting other types of membranes is not considered a plant modification.
- Feedwater pre-treatment is seen as constant.
- Economical tradeoff such as injection and retrieved oil and gas is not considered
- Chemical regime is considered optimized and thus not assessed. This includes preservation- and CIP wash chemicals and method.

1.4 Thesis outline

This report consists of 6 chapters and 11 appendices where the succeeding chapters are structured as follows.

Chapter 2 presents a study on the specific plant that is assessed in this thesis. The chapter starts by introducing the seawater system at Ivar Aasen to the readers not familiar with the plant. The remainder of this chapter is divided in to two main sections, one for the sulfate removal and the other for the oxygen removal. The intent is to lay the technical foundation for the project though an in-depth study on the equipment of interest. Thus, what equipment are we dealing with and how is it / has it performed before this project. Typical operational problems based on dialogue with the different manufacturers and suppliers is also presented in this chapter.

Chapter 3 is the literature review intended to understand the detailed mechanisms of nanofiltration and vacuum deaeration. The theory necessary to be able to theoretically evaluate the SRDP system performance at Ivar Aasen is presented here.

Chapter 4 presents the method, different plant tests and theoretical studies/derivation of a valve flow model and a theoretical performance model for mechanical deaeration. The main intention of the plant tests is to evaluate system response and to optimize certain aspects of the plant. A brief theoretical overview and theoretical performance assessments are given prior to presenting the individual tests. Thereafter each test in terms of implementation procedure, theoretical basis, predicted outcomes and limitations are presented.

Chapter 5 contains the results and discussion of the test that was implemented in the process. The focus during the assessment of the different test data is to evaluate whether the implementation optimizes the plant. Another important aspect is to assess and discuss the outcomes and to see if it is in line with theory.

Chapter 6 yields the conclusion of what has been found through the theoretical study and plant testing. Suggested further work is also presented in this chapter.

2 Ivar Aasen study – the SRDP

The following chapter is intended to lay the technical foundation for this project. Historical data wrt. different performance factors are also assessed in this chapter. It is necessary to know the details of the sulfate removal deaeration package (SRDP) at Ivar Aasen to set the frames for the literature study, theoretical calculations, and optimization.

Initially a general overview of the seawater system is given and thereafter a detailed assessment on the SRDP including important upstream elements affecting the system of interest. The initial overview in Ch. 2.1 explains the system and its unit operations briefly and is intended for the reader not familiar with the seawater system on Ivar Aasen. Typical operational problems based on the manufacturers/supplier's experience is also presented in this chapter.

2.1 The seawater system – an overview

Seawater is used in combination with produced water as pressure recovery in the Ivar Aasen reservoir. To prevent reservoir souring, corrosion and scaling in pipes and equipment it is important to remove most of the sulfate and oxygen in the seawater. This is done in the SRDP by membrane separation and oxygen deaeration before it being mixed with produced water. Seawater at Ivar Aasen is also used for other purposes prior to it being treated in the SRDP.

The flow diagrams given in Fig. 2.1 and 2.2 shows an overview of the entire seawater system on Ivar Aasen. Fluid legends and colored highlighting are drawn into these diagrams to make it easy to see how the different unit operations affect the seawater on its path to the SRDP and water injection. From these flow diagrams it is evident that seawater is used for many purposes besides supplementing water to pressure recovery, e.g.:

- Filling and pressurizing fire water system up to the closed fire sectioning valves.
- Distributing water to the electro chlorinator- and freshwater RO systems.
- Cooling medium for emergency-, essential-, and non-essential equipment.

Seawater lift pumps and coarse filtering

Seawater is lifted to the platform using electrical fixed speed sub-merged pumps. The intakes are at a depth of 65 meters below the mean sea surface. Chlorine is injected as sodium hypochlorite into the system to prevent bio-growth through inactivating microorganisms in the seawater. The first unit operation that the water encounters is the coarse filtering (50CA0001A/B) which removes particles greater than 50 microns (μm). One filter is in operation at a time, and they are interchanged (duty/standby) daily. Filter backflush is activated when the differential pressure reaches 0.8 barg. After this the seawater acts as a coolant for many utility and process systems before heading to the ultrafiltration package.

The flow diagram in Fig. 2.1 shows that the emergency- and essential seawater lift pump can distribute water to the system. These pumps are only running when Ivar Aasen is in emergency- and/or essential modes. Which is when the emergency- or essential power generators are running. These modes are not of interest to this case as the water injection will be stopped due to lack of power.

Seawater cooling

As can be seen from the utility flow diagram there are several cooling medium consumers. From an SRDP perspective the most interesting coolers are the suction- and discharge transfer gas coolers tagged 27HA0001 and 27HA0002 in Fig.2.2, respectively. These are of most interest as they are the heat exchangers with the highest loads, i.e., most heat transferred to the seawater. At the commingled seawater line downstream of the coolers there are manual valves installed that are used to balance the seawater temperature to the ultrafiltration and SRDP. One of these valves are marked “note 20” in Fig.2.1. With the membranes currently installed in the sulfate removal units (SRUs) the seawater temperature to the ultrafiltration package should not exceed 16 °C. This is an operational limitation not a design limitation and will be discussed in more detail later in this report. It should be noted that a shutdown of the transfer gas compressor (e.g., breakdown or lack of power) eliminates this major heat source for the seawater fed further on to the ultrafiltration and SRDP.

Ultrafiltration

After acting as cooling medium the seawater heads towards the ultrafiltration (UF) package shown inside bracket 29XX0004 in Fig.2.2. This package consists of 12 ultrafilters, six pairs (or twins) in parallel, where only one pair is shown in the flow diagram below. They remove particles down to 0.04 micron. The Δp across each membrane pair is monitored and the system will reduce- or shut in the specific pair that experiences to high pressure difference. Systematic backflushing of each pair with air is carried out by the control room operators at a regular basis. There is also a system for chemical CIP wash for these units with fresh water at elevated temperature in addition to sodium hypochlorite or acid as cleaning agents. A chlorine scavenger is injected downstream (wrongly marked upstream UF in Fig. 2.2) of the UF to remove free available chlorine, FAC. This is a preventive measure to protect the downstream SRU membranes from halogen damage as they are highly sensitive to oxidative substances like those associated with FAC [7]. The chlorine concentration is monitored by two online sensors in series which triggers rundown of the SRUs if the concentration gets too high.

Free available chlorine (FAC) is the accumulated concentration of Cl_2 , $NaOCl$, $Ca(OCl)_2$, $HOCl$ and OCl^- in water. By name; dissolved chlorine gas, sodium hypochlorite, calcium hypochlorite, hypochlorous acid, and hypochlorite ion, respectively. These substances form hypochlorous acid, $HOCl$, as shown in Rx. (R2.1 to R.2.3). Hypochlorous acid dissociates to hydrogen-, and hypochlorite ions in water as shown in Rx. (R2.4) [7]



The FAC is of interest in the field of membranes for two reasons. Firstly, chlorination is often used as disinfectant to prevent membrane biofouling in which introduces free available chlorine to the system. Secondly, membranes consisting of polyamide in the barrier layer are sensitive

to halogens like chlorine as it can yield the oxidative components termed FAC, which in turn can damage on the membranes and thus affect the membrane performance. [7] This is the reason for de-chlorination of the seawater upstream the SRUs.

Nanofiltration – Sulfate Removal Units

After UF the seawater is dosed with a scale inhibitor and the pressure is elevated with the SRU pumps (29PA0001A/B) before entering the SRUs, the initial part of the SRDP. To protect the membranes from scaling a trip is initiated if the scale inhibitor injection is lost for more than one minute.

The ultra-filtrated seawater enters the SRU shown inside bracket 29XX0005 in Fig. 2.2. The SRU module consists of two parallel and identical nanofiltration trains, SRU A and B. Each train consists of two parallel membrane banks in the first stage and one single bank in the second. The flow diagram only shows one train with a single first stage, this is not correct. Concentrate, typically named retentate in the literature, from the first stage is fed as feed to the second stage. The term of concentrate is used consistently throughout this report to be in line with the terminology used at Ivar Aasen.

Permeate seawater from both stages is mixed and the product stream should contain less than 30 ppmw sulfate. The sulfate concentration downstream the SRU is monitored, but there is no automatic trip function associated with it, only alarms that the operators can respond to manually.

The production of permeate from each SRU is controlled by two flow controllers with flow transmitters on feed, permeate and concentrate (from 2. stage). These flow transmitters control the flow into the package and the concentrate from the 2. stage. A SRU can have two permeate production modes, 360 or 416.5 m³/h. This means that the SRU essentially has four flow modes when run in parallel, 360, 416.5, 720 or 833 m³/h of permeate production. There is also a free mode where the control room operators can freely select setpoints between 360 and 416.5 m³/h for each SRU. This makes it possible to do a more gradual change in flow and produce permeate at other levels. In this thesis the assessments are based around the fixed flow modes.

Here, as for the UFs, pressure difference for each stage is monitored. This is the pressure difference from feed to concentrate side of the stages. Too high Δp for one of the stages initiates rundown of the SRU train in question. This in turn triggers chemical CIP wash which involves manual work and monitoring for several days. There is also a fouling factor criterion that can trigger run down and CIP wash, this factor is calculated from Δp measurements across the entire SRU trains.

A very common type of fouling for systems such as the SRUs is biofouling. To prevent/retard biofouling it is important to mitigate the biological growth in the system. This is done by chlorination and biocide batching upstream of the SRUs every second day. Biocide batching is necessary as microorganisms might pass into the SRUs not inactivated by the chlorine. Thus, if they enter the SRUs as “active” microorganisms, where no FAC is available, they might accumulate, and bio growth can occur. [7]

Oxygen removal - Deaeration Package

From the SRU the desulfated seawater enters the top of the vacuum tower, 29VH0001. This is a 17-meter tall, 3.3-meter diameter, pressure vessel designed to withstand full vacuum and an operating flow of 840 m³/h. The vacuum pumps and ejector generating vacuum in the tower are shown inside bracket 29XJ0001 in Fig.2.2. Dissolved oxygen in the seawater is released to a large extent inside the deaerator due to vacuum shifting equilibriums between gases in solution and in the gas phase towards the latter. The oxygen content should be reduced from an initial ~10 ppmw to about 50 ppbmol mechanically, and the remaining is removed chemically by injection of oxygen scavenger (Sodium bisulfite) to target O₂ content of less than 10 ppbmol. To be able to relate the introduced dissolved oxygen in the feed seawater to the target on the deaerator outlet the concentration units should be aligned. Thus, it can be shown that for oxygen dissolved in pure water 10 ppmw is equivalent to 5625 ppbmol. Pure seawater is used for the comparison as it is more complex to calculate the molar mass of the saline seawater from the SRU. Due to presence of salt in the feed to the DA the ppbmol is a bit higher than what presented above.

The operators adjust the flow of oxygen scavenger based on the oxygen content in the seawater downstream of the deaerator pumps. The oxygen content is measured with two online sensors, indicated with AI downstream the deaerator booster pumps (29PA0006A/B) in Fig. 2.2.

Membrane microbiocide is batched regularly to the SRUs, as mentioned previously, which neutralizes the effect of the oxygen scavenger during the batching. Thus, it is important to optimize the mechanical deaeration both to minimize O₂ introduced to the downstream system and reservoir during biocide batching and to reduce the use of chemicals to achieve the desired oxygen removal.

The green line in Figure 2.2 shows the “final product” from the SRDP. This treated water is then mixed with produced water (gray line) before it is injected to the reservoir. This is however outside the scope of interest in this thesis.

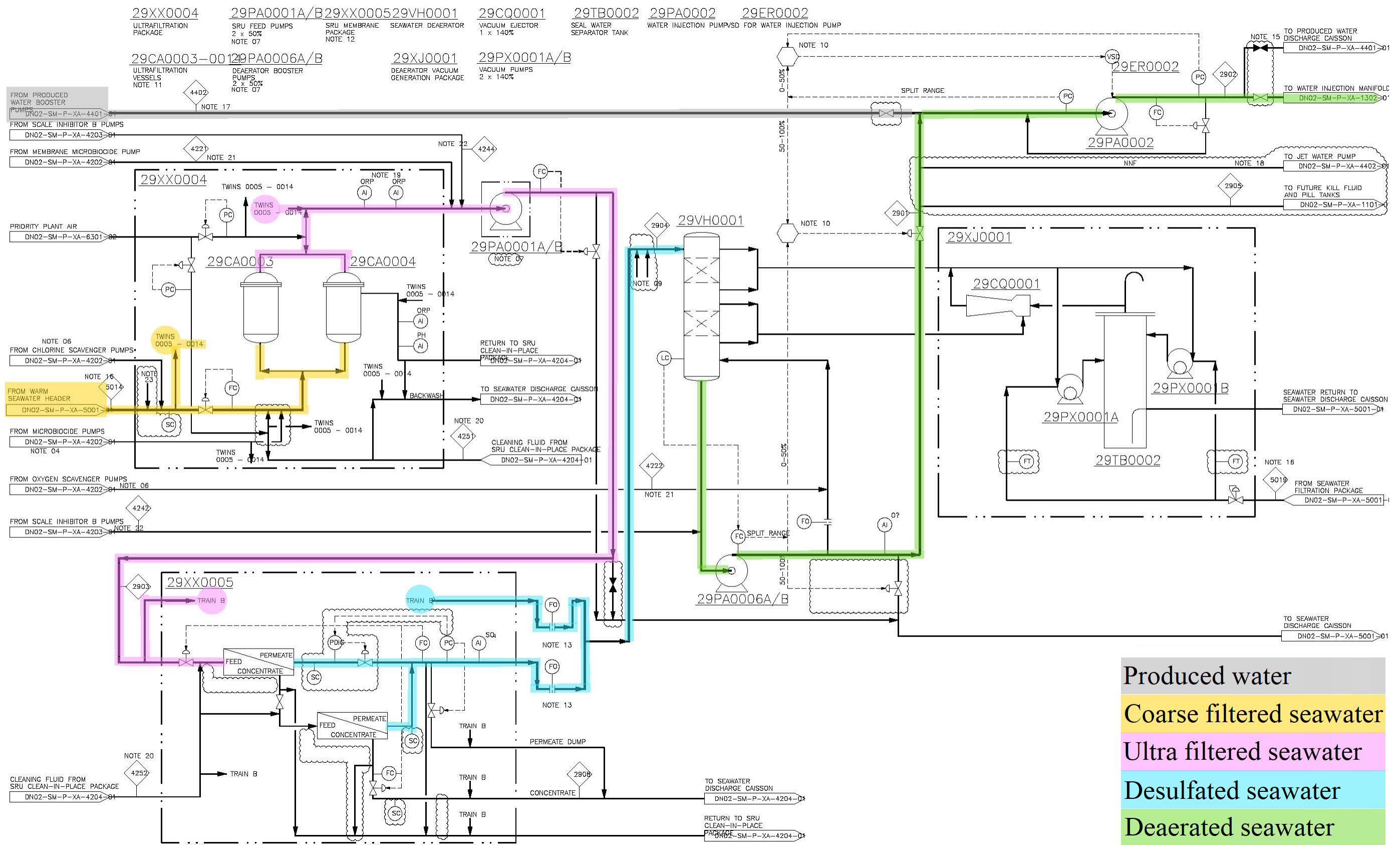


Figure 2.2: Overview of the ultrafiltration and SRDP on Ivar Aasen. Highlighted lines indicate main path for seawater though the system and is in accordance with the legend in the lower right corner.

2.2 Seawater characteristics

Table 2.1 represent the seawater characteristics at Ivar Aasen, i.e. this is the expected quality and content in the water supplied to the seawater system and subsequently to the SRDP. The analysis is performed by Intertek West Lab AS, on seawater sampled downstream of the seawater lift pumps. Hence, no unit operation has been performed on the sampled seawater. The only additive prior to this sample is chlorine in form of sodium hypochlorite. For more details on method, uncertainties, and more parameters see the entire report given in Appendix B.

Table 2.1: Fluid parameters and ion & elemental analysis. Seawater characteristic at Ivar Aasen.

	Parameter	Result
IONS	Chlorine, Cl ⁻	20100 mg/L
	Sodium, Na ⁺	11100 mg/L
	Sulfate, SO ₄ ²⁻	2700 mg/L
	Magnesium, Mg ²⁺	1330 mg/L
	Calcium, Ca ²⁺	413 mg/L
	Potassium, K ⁺	408 mg/L
	Bicarbonate, HCO ₃ ⁻	144 mg/L
	Strontium, Sr ²⁺	8.05 mg/L
	Boron	4.2 mg/L
	Barium	0.13 mg/L
	Phosphorous ¹	< 0.6 mg/L
	Iron ¹	< 0.1 mg/L
Elements	Lead	< 0.05 mg/L
	Zink	< 0.025 mg/L
Fluid properties	Total dissolved salt	36200 mg/L
	Total organic carbon	1.5 mg/L
	Specific gravity @ 15 °C	1.027
Notes:		
1. Result is below the practical qualitative limit of the test method applied.		

2.3 Sulfate Removal Units

The SRU package consist of two parallel two-staged nanofiltration systems (SRUs) fitted with DuPont SR90-440i membrane elements inserted in Pentair's CODELINE 80H60 membrane pressure vessels. The main intent of this unit operation is to reduce the sulfate content to below 30 mg/L before the seawater is further treated in the deaerator (explained in Ch. 2.4) and thereafter is commingled with produced water for pressure recovery in the reservoir. It is important to remove most of the sulfate ions in seawater to mitigate scaling (barium sulfate) and to reduce the availability of Sulfur in the reservoir to prevent souring via generation of hydrogen sulfide.

2.3.1 FilmTec™ SR90-440i membrane elements

The SR90-440i is a thin-film composite type of membrane packed in a spiral-wound configuration. DuPont, the manufacturer, states the following product specifications per membrane element:

- Active area: 40.9 m²
- Feed spacer thickness: 0.7112 mm
- Typical MgSO₄ rejection: 99.6 %
- Permeate flow rate: 39.7 m³/day

Where the permeate flow and salt rejection is based on 2000 ppm MgSO₄, 70 psi, 25 °C and 15 % recovered seawater in the permeate stream relative to the feed stream. The flowrates may vary ±20 % for the individual elements relative to the given permeate flow rate per membrane.

A general schematic build-up of these types of thin-film composite membranes is shown in Fig 2.3. Initially, against the feed side, an ultra-thin barrier layer is present. This is a dense polyamide layer, and it is resting on a microporous layer which in turn is supported by a support web. The ultra-thin barrier layer is of ~200 nm thickness, and the microporous layer of an average pore size of ~15 nm. [7] The exact composition of the SR90-440i membrane is not known as it is not publicly available.

Due to the combination of a dense and porous layer the solutes and solvent that permeates the membrane must first absorb and dissolve into-, diffuse through-, and desorb out of the dense polyamide layer. Thereafter, when desorbing the dense layer the permeate efficiently enters the microporous- and support layers which it needs to pass by convective flow to “become” permeate. What manages to pass the membrane is determined by a variety of complex mechanisms, in both the dense- and the porous layer, which will be discussed in more detail in Chapter 3.1.

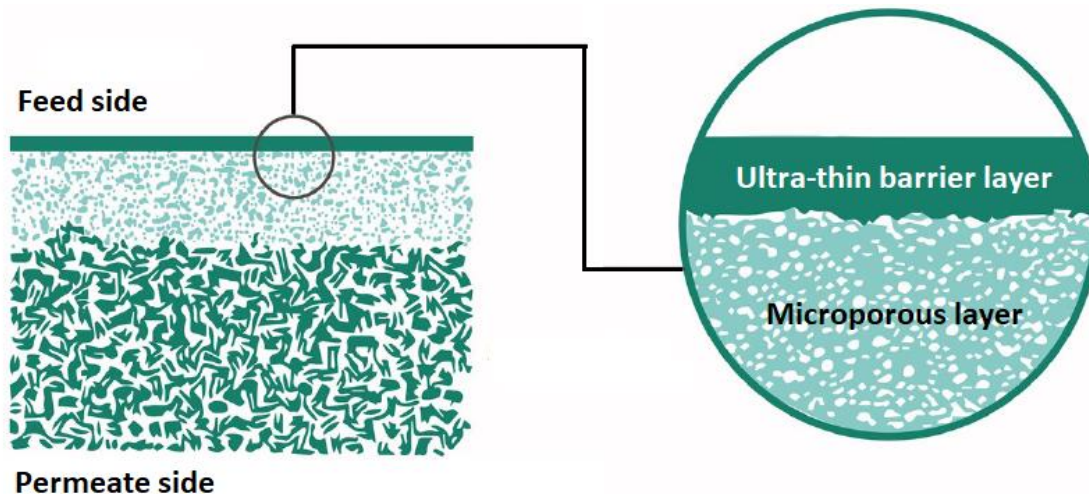


Figure 2.3: Schematic illustration of a Thin-Film composite membrane consisting of an ultra-thin polyamide barrier layer, microporous polysulfone layer, and a polyester support web. Modified from [7]

The SR90-440i membranes are designed to operate at maximum 41 barg with a pressure drop of maximum 0.7 barg per membrane element. The latter pressure drop criterion is along the feed channel, thus from feed inlet to concentrate outlet of a membrane cartridge. Since there are six membranes in series in each pressure vessel this indicates that the pressure drop from inlet to outlet of each stage should not exceed 4.2 barg. However, it is also noted in the supplier's data sheet that a maximum feed side differential pressure of 3.4 barg across the entire pressure vessel is not to be exceeded, that without any specification on the number of membranes in series inside the pressure vessel. Today the SRU trains are set to initiate rundown when $\Delta p \geq 3500$ mbar from feed to concentrate across a stage, 0.1 bar higher than what is recommended by DuPont. However, the pressure cells are placed at some distance from the SRU stages so that the actual feed-to-concentrate Δp will be lower due to piping pressure drop. The maximum operating temperature for this membrane is 45 °C. Besides this these membranes are designed to operate with feedwater within a pH of 5 to 9 with a maximum Silt Density Index (SDI) of 5, while it is recommended with an SDI time average below 3. And that the membranes do not tolerate free chlorine, and that the pH should lie within the range of 5 to 9.

SDI indicates the amount of particulate matter in water. It is calculated by a specific standardized method where the rate of decreased flow through a 45 μm filter upon plugging is measured as it is subjected to a constant feed pressure of the sample. SDI is typically used to estimate/predict fouling tendency in nanofiltration and reverse osmosis and is often referred to as fouling index. [7]

According to Aker BP documentation the SR90-440i is a "cold optimized" membrane designed to operate within 6.3 – 16 °C on the feedwater temperature. And it is stated that this type of membrane is to be used throughout the lifetime of Ivar Aasen. However, the base case was to use these cold optimized membranes in the initial phase of the project and then after some time switch to membranes suited for feedwater temperatures of 16 to 30 °C, SR90HR-440i. This base case was altered due to:

- Excess of cold seawater and the possibility to discard hot seawater from the transfer gas compressor coolers. Hence, able to keep feed temperature within the cold temperature range independent on Ivar Aasen production mode (free flow or compressor mode).
- high capital cost connected to exchanging all membranes to the “hot feedwater membranes”
- downtime on SRDP when Ivar Aasen is in free flow mode, since unable to reach > 16 °C without the transfer gas compressor running.

Free flow mode at Ivar Aasen is a production mode where the transfer compressor is stopped. This means that the separators are running at higher pressures only separating produced water from the hydrocarbons (oil and gas). In free flow mode the transfer gas coolers are not operational meaning that no additional heat can be transferred to the seawater entering the SRDP. Compressor mode is the normal production mode where the gas compressor is running.

The SR90-440i membranes are configured as spiral-wound membranes which are built as shown in the schematic in Fig. 2.4 and 2.5. These type of membrane modules are constructed with a membrane leaf and feed spacer mounted to- and rolled around an inner perforated core. All of which are inserted into a cartridge. From a single cartridge element point of view:

- **Membrane leaf** – performing the actual separation, from both sides. The membrane leaf consists of two semipermeable membranes that are glued together, about a permeate carrier material, with the permeate sides facing inwards. I.e., both sides of the membrane leaf are in touch with feed/concentrate. The term feed/concentrate is used throughout this report since feed entering a membrane becomes concentrate as concentration of the species rejected increases with movement along the feed spacer.
- **Permeate carrier material** – inner layer of a membrane leaf, it leads the permeate into the core. I.e., a spacer that provides a path into the inner product tube.
- **Feed spacer:** Separating the membrane leaf from itself upon rotation around the core so that feed/concentrate can flow along/ in between the membrane leaf. It helps inducing turbulence in the feed/concentrate stream which in turn reduces concentration polarization by reducing the thickness of the viscous stagnant layer.
- **Perforated product tube** – collects and transports permeate
- **Endcap** – locks and seals membrane cartridge against a previous- and succeeding membrane cartridge and/or start/end of the membrane pressure housing/vessel.
- **Anti-telescoping device** – prevents telescoping damage that can occur if feed/concentrate channel is exposed to too high pressure drop. Telescoping is that the spiral-wound element is “stretched” like a telescope due to high shearing force in the feed/concentrate flow direction. [7]

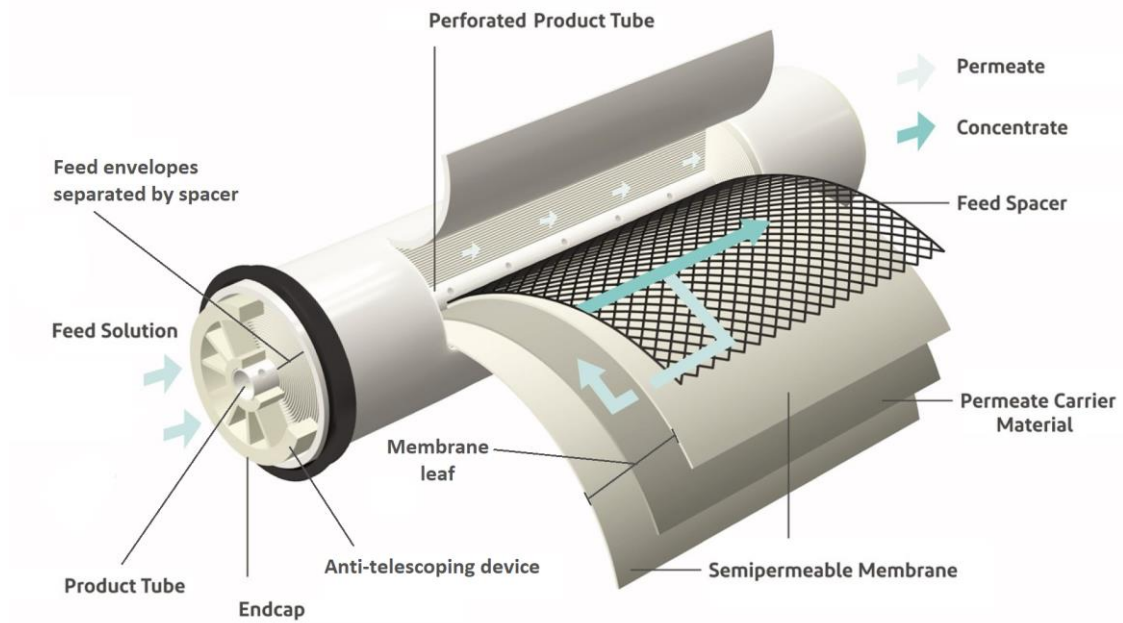


Figure 2.4: Schematic of DuPont's spiral-wound membrane elements. Modified from [7]

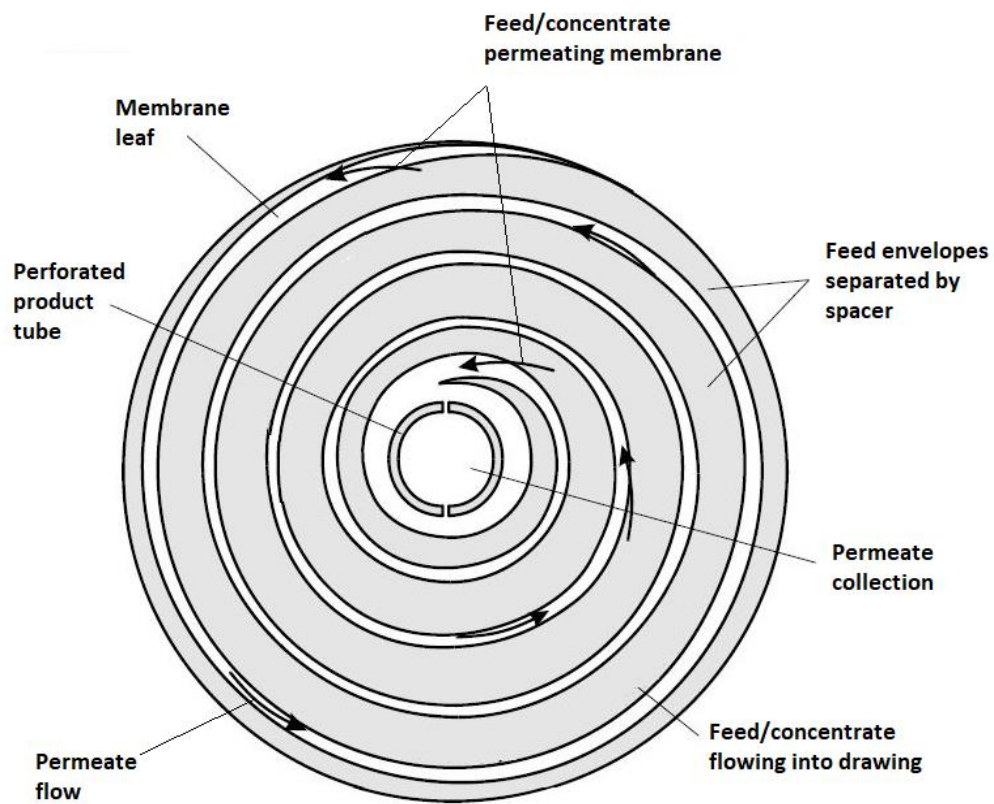


Figure 2.5: Cross-sectional view of a spiral-wound membrane. Permeate flow circulated inwards to the collection tube, while feed/concentrate flows axially (into the drawing). Modified from [8]

As a system these cartridges are mounted, six in series, inside of pressure vessels as shown by schematics in Fig. 2.6. Thus, feed enters axially between the feed envelopes made up by the membrane leaf separated by the feed spacer spirally attached to the perforated core. The part of the liquid that permeates the membrane will change direction normally to the feed stream as it starts circulating inwards to the core as illustrated in Fig. 2.5. Hence, this configuration yields a crossflow between the feed- and permeate side of a leaf. The part that is rejected by the membrane continues axially along the envelope and into the next cartridge in series. If it is the last cartridge in the pressure vessel it leaves as concentrate. Both feed/concentrate and permeate sides of the cartridge seals onto each other and/or into the start/end of the pressure vessel. This so that the permeate- and concentrate volumes are separated. The only connection between them is the thin-film composite membrane leaf.

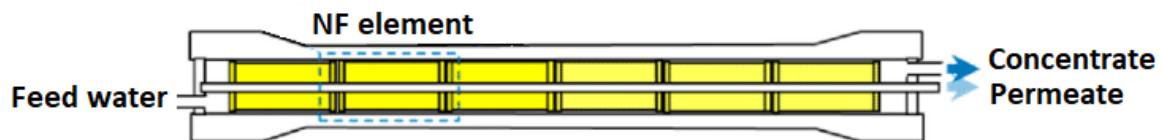


Figure 2.6: Pressure vessel schematic. Six membrane elements in series. The highlighted NF element indicates a spiral-wound element like the one illustrated in Fig. 2.4. Modified from [9]

It is recommended to keep the concentrate flow per pressure vessel equal to or higher than $3.4 \text{ m}^3/\text{h}$. This information is retrieved through dialogue with, Esther Lian, a membrane specialist working at National Oilwell Varco (NOV). NOV is a distributor of DuPont's membrane products. This minimum flow on reject per membrane is to ensure that the concentration polarization modulus does not exceeding 1.2. This in turn means that the turbulence in the feed/concentrate channel is the least it should be to mitigate biofouling and/or scaling. The topics of concentration polarization and scaling are described in detail in Ch. 3.1.5 and 3.1.6. This limit on concentrate flow indicates, for the SRUs, a minimum concentrate flow of 163.2 and $81.6 \text{ m}^3/\text{h}$ for the 1st and 2nd SRU stages, respectively. Thus, to follow this recommendation the lowest turndown per SRU is of $326.4 \text{ m}^3/\text{h}$ in terms seawater inlet flow with a total recovery of 75 % which is equivalent to a permeate production of $244.8 \text{ m}^3/\text{h}$ per SRU.

2.3.2 SRU staging

Each SRU train is of plugflow (no recirculation) multi-stage design. The SRUs on Ivar Aasen are two-staged systems with a staging ratio of 2:1. I.e., there are two stages where the initial stage has double the amount of membrane pressure vessels relative to the second stage [7]. Figure 2.7 shows the schematics of such a setup. The initial SRU stages on Ivar Aasen contain 48 parallel membrane vessels and the second stage 24. Each vessel contains six membrane elements in series. Hence, each of the first stages contains a total of 288 membranes while the second stages contain 144 membranes each. For such a system treating seawater the manufacturer of the membranes DuPont recommends a system recovery between 55-60 % [7]

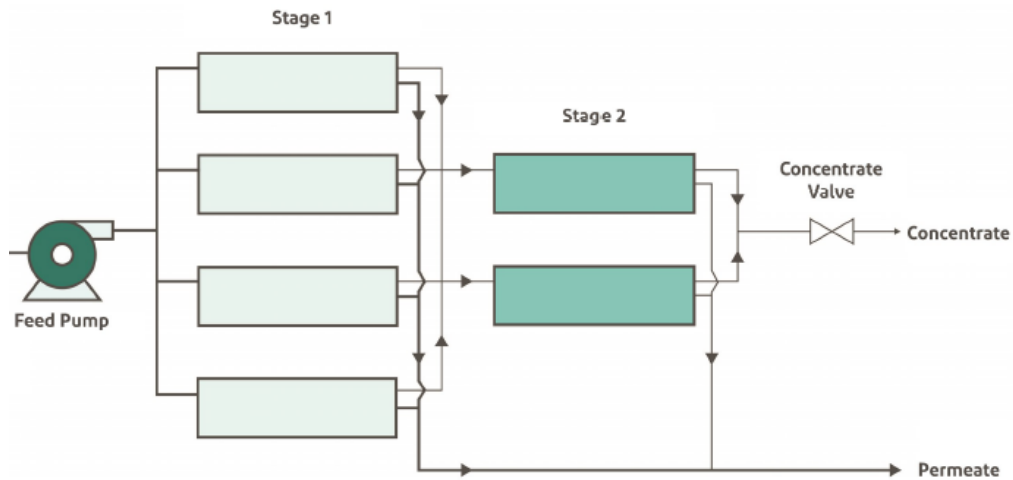


Figure 2.7: Schematic of a plugflow two-stage membrane system with 2:1 staging ratio. Modified from [7]

2.3.3 Membrane pressure vessels

The membrane pressure vessels installed are Pentair's CODELINE 80H60. These have an operating pressure of maximum 41.37 barg and an operating temperature range of -7 to 88 °C. Figure 2.8 shows the feed side of some pressure vessels at Ivar Aasen SRU where the above-mentioned operating conditions are marked. The membrane cartridges are stacked in series of six inside these vessels as shown in the schematic presentation in Fig. 2.6.



Figure 2.8: Feed side of a selection of membrane housings at Ivar Aasen SRU with nameplate indicating operating pressure and temperature.

It is possible, with special tools, to perform online probing of each membrane in series inside the pressure vessels. The probing tool consists of a valve arrangement and several meters of nylon tube connected and inserted to the central core via the red cap shown in Fig. 2.8. The

intent of this procedure is to check that the actual conductivity profile along the central tube increases according to a normal conductivity curve. For instance, a sudden steep increase in conductivity between the third and fourth cartridge can indicate that the fourth element is damaged as it permeates too much sulfate and other retained salts. The elements inside a pressure vessel will be distinguished via the length- or probing position. This type probing can be utilized to identify faulty membrane elements and to assess the overall pressure vessel conductivity profile. This means that one or more faulty cartridges can be localized and replaced instead of replacing all of them when the SRU does not deliver on the sulfate content criterion. [7] Aker BP's operation manual have more specifics about this procedure and a typical conductivity distribution for comparison of the measured data.

The reason that conductivity increases along the product tube is that increasingly more sulfate (and other retained salts) permeates the active membrane layer. This happens since the salt concentration increases along the feed/concentrate channel, which in turn gives an increasingly larger salt concentration gradient across the membrane active layer. This concentration gradient is the driving force for diffusion of sulfate through the membrane active layer. This is explained in more detail in Chapter 3.1.

2.3.4 Overall operating limits and feedwater requirements

The theory above shows that the membranes govern the SRU system operating limits. Table 2.2 gives a summary of both operating limits and feedwater requirements for this system.

Table 2.2: Summary of operating limits and feedwater requirements for the SRU based on assessment of technical documentation and SR90-440i datasheet.

Parameter	Value/range
Maximum pressure	41 barg
Δp_{\max} (feed-to-concentrate per pressure vessel)	3.4 barg
Maximum temperature	45 °C
Minimum concentrate flow per pressure vessel ¹	3.4 m ³ /h
Minimum permeate production per SRU ^{1,2}	244.8 m ³ /h
pH	5-9
SDI _{max} ³	5
pH (short time, batching)	2.5 – 11.0
Free chlorine ⁴	0 ppm
Notes:	
<ol style="list-style-type: none"> 1. Based on dialogue with NOV. 2. Based on total recovery of 75 % 3. SDI below 3 is recommended 4. Exposure to 1 ppm free chlorine for 200-1000 hours can result in permanently halogen damage. 	

2.3.5 Dimensions, design basis and performance guarantee

With both SRU trains running in parallel, it is designed to produce a yearly average of 20.000 Sm³ per day with a product (permeate) containing equal to or less than 30 mg/L sulfate. This permeate quality is guaranteed when system is operated with feed water temperature within 6.3 – 16 °C for the installed membranes. The design basis for sulfate concentration in the feedwater to the SRUs is ≤ 2800 mg/L, with a salinity of 3.5 %.

Salinity is the mass of inorganic salt per volume of water and is equivalent to Total Dissolved Salts (TDS). The two are used interchangeably in this report. TDS is often abbreviated for Total Dissolved Solids which accounts for all solids dissolved per volume of water, not only inorganic salts. And is for seawater almost equivalent to salinity due to being dominated by inorganic salts in the solution. In this thesis we either consider salinity or total dissolved salt.[7]

2.3.6 Control loops and adjustable parameters

For each SRU there are automatic control on the permeate flow and pressure difference between permeate from first and second stage. There is also a manual option for adjusting the feedwater temperature. This sub-chapter describes how the control loops are implemented and used on Ivar Aasen today with focus on normal operation. Figure 2.9 shows a simplified flow diagram where only the operational control loops are included. There are other control loops also which are in use during start-up, shut down and trips. E.g., the pressure controller that discards permeate (permeate dump) is “locked closed” by the software during normal operations. This is automated and used during start-up or trips.

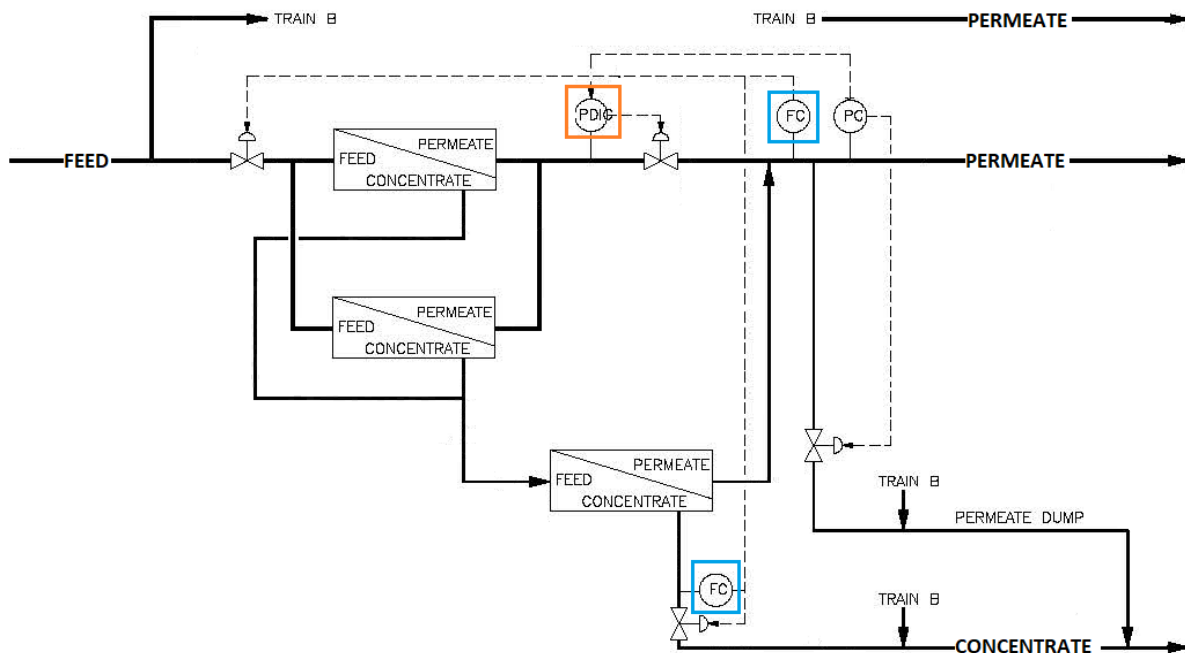


Figure 2.9: Simplified flow diagram with control loops for SRU A (identical for SRU B).

Temperature feedwater

There are no control loops for temperature on any parts of the SRU. However, it can be adjusted by use of manual valves by routing hot seawater from the transport gas heat exchangers to the UFs upstream of the SRUs. Figure 2.10 show a simplified flow diagram where these manual valves are highlighted in red brackets. The suction- and discharge coolers to the transport gas compressor are tagged 27HA0001/2.

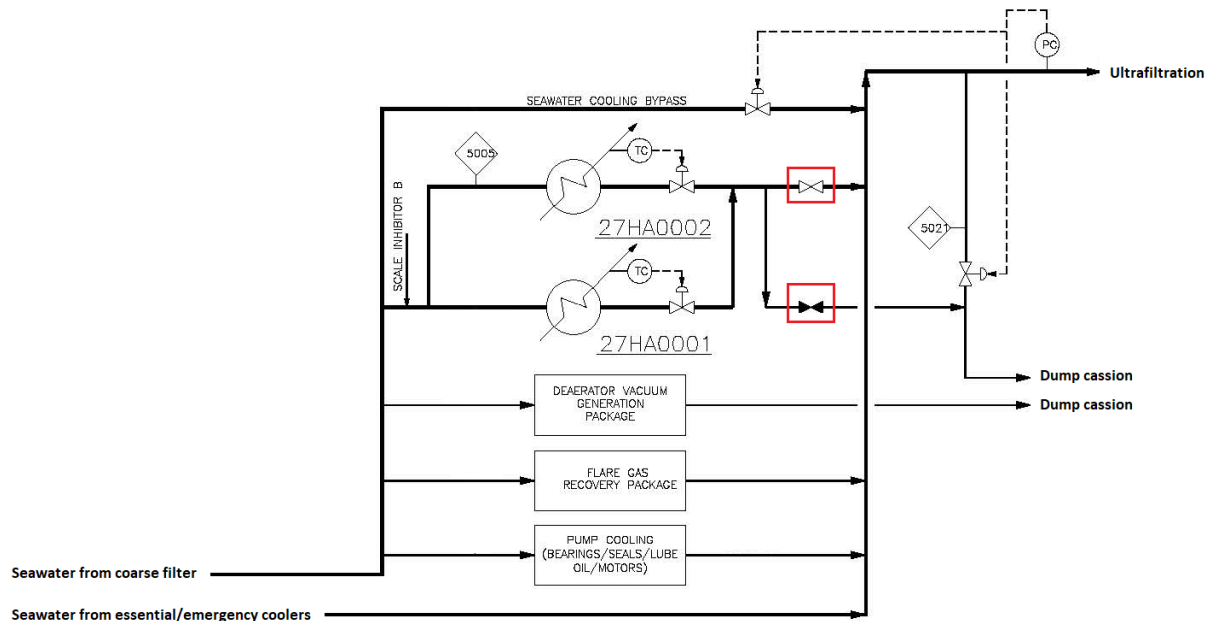


Figure 2.10: Flow diagram showing non-essential seawater coolers with highlighted manual regulating valves for seawater to UF and thereafter feed to SRU.

Permeate flow

The flow control consists of two control loops in a “flow ratio control” hierarchy marked with blue brackets in Fig. 2.9. There are flow measurements on permeate and concentrate out of the SRU. Actuated flow valves are installed on both feed to- and concentration out of the SRU.

The control room operator selects the desired permeate production mode which is either 360 or 416.5 m³/h for a single SRU running while 720 or 833 m³/h when both SRU operates in parallel . Alternatively the system is operated freely where the control room operators can select permeate setpoints in the range of 360 to 416.5 m³/h for each SRU. The feed flow controller calculates its setpoint as the sum of permeate and concentrate flow. While the concentrate flow controller calculates its setpoint as a factor of one third of the permeate flow, efficiently making it a “recovery controller”. Setting concentrate to be a third of the permeate flow implicitly regulates the system to a total recovery of 75 % which can be shown through Eqn. (2.1 -2.3), below.

$$\dot{Q}_c = \frac{1}{3}\dot{Q}_p \quad (2.1)$$

$$\begin{aligned} \dot{Q}_f &= \dot{Q}_p + \dot{Q}_c & \Rightarrow \\ \dot{Q}_f &= \frac{4}{3}\dot{Q}_p & (2.2) \end{aligned}$$

$$\begin{aligned} \mathcal{R} &= \frac{\text{water in permeate}}{\text{water in feed}} * 100\% & \Rightarrow \\ \mathcal{R} &\sim \frac{\dot{Q}_p}{\dot{Q}_f} * 100\% & (2.3) \end{aligned}$$

Where \dot{Q} is volumetric flowrate and subscripts f , p , and c denote feed-, permeate-, and concentrate flows. \mathcal{R} is the recovery which is more generally defined later in Tab. 3.1. Densities are implicitly assumed constant here as a volume flow balance is applied in Eqn. (2.2). This is no problem for the liquid phase due to incompressibility, thus the initial definition of the recovery is valid for the operating conditions at the SRU, low pressures and equal temperatures. However, a marginal error is introduced as the densities change slightly due to differences in salt concentrations between the flows. Thus, recovery is indicated with an approximation, $\mathcal{R} \sim$, in the above equation.

The recovery factor can be adjusted but that is done in the logic by the engineers, not by the operators in the control room. A total system recovery of 75% seems somewhat high relative to the recommended system recovery of 55-60 % given in DuPont's technical manual for a set-up like the one used in the SRUs [7].

The SRUs at Ivar Aasen are not fitted with separate measurements for the permeate flow from each stage. Thus, it is not possible to explicitly see how each stage performs with respect to recovery. This is a downside in turn of optimization as control over the specific recoveries is important. That is as to high recoveries can promote scaling, especially in the second stage treating water with much higher salt concentrations in the feed/concentrate channel.

Pressure difference between permeate 1st and 2nd stage

A pressure difference controller is installed (orange bracket in Fig. 2.9) to control Δp between permeate for the first and second stage. I.e. to control the pressure difference across the pressure valve on the 1st stage permeate outlet. Doing so regulates the system to a constant 1st stage permeate backpressure since the 2nd stage backpressure also regulated and constant. Thus, this control loop implicitly controls recovery distribution between the stages. This control loop will upon increased membrane fouling in the 1st stage shift the stage recovery from the 1st to the 2nd stage to keep the 1st stage permeate backpressure constant.

2.3.7 Performance Normalization

The intent with normalized performance is to be able to evaluate the SRU performance at different conditions. Hence, normalization enables the ability to observe presence of fouling that might be disguised in parameter changes like elevated temperature. Alternatively, a normalization against a reference point, typically clean membranes, to see if the plant experiences fouling above the expected degradation over time. [7] The DOW manual presents an algorithm for permeate flow normalization, however this is not applicable for this case as the SRU' are operated with fixed permeate flow.

Today the SRUs have a normalized fouling factor implemented in their control hierarchy. This algorithm seems flawed as it yields alarms, indicating need for CIP wash, when there is no need for this. For instance, the fouling factor alarm can be active upon start-up after CIP wash when the differential pressure across the SRU is at its lowest. The Algorithm is implemented by Siemens, and it uses the differential pressure across the SRUs. i.e. at feed side of 1st stages to the permeate after the permeate streams are coupled. It is a function of Δp and inlet temperature fitted with a set of parameters that depends on permeate production mode. Due to copyright and not being able to get in touch with Siemens about this topic the algorithm cannot be presented in this thesis. The technical documentation of it is does not show any data on how the parameters are fitted, thus it cannot be explained in any more details.

In a discussion with Halvor D., my Aker BP mentor, he argued that it is somewhat strange to base a normalized fouling factor on the differential pressure over the entire SRU, i.e. over both stages in which I agree. The reason is that the stages never will be fouled equally, thus the effects of this might enforce or counteract each other.

2.3.8 Membrane autopsy by Avista Technology

Back in June 2020 the membranes on SRU B had to be changed due to poor membrane performance. The package was unable to keep the permeate sulfate concentration below the criteria of 30 ppm. Aker BP hired Avista Technology to do a membrane autopsy on these used membranes to determine if:

- There were fouling, and the foulant nature.
- There was evidence of chemical or physical damages.
- The membranes were recoverable by performing cleaning trials.

Avista received 36 membranes but ended up analyzing three of them which was experiencing very low permeability and high differential pressure. Their conclusion from this autopsy was as follows:

“The first stage membranes were more heavily fouled that the second stage. The foulant was found to be mainly bacterial biological material and contained microorganisms as well as trace amounts of clay, calcium oxide and sand particles. All the membranes were suffering from compaction and halogen damage.”

Now, it needs to be emphasized that these membranes were not as operationally fouled as relative to when ordinary CIP washes are triggered. That is since these membranes were stopped due to lack of sulfate rejection not high differential pressure. Point is, it is important to distinguish between what initiates membrane changes and what triggers CIP. Hence, this conclusion might not be solely representative to the further investigation on reducing CIP frequency. It would have been interesting to see autopsy study on membranes subjected to rundown initiated by high differential pressure. However, due to the high costs of membrane changeout the membranes are typically not dismantled before the system cannot deliver on target. And for high differential pressure and low salt rejection to coincide is somewhat unlikely.

This autopsy indicates that it is highly likely that biofouling, clay, calcium oxide and sand particles all are contributing to membrane fouling and differential pressure build-up. Biofouling is likely to be the dominating type of fouling due as it was the most present type found in the autopsy. Besides this there are or have been in periods oxidative substances yielding halogen damages present. Probably due to exposure to free available chlorine.

Fouling in the lead element of the 1st stage is shown in figure 2.11. It is evidently more fouling present on the feed side of the element, to the right in this figure. Very little fouling was visible in the other two tail elements that was examined. Thus the initial part of an initial element was most heavily fouled. This is as described above, mainly biofouling.



Figure 2.11: Fouling on a lead element in the 1st stage of SRU B. Concentrate side to the left and feed side to the right. Fouling is mainly biofouling and is most evident on feed side. Membrane autopsy performed by Avista.

When it comes to membrane damage an interesting finding, besides compaction and halogen damage, was done on the lead element of the first stage. The feed spacer was protruding the concentrate side of the elements. Damages of such kind are often termed telescoping which

typically can occur if the axial pressure drop becomes is too high. Figure 2.12 below show both feed- and concentrate side of the membrane element in question. On the left-hand side is the feed side where a gap can be seen, while on the right side the spacer is visible as it has been protruded or telescoped out from its position. The netting showing in this picture should not be visible.



Figure 2.12: Telescoping of feed spacer on a lead element in the 1st stage of SRU B. Gapping in the membrane feed side to the left. And telescoped feed spacer at the concentrate side to the right. Membrane autopsy performed by Avista.

The next figure, Fig. 2.13, better show the spacer condition upon dissection/opening of the element. This spacer is from the same lead element as shown in Fig. 2.12. The other two elements studied, tail elements from both stages, did not show any kind telescoping.



Figure 2.13: Damaged spacer due to telescoping in one of the lead elements in the 1st stage of SRU B. Membrane autopsy performed by Avista.

There was also evidence of compaction which can be a result of normal wear and tear over the years of operation. Or membranes being exposed to too high differential pressure from feed/concentrate to permeate for a shorter period. Such as to late system rundown triggered by differential pressure from the feed to concentrate side of a SRU stage.

2.3.9 Historical performance

The frequency of CIP washes is considered the most important performance parameter. To do an assessment of it all available historical data on the system have been assessed. From the earliest available data until today it has been performed a total number of 21 CIP washes on SRU A and 18 on SRU B. The plot in Fig. 2.14 shows, from top to bottom, the temperatures in the SRUs and flow of cleaning fluid from the CIP tank. Flow from the CIP tank only enters the SRU mechanically aligned for it, thus spikes in temperature is an indicator of which SRU being subjected to CIP wash as the cleaning fluid is heated as it is circulated in the SRUs. Rulers are placed to separate years in this plot, thus a total period of ~4.3 years is plotted. The “X’es” marks of approximately when the membrane cartridges were replaced for each of the SRUs.

The annual average number of CIP washed on SRU A and B is 5.1 and 4.4, respectively. These averages are based on counting all CIP washes and membrane replacements (X’es in the plot) performed on the respective SRU. The annual medians are at the same time 5.5 and 4.5 for system A and B, respectively. If all CIPs and cartridge replacements are divided equally on each SRU the yearly average becomes 4.8 CIPs per SRU with a median of 5.

It should be mentioned that it is not considered how the SRUs are operated during this 4+ year period, e.g. down time, flow modes, and so forth. This can obviously affect the time interval between each subsequent CIP, and might explain why SRU has been subjected to more CIP washes compared to B. No written information about running the SRUs differently is found, so the only known difference is that SRU B have had “newer membranes” during this 4-year period as they were replaced in 2020 compared to A being replaced very recently.

Integration of volumetric flowrates to each SRU in this period shows that the total permeate production are almost identical for the SRUs with 11.254.008 m³ for A and 11.315.406 m³ from B. Thus, SRU B has produced slightly more (60.000 m³) during the evaluated time span of 4.3 years. This means that the higher CIP frequency for SRU A is caused by something else than production loading relative to B.

Based on this assessment it is probably most accurate to use the equally distributed average of 4.8 CIP washes per year per SRU. Thus, approximately 4 CIP washes can be expected during the project period.

2.3.10 Typical operational problems

In dialogue with NOV and DuPont they both stated that fouling in SRUs of ultrafiltrated seawater is almost exclusively due to biofouling. For that reason both DuPont and NOV recommend considering the FilmTec Fortilife SR90i membranes with improved spacer geometry. The Fortilife SR90i are designed for offshore sulfate removal applications and should operate at much lower differential pressure and be more resistant to biofouling than the SR90-440i. Lower pressure differences will yield lower power consume for the SRU pumps. They are of same dimensions and withstands the same operational parameters (temperature, pH, etc.) so that it should a simple change.

This project does not consider new types of membrane elements due to relatively fresh membrane elements installed in both SRUs . Thus, it is still of value to try to optimize the SR90-440i elements due to their long remaining lifetime. However, the Fortilife membranes should still be considered upon the next element replacements some years from now.

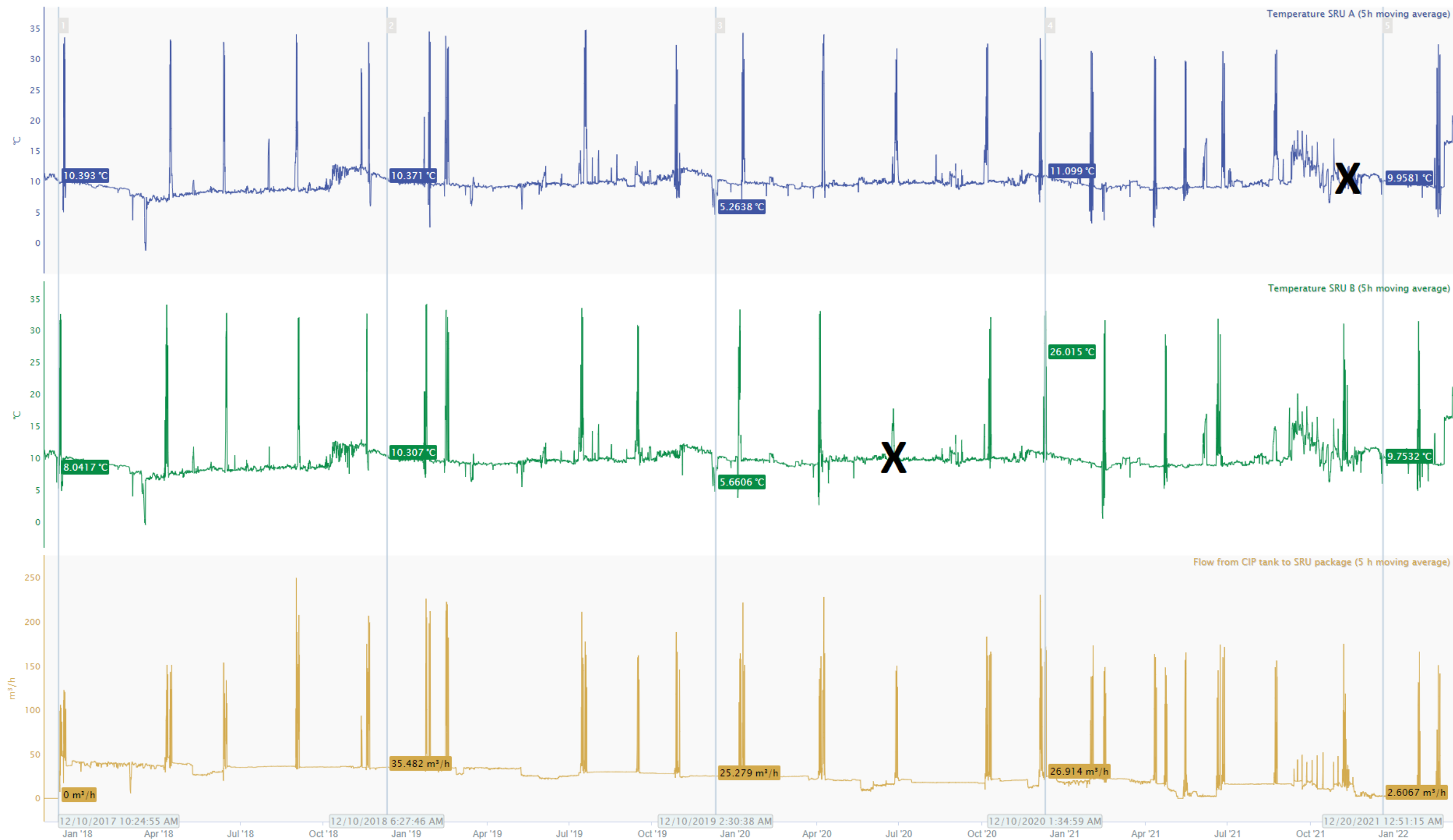


Figure 2.14: All available historical data on SRU liquid temperatures and cleaning fluid flow from the CIP tank towards the SRU package. Spikes in cleaning fluid flow (bottom lane) indicates that washing is in progress but not which SRU being washed as the flowmeter is on supply line capable of feeding both SRUs. Temperature spikes above 30 °C (mid and upper lane) indicate what SRU is washed as the cleaning fluid is heated while circulated through the SRU in question.

2.4 Deaeration package

The deaeration system at Ivar Aasen is a relatively simple system that utilizes vacuum to reduce the amount of dissolved oxygen in seawater. The main task for the system is reduce the oxygen content to less than 50 ppb by mechanical deaeration, and to less than 10 ppb with chemical treatment. The reason is to mitigate corrosion and aerobic bio growth in downstream system. Aerobic bio growth can in turn cause reservoir souring through bacterial hydrogen sulfide production in the reservoir [10].

2.4.1 Technical build-up and functionality

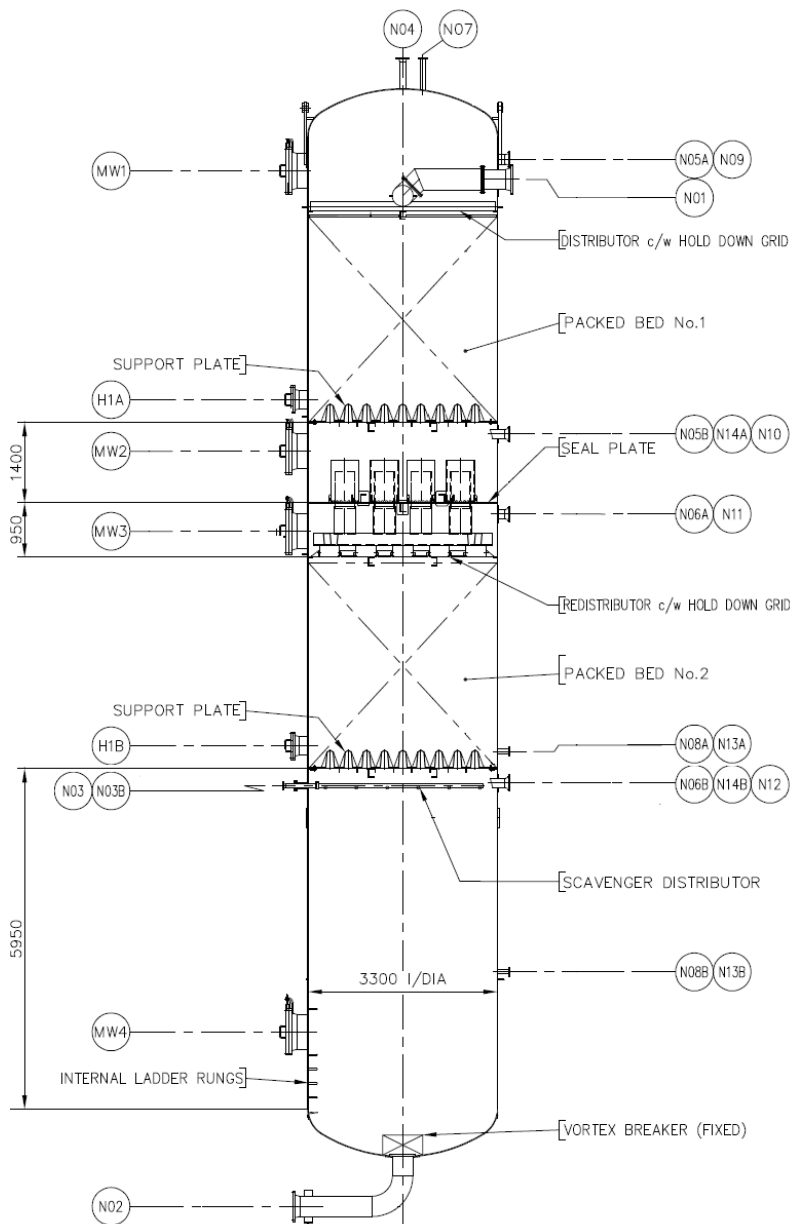
The main principle of the mechanical deaeration in the deaerator is based on that all gases dissolved in a liquid will exert an equilibrium pressure in an interfacing gas phase. Or equilibrium partial pressure if multiple gases are present. Altering the total pressure near a liquid interface makes all partial pressures follow proportionally and the amount of dissolved gases in the liquid will be affected. This pressure reduction shifts the dissolved gas equilibria towards the gas phase. This means that the dissolved gases will progressively be released from the solution and out to the gas phase until equilibrium is reached. Liquid temperature and salinity are also important parameters as they affect the equilibrium partial pressures.

With very low pressures and high surface area, as inside the deaerator, water evaporation will also occur to some extent. Boiling should not be present as the seawater saturation pressure always are beneath the gas phase pressures in the stages. This can be shown by plotting the vapor pressures against the total gas phase pressures as done in Appendix C. The released gases and water vapor are conveyed through a vacuum pump, maintaining the close to absolute vacuum inside the deaerator.

Deaerator – vacuum tower

The schematics shown in Fig. 2.15 visualizes the nozzles and internals of the vacuum tower installed at Ivar Aasen. This is the unit tagged 29VH0001 in the flow diagram presented in Fig. 2.2.

Seawater from the SRUs enters the top of the deaerator through nozzle N01 and is fed into the initial vacuum stage packed bed via a distributor. The distributor is a device intended to spread the water over the entire tower cross section area which is important to utilize as much of the packing material as possible. This tower is fitted with a tubular feed pipe type of distributor which is pipe network perforated with holes similar to the one being tested in Fig. 2.16. It is designed to operate efficiently in the range of 10 to 100 % of the deaerator design flow.



NOZZLE DATA TABLE		
ITEM	QTY.	SERVICE
N01	1	WATER INLET
N02	1	WATER OUTLET
N03	1	OXYGEN SCAVENGER INLET
N03B	1	OXYGEN SCAVENGER INLET ACCESS
N04	1	PRESSURE RELIEF
N05A/B	2	STAGE 1 VACUUM OUTLET
N06A/B	2	STAGE 2 VACUUM OUTLET
N07	1	VENT c/w BLIND
N08A/B	2	LEVEL TRANSMITTER
N09	1	PRESSURE CONNECTION
N10	1	PRESSURE CONNECTION
N11	1	PRESSURE CONNECTION
N12	1	PRESSURE CONNECTION
N13A/B	2	LEVEL TRANSMITTER
N14A	1	SAMPLE CONNECTION
N14B	1	SAMPLE CONNECTION
H1A/B	2	PACKING ACCESS c/w BLIND & HINGE
MW1	1	MANWAY c/w BLIND & DAVIT
MW2	1	MANWAY c/w BLIND & DAVIT
MW3	1	MANWAY c/w BLIND & DAVIT
MW4	1	MANWAY c/w BLIND & DAVIT

Figure 2.15: Schematic view of vacuum tower internals, with height scale of some internal sections in mm and a dedicated nozzle table. This figure is modified from the original unpublished drawing distributed by Eta Process Plant and is presented here with their consent.



Figure 2.16: Pipe liquid distributor tested with liquid. [11]

Seawater flows downwards through/over/around the packing material while dissolved gases are being released due to the vacuum. Thus, a multiphase flow of seawater and gases occurs where the gas phase primarily consisting of nitrogen, oxygen, and some carbon dioxide released from the seawater and some water vapor due to evaporation and entrainment.

The intent of the packed bed is to yield a high contact area between liquid and gas to increase the mass transfer of dissolved gases into the gas phase. The packed beds in the deaerator are randomly packed with Beta ring™ no. 2 shown in Fig. 2.17. This type of beta rings has a 94 % void fraction and is constructed to prefer vertical orientation of the axes so that the packed bed pressure drop is minimized [10].



Figure 2.17: Packing material Beta Ring™ no. 2. [10]

At the bottom of each packed bed there is a support plate mounted intended to prevent packing material from leaving the bed by gravity or seawater shearing. After the initial packed bed the seawater flows down onto the seal plate. This seal plate consists of a series of downtubes fitted with seal caps as shown in Fig. 2.18. The height difference between the fluid passage in the outer seal cap and the inner downcomers generates water locks preventing gas to pass between the stages. That to the extent of the pressure difference across the seal plate versus the hydrostatic water column in these water locks. The down pipes are in turn connected to a re-distributor system with the same intent and functionality as the above-described distributor.

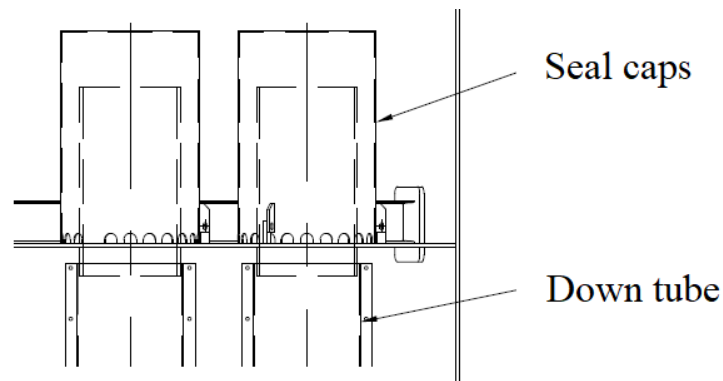


Figure 2.18: Schematic view of down tubes and seal caps through a section of the seal plate separating the two vacuum stages. This figure is modified from the original unpublished drawing distributed by Eta Process Plant and is presented here with their consent.

Vacuum in the 1st packed bed gas phase is induced by a vacuum pump connected via nozzle N05A/B. And by ejector, in connection with the same vacuum pump, via nozzles N06A/B in the 2nd packed bed. These two stages are separated with the above-mentioned seal plate which enables a staged vacuum treatment. The initial stage has a higher absolute pressure than the second, giving an ascending degree of vacuum from the 1st to the 2nd stage. This reduces the area subjected to the lowest pressures which can increase the vacuum pump efficiency due to reducing the water evaporation. [12]

The second packed bed is identical to the first in both dimensions and type of packing material. The only difference from the 1st stage is that this stage is subjected to a higher vacuum drawn by an atmospheric air driven ejector. This ejector is driven by the same vacuum pump as the one inducing vacuum in the first packed bed. Due to lower total pressures more dissolved gases are released from the seawater. The mechanical deaeration are in practice done as the seawater flows out of the 2nd stage and into to the liquid sump.

Beneath the support plate of the 2nd packed bed, via nozzle N03, a recycle line from the deaerator booster pumps is introduced. This is where the oxygen scavenger is injected to chemically deaerated the seawater down to the target oxygen content of less than 10 ppb mol. Introducing this chemical here facilitates the reaction through good mixing and a sufficient residence time. The liquid sump volume is designed to give the liquid 3 minutes residence time in the sump and is according to the manufacturer (Eta Process Plant) more than sufficient for a satisfactory chemical deaeration before seawater leaves the sump. To what extent the chemical deaeration reaction is done when the seawater is measured for dissolved oxygen downstream the deaerator pumps is unknown and will not be assessed in this project. The reaction is still occurring since the oxygen content is much lower at the further downstream sample point on the suction of the water injection pump. This is also affected by dilution of the seawater with produced water as these are mixed upstream the water injection pump.

Deaerated seawater leaves the vacuum tower via a vortex breaker that prevents liquid vortices that potentially can break the vacuum inside the tower. The seawater leaving the deaerator is stripped (to a certain extent) of both sulfate- and oxygen and it is mixed with produced water from the oil separators and injected into the reservoir as pressure recovery.

The vacuum tower is also fitted with both a series of manways and pressure connections, N09 – N12 and MW1-MW4. These are for maintenance, inspections, and troubleshooting of the packed beds.

Vacuum generation package – vacuum pump

The vacuum generation package shown in the brackets in Fig. 2.19 consists of two 100% vacuum pumps (29PX0001A/B), a gas ejector (29CQ0001) and a seal water system with a seal water separator (29TB0002).

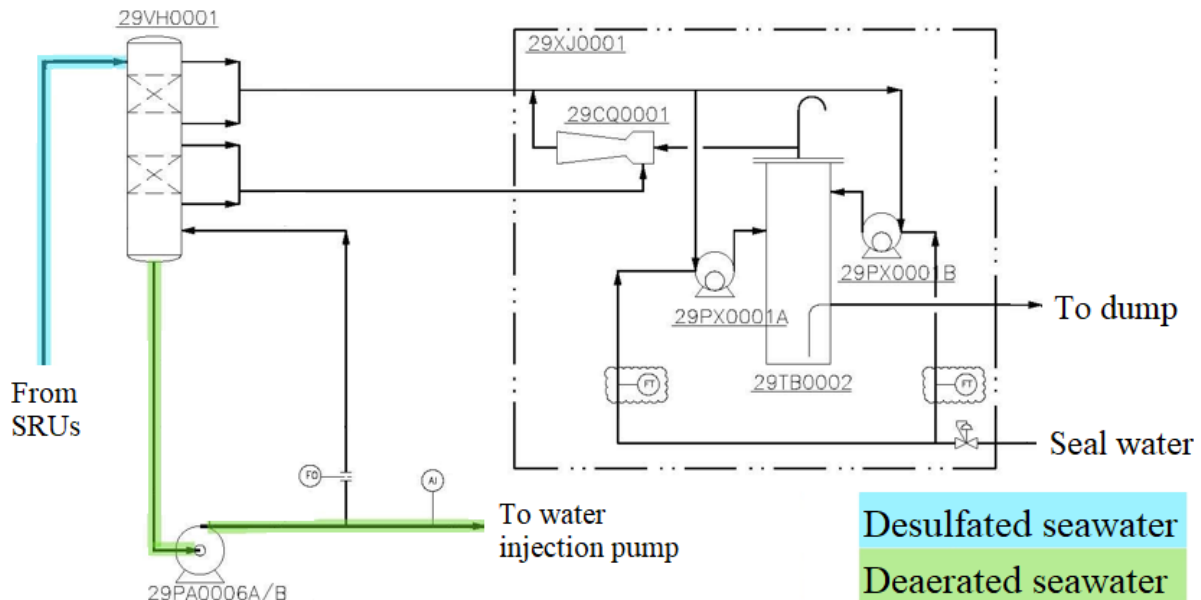


Figure 2.19: Overview of the vacuum generation package and its interface with the vacuum tower. Highlighted lines indicate main path of seawater through the system and is in accordance with the legend in the lower right corner.

The vacuum pumps used in the system are of type Busch GVT LB1507A, which is a two staged liquid ring vacuum pumps. Fig. 2.20 gives a good illustration of these type of vacuum pumps. The ultimate pressure rating for the pump is 33 mbara and it is **not** ultimate pressure proof. This means that operating it at pressures equal to or below this pressure will damage the pump [13].

The measured pressure in the 1st packed bed (in addition to piping pressure drop) is the pressure delivered by the vacuum pumps. Hence, the vacuum in the 1st packed bed should be somewhat higher than 33 mbara since there will be some degree of pressure drop between the pressure transmitter and the pump suction port. The actual stage pressures will also depend on seawater feed flow and temperature. The pressure in the 2nd stage is governed by an ejector, driven by the vacuum pump in operation, which boosts the vacuum.

The working principle of this type of pumps is based on a rotating liquid ring in contact with an off-centric impeller. This liquid ring, denoted “i” in Fig. 2.20, is formed by the rotating impeller in contact with water inside the pump housing. This liquid ring isolates the gas volumes between each impeller blade and blocks the gas connection between the suction and discharge of the pump. The “off centricity” generates a piston effect upon rotation sucking in, compressing, and discharging the conveyed gas with the different angular positions. Describing a full rotation of a singular gas volume between to neighboring blades gives a good understanding of the working principle: [13]

- At 12 o'clock the impeller volume should be entirely filled with seal water.
- From 11 o'clock to 8 o'clock the impeller volume is in connection with the pump suction "a". Due to the impellers "off centricity" the liquid starts to leave the impeller volume inducing suction of gas via this suction connection.
- From about 8 o'clock to 2 o'clock the impeller volume is isolated, i.e. not in connection with the suction or discharge ports.
- After 6 o'clock the impeller volume starts to compress as it gets gradually more liquid filled.
- From 2 o'clock to 12 o'clock the gas in the impeller volume is driven out through discharge port "e".

The liquid seal ring is obviously important for the functionality. And the manufacturer states that at pump stand still the liquid level inside the pump should be approximately at the level of the shaft centerline. It is also important to consider that this liquid seal is subjected to both compression and potentially heat of condensation if conveying a saturated gas. [13] There are also mechanical seals on the shaft on both sides of the pump which are flushed with fresh water. These are of no interest in this project as they do not affect the vacuum pump performance. For that reason discussion regarding seal water only relates to the liquid seal ring in this report.

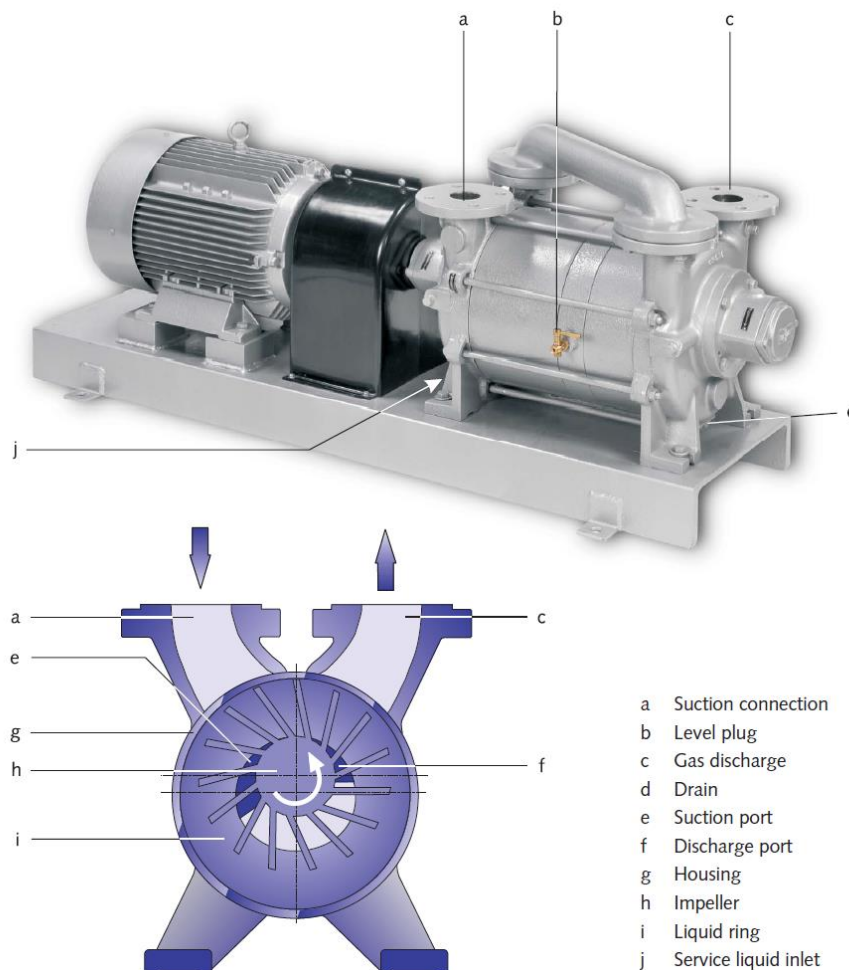


Figure 2.20: Two staged Busch liquid ring vacuum pump. Schematic view and pump externals. [13]

According to a performance assessment on the plant, performed by Eta Process Plant, the vacuum pumps are to be operated with the lowest seal water temperature of $\leq 12^{\circ}\text{C}$ or \leq feed water temperature to achieve max efficiency. The reason for this is most likely to induce sufficient cooling to the liquid seal ring so that it always remains liquid even though operating at low pressures. Thus, to prevent evaporation and bubble formation near the suction section (low pressure) and cavitation as the gas pressure increases with angular movement inside the pump [13]. Evaporation and liquid entrainment will also induce liquid loss from the seal ring which will affect its performance. The seal water used for the liquid seal rings at Ivar Aasen is seawater taken downstream of the coarse filters which have a temperature from ~ 6 to 12°C seasonally which is within the above-mentioned criterion.

The pumps and seal water separator are levelled and fitted with bypasses so that the seal water flow to the operating pump adjusts after the amount needed. This also ensures drainage to correct liquid level in the pumps when they are not running. The seal water liquid level in the seal water separator is slightly below the shaft centerline in the pumps. This introduces a pressure balance so that liquid level alterations in the running pump balances the seal flow between the two. An important note, for this to function across all operations modes the seal water flow introduced to the system must be enough to cover the most consuming operation mode.

A continuous feed of seal liquid must be supplied to the pump casing so that the liquid seal ring works as intended. Any excess liquid will simply be thrown out of the pump outlet. It is important for the pump performance that the seal pressure is not too high. The pump manufacturer states that it should not exceed 0.1 barg above the pump outlet pressure as it will deteriorate the performance [13]. The reason for performance deterioration is likely due to high seal pressure is increasing the casing pressure and thus reduce the impeller gas volumes which in turn reduces the pumps performance.

According to Aker BP's P&ID of this system the pressure control valve determining the seal feed pressure is to be set at 1 barg which is equivalent to 2.013 bara. This seems somewhat high as the pump discharge delivers gas to an atmospheric seal water separator. There will be some pressure loss in the piping from the pump discharge to the vent on this separator, but not as high as one bar. Operators at Ivar Aasen checked this seal pressure and flow to be 0.143 bara and $3.6\text{ m}^3/\text{h}$ the 14th of march. This pressure is within the recommendations, but the seal flow is very low. The operating and maintenance manual states that the seal water always must be greater than $6.5\text{ m}^3/\text{h}$. There was, in the design, a failsafe logic that would trip the running pump if the seal flow measurement read less than $6.5\text{ m}^3/\text{h}$.

The operators at Ivar Aasen could tell that the seal flow had been adjusted several times during the last 5 years with intent to maximize the vacuum pump performance. A review on most of these adjustments, relative to stage pressures, was done see if this strategy is favorable for the vacuum pump performance. The details and trends used for this is shown in Appendix D. Based on this simple analysis it was not possible to conclude that reducing the seal water flow increased vacuum performance. Some seal flow reductions gave higher stage pressure, and some gave lower. There were also some increases in seal flow during this time, some of them improved the vacuum and other did not. After discussion with the Aker BP supervisor the seal flow to both pumps was returned to the minimum flow of $6.5\text{ m}^3/\text{h}$.

Ejector

The ejector installed in the vacuum generation package is an atmospheric air driven ejector. Its schematic build-up is illustrated in Fig. 2.21 where in the actual process there are no bypass line. Air is introduced as motive gas by the pressure gradient induced by the operating vacuum pump. The ejector acts as an additional pumping stage yielding lower suction than what can be achieved by the vacuum pump alone.

The ejector concept is based on the relation between static pressure and fluid velocity or dynamic pressure. The motive nozzle increases the air flow velocity through gas expansion and generates a low-pressure region in the entry of the venturi tube. The static pressure in this low-pressure region is below that of the inlet pressure which in turn induces entrainment of the inlet gas into the motive gas. In the downstream diffuser the velocity is reduced, and pressure will reach that of the vacuum pump suction plus pressure drop between the two. Hence, the increase of velocity in the nozzle induces a suction with a lower absolute pressure than what the vacuum pump manages to induce in terms of suction pressure. [14]

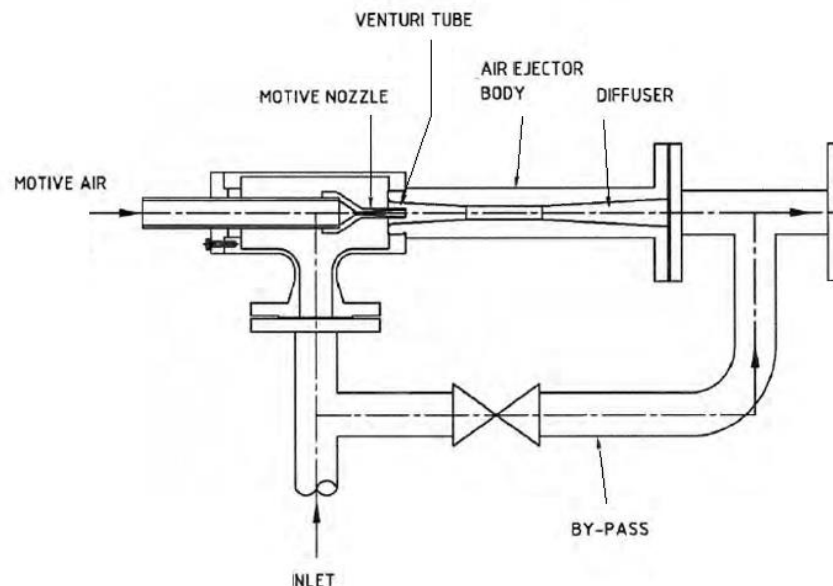


Figure 2.21: Schematic presentation of the atmospheric air driven ejector. This figure is taken from an unpublished drawing distributed by Busch Vacuum Solutions and is presented here with their consent.

After dialogue with the Aker BP supervisor it became clear that the motive gas line to the ejector have been modified some time ago. Earlier the motive gas was taken from the vent of the seal gas separator. Now these systems are separated so the motive gas is taken from the outside air. The flow diagrams in Fig. 2.2 and 2.19 shows the original design. This modification was done due to suspicion of freezing in the ejector as it was/is in repeated need of flushing due to losing its vacuum from time to time. Dialogue with the operators revealed that they typically need to flush the ejector every third day during summertime and up to 2-3 times a shift when it is colder ambient temperatures surrounding the ejector. A trend analysis on ejector flushing frequency was performed but gave no readable results due to the many variations, both operational and seasonal.

The Aker BP supervisor did a simulation on air and the Joule-Thomson effect in the ejector to see if it could cause freezing when subjected to the typical ambient temperature conditions. This showed that the Joule-Thomson effect was marginal and that it is not likely to be able to cause any freezing problems. Air temperature was also trended back several years back to check if this could be a problem during the coldest periods. But the air temperature seldom drops below 0 °C which is another indication that the ejector problems are not caused by freezing.

2.4.2 Dimensions, design basis and performance guarantee

The deaerator tower is designed to mechanically remove oxygen down to less than 50 ppb mol in a seawater flowrate of 840 m³/h holding a temperature between 16 to 30 °C containing a maximum of 10 ppmw dissolved oxygen. Including chemical deaeration, with oxygen scavenger, the dissolved oxygen content is guaranteed to be less than 10 ppb mol. For pure water, 10 ppmw is equivalent to 5625 ppb mol.

Fig. 2.22 shows the performance curve for the mechanical deaeration as function of seawater temperature of both the designed flowrate and a turndown to 20 % of that. This performance curve is established by the manufacturer of the system, Eta Process Plant. From this plot is evident that the “less than 50 ppb mol guarantee” is based on the seawater holding equal to or above 16 °C. The oxygen concentration is given in ppb in volume basis in this plot, but this is explicitly stated to be ppbv (molar) in the technical documentation discussing this plot.

The chemical deaeration is performed to ensure a dissolved oxygen content less than 10 ppb mol in the product stream. According to Eta Process Plant’s performance calculations the oxygen content at maximum seawater rate (840 m³/h) should be reduced from 50 to less than 10 ppb mol by injecting 2.62 L/h of oxygen scavenger with a concentration of 60 %. The oxygen scavenger used at Ivar Aasen 40 % which means that a dosage rate of ~2.8 L/h at 840 m³/h of seawater should be sufficient according to design. This is calculated with the same formula as used by Eta Process Plant which is not shared in this thesis as it is marked as confidential. The dosage rate is proportional to the seawater load which makes it easy to convert the design dosage rate of oxygen scavenger for different seawater inlet flows to the deaerator. It should be mentioned that Aker BP is considering a new type of catalyzed oxygen scavenger that reacts faster than the uncatalyzed variant. It is unknown if the above-mentioned dosage rates apply to this new type of oxygen scavenger.

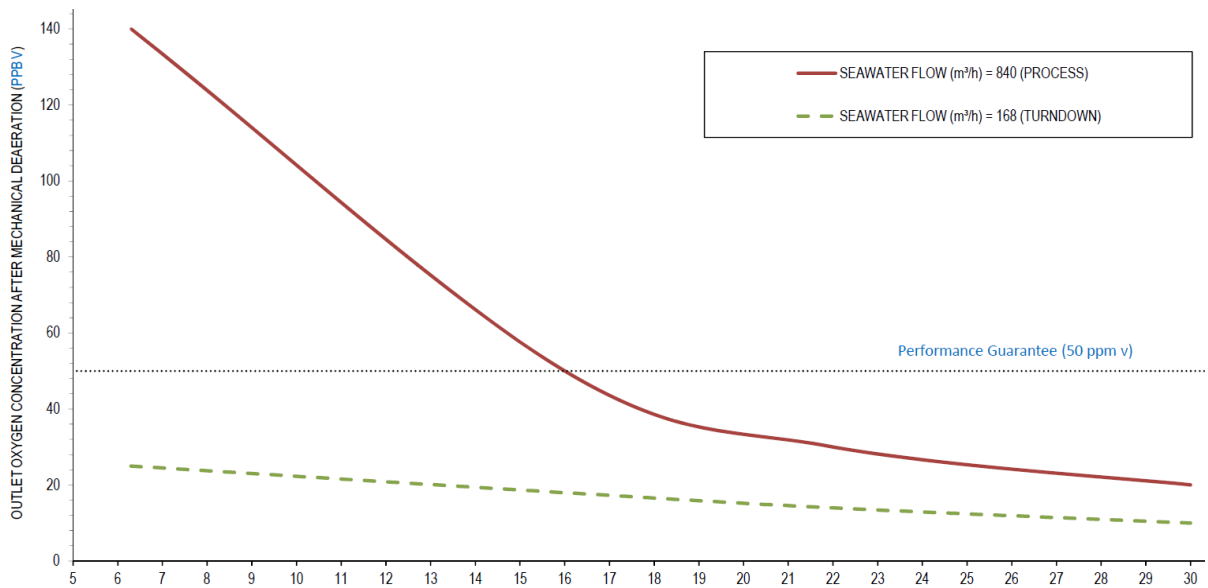


Figure 2.22: Performance curves for mechanical deaeration as function of seawater temperature. Red line indicates the designed maximum flowrate and green dotted a turndown to 20 % of the designed flow. This figure is taken from an unpublished document distributed by Eta Process Plant and is presented here with their consent.

According to datasheets the deaerator is designed to operate with pressures of -0.962 barg and -0.999 barg for the 1st and 2nd stage, respectively. This is equivalent to 51.25 and 14.25 mbar absolute pressures. The degree of vacuum during operation will depend on both operating temperature and feed flow. The plots in Fig. 2.23, made by Eta Process Plant, visualizes these relations for the deaerator. From these plots it is evident that the 2nd stage pressures are almost identical for the two flow modes presented, while the 1st stage pressure are almost equal but inverted. Why this happens is discussed with Eta Process Plant, but they have not been able to explain this yet.

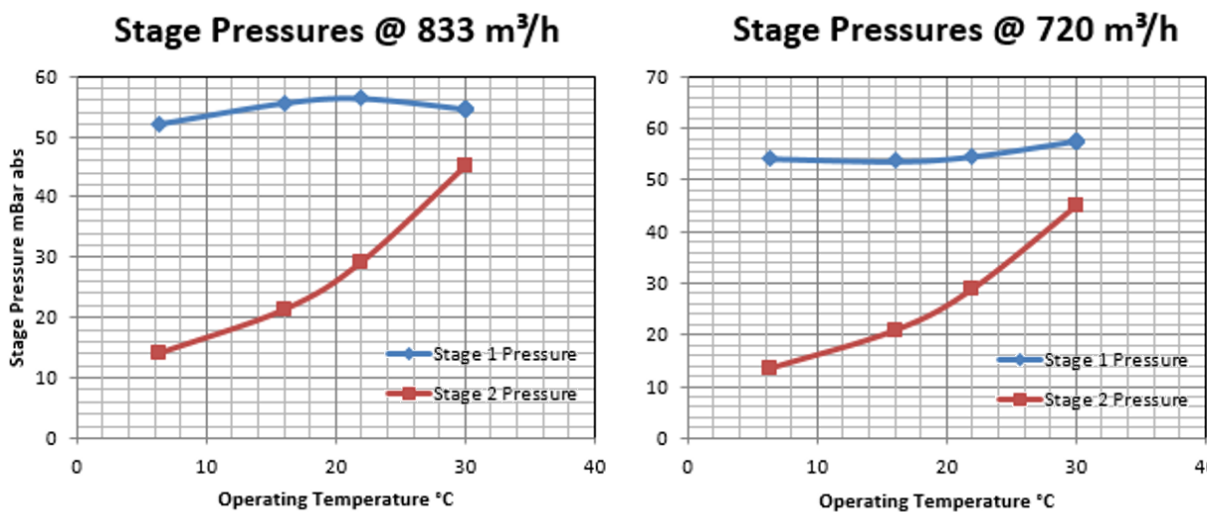


Figure 2.23: Deaerator stage pressures as function of operating temperatures for two different seawater feed flows. This figure is modified from the original unpublished operational manual distributed by Eta Process Plant and is presented here with their consent.

2.4.3 Control loops and adjustable parameters

There are only two control loops regulating in the deaerator system, namely liquid level and oxygen scavenger dosage rate. Level control is not of particular interest when assessing the deaerator efficiency. This is since it has no physical effect on the mechanical deaeration, which is of main interest in this project. The same goes for the oxygen scavenger flow control, but this might be an interesting parameter when evaluating the mechanical deaeration performance. The oxygen scavenger flow is adjusted by the control room operators based on the measured dissolved oxygen content in the seawater downstream of the deaerator booster pumps. They are instructed to try to keep the oxygen content below 20 ppb_{mol} but that the water is on spec if it is below 200 ppb_{mol}.

Operational parameters, such as seawater flow, temperature and tower pressures are more of interest, but none of them are controlled in the tower explicitly. The seawater flow is determined by the permeate production from the SRUs. The tower temperature is fully dependent on the permeate temperature. The deaerator stage pressures are a result of what degree of vacuum the fixed speed vacuum pump in operation can generate at different modes of operation. Thus, it will depend on both seawater flow and temperature.

To summarize, the following parameters can be adjusted:

- SRU production mode, which affects the volumetric flowrate of seawater to be treated in the vacuum tower. This will in turn affect the stage pressures due to higher liquid flow and more released vapor and dissolved gases in need of being conveyed by the vacuum generation package.
- Feed water temperature, as explained in Ch. 2.3.6, determines the tower temperature, it affects the tower pressures through affecting the release of vapor and dissolved gases.

2.4.4 Historical performance

Several years of data on the stage pressures, seawater temperature and seawater inlet flow are examined to do a simple historical performance analysis on the mechanical deaeration (see Appendix E). Assessing such a large timespan on an operational plant is not straight forward as there will be lots of variations induced due to starts, stops, trips and operational changes to the system. To keep structure the data was sorted into three different operation modes with respect to different flowrates of seawater to the deaerator. These operation modes are seawater flows of above 800 m³/h, ~720 m³/h, and 350 to 420 m³/h. For each operation mode randomly picked data points are used to calculate the average stage pressures and seawater temperatures. The plant has not been operated at flowrates above 800 m³/h as much as it has been operated at the other two modes. That means that the dataset for this mode is the least representative selection of the three.

Stage pressures is used as a performance indicator in this analysis since it is generated by the deaerator package itself and due to it being the governing parameter for the mechanical part of the oxygen deaeration. Analyzing oxygen content in the deaerated seawater is not straight forward as it is hard to differentiate between the mechanical and chemical contribution with respect to deaeration.

Based on these randomly picked datapoints the following averages are calculated for the three operation modes:

- > 800 m³/h: 39.4 and 27.2 mbara @ 9.2 °C̄
- ~ 720 m³/h: 41.8 and 22.2 mbara @ 8.9 °C̄
- 350 – 420 m³/h: 36.0 and 19.5 mbara @ 9.0 °C̄

The first and highest mentioned pressures in each pair is the pressure in the 1st stage, while the second are the 2nd stage pressures. The temperatures are the average temperatures for each data set used.

Due to few data points and no statistical proof of the selection being representative the above averages must be assessed with care. Comparing the averages for the two highest production modes to the pressure-temperature plots shown in Fig. 2.23 indicates that the 1st stage performs better than design and that the 2nd stage is underperforming. This seems to be caused by the vacuum ejector since the pressures in the 1st stage delivers above the expected performance.

Remember that the motive gas line to the ejector has been altered to prevent supposed freezing problems as mentioned before. This might have an impact on the ejector performance. If, and to what degree is not assessed in this thesis.

2.4.5 Typical operational problems

Eta Process Plant states that mechanical underperformance for any type of vacuum deaeration usually can be explained by one or both of the following cases:

Oxygen leakage into the deaerator liquid sump due to vacuum. Seawater in this sump is highly deaerated so that any introduced oxygen would very easily dissolve back into the seawater. The leaks cannot be seen on the vacuum performance in the deaerator as they are very small and efficiently dissolved into the water so that it will not reach or stay as a gas in the gas phase. Typical leakage points are instrumentation in connection with the deaerator sump such as level transmitters. Any such leakage problems not addressed needs additional chemical deaeration to be mitigated. Thus, more oxygen scavenger to be introduced.

Foaming of seawater subjected to turbulence and vacuum. This forms bubbles in the water which can pass through the liquid seal between the 1st and 2nd stage in the deaerator. This transfer of gas to the 2nd stage packed bed will alter how the ejector is loaded. This can ultimately prevent the ejector from functioning. This can be seen if the 2nd stage pressure is equal to or above the 1st stage pressure. The 2nd stage pressure can in fact get higher relative to the 1st stage due to introduction of motive air when the ejector does not function as intended. Too high pressure in the 2nd stage will in turn manifest itself as off spec seawater in the liquid sump. This problem can be mitigated with antifoam chemicals. Eta Process Plant also states that the same pattern can be caused by a physical fault on the seal caps on the seal plate downcomers.

An assessment of the pressures in both stages is done in Fig. 2.24 to see if there are any typical signs of foaming in the deaerator. Here it is evident that the 2nd stage pressure has been higher than that in the 1st stage over a ~1-month period during the last 4.8 years. From the 17th of June to 20th of July in 2018, marked with a red circle in the plot. This could indicate foaming issues or some other issues with the ejector, like freezing or fouling. This period is checked against seawater flow and temperature supplied to the deaerator, and up against chemical dosage rate of chlorine scavenger, scale inhibitor and biocide. None of which are operated unnormal

relative other periods in time where the stage pressures are as it should be, descending between the stages. Besides this, the pressures seem normal in that they do not indicate any foaming issues. There are other cases where the 2nd stage pressures ascend the 1st stage but that seems to be in line with manual flushing of the ejector, mentioned before. These incidents are not likely to be induced by foaming as it seems to be reversible upon flushing of the ejector. Flushing the ejector nozzle via the motive gas should not help if there is persistent foaming and carryover of gas from 1st to 2nd stage. For that reason no further assessment on foaming is done in this project.

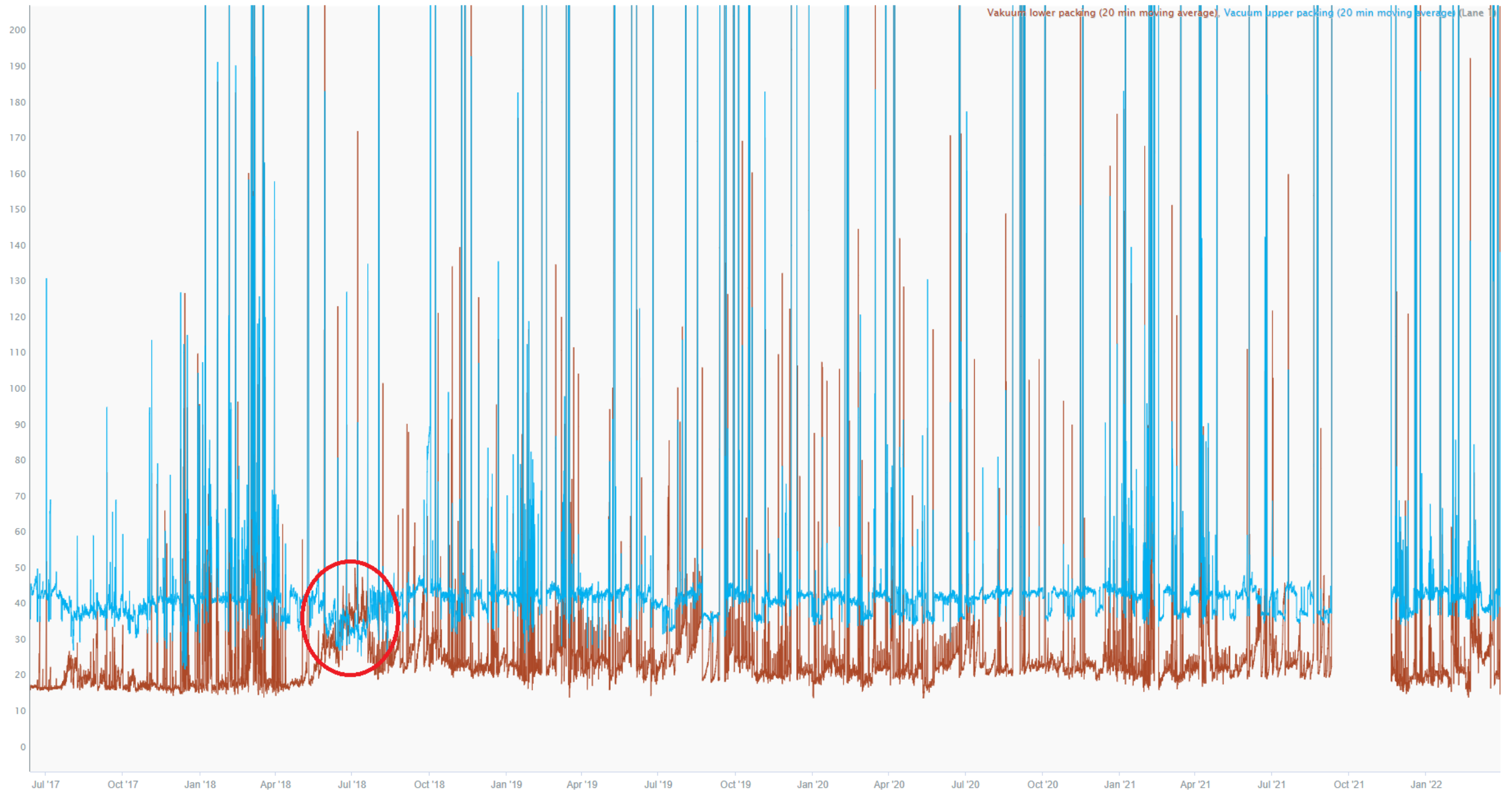


Figure 2.24: All available historical data on pressures of both stages inside the deaerator. The blue line is pressure in the 1st stage, brown line in the 2nd stage, while the y-axis is in units of mbara. The red circle marks a significant period where the 2nd stage pressure for some reason became higher than that in the 1st stage. This could be an indication of foaming.

3 Literature review

This chapter contains the theory necessary to understand the detailed mechanisms of sulfate removal by nanofiltration and vacuum deaeration of dissolved oxygen in seawater. The intent is to be able to theoretically evaluate the SRDP system performance at Ivar Aasen. In addition to be able to the understand and predict how the systems responds to changes in the parameters and process variables (pressure, temperature, flowrates, recoveries, etc..).

This literature review is tied to the SRDP theory in Chapter 2 through explicit examples and in terms of how the theory is explained. This is done to tie the literature review and plant theory better together.

3.1 Membrane separation

The intention with the following sub-chapter is to present the theory necessary to understand the mechanisms of the of the sulfate removal by the nanofiltration of seawater. The principles of concentration polarization, fouling and membrane degradation is also presented here.

3.1.1 Overview and terminology

Membranes in an industrial aspect is a unit operation for separating species within fluids. In general, a membrane system consists of a semi-permeable membrane separating two phases as illustrated with the diagonal line in Fig. 3.1. [15] Separation of species mixed in, in multiphase with, dissolved in, or carried by a fluid is induced due to the transport selectivity in the membrane.

Membranes can have different purposes depending on the system it is installed in. The main, and most obvious, categories are [16]:

- **Purification:** Remove or reduce concentration or presence of an unwanted species in a fluid.
- **Concentration:** Elevate concentration of a solute in a solvent by removing solvent.
- **Fractionation:** Separating a mixture of species to two or more products.

In the figure below a simple schematic of a membrane process is presented. In this project a purification process is assessed. Thus, where the unwanted specie (sulfate) is mainly rejected to concentrate, and the useful specie (water) permeates to the permeate stream. Separation is not absolute so there will be water in concentrate and sulfate in the permeate.

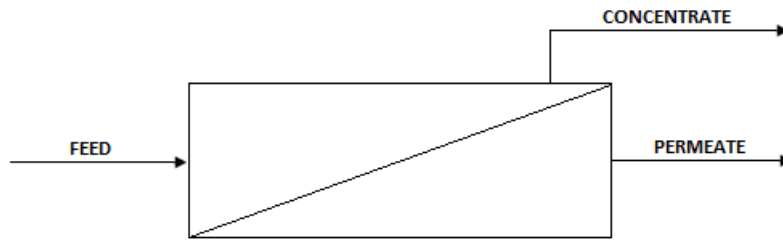


Figure 3.1: Schematic presentation of a membrane process.

Membrane processes can be distinguished by their driving forces, i.e. the main force initiating flow through the membrane barrier. These forces are differences in pressure, concentration, temperature, and electrical potential [16]. The focus here will be on pressure driven membranes which in turn can be subdivided into four classes by their filtration range as illustrated in Fig. 3.2. These are reverse osmosis (RO), nanofiltration (NF), ultrafiltration (UF) and microfiltration (MF). Conventional filtration is also indicated in this diagram simply to illustrate where the line is drawn between conventional filtering and pressure driven membrane separation.

The diagram in Fig. 3.2 gives a good overall view of pressure driven membranes. It is evident that the pressure driven membranes operates in separation of particles that ranges from 10 microns to 0.1 nanometers. NF sorts in the molecular level, i.e. in the transition between RO and UF, and can be expected to be selective (reject species) down to 0.001 microns, or 1 nanometer.

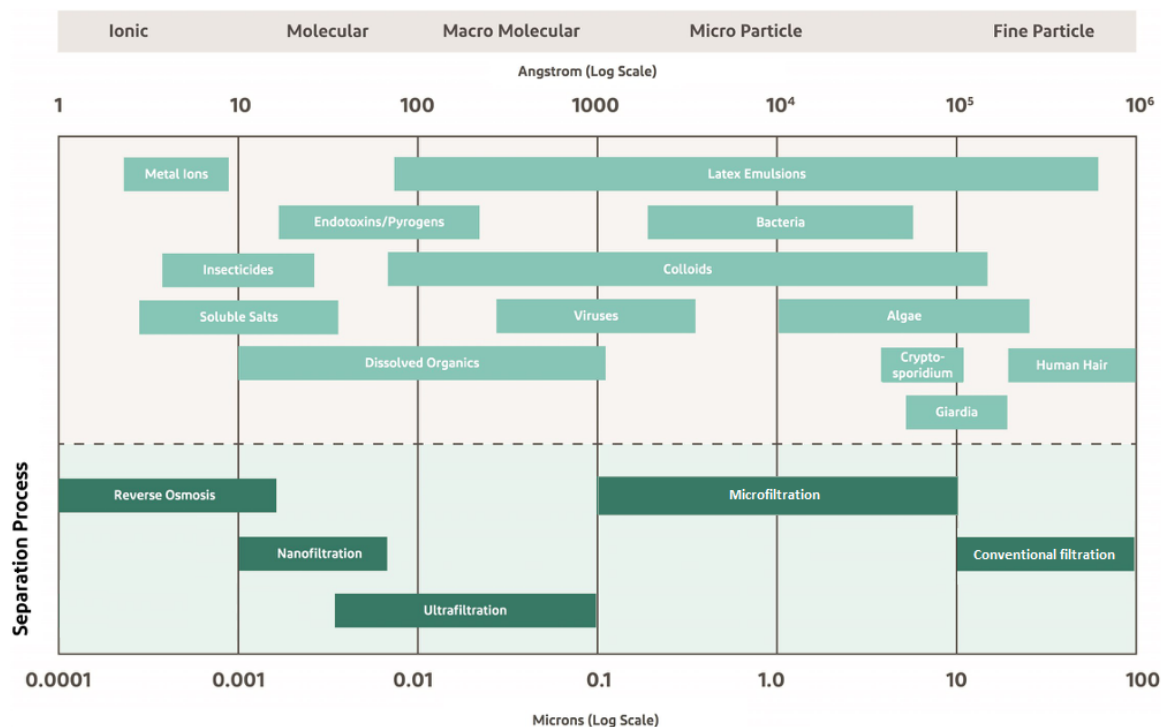


Figure 3.2: Different pressure driven membrane operations distinguished by filtration range and pore size. Modified from [7]

Another coarse view on difference in rejections for the different pressure-driven membranes in are shown in Fig. 3.3. From this it is evident that NF is selective to divalent ions such as sulfate while permitting monovalent salts like sodium (Na^+) and chloride (Cl^-). This is obviously not absolute since a NF membrane will not reject all monovalent ions nor will it have total rejection on divalent ions.

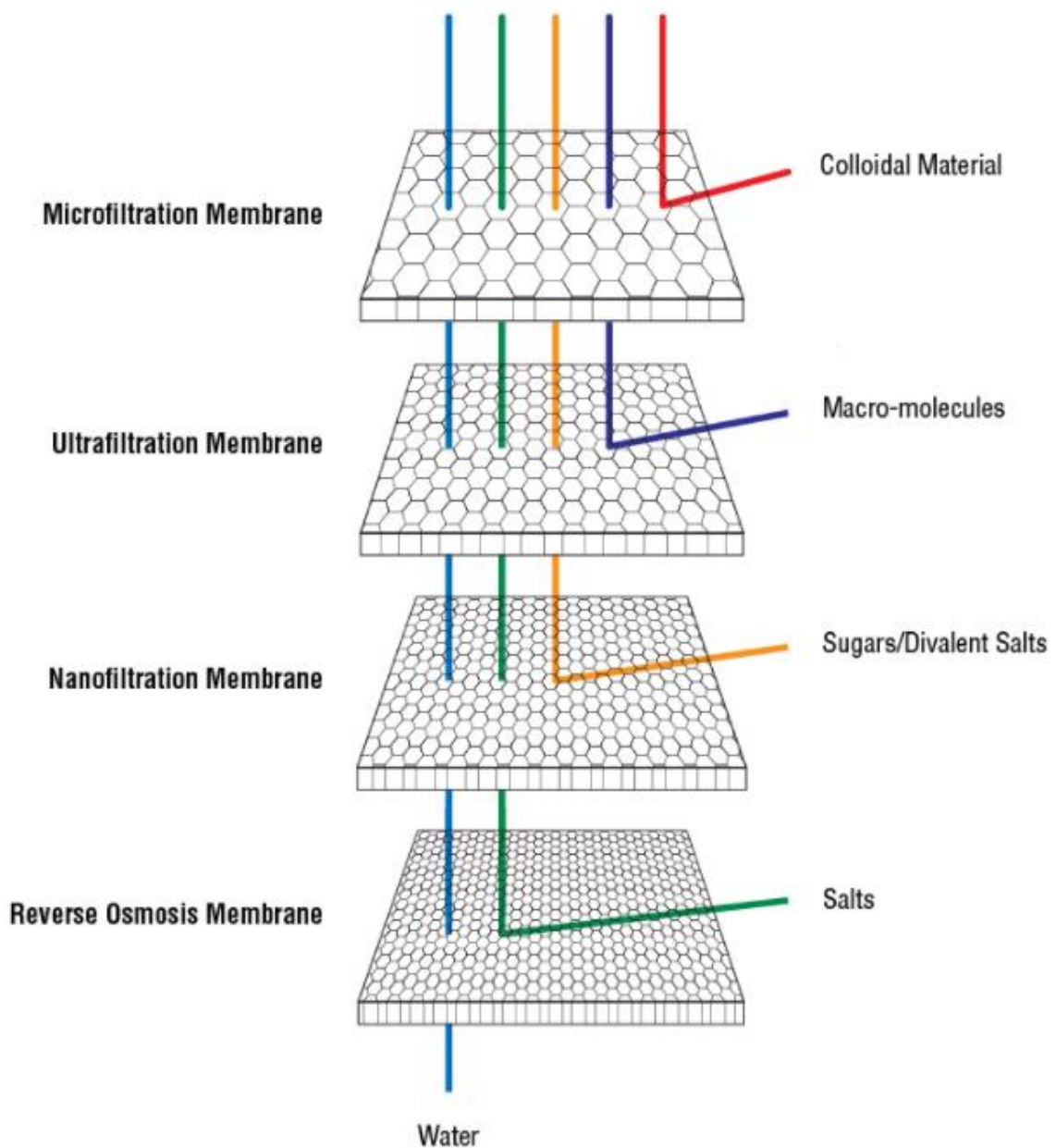


Figure 3.3: Schematic (rough) classification of pressure driven membranes by species rejections. [17]

Terminology

There are, as in other fields of science, a specific terminology that is used when it comes to membranes. Table 3.1 gives an overview of the most important terms used throughout this report. The terms of feed, permeate and concentrate (retentate) are considered elementary and not presented in the table.

Table 3.1: Key terms for (liquid) membrane separation [15][18]

Term	General description	Specific description for SRU
Flux	Flowrate of volume or matter of a specific component crossing per unit membrane area normal to the thickness direction of the membrane.	Flux of desulfated seawater
Permeability	Product of a species diffusion- and sorption coefficient.	Sulfate permeability
Volume flux/flow	Volume flow that permeates the membrane per membrane area. Often referred to as “total volume flow” or “volume flux”.	Desulfated seawater
Recovery	Percentage of useful specie in the feed collected (recovered) in the product stream ¹ .	Desulfated seawater
Rejection ²	Fraction of component rejected from feed to permeate in a membrane. I.e., concentration difference across membrane divided by the feed concentration.	Sulfate rejection
Selectivity	Different permeabilities for different species	Sulfate selectivity
<p><u>Notes:</u></p> <ol style="list-style-type: none"> 1. The “useful” specie might be retained or permeated. Hence, the product stream might be the concentrate-, or the permeate stream, or both. 2. “Apparent rejection” uses bulk concentrations (disregards concentration polarization, see Ch. 3.1.5), while “Intrinsic rejection” considers concentrations at the membrane surface 		

3.1.2 Osmotic pressure and reverse osmosis

Understanding of osmotic pressure is a key feature in the understanding of an important class of transport mechanisms for RO and partially NF called Solution-diffusion. This model is assessed in depth later in Ch. 3.1.4.

Let us consider the effects of osmotic pressure with a simplified system. Consider a membrane system like the one shown in Fig. 3.4 where pure water is separated from a saline solution (salt dissolved in water) by a membrane only accepting pure water to pass.

On the left-hand side it is evident that water passes across the membrane into the saline side when no external pressure is applied to the system. This is a product of the concentration gradient for water and the process is known as forward osmosis. [19]

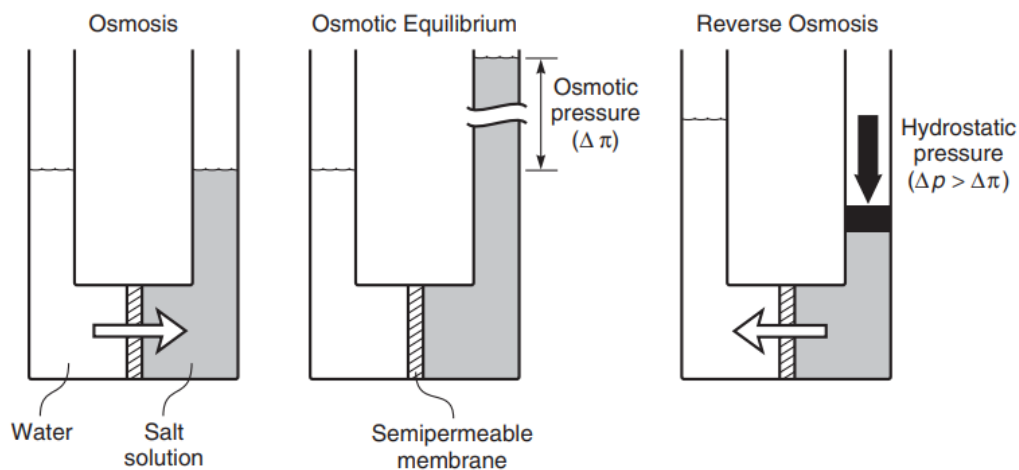


Figure 3.4: Osmosis, osmotic pressure, and reverse osmosis. Modified from [19]

After some time, the system will reach osmotic equilibrium as shown in the middle figure. This is achieved when the solution side reaches a sufficiently higher pressure to withstand the flow induced by the difference in chemical potential gradient for water. This pressure difference is known as the systems osmotic pressure. [19]

To utilize the membranes selectivity on salts, e.g. to generate fresh water, a pressure that is higher than the osmotic pressure must be applied to the saline side. This initiates RO as shown on the right-hand side of the figure. [19]

Since NF is less selective on salts relative to RO (see Fig. 3.2 and 3.3) it is also less affected by the osmotic pressure since osmotic pressure is directly proportional to concentration differences. RO that restricts almost all salts (both mono- and divalent) have a very high difference in salt concentration across the membrane which in turn yields a high osmotic pressure difference to overcome to initiate RO. Hence, NF can typically be operated at significantly lower pressure difference compared to that of RO.

3.1.3 Transport mechanisms

In the field of membrane science there are two main mechanisms that explain the permeation of species through a membrane, namely the solution-diffusion- and the pore-flow models. In general, these models are used on dense- and porous membranes, respectively. [19] There are many different membrane transport models available in the literature and many of these seem to have roots in these main mechanisms.

Figure 3.5 gives a basic illustration of these concepts where pore flow carries components (molecules, ions, solids, bacteria, virus, etc.) through a membrane pore on the left-hand side, while on the other side a component solutes/dissolves in a dense membrane and diffuses through it. [19]

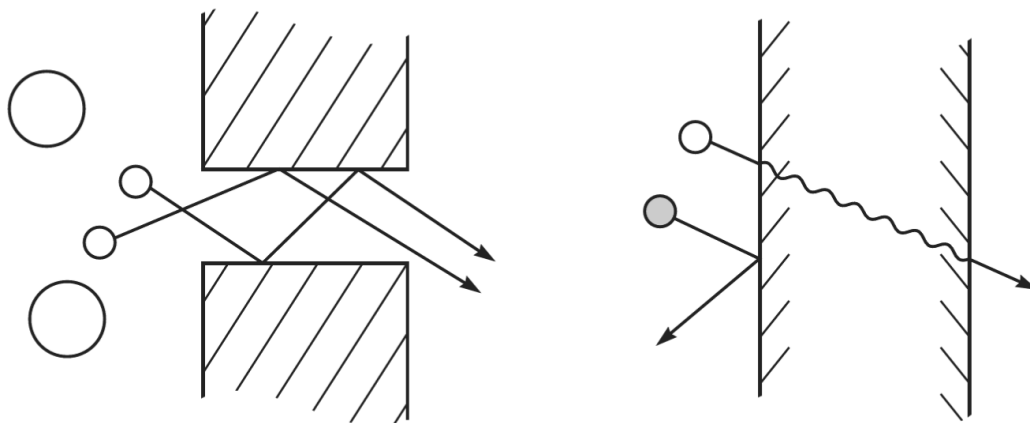


Figure 3.5: Different components passing porous membrane to the left and dense membrane to the right. [19]

Solution-diffusion describes permeation with feed components absorbing and dissolving into the membrane, diffusing through it, and desorbing on the other side. The separation of different components occurs due to differences in solubility and -diffusivity to/in the membrane material. When it comes to pore-flow it explains permeation as convective flow within permanent pores in the membrane material. Separation occurs mainly due to relative pore sizes where components with size above-, equal to-, or too close to the smallest pore will be hindered yielding different degrees of separation. [19]

NF lies in the transition between these main transport mechanisms as it often consists of both a dense- and a porous membrane layer. This puts it in between pore-flow explaining UF and MF, and that of solution-diffusion explaining RO. Intuitively this implies that NF transport mechanisms could become somewhat more complicated relative to that for RO or UF and MF.

Spiegler-Kedem developed a model, shown in Eqn. (3.1) and (3.2), that considers both pore-flow and solution-diffusion having a coupled effect on solute- and solvent transport. They introduced a reflection coefficient, σ , which weighted the two mechanisms for the membrane system evaluated. [20]

$$J_V = L_w(\Delta p - \sigma \Delta \pi) \quad (3.1)$$

$$J_j = (1 - \sigma) \bar{c}_j J_V - w \Delta \pi \quad (3.2)$$

In these equations L_w is the permeation coefficient of pure water, Δp the pressure- and $\Delta\pi$ the osmotic pressure difference across the membrane, \bar{c}_j is the average solute concentration of both feed and permeate side of membrane surface, and w is the solute permeation coefficient. [20] Note that, J_V , is the volume flux which is often applied to describe the solvent flux while J_j is the mass flux. Convection flow of species in solvent in pores is accounted for by the product of volume flux to the average solute concentration, $c_j J_V$. The reflection coefficient balances pressure difference to osmotic pressure for the solvent, and convection to osmotic pressure for the solute. It can be shown that by assuming high membrane selectivity between solvent and solute, such as saltwater in RO, the osmotic pressure difference is negatively proportional to species diffusion in dense membranes [19]. Thus, this model balances the two main transport mechanisms in membranes.

A lot of research has been performed on transport mechanisms and modelling of NF systems during the last 20+ years. There are many publications on different approaches in explaining the transport through these membranes. Assessing a lot of these seems to underline the suggestion that the two main mechanisms of pore flow and solution-diffusion is the basis for many of the later models developed and assessed for NF membranes.

Several of these studies imply that for NF membrane systems like the one assessed in this thesis the pore-flow aspect is negligible. For instance, R. Wang and S. Lin in [21]] states that the polyamide layer governs the rejection of solutes when considering fluid transport through thin-film composite NF. The main argument is that the porous layers have much larger pore sizes than the dense polyamide film. Hence, it is often a reasonable assumption that the porous layers can be ignored when modeling transport of both solvent and solute. Another interesting finding by A. Yaroshchuk et. Al. in [22] states that the solution-diffusion approach is more correct than that of pore-flow as it better explains the high rejections of sulfate and chloride from electrolyte mixtures relative to what is achieved through pore-flow models. They also site another study done by Freger and co-workers that showed the convective coupling between solute and solvent to be very weak in the membrane phase of several commercial NF membranes. Lastly, S. Bason et.al. also states that convective coupling for ion transport in NF is very weak, especially for thin-film composite membranes in [23][24].

Based on these findings in very relevant literature the solution-diffusion is assumed to be the governing transport mechanisms for SRUs at Ivar Aasen. Thus, any contribution of porous flow to the separation are considered negligible.

However, according to a study by A. Yaroshchuk et. al. this applies to neutral fluids and single salt fluids [22] which is not the case for sulfate removal from seawater in the SRUs. To model transport of multi-ionic solutions through a NF membrane it is necessary to consider other effects on rejection like membrane charge, ion partitioning (ions passing and affecting membrane), and coupling between flow of ions within the membrane. Also, ions come in pairs, thus the cation and anion will suffer differences in permeabilities depending on the membrane surface characteristics. A charged membrane will also induce selectivity between mono- and divalent ions as the latter (with larger charges) is more affected by the membrane charge. I.e., the membrane will have higher rejection to divalent ions due to stronger electrostatic repulsions [16]. There are models available in the literature that considers these types of effects, for instance the extended Solution-diffusion-film-model or Solution-Diffusion-Electro migration assessed in [22][25]. Both of which are based on the solution-diffusion model.

These electrostatic effects on selectivity between ions are obviously important to understand the details of NF of seawater. However, it is not possible to predict these effects in detail for

the SR90-440i membranes as the membrane surface characteristic are not publicly available due to company secrets. Also, for the SRU study two elements are of particular interest, namely sulfate removal and water permeability. Thus, the solution-diffusion should be sufficient for the purpose of understanding the mechanisms of interest in this project. For that reason, the solution-diffusion model is utilized with the intent to give some basic insight in how separation of sulfate from seawater can be explained in a thin-film membrane. And, due to lack of technical details, the theory in general is intended to predict “directional dependencies” between changes in parameters and outcomes. Such as what will happen to the system if a particular parameter is altered, e.g. increase of seawater temperature.

3.1.4 Solution-Diffusion

Fick’s law

The solution-diffusion flux through a dense membrane can be mathematically described by applying Fick’s law of diffusion shown in Equation (3.3). [19]

$$J_i = -D_i \frac{dc_i}{dx} \quad (3.3)$$

Where J_i is the flux, D_i is the diffusion coefficient, c_i is the concentration for component i , and x is the spatial direction normal to/ through the active layer. Separating the variables and integrating this across the membrane thickness, l , gives Eqn. (3.4). [19]

$$\int_0^l J_i dx = -D_i \int_{c_{i,0(m)}}^{c_{i,l(m)}} dc_i \quad \Leftrightarrow$$

$$J_i = \frac{D_i}{l} (c_{i,0(m)} - c_{i,l(m)}) \quad (3.4)$$

The subscript (m) is used to denote that the parameter is to be evaluated in the membrane phase. E.g., $c_{i,0(m)}$ is the concentration of species i at the feed interface between feed and membrane **in the membrane phase**, while $c_{i,0}$ will be the feed concentration of i **in the feed fluid phase** adjacent to the membrane.

In this report the coordinates shown in Figure 3.6 is employed. This figure illustrates the coordinates on a membrane leaf rolled out from its core of a spiral-wound cartridge as shown in in Fig. 2.4 . Thus, x-direction is in the radial direction through the active membrane layer, from feed or concentrate to permeate. This direction is normal to the membrane leaf from both sides of it. The y-direction is the axial movement inside of the membrane. This direction is parallel to the core. And the z-direction is a “rotational inward movement” inside of the membrane towards the core. Each incremental movement (neglecting curvature) is 90° on both x- and y-directions.

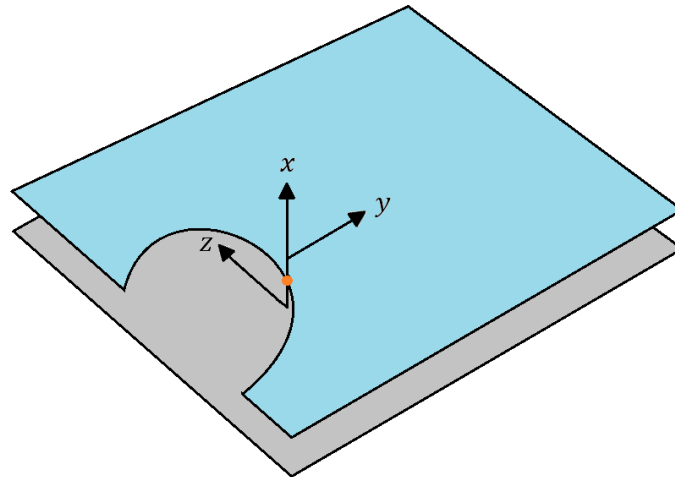


Figure 3.6: Coordinates employed in this report relative to a rolled-out membrane leaf from a spiral-wound cartridge. Perforated permeate core, not drawn in figure, runs from upper left- to upper right corner as shown in Fig. 2.4. The orange dot indicates the x-coordinate axis passing the upper membrane leaf.

Based on the above coordinates the diffusion to be modelled only needs to be assessed in one direction. This is a valid simplification since the diffusional direction normal to the active membrane layer describes the transport of interest. There will also be gradients in y-direction or axial direction inside the membrane due to the gradually changing feed/concentrate composition along the feed/concentrate channel. This induces a gradual reduction in permeate flow along the cartridge due to increasing osmotic pressure as salt concentration in the feed increases. Hence, at all axial positions in the membrane cartridge the model about to be derived can describe transport through the active membrane layer. If it is necessary to assess the full length of a cartridge that can be done by integration of concentration profiles along the active membrane layer.

Fick's law implies that the diffusion coefficient can be considered spatially constant. This will however depend on whether parameters such as temperature and pressure changes within the domain. However, a thermodynamic approach in deriving the solution-diffusion model in a dense membrane leads to Fick's law by the following assumptions: [19]

- Constant pressure inside the membrane equal to the highest pressure outside of the membrane.
- Chemical potential is expressed only through concentrations gradients, i.e. both temperature- and electrical potential gradients is assumed constant.
- Activity coefficient is assumed constant making it a parameter explaining the diffusion, not a variable [20].

To predict the flux of solvent and solutes by use of Fick's law it is necessary to express the concentrations at the feed- and permeate interfaces on the inside of the membrane of parameters more readily available. For that purpose, the chemical potential utilized. For an incompressible liquid the chemical potential of a specie in solution, μ_i , when considering concentration- and pressure gradients, can be formulated as shown in Eqn. (3.5). [19]

$$\mu_i = \mu_i^\circ + RT \cdot \ln(\gamma_i X_i) + v_i(p - p_{i,sat}) \quad (3.5)$$

Here μ_i° is the chemical potential of pure species i at reference pressure $p_{i,sat}$, while γ_i and X_i are the activity coefficient and mole fraction, respectively. The subscripts i and j used throughout this derivation simply denotes different species, solvent i and a solute j . The activity coefficient of a component describes the deviation from an ideal solution for the specific component within a specific solution. It is probably more familiarly known as the coefficient used to describe the deviation in Raoult's law, which in its "normal form" only apply to ideal liquids in mixture. Thus, the product of activity coefficient and mole fraction, $\gamma_i X_i$, is the species activity in the solution. [26] An ideal liquid solution is a solution where the forces between all the molecules within the mixture are equal [27].

The first step in the derivation of the Solution-Diffusion model is to equate the chemical potential across the feed side interface of the membrane surface as shown in Eqn. (3.6). [19]

$$\begin{aligned} \mu_{i,0} = \mu_{i,0(m)} & \Rightarrow \\ \mu_i^\circ + RT \cdot \ln(\gamma_{i,0} X_{i,0}) + v_i(p_0 - p_{i,sat}) = & \\ \mu_i^\circ + RT \cdot \ln(\gamma_{i,0(m)} X_{i,0(m)}) + v_i(p_{0(m)} - p_{i,sat}) & \end{aligned} \quad (3.6)$$

This approach assumes that the chemical potential of i is equal across this interface when the system is in equilibrium or steady state. The same assumption will be done for the interface at the permeate side. This assumption implies that the diffusion within the membrane is the limiting factor, i.e. diffusion is much slower than the absorption and desorption at the surfaces. [19]

The temperature, molar volume, reference- pressure and chemical potential and molar volume, T, v_i, μ_i° and $p_{i,sat}$, are all equal in both phases and cancels out. The molar volume is unchanged as the liquid is assumed incompressible under the operating condition. It is normal to assume that the pressure inside dense membranes is constant and equal to the highest pressure of feed and permeate. With respect to the SRUs the feed pressure will be highest so that $p_0 = p_{0(m)}$. This leads to expression shown in Eqn. (3.7). [19]

$$\begin{aligned} \ln(\gamma_{i,0} X_{i,0}) = \ln(\gamma_{i,0(m)} X_{i,0(m)}) & \Leftrightarrow \\ X_{i,0(m)} = X_{i,0} \frac{\gamma_{i,0}}{\gamma_{i,0(m)}} & \end{aligned} \quad (3.7)$$

To convert from fractions to concentrations it is utilized that mass concentration equals the product of mole fraction, molar- mass and density as shown in Eqn. (3.8). [19]

$$c_i = M_i X_i \tilde{\rho} \cdot 10^{-3} \quad \Leftrightarrow$$

$$X_i = \frac{c_i}{M_i \tilde{\rho}} \quad (3.8)$$

Inserting this relation into Eqn. (3.7) gives Eqn. (3.9).

$$\frac{c_{i,0(m)}}{M_{i,0(m)} \tilde{\rho}_m} = \frac{c_{i,0}}{M_{i,0} \tilde{\rho}_0} \frac{\gamma_{i,0}}{\gamma_{i,0(m)}} \quad \Leftrightarrow$$

$$\frac{c_{i,0(m)}}{c_{i,0}} = \frac{M_{i,0(m)} \tilde{\rho}_m}{M_{i,0} \tilde{\rho}_0} \frac{\gamma_{i,0}}{\gamma_{i,0(m)}} \quad (3.9)$$

The species molar masses remain constant and is eliminated. The densities are different as one is the density on the fluid side, while the other is that of the membrane side. This leads to the following Eqn. (3.10). [19]

$$\frac{c_{i,0(m)}}{c_{i,0}} = \frac{\tilde{\rho}_m}{\tilde{\rho}_0} \frac{\gamma_{i,0}}{\gamma_{i,0(m)}} = K_i \quad (3.10)$$

The ratio between the activities and molar densities of component i across the feed interface is the sorption coefficient, K_i . After rearranging this equation, it links the feed side concentration with membrane side concentration about the interface as shown in Eqn. (3.11). [19]

$$c_{i,0(m)} = c_{i,0} K_i \quad (3.11)$$

The next step in this derivation is to follow the same procedure for the permeate interface. Here it is important to remember that the pressure inside the membrane is constant and higher than the pressure in the permeate fluid, $p_o = p_{o(m)} = p_{l(m)}$. Due to this difference in pressure across the permeate interface there is a pressure contribution to the chemical potential on this side of the membrane. Thus, the pressure terms do not eliminate like they did across the feed interface, neither does temperature and the universal gas constant. The derivation starts from equating the chemical potential and leads to Eqn. (3.12). [19]

$$\mu_i^\circ + RT \cdot \ln(\gamma_{i,l} X_{i,l}) + v_i(p_l - p_{i,sat}) =$$

$$\mu_i^\circ + RT \cdot \ln(\gamma_{i,l(m)} X_{i,l(m)}) + v_i(p_o - p_{i,sat}) \quad \Leftrightarrow$$

$$\ln\left(\frac{\gamma_{i,l} X_{i,l}}{\gamma_{i,l(m)} X_{i,l(m)}}\right) = \frac{v_i(p_o - p_l)}{RT} \quad \Leftrightarrow$$

$$\frac{\gamma_{i,l}}{\gamma_{i,l(m)}} \frac{\tilde{\rho}_m}{\tilde{\rho}_l} \frac{c_{i,l}}{c_{i,l(m)}} = e^{\frac{v_i(p_o - p_l)}{RT}} \quad \Leftrightarrow$$

Through assuming constant activity coefficients and water densities ($\tilde{\rho}_l = \tilde{\rho}_0$) the sorption coefficients on both sides of the membranes becomes equal, $K_{i,l} = K_{i,0} = K_i$. Hence, the absorption- and desorption coefficients equals.

$$K_i \frac{c_{i,l}}{c_{i,l(m)}} = e^{\frac{v_l(p_0 - p_l)}{RT}} \Leftrightarrow$$

$$c_{i,l(m)} = c_{i,l} K_i e^{\frac{-v_l(p_0 - p_l)}{RT}} \quad (3.12)$$

This equation links the concentrations across the permeate interface. Inserting Eqn. (3.11) and (3.12), into the integrated form of Fick's law (Eqn. (3.4)) gives an expression for flux of component i as function of pressure and concentration in the fluid side of the interfaces as shown in Eqn. (3.13). Hence, the parameters inside of the membrane domain, which are not readily available, is eliminated. [19]

$$J_i = \frac{D_i}{l} \left(c_{i,0} K_i - c_{i,l} K_i e^{\frac{-v_i(p_0 - p_l)}{RT}} \right) \Leftrightarrow$$

$$J_i = \frac{D_i K_i}{l} \left(c_{i,0} - c_{i,l} e^{\frac{-v_i(p_0 - p_l)}{RT}} \right) \quad (3.13)$$

According to Tab. 3.1 the product of a component's diffusion and sorption coefficients is its permeability, P_i . Utilizing this yields Eqn. (3.14). [19]

$$J_i = \frac{P_i}{l} \left(c_{i,0} - c_{i,l} e^{\frac{-v_i(p_0 - p_l)}{RT}} \right) \quad (3.14)$$

This equation predicts flux of component i , which is sulfate reduced seawater (solvent) in this project, through the dense layer of the thin-film composite NF membrane. An equivalent expression can be made for each solute in the solvent by the exact same approach. Eqn. (3.15) shows the general flux for solutes according to the solution diffusion model.

$$J_j = \frac{P_j}{l} \left(c_{j,0} - c_{j,l} e^{\frac{-v_j(p_0 - p_l)}{RT}} \right) \quad (3.15)$$

The solution-diffusion model shown in Eqn. (3.14) and (3.15) seems to have a simple functional relation to pressures and temperature. It states that solute and solvent have similar dependencies to both parameters in that increased temperature decreases fluxes, increased feed pressure increases fluxes, while increased permeate pressure reduces fluxes. The degree in response and the magnitude of fluxes will be different between species if they have different permeabilities, molar volumes and/or feed concentrations. Thus, differences in permeability

(and molar volumes) scales the fluxes and is what makes the membrane selective. A more thorough graphical assessment on these functional relations and scaling is shown in Appendix F.

It is very important to state the above-mentioned relations assumes that both permeability and molar volumes are constant and independent of temperature and pressure. This is not true, and it will be argued through the succeeding sub-chapters that both permeability and molar volume depend on temperature so that the system fluxes are most likely to increase upon increased temperatures, contradicting the solution-diffusion model temperature dependency. The presence of membrane selectivity is also explained though an example calculation on approximate molar volumes and permeabilities for sulfate and seawater at Ivar Aasen SRUs.

3.1.4.1 Molar volume - Temperature dependence

For a single component the molar volume can be defined as shown in Eqn. (3.16) where M_i and ρ_i is the molar mass and density of the component assessed, respectively. From this it is evident that the molar volume of a component is inversely related to density which in turn is inversely dependent on temperature (for most liquids). When it comes to pressure dependency molar volume can be assumed independent for liquid systems though incompressibility, at least within reasonable pressure such as the operational pressure range for the SRUs. Hence, molar volume can be assumed pressure independent and proportionally dependent on temperature. [28]

$$v_i = \frac{M_i}{\rho_i} 10^{-3} \quad (3.16)$$

It is not possible to use this equation directly to calculate the molar volumes for solutes within a solvent. The main reason, for the case of electrolytic solution with ions in a polar solvent like water, is that the volumes of pure solutes and pure solvent is not additive due to electric effects between the molecules in the solution. E.g., 100 mL of pure water mixed with 100 mL of a NaCl solution does not yield a 200 mL mixture combined. This in turn affects the density and thus molar density of the solution. Neither is this effect linear to solute fraction in the solvent, i.e. the solution volume is dependent on solute concentration in a non-linear manner. When considering such systems the focus is turned to partial molar volumes rather than molar volumes. This is basically the partial derivative of volume to the amount/moles of the specific solute added to the mixture. [29] There will be no further assessment of this in this thesis as Eqn. (3.16) is assumed to give sufficient insight on molar volume temperature dependence for liquids.

The absolute value of the molar volume is of interest as it scales the exponential expressions in Eqn. (3.14) and (3.15). In this study the species of water and sulfate are both central. At 15 °C pure water has a density of 999.10 kg/m³ [30] and a molar mass of ~18.01 g/mol, thus its molar volume can be estimated to 1.803·10⁻⁵ m³/mol by using the definition above shown in Eqn. (3.16).

On the other hand, A. Poisson and J. Chanu estimates a partial molar volume for sulfate ions in seawater to be 30.2 cm³/mol, or 3.02·10⁻⁵ m³/mol in SI-units, at 15°C and 3.5% salinity [31]. The total dissolved salt in the feedwater to the SRUs at Ivar Aasen is 36200 mg/L (see. Tab.

2.1) which is equivalent to a salinity of approximately 3.62 % This is estimated through calculating weight percentage of salts using pure water density at 15 °C. Any dissolved organics is neglected in this estimate, i.e., the salinity is somewhat overestimated. Anyways, it is close to the salinity that A. Poisson et. al. used in their estimate of the sulfate partial molar volume, an indication that their reported partial molar volume is applicable in this comparison. Thus, sulfate has a molar volume almost twice that of water. This difference, as differences in permeability, induces membrane selectivity between different species.

3.1.4.2 Permeability – Temperature dependence

The permeability of a specie through a dense membrane is the product of the sorption- and diffusion coefficients of the specie. The permeability of charged solutes is also likely to be dependent electrical effects such as on surface charges on the active layer of the membranes. Net surface charge might in turn be affected by fluid temperature if this affects ion migration via permeability. These effects are not assessed in depth in this thesis.

The absorption coefficient is defined as concentrations differences across the membrane interfaces as shown in Eqn. (3.10). Sorption, which is a common name for both absorption and desorption, can be seen as a type of equilibrium coefficient for the species distribution across both the feed and permeate interfaces. Looking at this definition it indicates that the solubility of species in the membrane is proportional to the absorption coefficient. In general, solubility of species not volatile increases with temperature due to higher molecular kinetics of the specie and larger molecular distances in solids. Thus, by assuming the adsorption and desorption equal it is likely that the sorption coefficient increases with temperature. Specie concentrations do not depend on pressure nor should the sorption coefficient. This reasoning is not found in literature explicitly but is based on the authors understanding of the involved physics. An indication of that the reasoning is correct is that DuPont’s temperature correction factor for water permeability increases exponentially with temperature as shown in Eqn. (3.17) and (3.18).

DuPont have derived Temperature Correction Factors (TCF) for water permeability in their FilmTec membranes which is shown in Eqn. (3.17) and (3.18). From these it is evident that the permeability through their thin-film composite membranes depends exponentially to the temperature. [7]

$$TCF = e^{2640\left(\frac{1}{298} - \frac{1}{T}\right)}, \quad T \geq 298.15 \text{ K} \quad (3.17)$$

$$TCF = e^{3020\left(\frac{1}{298} - \frac{1}{T}\right)}, \quad T \leq 298.15^\circ\text{C} \quad (3.18)$$

This correction is used as a factor in their modeling on permeate flow. Whether these equations are empirically- or theoretically based is not stated by DuPont. For that reason, they are assumed specific for their FilmTec membranes which are also in use in the SRU at Ivar Aasen. DuPont makes no comments on sorption coefficients or molar volume and their temperature pressure dependence. Neither do they discuss any temperature dependence on the concentration gradient in the membrane as illustrated in Fig. F.3 in Appendix F. However, they do state that both permeate flux and salt passage will increase with increased temperature in their FilmTec

membranes [7]. This underlines the above statement that increased temperature increases the fluxes within the normal operability range.

A study that underlines these correction models from DuPont (Eqn. (3.17) and (3.18)) states that the diffusion coefficient of a water in a polymer (e.g. polyamide) will have a dependence on temperature like described by Arrhenius equation shown in Eqn. (3.19). [32] From this equation it is obvious that the water diffusion increases with increased temperature. An intuitive understanding of this temperature dependency is that the molecular distances in the polyamide active layer increases, thus increased volumes between the molecules for the dissolved solute and solvent to diffuse through.

$$D = D_{\infty} e^{-\frac{E_a}{RT}} \quad (3.19)$$

Here, D_{∞} is the theoretical diffusion coefficient at infinite time, E_a the self-diffusion activation energy, R the universal gas constant and T is the temperature. This relation assumes that the water does not influence the physical properties of the polymer as it diffuses through it, and that the activation energy of the diffusion process is independent of temperature. [32]

This study, regarding Arrhenius dependence on the water in polymer diffusion coefficient, also states the permeability coefficient of water in polymers can be expressed as the product of diffusion- and solubility coefficients. Doing so will account for the water-polymer interactions neglected in Eqn. (3.19). Thus, the mathematical form of DuPont's TCF seems very feasible from a theoretical point of view since both solubility and permeability coefficient follows this form of Arrhenius relation. [32]

There are some limitations in applying Arrhenius equation to estimate these coefficients. The most important for this matter is related to the glass transition temperature of polymers. I.e., when its structure goes from a solid like to a rubberier like structure. Arrhenius does not account for that molecular movement decreases rapidly in this transition [33]. The glass transition temperature for the polyamide layer in the SR90-440i is not known due to lack of detail. However, from an old datasheet retrieved from Aker BP the SR90-440i cannot be operated at higher temperature than 45°C. Hence, the transition temperature is certainly somewhat above this temperature. temperature much higher than the operating temperature for the SRUs, which is about 10 °C.

If the solute is assessed in the same manner as water, with respect to the membrane, the solute permeability will also depend proportionally on temperature. Thus, solute permeation will like water flux increase upon increased temperature. Again, in line with what reported by DuPont for salts in their manual [7]. Overall solute diffusion in the membrane is likely to also depend on solute in solvent diffusion to some extent. That is since these solutes are dissolved in the solvent inside the polymer. Solute in solvent diffusion can be described with Stokes-Einstein relation shown in Eqn. (3.20)[19]

$$D = \frac{k_B T}{6\pi\eta r_s} \quad (3.20)$$

Where, k_B is Boltzmann's constant, η the dynamic viscosity, and r_s the solute radius. This equation gives a good approximation of a solute's diffusion coefficient in a liquid for solute radii up to 0.5 to 1 nm. [19] Thus applicable for the purpose of describing diffusion of sulfate in water as it has an ionic radius of approximately 0.24 nm [34].

Stokes-Einstein indicates proportionality between temperature and diffusion of solute in solvent. The pressure effects on permeability via viscosity are probably marginal in this project since water viscosity is very little affected by pressures for such liquid systems. [35]

3.1.4.3 Membrane selectivity – The scaling effects of permeability and molar volume

The assessment done in the previous sub-chapter isolates effects of pressure and temperature dependencies on the singular species. However, it does not assess the effects of the actual differences in permeabilities between solutes and solvents. To do so, the permeabilities for sulfate and water are estimated for the SRUs at Ivar Aasen based on laboratory measurements and process data from October 2017 at ~ 14:00. The data are used in the solution-diffusion model to visualize fluxes as functions of feed- and permeate pressures as shown in Fig. 3.7. All values and formulas used to do these estimates are listed in Tab. 3.2.

The permeabilities were calculated by rearranging Eqn. (3.14) and (3.15), isolating permeabilities. It should be noted that this is a coarse prediction since it is calculated with both SRUs running in parallel. Also, the measured data (sulfate concentration and TDS) are measured downstream of the deaerator. Thus, oxygen has been removed and some chemicals introduced (oxygen scavenger and scale inhibitor) which could affect the calculations. However, this uncertainty is not considered a problem for the purpose of comparing fluxes between sulfate and water with the solution-diffusion model. I.e., it is the difference in order of magnitude between solute and solvent that is the key feature here.

Table 3.2: Estimated permeabilities and values applied do the estimation. Estimation is done across both SRUs as they were running in parallel at the time of sampling. Values in *italic* are measured values (at specific sample points 19. August 2017), **bold** denotes process data retrieved at the same time as the samples. Other values are either calculated or given in the theory and specified by notes. In this table subscripts *i* and *j* denotes water and sulfate specifically.

Parameter	Value	Units
Concentrations ¹	$c_{j,0} = 2.990, c_{j,l} = 0.013, c_{i,0} = 988, c_{i,l} = 998$	kg/m ³
Total dissolved salt, (TDS)	$TDS_{feed} = 39, TDS_{permeate} = 29$	kg/m ³
Temperature	282.95	K
Total permeate flow	$\dot{Q}_p = \mathbf{0.20053}$	m ³ /s
Average pressures	$p_l = \mathbf{0.11 \cdot 10^5}, p_0 = \mathbf{23.70 \cdot 10^5}$	Pa
Active membrane area ²	$A_m = 35337.6$	m ²
Thickness active layer ³	$l = 200 \cdot 10^{-9}$	m
Molar volumes ⁴	$v_j = 3.02 \cdot 10^{-5}, v_i = 1.803 \cdot 10^{-5}$	m ³ /mol
Calculated fluxes	$J_j = 7.380 \cdot 10^{-8}, J_i = 5.663 \cdot 10^{-3}$	kg/(m ² s)
Estimated permeabilities	$P_j = 4.955 \cdot 10^{-15}, P_i = 1.437 \cdot 10^{-10}$	m ² /s
Formulas applied	$c_{0,i} = \rho_{seawater} - TDS_{feed}$ $c_{l,i} = \rho_{seawater} - TDS_{permeate}$ $J = \dot{Q}_p \rho_{seawater} / A_m$	
<p><u>Notes:</u></p> <ol style="list-style-type: none"> 1. Water concentrations is based on measured TDS and seawater density at 10°C with 3.5% salinity. 2. Calculated based on active area per membrane (Ch. 2.3.1) and number of membranes in both SRUs (Ch. 2.3.2.) 3. From membrane description in Ch. 2.3.1 4. Molar volumes are defined for 15 °C (see Ch. 3.1.4.1) and assumed applicable at 9.8 °C (282.65 K) 		

Below, in Fig. 3.7, fluxes of water and sulfate is presented as functions of pressures by use of the solution-diffusion method. The applied permeabilities are estimated as described above. Flux for sulfate is somewhat hard to spot in this plot as they are both coinciding with the x-axis. Thus, compared to water, sulfate flux can be considered independent of pressures. If the plot is scaled/fitted to show how the sulfate flux change with pressure it will show that it is in the range of 10^{-12} kg/m² across the given pressure range on the x-axis.

This means that the sulfate rejection will increase with increased inlet pressure, and it will decrease with increasing outlet pressure. This as the sulfate permeate concentration decreases due to increased water flux when increasing inlet pressure, while the opposite effect for increased permeate pressure as water flux drops. This effect is in line with what is reported by DuPont for their membranes in [7].

There is not enough information available to compare fluxes of sulfate and water as function of temperature. To be able to do so it is necessary to have a temperature correction factor for sulfate permeability such as those for water shown in Eqn. (3.17) and (3.18) and molar volumes as functions of temperature. Alternatively, have knowledge of the initial diffusion coefficients and then model changes to it through dependencies like Arrhenius and Stokes-Einstein on the diffusion coefficients. In addition, sorption coefficients and their functional dependence to temperature is also needed. This is information that is hard to retrieve from literature or in technical documentation. The main reason is that the necessary details about the SR90-440i is not publicly available. And, to relate partial molar volume of sulfate to temperature it is necessary with an experimental set-up to track how the volume derivative changes upon addition of sulfate at different temperatures. Such a set-up is not available for use in this project.

However, DuPont states in [7] that permeate flux increases while salt rejection decreases with increasing temperature. Thus, temperature changes most likely have a higher impact on the sulfate concentration in the permeate stream compared to what seen for pressure changes.

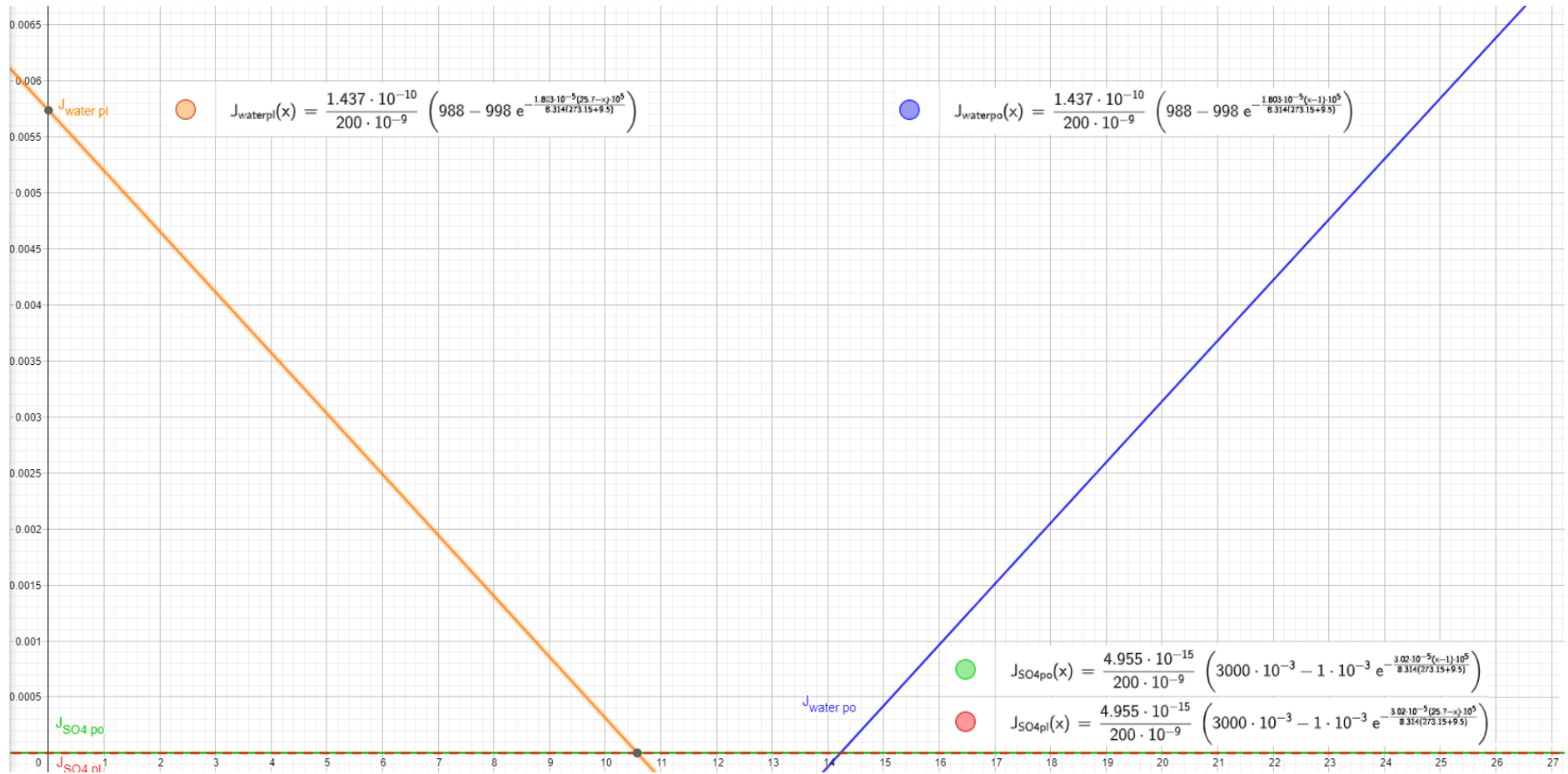


Figure 3.7: Flux as function of feed- and permeate pressures at a fixed temperature of 9.8 °C. “J” indicates fluxes, species are sub-noted “water” and “SO4”, while *po* and *pl* indicates the specific graphs variable in feed- and permeate pressures, respectively. Dotted lines at x-axis visualizes how little pressure dependency on sulfate flux compared to water flux. Pressures on the x-axis is in barg, while the y-axis is flux in units of kg/(m²s).

3.1.4.4 Flux dependence on operational parameters

The above theory indicates that both permeability and molar volume increases with increased temperatures which in turn increases fluxes via the solution-diffusion model. Thus, these effects will counteract the temperature effect indicated by the solution-diffusion model (Fig. F.3 in Appendix F) where increased temperature reduces concentration gradients in the membrane. For this reason fluxes will most likely follow and be proportionally dependent on temperature. Increasing pressure on the feed side increases fluxes while increasing pressure on the permeate side decreases fluxes.

The example in Ch. 3.1.4.3 visualizes how differences in permeability and molar volume scales the system and introduces the membranes selectivity. In these examples sulfate fluxes is independent to pressure changes relative to that of water fluxes. This scaling will also be present when adjusting temperature, but to what extent cannot be estimated without knowing the functional relations to temperature for permeabilities and molar volumes of the species.

3.1.5 Concentration polarization

Concentration polarization (CP) is the phenomena where permeation of species through a membrane is affected by concentration differences between fluids in the bulk flows and the fluid in the layers adjacent/close to a membrane interface(s). This occurs due to imperfect mixing and membrane selectivity. [19] I.e., if the membrane does not separate species, neither will it affect concentrations. And if the fluids on each side of the membrane is perfectly mixed both would be homogenous fluids, thus no CP. The solution-diffusion model does not account for this and due to its dependencies on surface concentrations of species this phenomenon is obviously important and needs further attention.

From this project's perspective, assessing spiral-wound elements, the imperfect mixing on the feed/concentrate-side takes form due to channel flow with wall friction and viscous effects inducing a laminar flow adjacent to the membrane surface [19]. At the permeate side the fluid, when leaving the dense thin-film layer, enters a microporous- and support layer before crossflowing spirally inwards to the core. Thus, on the permeate side both internal concentration polarization (ICP) in the porous layer adjacent to the thin-film layer, and CP in the fluid adjacent to the porous layer can occur. The latter is most likely negligible as the ICP will govern the permeate side CP effects due to the very coarse support layer being adjacent to the permeate flow.

However, as it is assumed (in Ch. 3.1.3) that the active thin-film layer governs the transport mechanisms via the thin-film composite membrane, the effect of the CP in the microporous- and support layer on the permeate side is also neglected. Neglecting the effect of CP on the permeate side, for the case of the SRUs, seems to be in line with relevant theory. This as membrane processes with significant permeate flow, such as the nanofiltration of seawater, will depend on the ratio of fluxes for the different species and there will be no CP on the permeate side [19].

To be consistent the same coordinates argued in Ch. 3.1.4 is applied here so that this theory aligns with the theory to that of the spiral-wound elements used in the SRUs. Thus, CP is assessed for a spiral-wound cartridge in the direction normal to the active membrane layer, i.e. radial direction designated x-direction.

3.1.5.1 Laminar boundary layer

In the feed/concentrate channel a flow of feed/concentrate is present normal to the active membrane layers such as illustrated on the left-hand side of Fig. 3.8. Due to viscous effects in the fluid and wall friction a laminar boundary layer (LBL) adjacent to the membrane surface will be induced. The thickness of this LBL, δ , will depend on its Reynolds number and thus bulk flow velocity, viscosity and feed-channel geometry and thickness. On the right-hand side of this figure there is also an illustration of how spacer netting employed between the membrane leaves will help induce turbulence to reduce CP through better mixing reducing δ . [19]. It is one membrane leaf and spacer netting rolled around the core. Thus, this leaf become neighboring “leaves” upon spiral mounting to the core.

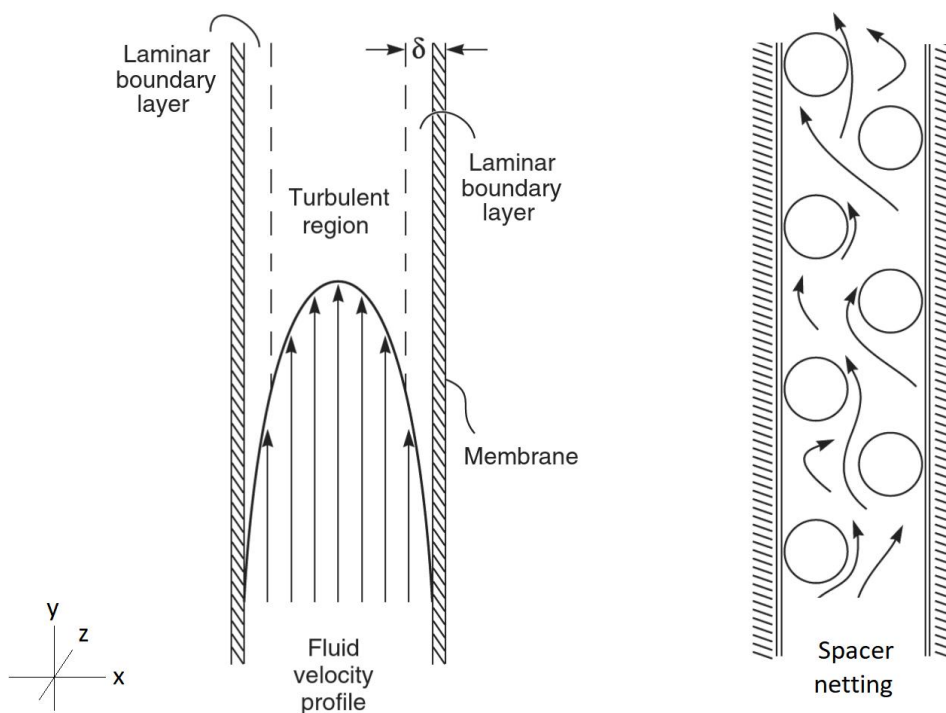


Figure 3.8: Channel flow in between membrane leaves. On the left side are flow regimes and laminar BL thickness (δ) illustrated, while on the right-hand side are an illustration of a channel flow with a spacer netting inducing turbulence. layer. Modified from [19]

For either case, spacer or not, due to mixing effects of turbulent eddies present at some distance (δ) away from the membrane layers the fluid will be well mixed and assumed homogenous. The axial velocity (y-direction) in the LBL is much lower, essentially zero adjacent to the membrane layers. Thus, in the laminar layers the mixing occurs mainly by diffusion. CP is assumed to restrict itself to concentration gradients within the LBL. This means that the bulk flow is considered homogenous for each axial position even though it is drawn with a laminar profile in Fig. 3.8. [19]

3.1.5.2 Concentration polarization – Boundary layer film model

The concentration profile of species j inside the LBL is shown in Fig. 3.9. This is the concentration polarization of that specie at that axial (y) position. The normal convention is to relate CP to the minor species [19], thus sulfate for the case of the SRUs. This illustration shows how the minor species j rejected, to some degree by the membrane, will enrich inside the laminar layer and thus induce CP. If the minor specie had been less rejected than the other species, the polarization would have occurred in form of depletion of that specie inside the LBL. [19] How the concentration profile develops depends on the balance between permeation of it through the membrane and the diffusion of it between the LBL and bulk flow. Permeation of the species from the bulk stream is driven by the volume flux, J_V , as it induces a convection of species from bulk and into the LBL. While the diffusive term within the LBL is driven by the CP itself. [19]

From the SRU perspective this diffusion will be in form of “back-diffusion”, thus diffusion from the laminar layer and back into the turbulent bulk flow. This would obviously be “forward-diffusion” for a depleted specie as the CP then will drive diffusion from bulk and into the LBL. [19]

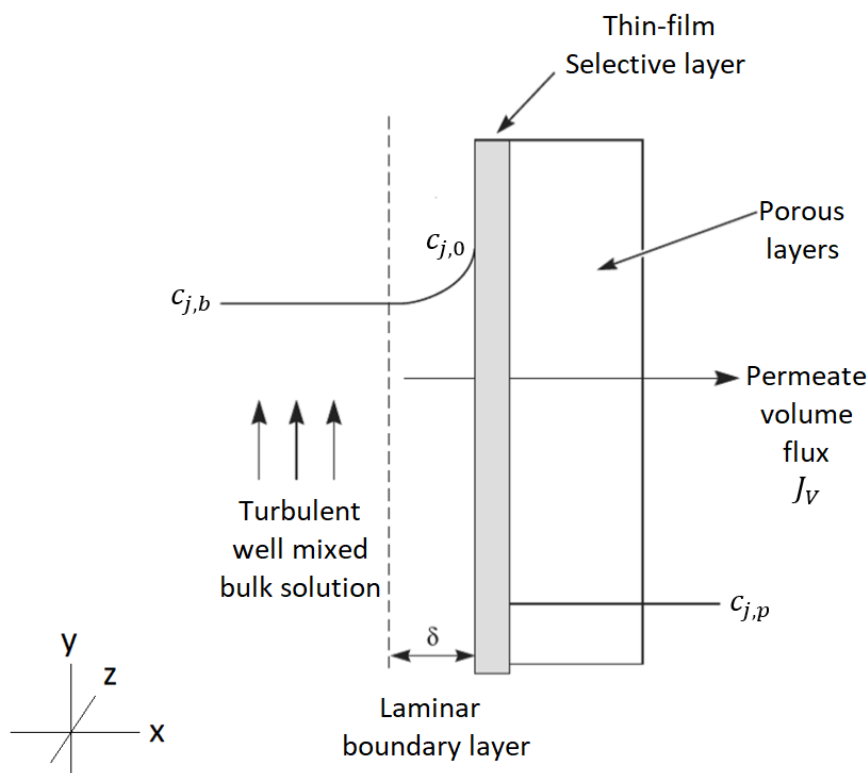


Figure 3.9: Concentration polarization by enrichment of species j within the laminar boundary layer on the feed side of a thin-film membrane. Modified from [19]

The feed/concentrate composition changes in the axial direction (y -direction) as the separation process concentrates the rejected species as fluid passes along the active membrane layers. In the SRUs the sulfate concentration increases in the axial direction of the feed/concentrate channels. This means that the density of the feed changes as it becomes increasingly concentrated. Thus, the permeate density will differ somewhat from the gradually changing feed/concentrate flow.

However, as the SRUs mainly rejects sulfate (and other divalent salts) from seawater the system can be assumed dilute. Assuming constant density in the entire SRU introduces an error of approximately 2.6 %. To verify this error a comparison of seawater vs. freshwater densities can be done. The error calculated above is based on densities at 15 °C and 3.5% salinity for seawater given in [30][36]. [19] Since the SRUs considered in this project is a NF system permitting most monovalent salts this suggested error by assuming constant density will be in the high range of what is introduced. That is since less salt rejection means less of a difference in densities between feed, concentrate and permeate. A RO system will probably achieve sufficient salt removal to introduce close to such figures of error by assuming constant water densities.

As the density can be assumed constant both volume flow and mass flow is conserved with the constant density scaling them as shown in Eqn. (3.21).

$$\dot{m} = \dot{V}\rho \Rightarrow \dot{m} \propto \dot{V} \quad (3.21)$$

A constant density also implies that flux is directly proportional to mass flow as the fluid does not expand or contract. Thus, the permeate volume flux is conserved from bulk-LBL interface to permeate.

From Fig. 3.9 it is evident that it is, from a transport mechanism point of view, of interest to be able to describe the concentration of a specie at the membrane surface as function of the bulk concentration of the specie. The reason is that the bulk concentration is typically more available for measurement in an operational system. For instance, if solute j is the minor species of interest the concentration of this specie at the surface should be functionally related across the LBL to the bulk concentration of it in the feed/concentrate flow, $c_{j,0} = f(c_{j,b}, \dots)$. To do so the net transport of j need to balance at each position in the LBL with the permeate flux of it through the membrane. Thus, to fulfill mass conservation for any specie inside the LBL, the sum of convection towards- and the diffusion towards/away from the membrane must equate the permeation of that species through the membrane. [19]

A mass balance can be expressed with mass fluxes as shown in Eqn. (3.22). That is by use of the permeate volume flux, J_V , and the positional concentration of the species in question. The concentration of j in the permeate, $c_{j,p}$, is constant. While its concentration inside the LBL, c_j , is changing. [19]

$$J_V c_j - D_j \frac{dc_j}{dx} = J_V c_{j,p} \quad (3.22)$$

The initial term from the left is the convective term of j towards the membrane, while the second term describes diffusion where Fick's law (Eqn. 3.3) is utilized to express diffusion of j in the domain. On the right-hand side is the permeate flux of species j . The differentials are separated by some rearranging and integrated over the laminar BL. This yields Eqn. (3.23) describing the concentration of the solute in the feed adjacent to the membrane surface. [19]

$$\begin{aligned}
J_V dx &= D_j \frac{dc_j}{c_j - c_{j,p}} && \Leftrightarrow \\
J_V \int_{\delta} dx &= D_j \int_{c_{j,b}}^{c_{j,0}} \frac{dc_j}{c_j - c_{j,p}} && \Leftrightarrow \\
J_V \delta &= D_j \ln \left(\frac{c_{j,0} - c_{j,p}}{c_{j,b} - c_{j,p}} \right) && \Leftrightarrow \\
\frac{c_{j,0} - c_{j,p}}{c_{j,b} - c_{j,p}} &= e^{\frac{J_V \delta}{D_j}} && \Leftrightarrow \\
c_{j,0} &= (c_{j,b} - c_{j,p}) e^{\frac{J_V \delta}{D_j}} + c_{j,p} && (3.23)
\end{aligned}$$

This expression can be utilized in the solution-diffusion equations, Eqn. (3.14) and (3.15), to account for CP. To do so the LBL thickness must be estimated, which is not readily available. This can be estimated by use of, e.g., Blasius method but is not assessed in this thesis.

Considering the transport mechanisms assessed through the solution-diffusion model in Ch. 3.1.4 CP will obviously decrease the system efficiency through affecting the concentration gradients negatively. For the SRUs it increases the sulfate gradient, thus increasing its flux, while at the same time it reduces the water gradient and restricts its flux. The polarization thus induces a higher osmotic pressure to overcome when enriching the salt concentrations in the LBL. These negative effects on system performance are not considered as fouling per say as it is reversible by adjusting operational parameters which is discussed below [20].

In this project, coupling bulk- to surface concentration via Eqn. (3.23) is of little use as there is too little information available on the membranes used in the SRUs to perform a sufficiently precise modelling of transport through the membrane. However, the degree of CP is of more interest which can be described by the concentration polarization – modulus. This CP-modulus defined as the ratio between feed-surface concentration and bulk concentration of the solute in question, i.e. $c_{j,0}/c_{j,b}$. The modulus describes the degree of CP which is very relevant due to the negative effects of this phenomena, such as increased osmotic pressure when enriching salts adjacent to the membrane, facilitating fouling, etc.. [19] Rearranging Eqn. (3.23) to express the modulus yields Eqn. (3.24) as shown below:

$$\frac{c_{j,0}}{c_{j,b}} = \left(1 - \frac{c_{j,p}}{c_{j,b}} \right) e^{\frac{J_V \delta}{D_j}} + \frac{c_{j,p}}{c_{j,b}} \quad (3.24)$$

Thus, a modulus of one means that there are not CP, while a modulus deviating from this means that a polarization takes place. [19] For pressure-driven processes such as the NF in the SRUs it is most likely to encounter a CP above unity, thus enrichment of the minor species in the LBL. And, to conserve mass, when concentration of a specie increases in a fixed fluid volume

another species concentration must decrease. Thus, the presence of CP in the SRUs is present as enrichment of sulfate (and other retained salts) and reduced water concentration in the LBL, efficiently reducing the water flux and increasing sulfate flux. That is, both through changing concentration gradients in the membrane and by increasing the osmotic pressure as the solute concentration across the membrane increases.

From Eqn. (3.24) it is evident that the Peclet number is governing the degree of CP. Thus, it is the ratio of convective- to diffusive transport and the domains characteristic length that governs the degree of CP. Reducing the permeate volume flux and/or the LBL thickness exponentially reduces the CP modulus. Or, by same functional dependence, by increasing the diffusion coefficient of the solute in the solvent. [19] These effects can be broken down and explained in the following way:

- **Increasing the permeate volume flux increases CP** because convection will supply the LBL with more solute from the feed bulk, thus increasing the concentration gradient of it. I.e., increasing J_V will eventually increase permeation of the solute through the membrane, but not before the concentration gradient of has increases in the LBL as that is its driving force for permeation inside the dense membrane (see Eqn. (3.14)). A side-effect is that the flow regime in the feed/concentrate channel becomes less turbulent through reduced feed/concentrate flow in the system.
- **Increasing LBL thickness increases CP** as the domain governed by diffusional mixing gets larger.
- **Increasing the diffusion coefficient of the solute in the solvent reduces CP** due to its contribution to remove the concentration gradient by diffusional transport back into the feed bulk increases. The general diffusional mixing inside the LBL also increases as waters self-diffusion increases (see. Eqn. (3.20)).

3.1.5.3 Concentration polarization dependence on operational parameters

From the above assessment it is obvious that recovery (i.e. feed- and permeate flow velocities) and temperature are important. Increased recovery increases the volume flux and thereby increases the CP. For the SRUs, running with fixed total recovery, the balancing of recovery over each stage can be an important factor in achieving the lowest total CP. However, to prevent scaling it is important to consider the elevated sulfate concentration in the feed to the 2nd stage [7]. While increased temperature will reduce δ through increased Reynolds number as water viscosity decreases [36], but also by increasing the diffusion coefficient of sulfate in water. All of which will contribute to reducing the polarization. Diffusion coefficient of solutes in water is described by Stokes-Einstein equation shown in Eqn. (3.20) which shows its proportionality to temperature, T . [19]

Amongst these two approaches, recovery- and temperature changes, the latter will probably only marginally affect the CP. That is based on that:

- The diffusion coefficient of the sulfate (minor specie) scaled through the ratio of Boltzmann's constant to the solute radius and solution viscosity as seen in Eqn. (3.24). Thus, $D_j \propto T * 2.4 \cdot 10^{-12}$. This figure is found by inserting tabulated values for seawater with 3.5% salinity at 15 °C into Stokes-Einstein's relation in Eqn. (3.20). [36]

- The increased degree of induced turbulence is small as the denominator in Reynolds number is subjected to a very small viscosity change within the normal operational temperatures for the SRUs. More specifically, the dynamic viscosity reduction is approximately $\sim 1.9 \cdot 10^{-4}$ Pa·s when the temperature of seawater is elevated from 10 to 15 °C [36].

For the case of controlling CP with the volume flux flow pulsing is a technique that can be applied to reduce polarization through inducing dynamics to the LBL, thus fluctuate its thickness. [37]

NOV, a distributor of the SR90-440i, recommends a modulus below 1.2 for the membranes used in the SRU which means that the sulfate concentration at the membrane surface on the feed side is not to exceed 1.2 times that of the bulk concentration. This upper limit ensures sufficient turbulence to control the contribution of CP on biofouling and/or scaling. Biofouling and scaling are facilitated through introduction of a laminar/stagnant region and through elevated salt concentrations [7]. To estimate average CP modulus DuPont have established a set of mathematical equations shown below in Eqn. (3.25) and (3.26) modified from [7].

$$\bar{\mathcal{R}} = 1 - (1 - \mathcal{R})^{1/n} \quad (3.25)$$

$$\overline{CP} = e^{0.7\bar{\mathcal{R}}} \quad (3.26)$$

In these relations $\bar{\mathcal{R}}$ is the average spiral-wound element recovery, \mathcal{R} the system recovery, n the number of elements in series, and \overline{CP} the average polarization factor per element. Inserting a 75 % system recovery (0.75) when 12 elements in series, which is the case for the SRUs, the average CP is estimated to 1.08. Considering the stages separately, 50 % recovery over 6 elements in series, gives the same estimate.

However, it is important to consider that the CP will change axially or y-directional through the system. That is since the well mixed feed/concentrate stream will get gradually- lower water concentration and higher salt concentration. Thus, from a water perspective, water flux through the membranes decreases with axial movement along the elements. This happens due to decreased water diffusivity in the active layer and increased osmotic pressure difference with increasing difference in salt concentration across the membrane. This implies that CP will be more prominent in the initial elements as the volume flux across them are the highest. An indication of that this is indeed occurring in the SRUs was observed by Avista in their membrane autopsy as much more fouling was found in the initial stage and the initial membranes. Avista reported a thick layer of foulant on the 1st stage lead element autopsied while very little foulant were visible on the tail elements tested.

Even though it is reasoned to neglect electrostatic effects when considering the solution-diffusion model it should be mentioned that CP of ions in electrolytes can affect ion mobility. The reason is that enrichment of e.g. anions like sulfate can cause higher degree of repulsion of other anions in the feed. If such effects occur in the LBL this will effectively alter permeabilities for different ions in the electrolyte. This is, like for the solution-diffusion model, not assessed any further.

3.1.6 Fouling and membrane degradation

For dense membranes, such as the active layers for the SRU membranes, membrane fouling occurs due to accumulation of ‘materials’ on the spacer material and/or at the membrane surface. Thus, fouling is deposits forming layers inside the membrane’s feed/concentrate channel. [7] Fouling is distinguished from CP in that it is not reversible during normal operation. I.e., to retrieve performance due to fouling it is necessary to stop production and perform chemical restoration or membrane replacement. However, even though CP is not considered fouling its degree of presence can probably cause it through facilitating both a calm fluid region for layer formation-, and by elevated solute concentrations inducing scaling at the active membrane layer. [38]

The feedwater introduced to the SRUs at Ivar Aasen are pretreated by ultrafiltration and chlorination/de-chlorination to remove particles over 0.04 microns and to retard bio growth as discussed in Ch. 2.1. By averaging all available Silt Density Index (SDI) lab tests on the seawater introduced to the SRUs yields an average of ~0.5, one sixth of the recommended level of 3 shown in Tab. 2.2. The tests are taken monthly downstream each of the six UF twins, and the data available dates back to March 2020.

Based on this pre-treatment and historical data the dominating types of fouling material for the SRUs are most likely due to biological fouling, scaling, and dissolved organics. [38][7] Fouling by colloids and particulate matter are more of a concern for the UFs which is not a part of this project scope. UF also mitigates the larger sized molecular dissolved organics meaning that biofouling and scaling are of most interest. This includes mitigating most of the algae that varies seasonally. [7] Thus, the seasonal algae effects will be more of a concern for the UFs than the SRUs.

Through the assessment of CP in the previous sub-chapter it is evident that this phenomenon can induce accumulation of “materials” and thus induce fouling. That through presenting slower moving some adjacent to active membrane layer and though polarization of concentrations within it. Enrichment of nutrients and salts can facilitate both bio growth and scaling. And the presence of slower moving regions will be a natural place for any deposition of materials that might be carried with the feed.

Literature on fouling for NF systems such as the SRU states that biofouling typically is the dominating type of fouling, e.g. as stated in [39]. This was also confirmed by both NOV and DuPont through dialogue with their representatives, which is based on their experience with NF of seawater pretreated with UF. Due to this, and the assessment above, biofouling and scaling is assessed in this sub-chapter on fouling.

Biofouling:

This type of fouling, assessing the SRUs, occurs due to dissolved nutrients like nitrogen and phosphorous present in the seawater being partly retained by the active membrane layer. Nutrients are biodegradable components and acts as feed for microorganisms. The nutrients are introduced to the SRUs as they are not retained in the pretreatment by UF, and also through chlorination which can introduce biodegradable fragments as it breaks down organic molecules present in the water. [7]. Figure 3.10 shows examples of bio film formation on both the active membrane surface and on the feed spacer netting.

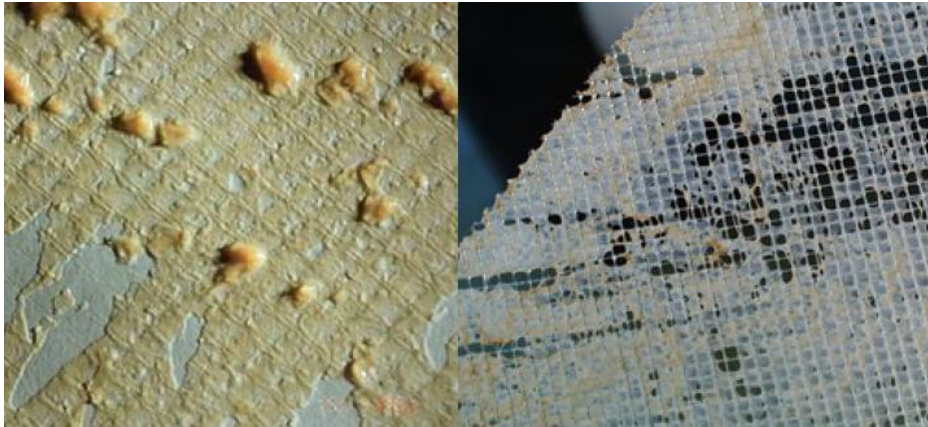


Figure 3.10: Biofilm on active membrane surface and spacer netting. Modified from [7]

The combination of CP and membrane selectivity for these nutrients facilitates a nutrient enriched slow moving/stagnant fluid layer. The degree of which depends on the degree of polarization. Microorganisms, not inactivated by chlorination, introduced to such an environment may thrive and thus accumulate on the membrane surface and/or spacer material. With accumulation of microorganisms a bio film also forms which efficiently protects the microorganisms against flow induced viscous effects (shear) and against biocide chemicals. [7][38] The preventive measure for this at Ivar Aasen is to continuously chlorination (with dechlorinated to prevent halogen damage) and biocide batching.

A study on biofouling for spiral-wound NF membranes states that biofouling is a feed spacer problem [39]. Here it is emphasized that hydrodynamics is very important to consider during design of the feed spacer, also the surface characteristics of the spacer itself. However, it is not possible to adjust the spacer design without replacing the membranes with another type.

Even though the reasoning about to be given in this paragraph is not found in the literature explicitly it is somewhat intuitive to consider the presence of a slower moving liquid adjacent to the spacer netting being related to biofilm forming on the spacer netting to some extent. To what extent this suggested relation facilitates biofouling on the spacer netting is hard to conclude. However, as for the LBL thickness, the degree of it should be very related to the feed velocity and thus recovery. For the SRUs it is evidently also an “active layer issue” since the PV on the 1st stage permeate stream closes to maintain its desired pressure difference as the Δp in the feed channel increases. Thus, clogging the active layer might contribute to increased feed-to-concentrate pressure difference as more feed must pass through the feed/concentrate channel when the active layer fouls.

Thus, for biofouling in general the subject of concentration polarization and LBL thickness is of high interest. Reducing zones enriched with nutrients will retard biofouling and reducing LBL thickness might help to wash away, prevent, or reduce accumulation of any bio-growth. This “washing effect” is due to viscous shearing effects between the moving fluid and the solid surfaces. Flow pulsing, as mentioned before, might also be an approach on this issue.

Another factor that probably affects the rate of biofouling is the seawater temperature through facilitating the bacterial growth. The theory of this is not assessed in this thesis, but there are articles that state that the biofouling activity and membrane pressure drop increases with increased temperature for reverse osmosis operations within the temperature range of interest in this project. [40] Thus is it likely that the same effect can be seen in the SRU nanofiltration.

Scaling:

Scaling is the product of precipitation and deposition of salts in the system due to concentrations of scale-forming species exceeding that of the solubility in the liquid. Scaling potential must be considered for each salt present in the liquid. And in general, scaling is not an issue if the ion product of a particular salt is less than its solubility product in the conditions the potential is assessed, i.e., the concentrate stream is of most interest. [7]

To give a brief explanation of the solubility product a saturated water-single salt system can be considered. I.e., salt molecules are present in solid form and its ions present in the liquid phase. This means there is an equilibrium between the ions of the salt and the solid salt as shown in (R3.1). [41]



Here AB is a general salt that will fully dissociates to ions in water, i.e. when the salt dissolves it only forms the ionic forms. The subscripts indicate solid and aquatic phase, and the superscripts indicate the cation and anion. While a and b simply denotes the stoichiometric number of cations and anions. E.g. for disassociation of magnesium hydroxide, $Mg(OH)_2$, b would be equal to two. [41]

By considering the concentrations of the above ion dissociation equilibrium the solubility product of it can be expressed mathematically via the ion concentrations (denoted by [brackets]) as shown in Eqn. (3.27). [41]

$$K_{sp} = [A^+]^a [B^-]^b \quad (3.27)$$

The solubility product, K_{sp} , is assessed from the definition shown in Rx. (R3.1), thus at equilibrium when both solid salt and liquid ions are present in the liquid. This means that the solubility product is defined from the ionic concentrations when the rate of disassociation of solid salts to ions equals the rate of precipitation of salt. I.e., no net disassociation or precipitation.

The ion product, K_{IP} , of a particular salt is defined in almost the same way, but at a particular time, thus not necessarily in the state of equilibrium. The definition of the ion product is shown in Eqn. (3.28). [41]

$$K_{IP} = [A^+]_t^a [B^-]_t^b \quad (3.28)$$

This means that scaling or precipitation will occur if the calculated ion product of a particular salt in a solution is higher than the solubility constant, $K_{IP} > K_{sp}$. For a batch system precipitation of the salt will not stop until the concentration yielding that ion product is equal to the saturation concentrations defining the solubility product shown in Eqn. (3.27). While, in theory, a dynamic process like the SRU will have continuous precipitation until operating

conditions is changed either increasing the salt solubility- or reducing the ion concentrations sufficiently in the liquid considered. “In theory” as scaling efficiently changes the operating conditions as it fouls the system, thus the accumulation of scale will very likely affect the formation of it. However, considering a specific point in time the above assessment is correct.

Evaluation of the ion product and solubility product of a salt indicates the three following scenarios: [41]

- $K_{IP} > K_{SP}$: Super saturated, precipitation will occur.
- $K_{IP} = K_{SP}$: Saturated, system is in equilibrium. No net precipitation or disassociation.
- $K_{IP} < K_{SP}$: Unsaturated, no precipitation but more salt can disassociate

Thus, for the SRUs, precipitation can be predicted by estimating the different ion products in the concentrate stream and compare these to the different solubility products in the same conditions. And one should secure that the recovery is operated so that the salt concentrations in the concentrate are unsaturated in the liquid so that no scaling occurs.

When treating a multi-ionic solution the non-ideality of the liquid must be considered. That is, the solubility product of a particular salt in an electrolyte must be defined for the salt in question in the environment it is in. DuPont present the ASTM standards in chapter 2.4 of [7] for this purpose, thus methods to determine scaling potentials for different types of scales. To assess scaling potential, they utilize the ionic strength of the multi-ionic liquid in question and compares k_{sp} 's for that particular ionic strength with the correlating ion pairs ion product in the same conditions (i.e., in that ionic strength).

Ionic strength is defined as shown in Eqn. (3.29) and derived so that it reflects the ionic activity coefficients and thus how ions in the solution affects the electrolyte activity. [42] Different salts solubility products can be found tabulated against ionic strengths in the literature.

$$I = \frac{1}{2} \sum N_j z_j^2 \quad (3.29)$$

Here j denotes the different ions in the solution, while N and z is the ion concentration in molality and charge number, respectively.

The tricky part, when it comes to NF, is to find the ionic strength in the concentrate without performing explicit measurements. For RO on the other hand one can simply assume complete rejection of all salts and relate the (often known) feed concentrations with the concentrate concentrations via recovery. This correlation can be done as shown in Eqn. (3.30) [7].

$$I_c = \frac{I_f}{1-\mathcal{R}} \quad (3.30)$$

The subscripts of c and f in Eqn. (3.30) denotes concentrate and feed, respectively. And the denominator efficiently acts as the water rejection factor as \mathcal{R} is the water recovery. This

relation is true if all salt is rejected by the membrane, as ionic concentration then only changes due to removal of water, i.e. all salt ions are still in the assessed domain.

Scaling is generally less of a problem for NF relative to RO as the salt passage is much higher for NF. However, for the second stage treating concentrate from the initial stage one can yield salt concentrations high enough to cause scaling if the recovery is set to high. Thus, it is important to have control over the recovery over both stages and not exceed the recommendations from the manufacturer which is for the SRU set-up 55-60 % system recovery as stated in table 26 in DuPont's technical manual for RO and NF [7]. Considering scaling, this recommended recovery might not consider the fact that a scale inhibitor is injected into the feedwater before entering the SRUs. This will obviously increase the different/particular salt solubility products. To what extent is not assessed in this thesis due to lack of public information on the scale inhibitor applied. As little is known about the effect of the scale inhibitor used in the SRUs there is no reason to estimate any of the scale potentials. That is since it cannot be stated to what degree the different solubility products, K_{sp} s, is shifted by the scale inhibitor.

From the above assessment it is obvious that increased recovery moves us closer to the scaling potentials in the concentrate stream due to elevated ionic concentrations. Other affecting parameters are temperature and pH. The latter is not an available variable for the SRU and is thus not assessed any further. When it comes to temperature a general dependency is that salt solubilities increase with increased temperature [43][44]. This will highly likely also be the case for salts in a multi-ionic solution like seawater.

If any scaling potentials needs assessment for the SRUs it is those salts derived with the ions of highest rejections in the SRU that should be investigated such as sulfate-, magnesium-, strontium- and nitrate ions. Aker BP have not assessed scaling potentials by performing such calculations for the SRUs, neither will it be done in this project.

Membrane degradation

Membrane degradation is the performance decline due to normal wear and tear for membranes being subjected to flux and thus pressure drop. The main two mechanisms of degradation are compaction and intrusion. Compaction refers to the membrane layer being compressed due to pressure drop across. While intrusion is when the membrane is intruded into the permeate spacer. Both phenomena also depend on temperature as the membrane layer tends to soften at increased temperature and since water viscosity is lowered. [7]

Even though fouling is not to be confused with normal degradation it is important to not let it trigger to high differential pressures prior to CIP wash. Doing so might induce higher rate of formation of both compaction and intrusion relative to what is expected. Thus, membrane degradation is the degradation to expect when the system is operated according to design.

When in dialogue with Avista about the membrane autopsy done on Aker BP behalf they stated that membrane projection software often factors a 7% annual performance decline for solvent flux of membrane systems such as the SRU. Normal performance indicators would typically be water flux and rejection.

DuPont's three-year element warranty states that each element should deliver at least 70 % of the specified average permeate flow when operated below 40 °C, and that the maximum salt

passage should not exceed 1.35 of the specified maximum salt passage. [45] Both these limits refer to the datasheet of the specific membrane in question.

The datasheet for the SR90-440i contains no average permeate flow or maximum salt passage explicitly, but states that the typical sulfate rejection is 99.6 %. If this typical sulfate removal is used as basis the warranty states that the annual decline in rejection should not exceed 0,45 %. I.e., with a fixed feed sulfate content of 3000 mg/L, after 3 years operation the sulfate content in the permeate can increase from 12 to 16 mg/L and still be within the warranty. This can be estimated utilizing simple percentage calculations and some iterations to solve the third-degree polynomial equating the salt passage on the third year relative to the initial passage. This is a coarse comparison as this warranty depends on a set of operational conditions, measurements, correct preservation if shutdowns, etc.. And it is somewhat uncertain whether the initial condition of 99.6% sulfate rejection is the correct one. On the other hand, a decline from “100 % flux” to 70% over a three-year period implicates that the flux can decrease with 11,19 % annually and still be within the warranty. This will not be seen in the SRUs as they operate with constant recovery. This will instead manifest itself as increased pressure drop across the active membrane layer.

3.2 Vacuum deaeration

The focus in this sub-chapter is to present the necessary theory to assess the deaerator efficiency. Thus, Henry’s law is the most central theory in describing the equilibrium distribution of a dissolved gas between the liquid- and gas phase.

3.2.1 Henry’s law

The English physicist William Henry experimentally found that the amount of a dissolved gas in a volume of liquid is proportional to that species contribution to the total pressure, via its partial pressure, in the gas phase above it. This is what is known as Henry’s Law, shown in Eqn. 3.31, which is valid only for systems ideal in both liquid and gas phase, and ideal-dilute solutions ideal in the gas phase. Thus, Henry’s law can be used for solutions of gases in liquids when both phases (liquid and gas) approaches ideality. [27][26]

$$p_j = H_{v,j,i} X_j \quad (3.31)$$

Where p_j and X_j is the partial pressure in gas phase- and liquid solubility of the dissolved gas in question, respectively. While $H_{v,j,i}$ is Henry’s volatility constant of species i dissolved in solvent j . In this case the most interesting species j , or dissolved gas, is oxygen. The solvent i is the seawater introduced to the SRDP. This formulation of the law is based on Henry volatility as increased henry constant is related to decreased solubility. Thus, taking the reciprocal of the henry constant yields a Henry solubility form of the law as shown in Eqn. (3.32). This is the form which is the form applied in this project and it has the same validity criterions as the volatility form [46].

$$\frac{1}{H_{v,j,i}} = H_{s,j,i} = \frac{X_j}{p_j} \quad \Rightarrow$$

$$X_j = H_{s,j,i} p_j \quad (3.32)$$

Here $H_{s,j,i}$ is the Henry's solubility constant of species i dissolved in solvent j , which is proportional to the particular solubility. It should be noted that there are many different definitions within the two main classes of Henry constants (solubility and volatility). In this thesis the Henry solubility form is applied. And the Henry solubility constant is defined with units of mol fraction per mbar, $[\text{mol}_j/(\text{mol}_{\text{tot}} \cdot \text{mbar})]$. This aligns our calculations with the assessed plants units for the dissolved (or residual) oxygen criterion in ppbmol by multiplying the results in Eqn. (3.32) with 10^9 .

Being valid for ideal solution, a solution where the forces between all different species in the liquid are equal, means that the molecular interactions in the liquid are independent of concentrations. [27] The validity with ideal-dilute solutions is also based upon these molecular interactions but how they become increasingly similar the more diluted the specie in question becomes in a real liquid. Thus, an ideal-dilute liquid is a real liquid where the solvent molecules experience a system that differs marginally from that of a pure solvent [26]. The PX-diagram shown in Fig. 3.11 shows a general case for how Henry's law is close to predicting the vapor pressure of the real solution when in the dilute range of solute j dissolved in the solvent. In this plot the solute, or minor species, is the most volatile as the mixture vapor pressure increases with increased content of it. The superscripted asterisk indicates pure substance, thus p_j^* is the vapor pressure of pure solute.

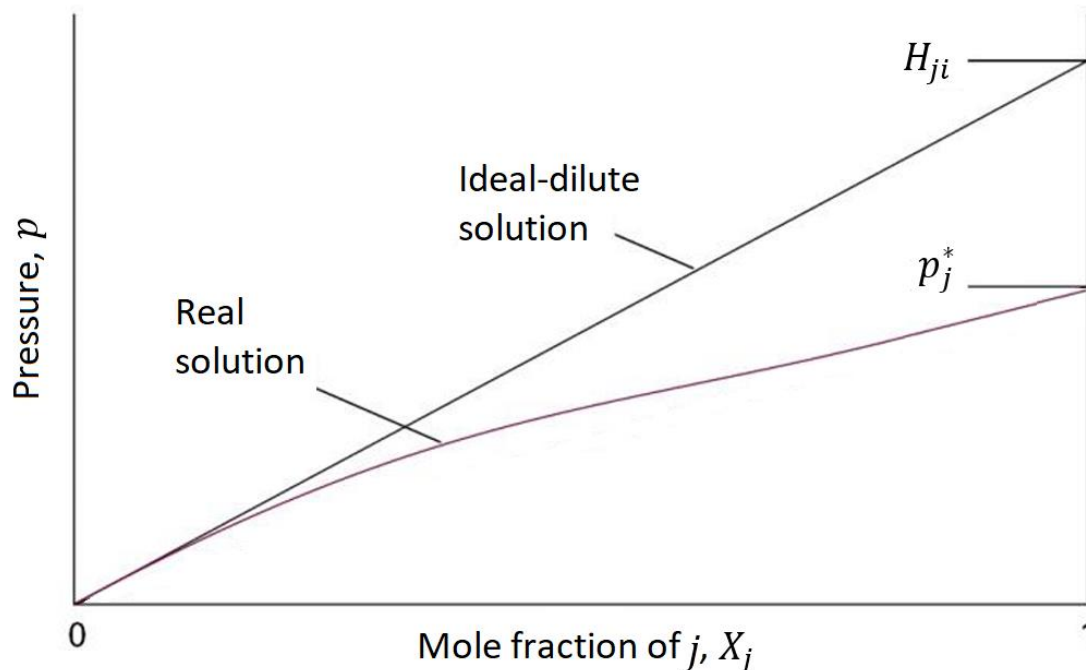


Figure 3.11: PX-diagram showing the validity range for Henry's law in the dilute region of the solute. Modified from [26]

This diagram illustrates how Henry's law is applicable for dilute mixtures. In other words, it is a limiting law as the slope of the ideal-dilute solution has its basis in the region where the concentration of the minor species (dissolved gas) approaches zero. This brings about the definitions of the solubility and volatility constants as shown through Eqn. (3.33) and (3.34) in Henry volatility- and solubility constant, respectively. [46] Henry volatility constant is the slope of the ideal-dilute solution gas phase pressure as X_j approaches zero, while Henry solution constant is its reciprocal.

$$H_{v,j,i} = \lim_{X_j \rightarrow 0} \frac{p_j}{X_j} \quad (3.33)$$

$$H_{s,j,i} = \lim_{X_j \rightarrow 0} \frac{X_j}{p_j} \quad (3.34)$$

Ideal gas is well known and is a gas where there are no acting forces between the molecules. Systems with moderate pressures and not too high temperatures are typically assumed ideal as this means large distances between- and slower moving molecules. Thus, negligible interactions between the molecules in the gas. Our system is very much within these demands as it acts under vacuum at moderate temperatures.

Assessing tabulated values for oxygen content, in seawater at 5 to 15°C with respect to its solubility when subjected to air at atmospheric pressure, they are in the range of ~ 8 to 10 ppmw. [47] These figures are converted to ppmw from mass concentrations by assuming a density of water of 1 kg/L. This temperature range is of interest as it covers the seawater feed temperature introduced at Ivar Aasen through the different seasons. The salinity of the seawater referenced above is 3.5 % slightly lower than the salinity of the seawater introduced to the SRDP at Ivar Aasen which is ~3.62 %. This use of the term "oxygen solubility in seawater" could be considered somewhat erroneous as air contains ~21 volume percentage of oxygen. Thus, oxygen's partial pressure in air is roughly 20 % of the atmospheric pressure which means that the solubility of pure oxygen gas in seawater is five times the above-mentioned [47].

Oxygen content in seawater at 65 m depth, where seawater at Ivar Aasen is retrieved, might not be equal to the content at the sea surface. To what degree depends on the thickness of the ocean mixed layer, water stratification, etc., topics not considered in this thesis. Oxygen content at this depth is not higher than surface water as it is further away from the source of oxygen, which is the important point to be made relative to the above assumption of an ideal-dilute system.

Thus, 8 to 10 ppmw oxygen content in seawater indicates a relatively dilute system. However, the definition of a dilute system is somewhat unclear. According to J. M. Prausnitz et. al. a rule of thumb for the validity of Henry's law is that the partial pressure of the species in question should not exceed 5 – 10 barg and that the solubility should not be higher than 30 mol % , or 30000 ppmmol. Above these pressures Henry's constant also becomes a function of pressure [48]. For the limits on the solubilities (dilute system), 30000 ppmmol is equivalent to 53333 ppmw for pure water. Keeping it within this range of solubility should keep the system as in the lower left corner in Fig. 3.11. This rule of thumb applies to systems where the solute and solvent are not highly dissimilar. In such cases deviations can be seen at much lower solubilities. Thus, the seawater introduced to the DA is within both criteria. This means that Henry's law should be valid, and the Henry constant should not be a function of pressure.

Pressure can simply be factored linearly via the Henry constant if the system is in the ideal-dilute region. However, the Henry constant will be a function of temperature and salinity both of which is important considering the DA system at Ivar Aasen. [49] Besides this it is also important to know how oxygen partial pressure depends on the operational parameters of temperature and flow.

From Henry's law it is evident that it is the lowest pressure inside the DA that is governing for the residual dissolved oxygen in the seawater after mechanical deaeration. Thus, the 2nd stage pressure is applied to do a theoretical assessment on the expected oxygen content in seawater entering the liquid sump (before chemical deaeration).

3.2.2 Temperature and salinity dependency for Henry's constant

An initial clarification so that this section does not confuse the reader as it did the author while writing. Solubility is X_j in Eqn. (3.31) and (3.34), and its dependence to temperature and salinity is described by the Henry constants, $H_s(T, S)$ and $H_v(T, S)$.

Solubility of gases in liquids depends on the system temperature.. How this functional relation is depends on the considered system. Fig. 3.12 shows how Henry volatility constant with unit in bars is related to temperature for a variety of systems. Note that this is the volatility constant which is inversely related to the solubility. It is evident that oxygen solubility in water decreases from approximately 0 to 100 °C, and thereafter increases with temperatures above this range. Nitrogen in water shows similar but shifted relation, while other systems behave entirely different. Thus, there are no simple generalized relation to cover all different systems of gas-liquid equilibrium constants to temperature. [48]

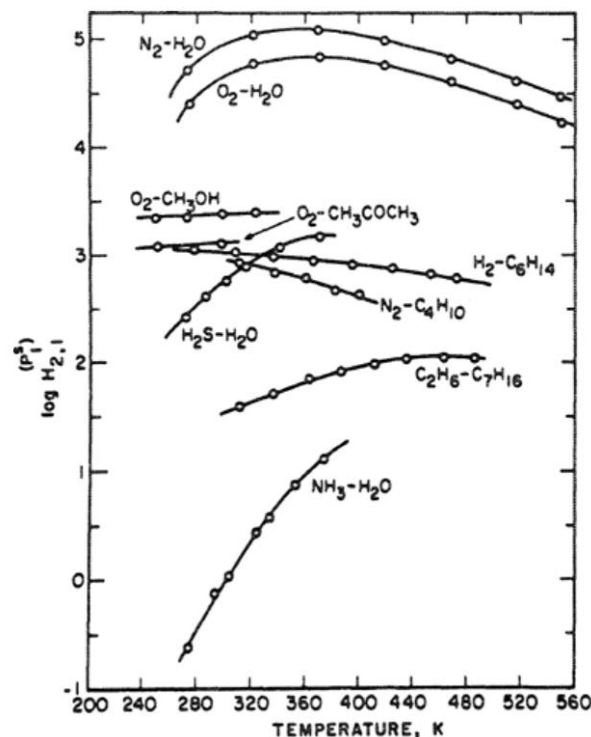


Figure 3.12: Henry volatility constants [bar] for several different binary gas-liquid systems. [48]

When it comes to how salinity affects solubility of gases in liquids several studies reports that the solubility of air gases, and thus oxygen, is lower in seawater compared to fresh water. This effect is called “salting-out” and is to some extent product of ions forming complexes with water molecules and affecting the water molecule structure. This leads to less available water molecules to dissolve gases. Thus, solubility of species typically decreases upon increased salinity in water. [46][48]. Ion-water complexes can be seen as ions surrounded by water molecules due to electrostatic charges. The degree of it and strength of bonding depends on the ion strength. Water molecules has partial charges, polarity, due to dipole moment as oxygens electron negativity is higher than that of hydrogens. Thus, they will interact with salts in the water. [41] Some species can be subjected to “salting in” effect with increased salt content, but this is not relevant to the system assessed in this project [48]. The “salting-out” effect in saline systems can be described by the Setchenov equation. This is not shown here but it is utilized in the equation applied to theoretically assess the deaerator performance. [46].

For the system at Ivar Aasen both temperature and salinity are of importance. The latter is not an explicit variable as it depends on the SRU performance, but its contribution to the Henry solubility constant is of importance when assessing the theoretical deaerator efficiency with respect to mechanical deaeration.

To account for both parameters a generalized Henry-Setchenov equation for air – water - seawater systems is utilized. Air is restricted to oxygen, nitrogen, and argon in this work. The general approach for the sets of models in this article is to combine of Henry’s constant and the Setchenov parameter to describe the temperature- and salinity dependence, respectively [50]. The authors have approached generalization between the different gas species by relating each model to the species acentric factor.

The acentric factor is a measure to account for how non-spherical molecules deviate from the Principle of Corresponding States. This is in turn is a state where all fluids consisting of spherical molecules deviate to the ideal-gas behavior to the same degree. Thus, the compressibility factor becomes approximately equal. This state is defined at equal reduced-temperatures and pressure between the species which is the actual temperature and pressure normalized to the species critical temperature and pressure [51][52]. The Principle of Corresponding States can be used to generalize equations of state, and the acentric factor can extend it to apply for other than spherical molecules. Critical temperatures and pressures are defined at the species critical point where there is no longer a distinct phase transition between the liquid and fluid region as shown beyond point C in the PT-diagram for an arbitrary pure substance in Fig. 3.13. [52] The acentric of a specie is related directly its vapor pressure which is what is utilized to generalize the temperature dependence part of the Henry-Setchenov equation.

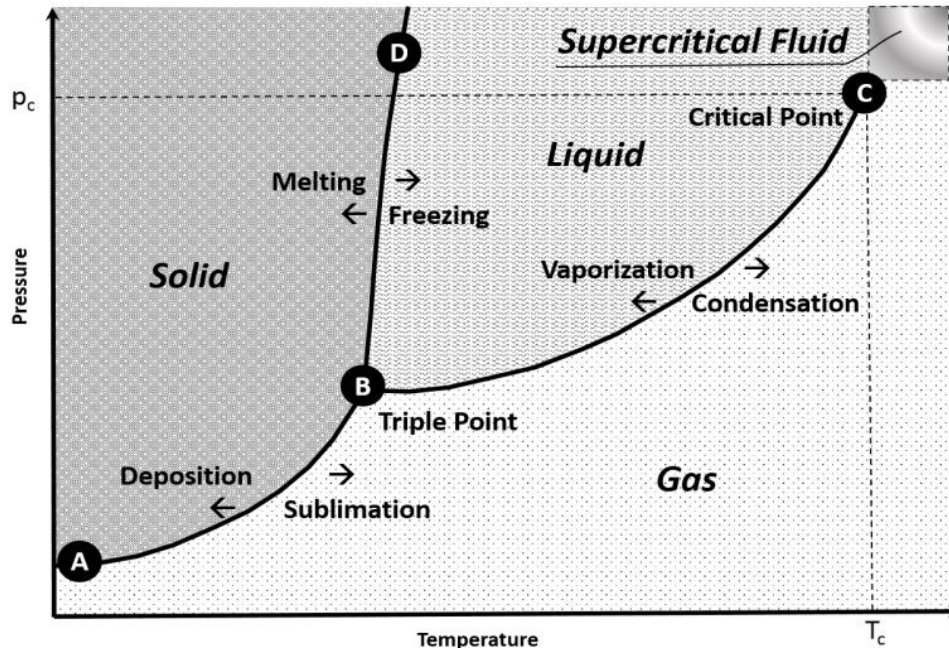


Figure 3.13: PT diagram for a pure substance. [53]

All presented models, including the one used in this project, are compared to experimental data so that both average- and absolute deviations to real data are presented. The Henry-Setchenov relation applied for the theoretical efficiency assessment is shown in Eqn. 3.35 and 3.36, with the parameters used listed in Tab. 3.3. All of which, besides the acentric factor, is retrieved from equation C, table 4 in [50].

$$\ln(H_{S_{j,i}}) = \ln(H_{S_{j,i}}^{\circ}) + \left[\frac{d_1 + d_2 T}{1 + d_3 T} \right] S \quad (3.35)$$

$$\ln(H_{S_{j,i}}^{\circ}) = \frac{(a_1 \omega + a_2) + (b_1 \omega + b_2) T}{1 + (c_1 \omega + c_2) T} \quad (3.36)$$

In these relations $H_{S_{j,i}}^{\circ}$ is the Henry solubility constant of oxygen in pure water, ω is the acentric factor, S is the salinity and T is temperature. All subletter characters ($a_1, a_2, b_1, b_2, \dots$) are parameters and their values are shown in Table 3.3.

These relations are utilized to estimate the Henry solubility constant for the theoretical performance assessment on the mechanical deaeration in Ch. 4.1.3, with an acentric factor of 0.022 for oxygen [52].

Table 3.3: Values for parameters in the Henry-Setchenov model in Eqn. (3.35) and (3.36). [50]

Parameter	Value	Parameter	Value
a_1	$3.12 \cdot 10^4$	c_2	-0.8770
a_2	$-1.409 \cdot 10^3$	d_1	0.3089
b_1	$-2.274 \cdot 10^2$	d_2	$-5.233 \cdot 10^{-4}$
b_2	10.49	d_3	$7.451 \cdot 10^{-2}$
c_1	-19.12		

4 Method

In this chapter the different plant tests and assessment/ derivation of the theoretical models are presented. The plant tests are intended to evaluate and optimize plant performance in addition to validating the derived theoretical models. The theoretical models are intended to evaluate system performance on a theoretical basis and to do a mathematical flow calculation of the separate SRU stages permeate flow to give control over the stage recoveries.

Initially in this chapter a theoretical summary on the parameter dependencies for the SRUs are given. This was a compromise due to not being able to derive a theoretical performance model for the SRUs. This summary is based on the literature review and is used as a theoretical basis for the plant tests presented later. The assessment and derivation of the other theoretical performance- and permeate flow model are given in the same sub-chapter

The method to evaluate the system performance and optimization potential was to relate the details of the SRDP at Ivar Aasen to relevant theory found in the literature review to establish theoretical models of performance. Knowledge gained from the theoretical study of nanofiltration and vacuum deaeration was used to construct ideas thought to be able to improve the SRDP performance, which led to the plant tests presented late in this chapter.

4.1 Models and SRU parameter dependencies

This sub-chapter contains a summary of SRU parameter dependencies and the assessment/ derivation of the theoretical models of permeate flow and theoretical mechanical deaeration performance. All of which is based on the theory presented in the previous chapters, except the permeate flow modelling in Ch. 4.1.2. This is an assessment of previous work done by Aker BP which in turn is modified with intent to improve the permeate flow calculation.

4.1.1 Parameter dependencies for the SRUs

The specific plant study and literature review showed that it was not possible to establish a detailed model to evaluate the SRU performance explicitly. The main reason was that too little information was available publicly on the membranes in use for sulfate removal at Ivar Aasen. For that reason the theoretical study regarding the SRUs and membrane separation is used to understand the directional dependencies between the process variables and system response. Table 4.1 summarizes the isolated membrane effects upon adjusting the available process variables or parameters in the SRUs at Ivar Aasen. This table is based on the theory assessed in Ch. 3.1 and can be used to predict effects of parameter changes which is utilized to design the different tests presented in Ch. 4.2. The absolute changes between the different effects are unknown, i.e. the relative changes between counteracting effects are also unknown. This goes for increasing the permeate production which states that the concentration polarization will both increase and decrease.

Table 4.1: SRUs at Ivar Aasen: Available process variables / parameters and expected effects upon **increasing** them.

Parameter	Main effect	System effects
Seawater temperature	Increased molecular distances in the dense membrane layer	<ul style="list-style-type: none"> - Increased overall permeability. <ul style="list-style-type: none"> o Higher sulfate content in permeate. o Reduced risk of scaling. o Decreased feed-to-permeate pressure drop. <ul style="list-style-type: none"> ▪ Less wear and tear on membranes.
	Increased diffusion	<ul style="list-style-type: none"> - Increased overall permeability... - Decreased CP (marginal effect)
	Decreased seawater viscosity	<ul style="list-style-type: none"> - Decreased feed-to-concentrate pressure drop. <ul style="list-style-type: none"> o Less wear and tear on membranes. - Increased feed bulk turbulence. <ul style="list-style-type: none"> o Decreased CP - <i>Unknown if viscous shearing changes.</i>
	Increased salt solubility ¹	<ul style="list-style-type: none"> - Reduced risk of scaling.
	Increased bio activity	<ul style="list-style-type: none"> - Increased membrane pressure difference build-up.
Recovery (shifting² or system recovery)	Increased salt concentration in concentrate	<ul style="list-style-type: none"> - Higher risk of scaling
	Reduced feed bulk turbulence	<ul style="list-style-type: none"> - Increased CP - Decreased viscous shearing against surfaces.
	Increased volume flux	<ul style="list-style-type: none"> - Increased CP - More wear and tear in radial direction (compaction and intrusion) - Less axial stress on spacer and membrane leaf, reducing chance of telescoping.
Production mode	Increased feed bulk turbulence.	<ul style="list-style-type: none"> - Decreased CP - Increased viscous shearing against surfaces.
	Increased flux and feed/concentrate flow	<ul style="list-style-type: none"> - Increase CP - More wear and tear
Back pressure³	Reduced water flux	<ul style="list-style-type: none"> - Reduced sulfate rejection.
	Balance cartridge loading	<ul style="list-style-type: none"> - Can help to load the initial- and end cartridges inside pressure vessels more evenly.
<p>Notes:</p> <ol style="list-style-type: none"> 1. Salt solubilities should be checked for salts considered close to the scaling point to ensure that the solubility in fact increases. 2. Shifting relates to altering the recoveries between the stages while keeping the total system recovery constant. The stage experiencing reduced recovery will experience opposite effects relative to what is listed in the table. 3. The system is operated with fixed recovery. Thus, an increased backpressure will ramp up feed pressure to compensate so that flux is constant. 		

4.1.2 The old permeate flow model

Back in 2018 Aker BP did a flow measurement test on SRU B with intent to verify a theoretical flow model for the 1st stage permeate stream. This flow model, if verified, would be used as a soft-tag flow measurement in the control system. This is very valuable as it gives better control over individual stage recoveries. They also sought to determine if the permeate flow from each stage was wrongly distributed, which they did. The target distribution was 66.7 % permeate from the 1st stage and 33.3 % from the 2nd, which is equivalent to 50 % recovery in each stage. It is important to notice that the pressure difference control across the 1st stage permeate pressure valve will shift the stage recovery towards the 2nd stage with increased 1st stage fouling. Thus, this 50 % stage recovery target should be a target for clean membranes if a constant permeate backpressure is still desired.

The test scheme used by Aker BP is illustrated in Fig. 4.1, where the necessary data was collected by manually altering the pressure valve (PV) while recording the 2nd stage permeate flow with a clamp-on flowmeter. The total permeate flow completes the permeate mass balance so that the permeate streams from both stages can be calculated.

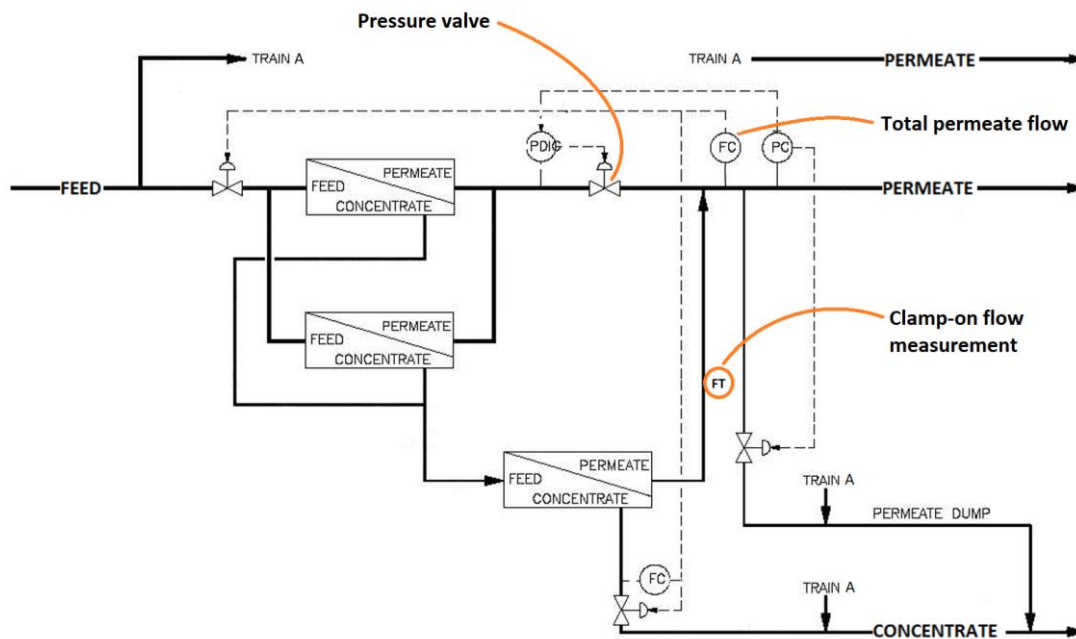


Figure 4.1: Mass flow test scheme to verify the theoretical flow model and to check the stage recoveries.

Soft-tag flow model

The theoretical model that Aker BP was to verify, referred to as the old model from now on, uses the basic valve equation on the 1st stage permeate PV with valve position and pressure drop across it as input variables. The mathematical form of the old model is shown in Eqn. 4.1. The calculation domain, or PV, is a globe valve and its inherent valve characteristics are linear. Inherent characteristics are the valve properties reported from the manufacturer that subjects the valve to constant pressure drop when establishing the relation between the valve coefficient and valve opening [54].

$$\dot{Q} = C_v f(u_{\%}) \sqrt{\frac{\Delta p_{meas}}{SG}} \quad (4.1)$$

In this equation \dot{Q} is the volumetric flowrate, C_v the valve coefficient, SG the specific gravity, Δp_{meas} is the measured valve pressure drop, $f(u_{\%})$ the valve opening function while $u_{\%}$ is the valve opening percentage. A linear relation is used for the valve opening function in the old model with a valve coefficient of 166.08. They used this valve coefficient due to it having almost a linear relationship to valve opening from the valve datasheet. This means that the flowrate is directly proportional to the valve opening if the pressure drop across the valve is constant.

The old model verification done by Aker BP is presented in Fig. 4.2. In this plot the measured and calculated flows are compared in addition is the PV movement during the measurement run presented. And as the diagram title indicates this test was done during 385 m³/h production in SRU B. The original template for data collection is presented in Appendix G where two of the collected datapoints are removed from use in this verification. This is done due to suspicion of erroneous logging which is reasoned and explained in the appendix.

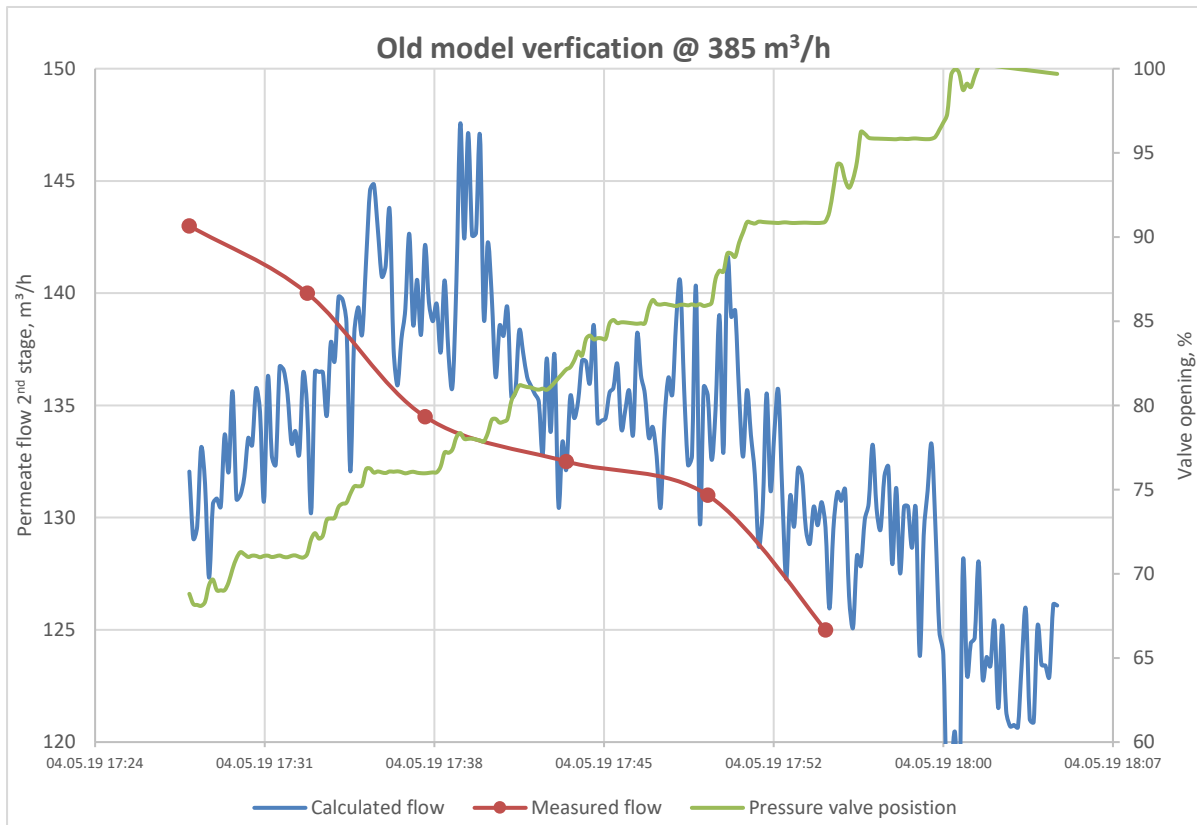


Figure 4.2: Verification of the old model on SRU B during 385 m³/h production mode by comparing model estimation against measured flow (red dots) of the 2nd stage permeate flow. The measured flow is done with a clamp-on flowmeter and flow changes induced by altering the PV opening.

This verification (Fig. 4.2) shows that the model did not predict the flow as intended. The reason for this is believed to be two-folded:

- A linear valve opening function is used. This will probably not be correct since the valve pressure drop is not constant, it behaves negatively exponentially to valve opening as shown in Figure 4.3.
- Assuming constant valve coefficient when operating at different valve pressure drop. The inherent valve characteristics of a valve relates the valve coefficient to the valve position at constant valve pressure drop. [54].

If the above-mentioned reason for model error is correct then the irregularity for the old model occurs due to a competing relation between pressure changes across the valve and the valve opening. Opening the PV reduces the pressure difference across it and these effects pull the flowrate in opposite directions. Thus, the error is believed to occur since these competing effects are scaled through the same constant valve coefficient making the valve equation not valid.

The next plot, Fig. 4.3, shows how the linear valve opening scheme during the verification test resulted in a negative exponential behavior for Δp .

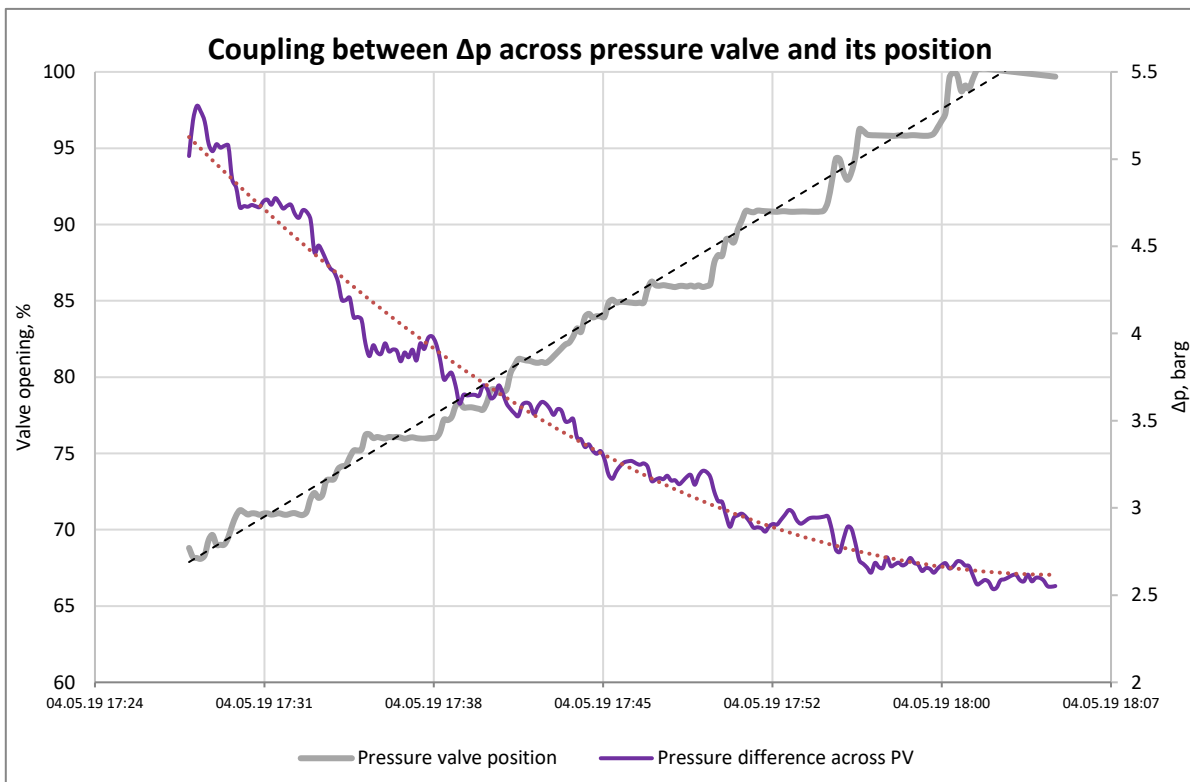


Figure 4.3: Pressure drop across the PV versus PV position during the test presented in Fig. 4.2.

An attempt was made in this project to improve this permeate flow model. This new model, explained in Ch. 5.1.1, is also based on the valve equation but it is fitted with a correction term based on the flow orifice equation [55]. This is thought to better handle flow changes to the changes in pressure drop across the valve. In addition, the valve opening function in the valve equation term of this new flow model is squared to model quick opening valve characteristics [56].

4.1.3 Theoretical mechanical deaeration performance

In this section a theoretical assessment and derivation of the mechanical deaeration performance for the vacuum deaerator is presented. Henry's law is the basis for this assessment where the system pressure as function of seawater flow and temperature is introduced from the plot in Fig. 2.23. A variant of Henry-Setchenov model is utilized to model Henry solubility constant as function of temperature and salinity. The performance curves established in this chapter assumes that all liquid subjected to the pressure present in the 2nd stage will reach equilibrium for oxygen between the phases. This assumption is based on that the deaerator system is operated according to design criterions.

The total pressure in the 2nd stage of the deaerator as function of temperature and seawater flow are presented in Fig. 4.4. These plots are established by digitizing Eta's pressure plots shown in Fig. 2.23. This is done by making .csv files (comma separated values) with a software called "graph grabber" to process in Excel. The turndown to flows below 720 m³/h are estimated by us of the pressure change to flow change ratio, $\frac{\Delta p}{\Delta Q} |_{833-720 \text{ m}^3/\text{h}}$, between the 840 and 720 m³/h curves established by Eta Process plant. It should be mentioned that this approach is very coarse as the difference in pressures between the modes calculated by Eta are very small.

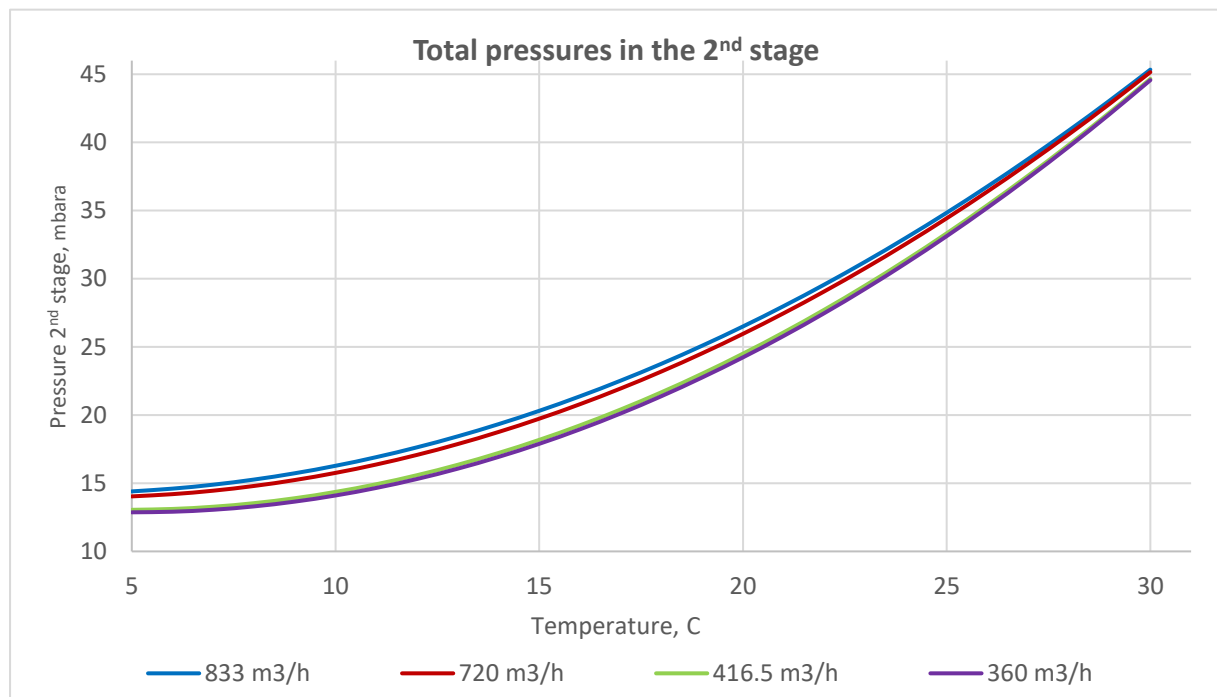


Figure 4.4: Total pressure in the 2nd stage as function of temperature at different flows of seawater to the deaerator. The curves for 365 and 416.5 m³/h are estimated with $\Delta p/\Delta Q$ ratio from pressure curve at 720 m³/h seawater loading of the deaerator. Based on Eta Process Plant pressure curves shown in Fig. 2.23.

It is necessary to convert total pressures- to partial pressures of oxygen in the 2nd stage. This is done with Eqn. (4.4) derived by use of the ideal gas law. For an ideal gas the partial pressure can be calculated with mol fractions multiplied with the total pressures as illustrated with Equations (4.2) to (4.4).

$$p_{O_2} = \frac{n_{O_2}RT}{V_{tot}} \quad (4.2)$$

$$p_{tot} = \frac{n_{tot}RT}{V_{tot}} \quad (4.3)$$

Dividing these yields:

$$\frac{p_{O_2}}{p_{tot}} = \frac{n_{O_2}}{n_{tot}} \quad \Leftrightarrow$$

$$p_{O_2} = \frac{n_{O_2}}{n_{tot}} p_{tot} \quad \Leftrightarrow$$

$$p_{O_2}(T, \dot{Q}) = \frac{n_{O_2}}{n_{tot}} * p_{tot}(T, \dot{Q}) \quad (4.4)$$

where $p_{tot}(T, \dot{Q})$ and $p_{O_2}(T, \dot{Q})$ is the 2nd stage total- and partial oxygen pressure as function of temperature and volumetric flowrate of seawater to the deaerator. The total pressure is introduced by coupling it to the functions graphed in Fig. 4.4. The total amount of moles and moles of oxygen in the gas phase, n_{tot} and n_{O_2} , is used to calculate the gas phase oxygen mole fraction which converts the total pressure to oxygen partial pressure

The mole fraction used in this assessment is based on the manufacturers estimated mass flows to the ejector when the deaerator is treating 840 m³/h of seawater shown in Tab. 4.2. The mole fraction is assumed constant across all production modes and temperatures. This assumption might induce some error if evaporation of water and release of dissolved gases does not change proportionally upon temperature and pressure changes. However, since Eta's mass balance is given across the temperature range of interest, (6.3 to 30 °C), a constant oxygen mole fraction is assumed.

Table 4.2: Mass flows to the ejector utilized to transform total pressure to partial pressure of oxygen in 2nd stage of the deaerator. The calculation is done at 840 m³/h production mode and stated to apply for the temperature range of 6.3 to 30 °C. Mass balance performed by Eta Process Plant and presented here with their consent.

Specie	O ₂	N ₂	CO ₂	H ₂ O _(vapor)
Mass flowrate [kg/h]	0.713	0.868	0.179	3

Henry's law on solubility form, Eqn. 4.5, is used to plot dissolved oxygen as function of temperature, flow, and salinity in the 2nd stage. The calculation is based on the 2nd stage as it has the lowest pressure which will represent the extent of the mechanical deaeration in the deaerator.

$$X_{O_2}(T, \dot{Q}, S) = H_{S,j,i}(T, S) * p_{O_2}(T, \dot{Q}) \quad (4.5)$$

$X_{O_2}(T, \dot{Q}, S)$ is the dissolved oxygen (or solubility of oxygen) as function of temperature, volumetric flowrate, and salinity. $H_{s_{j,i}}(T, S)$ is the Henry solubility constant modelled by Henry-Setchenov shown in Eqn. (3.35) and (3.36). Partial pressure changes for oxygen, $p_{O_2}(T, \dot{Q})$, is introduced by coupling Eqn. (4.4) into Eqn. (4.5). It is this coupling that introduces flowrate of seawater as a “variable” in the model.

The permeate salinity from the SRUs should increase with increased seawater temperature via how membrane permeability increases with temperature. To estimate this relation, salinity to temperature, it was necessary to use test data from the plant. Appendix H shows how this functional relation is derived based on measured conductivity data. It also views the error introduced by considering permeate salinity constant with temperature.

The performance curves in Fig. 4.5 shows a theoretical performance of the mechanical deaeration with seawater temperature and flowrate. It considers how salinity changes with temperature (Appendix H) but not how salinity increases with membrane degradation. Membranes will decrease its rejection of salts due to normal wear and tear during operation and modelling of it is too complex to consider. It should be noted that the salinity to temperature function is based on a very simple estimate and that it assumes a constant linear relation between temperature- and salinity changes. It also sets an upper temperature limit at 27 °C with respect to validity range for this theoretical performance model.

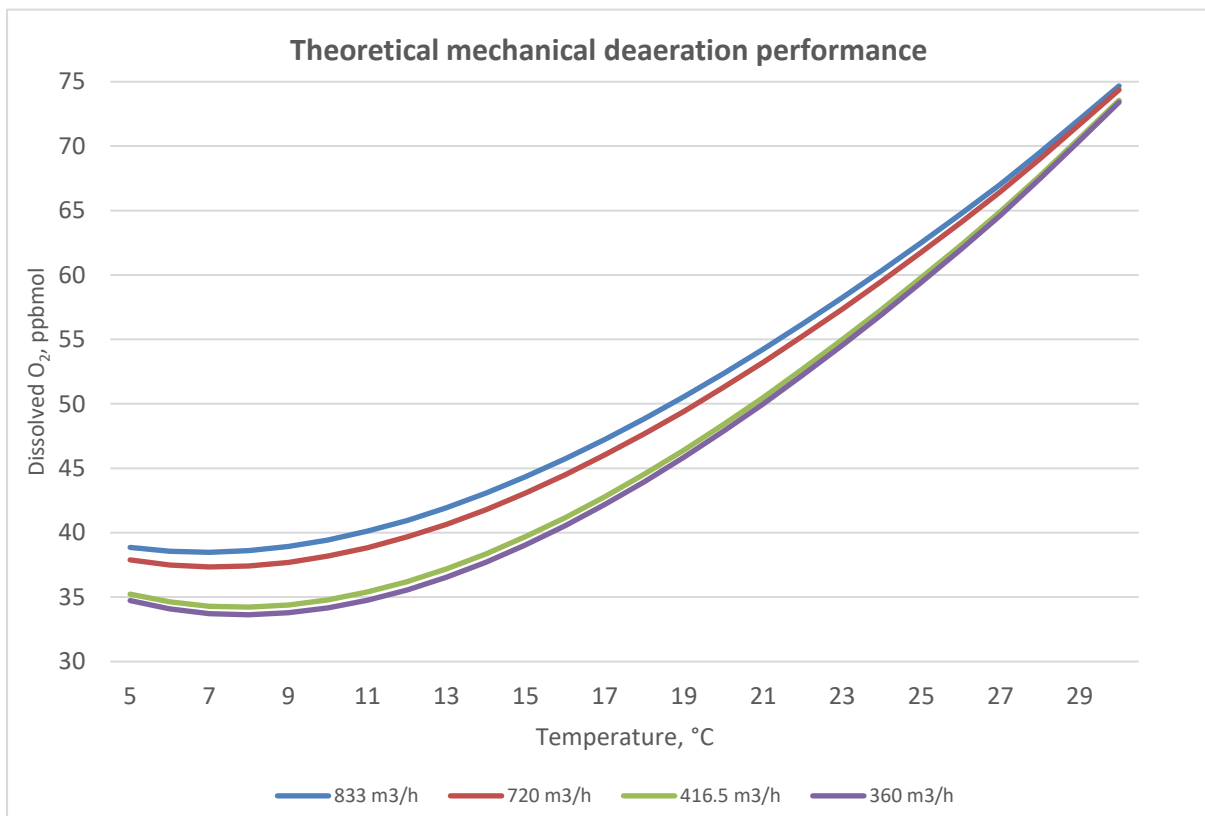


Figure 4.5: Theoretical dissolved oxygen content in seawater after mechanical deaeration in the vacuum tower at Ivar Aasen as function of seawater temperature and flow. The validity range is from 5 to 27°C.

4.2 Plant tests

In this sub-chapter the different tests are presented. Each test is described from a theoretical point-of-view where the predicted outcomes and system effects are elaborated. The test limitations, if any, are stated and described. These limitations can be based on both design- and optimization criteria and are intended as a framework for the operators upon implementation. A short description of the implementation is also presented for each test.

4.2.1 Test 1 - Increased feedwater temperature

Increase the feedwater temperature to the SRUs and deaerator to assess process behavior and to validate the theoretical performance of mechanical deaeration modelled in Fig. 4.5.

Theoretical basis, arguments, and predicted outcomes:

Increasing the seawater temperature should reduce the overall pressure drop in the system due to increased permeabilities for salts and water in addition to decreased water viscosity. This will in turn induce higher sulfate content in the permeate, less wear and tear on the membranes, and lower power consumption for the SRU pumps. Diffusion in water will also increase with higher temperatures which will help mitigate concentration polarization via more rapid back-diffusion from the laminar boundary layers to the feed bulk. The system will also most likely be less prone to scaling as salt solubilities increase with temperature.

The degree of fouling might increase for two reasons, increased bio growth and higher SDI in the feedwater to the SRUs. The first is based on that the rate of growth can be facilitated by higher temperatures. Whether or not this is counteracted by the decrease in concentration polarization is unknown. The increased SDI can occur if the ultrafiltration permits more silt to pass when subjected to higher temperatures.

For the deaerator increased temperature should according to the manufacturer be favorable as seen in Fig. 2.22. According to the derived performance model shown in Fig. 4.5 increased temperature can reduce the mechanical deaeration performance. Either way, due to that the ejector seems to underperform and the reports on less problems with it during summertime compared to wintertime the increased liquid temperature might compensate for the potential loss in performance. Regarding validation of the theoretical performance model it will be hard to distinguish the mechanical- from the chemical deaeration contribution upon temperature changes. That since the chemical deaeration reaction rate and its temperature dependence is unknown. Running without any chemical deaeration is not an option due to causing damage to the downstream systems, process equipment and reservoir.

Limitations:

- The temperature should not exceed 40 °C as it is closing in on the temperatures where the membranes will suffer permanent damage. This is prevented with 29TST3102 that trips the SRUs at temperatures ≥ 34 °C.
- Keep within the target of 30 mg/L of sulfate in the permeate.
- Keep the dissolved oxygen within target of 200 ppb mol oxygen.

- Monitor the differential pressures development. If a significant change in the slopes (positive slopes) after the adjustment is done, consider ending the test. This might be induced by a significant increase in fouling through bio growth or higher SDI in the seawater after ultrafiltration.

Implementation:

- Route as much of the seawater as possible from the gas compression coolers 27HA0001/2 (Fig. 2.1) to the ultrafiltration package. This is done by initially opening 50BU1018 to a 100 % and thereafter closing 50BU1019 to 0 %.
- Alternate the seawater temperature during stable periods with constant permeate production and seawater flow through the deaerator to induce system dynamics solely caused by temperature changes. Keep the oxygen scavenger dosage rate constant until the system reaches steady state after the temperature change as long as the dissolved oxygen content is within the target.

4.2.2 Test 2 - Validate permeate flow model

Measure the permeate flow from one of the stages, preferentially in SRU A at different permeate flows and seawater temperatures to validate the new permeate flow model. The model in question is presented as Eqn. (5.1) in Ch. 5.1.1 and is referred to as the new model or the new flow model in this report.

Theoretical basis, arguments, and predicted outcomes:

The new flow model should be tested on SRU A as it is derived based on measurements and data on SRU B.

The main intention with this test is to see if the new model can correctly predict stage permeate flows at different degrees of membrane fouling. To check this the test should be done at two different permeate production flows and with two different seawater temperatures for one or both these levels of permeate production. Changing the temperature alters the membrane pressure drops due to changes in viscosity and membrane permeability. This simulates the changes induced by differences in membrane fouling. The 2nd order polynomial regression curve of PV position to measured flow (with clamp-on flowmeter) should remain unchanged when measuring the constant permeate production at two different temperatures. If it changes the model is not valid for use and in need of adjustments, likely by introducing the membrane feed-to-concentrate pressure difference as a variable.

This fouling-test can alternatively be tested by doing a new clamp-on measurement at 385 or 417 m³/h permeate production like Aker BP did in 2019 and see if the new model needs flow correction. If flow correction is needed this is a sign on that the new model fails to predict flows at different degrees of fouling. Unless the singularity of identical degree of fouling between the 2019 tests and these new tests occurs, which is highly unlikely. This can be checked by comparing the membrane pressure differences between the tests. However, this approach is likely not as good as the temperature alteration at constant permeate production for two reasons. Firstly, it fixes the test to one of two flows which can cause operational efficiency problems if another volume of permeate is needed for reservoir pressure recovery. Secondly, the test done by Aker BP in Fig. 4.2 and 5.2 consists of very few measured datapoints, six and nine to be precise. The reason for this is that they used a simpler clamp-on flowmeter with no recording possibility. The clamp-on flowmeter used in this test will record data each 10th second. Thus, a flow correction might be necessary due to the very large difference in resolution between the measured values between this test and the basis used to curve fit the new flow model.

The permeate production should in one of the tests be at another level than the tests done by Aker BP. This to see if the model can be corrected the same way that is done with the 417-mode version of the new model later in Ch. 5.1.1.

Limitations:

- Consider plant behavior when adjusting the PV towards its minimum opening limiter. The test shall not damage or trip the producing plant. It is not necessary to close this valve to its minimum value of 57 % if it involves a risk of tripping the SRU or any other coupled systems.

- If something happens in the control room that needs attention consider stopping the test scheme and resume to automatic pressure difference control. The PV should not be left at its extremes for any longer than the test scheme states.

Implementation:

The procedure to collect data for this test is to record the measured permeate flow on the 2nd stage permeate stream on a SRU while manually stepping the 1st stage permeate PV 5 %-points each 15 minutes. The sequence starts from the valve opening present when the controller is switched to manual mode. The valve opening is stepped up to 100 %, and thereafter down to the minimum valve opening before stepping it back to the initial valve position. This sequence should be done at two different permeate production levels and two different seawater temperatures at constant permeate production. The test procedure shown in Appendix I was handed to the control room technicians prior to test initiation.

4.2.3 Test 3 – Recovery and backpressure adjustments

Increase the 1st stage recovery by reducing permeate backpressure and evaluate the SRU behavior.

Theoretical basis and arguments:

Based on the flow measurement done in 2019 discussed in Ch. 4.1.2 the SRUs at Ivar Aasen likely operates with higher recovery in the 2nd stages compared to that in the 1st stages. This hypothesis is based on that the pressure difference controller across the 1st stage permeate PV operates with a Δp setpoint of 6 barg today relative to Fig. 5.4 and 5.5 presented later in the results given in Ch.5.1.1.

The recoveries between the stages will gradually be affected by the degree of membrane fouling as it affects the pressure drop from feed/concentrate to permeate. This means that a static Δp across this PV will not keep the stage recoveries constant. For instance, increased 1st stage fouling will increase the feed-to-permeate pressure drop in this stage which makes the PV to choke back to keep its setpoint on pressure difference. This in turn means that the recovery loading will gradually shift towards the 2nd stage. This means that this test will not be able to regulate the recovery to 50 % in each stage, neither is this the intent of the test. It will assess the system behavior to recovery and backpressure changes. And it is chosen to increase the recovery in the 1st stage to do so based on that the 1st stage recovery could be too low. Due to the uncertainty to the actual recoveries the test will be kept relative short to reduce the time of operation if the recovery exceeds a level where fouling problems can be increased significantly through inducing too high concentration polarization.

Considering that the 2nd stages operate at significantly higher salt concentrations, and that the 1st stage has double the amount of membrane elements it should be a good idea to balance this towards a 50 % recovery in each stage for clean membranes. This will as stated above shift upon fouling build-up with time until the next CIP wash is needed. This strategy was also recommended by NOV in a conversation with one of their membrane experts. Another indication on that the recovery should be increased in the 1st stage is that Avista found telescoping on the feed spacer on a lead element in this stage. This type of damage is prone to happen if too much axial stress in the membrane feed/concentrate channel. Thus, increasing recovery increases permeation flux which reduces the feed-to-concentrate pressure drop.

Predicted effects:

- Increased concentration polarization in the 1st stage.
- Decreased concentration polarization in the 2nd stage.
 - o The sum of these is of interest in light of optimization.
- Reduced risk of scaling in the 2nd stage
- More uneven cartridge loading in the 1st stage due to steeper pressure gradient in the permeate tube/core.
- Increased sulfate rejection in the 1st stage due to increased water volume flux.
- Decreased sulfate rejection in the 1st stage due to decreased feed flow while constant concentrate flow due to fixed total recovery.

Limitations:

- Monitor the differential pressures development. If the slopes steepen (positive slope) after the adjustment is done consider ending the test as it can indicate scaling. This should not happen since increasing the 1st stage recover will reduce that of the 2nd stage. This should move the system further away from its scaling point in the 2nd stage that has the highest salt concentrations.
- Short test duration as there is no trustworthy control over the actual stage recoveries. It will be estimated with the new flow model introduced later in Eqn. (5.1), but this model is not validated.
- The 1st stage concentrate flow should be higher than 163.2 m³/h to maintain concentration polarization modulus beneath 1.2 (see Tab. 2.2). This flow is not measured so it is hard to know if this is maintained or not. However, when producing 360 m³/h permeate with a 50 % recovery in the 1st stage the concentrate flow from this stage should be 240 m³/h. Thus, this should not be an issue but to be on the safe side the new model introduced in Eqn. (5.1) will be applied to estimate this flow. The test will be terminated if it predicts to low concentrate flow.
- If the PV reaches saturation (100 % valve opening) reduce the setpoint until it regulates.

Implementation:

Chose the SRU that will be left running the longest if the need for seawater drops. Gradually step down the Δp setpoint in the pressure difference controller for the 1st stage permeate to one of the following setpoints:

- 3.3 barg if ~360 m³/h permeate production
- 4 barg if ~417 m³/h permeate production.

These setpoints are based on what was measured during the clamp-on test in 2019 and are only a base for the test. The Δp setpoint yielding 50% recovery in the 1st stage will depend on the degree of membrane fouling. A time after test initiation the recovery will be estimated with the new flow model shown later in Eqn. (5.1) and Tab. 5.1. Based on this calculation the Δp setpoint will be adjusted to move closer to the targeted recovery spilt between the stages.

5 Results and discussion

This chapter consist of the results and discussion of the plant tests performed in addition to the theoretical approaches on mechanical deaeration performance and flow modeling of the permeate streams in the SRUs evaluated in Ch. 4.1.2 and 4.1.3. The initial sub-chapter evaluates the models for mechanical deaeration and permeate flow on a theoretical basis while the second sub-chapter assesses the practical plant tests.

The different discussions in this chapter focuses on system optimization and comparing process behavior to theoretically predicted outcomes. For all presented laboratory measured data the tag of the sample points is given for reproducibility reasons. These tags are not presented in the flow diagrams given in this report and is for that reason only of value to Aker BP readers.

It should be mentioned that Ivar Aasen is an operational plant where production- and parameter changes, out of the control of this projects, happens from time to time. Thus, the tests are not as controlled as they would have been in a lab scale test. For that reason, the results must be considered with care as there are a lot of variables to assess.

A large upset occurred for Ivar Aasen during this project which affected the time and resources available for plant testing. Loss of main power to Ivar Aasen tripped the 21st of March due to turbine issues on Edvard Grieg. This power loss resulted in a total stop of main production (oil and gas) at Ivar Aasen which in turn resulted in an abrupt stop in Test 1, evaluated in Ch. 5.2.1. The SRDP was restarted and kept in operation for most of the time, during the main power loss, with the essential power generators. But the possibility of heating the seawater with the gas compression coolers was not in place until after the project period. In addition, due to this power failure, Aker BP decided to start their turnaround (maintenance work) sooner than planned. This occupied all their offshore resources during the period planned for practical tests. The 22nd of April the oil production resumed but the gas export was still restricted due to the issues on Edvard Grieg. The gas export is estimated to be reassumed the 23rd of May which is after the submission deadline of this thesis. Due to this upset the practical part of this project was stressed and in need of additional testing after the project period.

5.1 Theoretical assessments

This chapter assesses the models presented in Ch. 4.1.2 and 4.1.3. Initially the results from assessing the work done by Aker BP regarding the permeate flow model is presented through a new and seemingly improved flow model. And secondly is the theoretical mechanical performance model compared to the mechanical deaeration model given by the manufacturer of the deaerator system.

5.1.1 The new permeate flow model and stage recoveries in the SRUs

This sub-chapter presents new permeate flow model and estimations of stage recoveries both of which are based on the assessment done in Ch. 4.1.2.

The new flow model

The altered flow model, referred to as the new model from now on, is shown in Eqn. 5.1. It consists of two terms so that the volumetric flowrate can be scaled separately to the valve opening and pressure difference. The initial term is the valve equation, while the second term is based on the orifice flow equation [55]. The initial term only depends on valve opening, while the second on valve opening in addition to the pressure difference across the PV.

$$\dot{Q} = C_v \sqrt{\frac{u_{\%}}{100\%}} * \sqrt{\frac{\Delta p_{max}}{SG}} - C_f \frac{u_{\%}}{100\%} * \sqrt{\frac{\Delta p_{max} - \Delta p_{meas}}{SG}} + C_c \quad (5.1)$$

In this equation C_v and C_f are the valve- and orifice coefficients, $u_{\%}$ is the valve opening percentage, SG is the specific gravity of the permeate passing the valve, and C_c is a model constant. The differential pressures, Δp_{max} and Δp_{meas} , are a constant and a measured variable respectively. This formula is constructed by a combination of trial-and-error and physical interpretations of the author. This model is to the authors knowledge not to be found in literature as presented in Eqn. (5.1).

This new model utilizes the valve equation to model flow through the valve at a constant reference pressure difference. This reference was set to be equal to the shut-off pressure defined in the datasheet of the valve. This will overestimate flow through the valve for all valve pressure differences lower than the reference point, Δp_{max} . For that reason, a correction term is introduced with basis from the orifice flow equation. It is fitted with a reversed term for the pressures in its roots so that its contribution increases with decreasing pressure drop across the valve. To make the correction correct the valve opening is factored in to depict what the “orifice opening” is at the time of correction. The model shows that when correction term becomes zero when $\Delta p_{meas} = \Delta p_{max}$. This means that depends solely on the valve equation when the valve pressure drop is constant and equal to the reference point.

The initial root in the first term of Eqn. (5.1) is the valve opening function typically used for quick opening type valves. The valve assessed is a linearly opening globe valve, but the installed characteristic of linear opening valve resembles that of the quick opening valve. The reason is the changes in Δp across the valve, and how it changes more upon the initial valve opening as illustrated in Fig. 4.3. [56]

A simple verification of the new model is shown in Fig. 5.1. This is the exact same dataset as used for Aker BP’s model evaluated in Ch. 4.1.2, and it predicts the 2nd stage permeate flow relatively well.

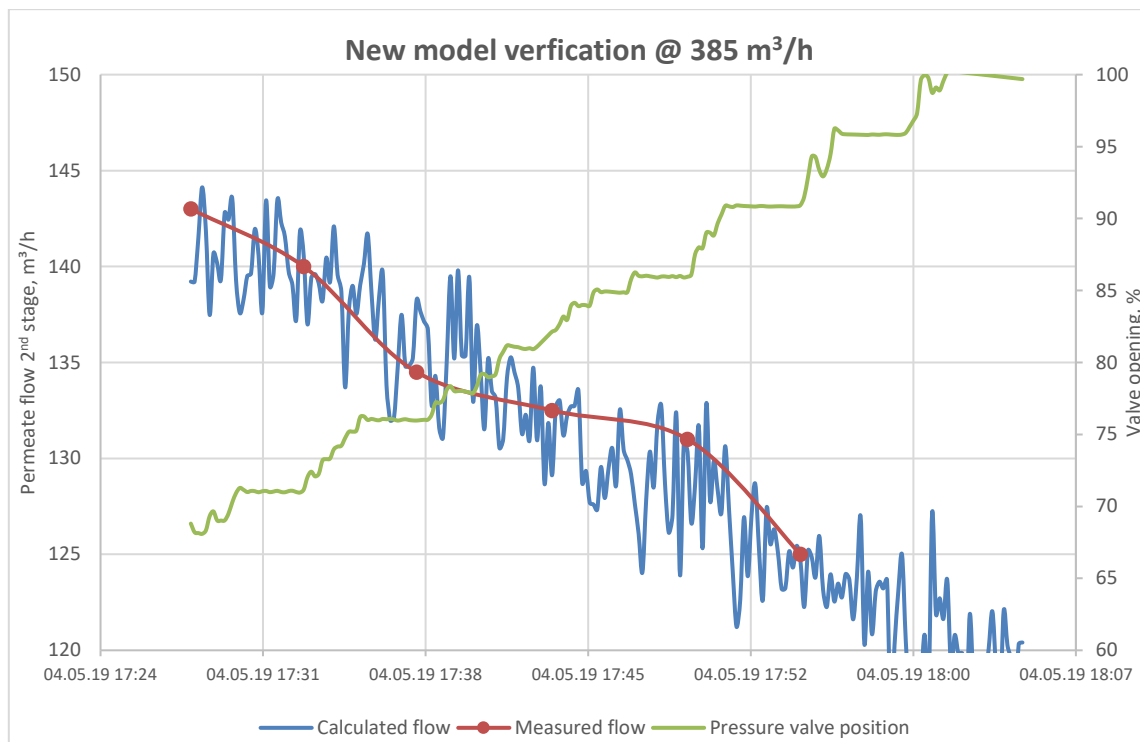


Figure 5.1: Verification of the new model on SRU B during 385 m³/h production mode by comparing model estimation against measured flow (red dots) of the 2nd stage permeate flow. The measured flow is done with a clamp-on flowmeter and flow changes induced by altering the PV opening.

There was another mass flow test done during 417 m³/h permeate production mode in SRU B. This test was somewhat more structured relative to PV alterations. The PV steps was equal in size with more consistent time difference between them. There was also devoted much more time between each PV alteration so that the system had more time to reach a steady state after each change. The original test record for this test has not been found, and the data shown here were found plotted in the Excel spreadsheet Aker BP used for their model verification. Figure 5.2 and 5.3 shows model verifications of the old Aker BP model and the new model, respectively. Again, the old model performs poorly while the new model predicts the flows relatively well.

It should be mentioned that the new model, Eqn. 5.1, needs a correction term to predict “accurate” at different flow modes. For that reason, a “flow correction ratio” term was introduced to better correlated the flow estimations. This was defined by taking the ratio of the 2nd order polynomial regression lines of the measured flow from each test as function of the PV position. The measured flow is converted to 1st stage permeate flow in the regression analysis. The need of such a flow correction means that new measurements and regression analysis must be done for the model to handle permeate production levels other than 385 and 417 m³/h. Also, temperature affects the SRU pressure drops which might introduce a model error in need of correction. The same goes for degree of membrane fouling in the 1st stage. The ability of the new flow models to deal with this (fouling and temperature changes) must be tested in order to validate it.

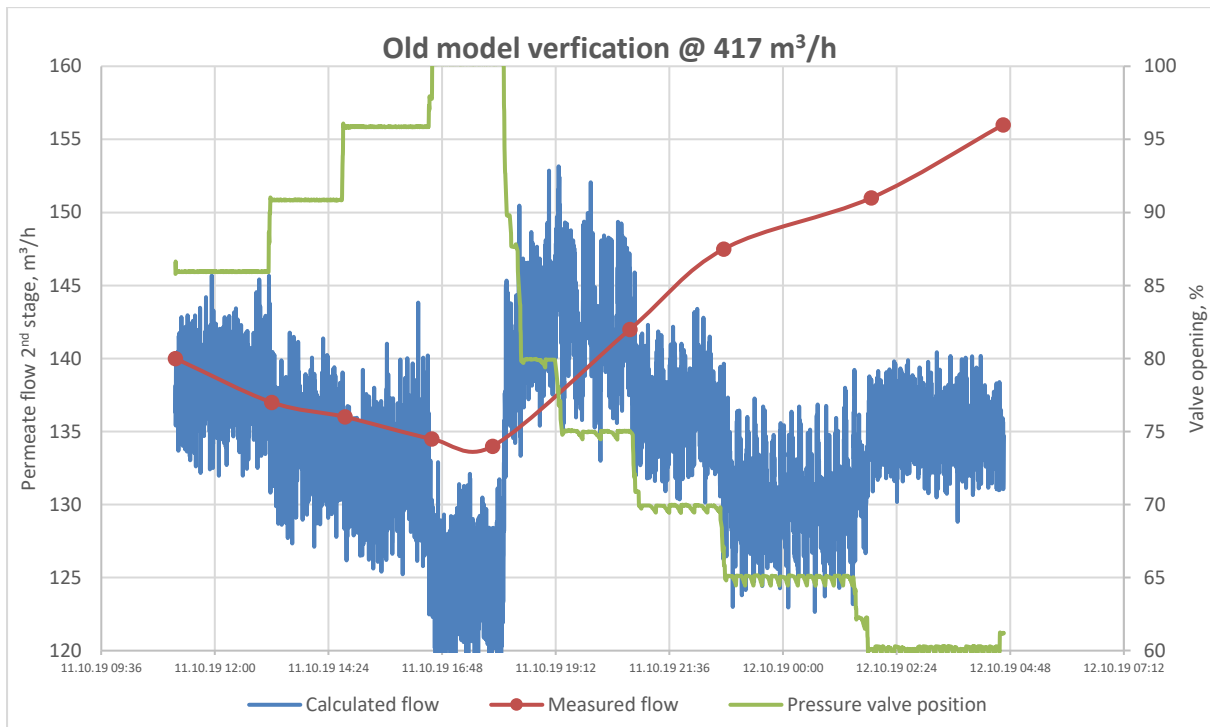


Figure 5.2: Verification of the old model on SRU B during 417 m³/h production mode by comparing model estimation against measured flow (red dots) of the 2nd stage permeate flow. The measured flow is done with a clamp-on flowmeter and flow changes induced by altering the PV opening.

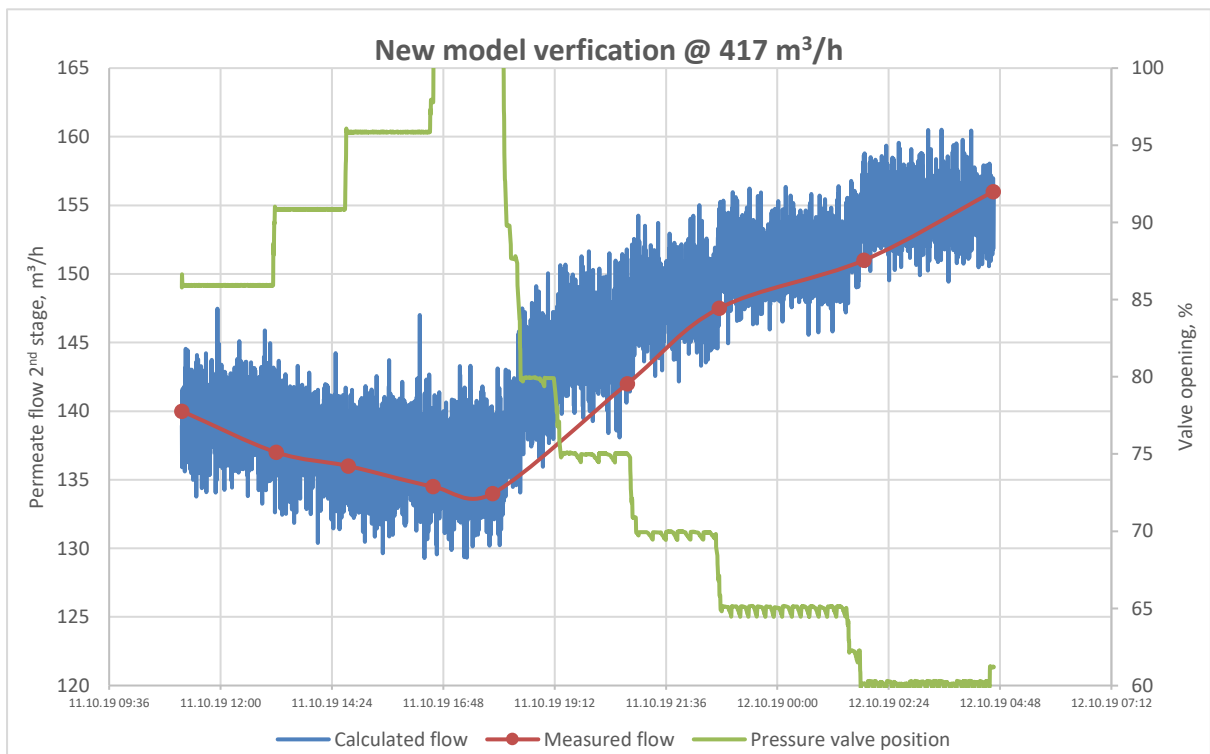


Figure 5.3: Verification of the new model on SRU B during 417 m³/h production mode by comparing model estimation against measured flow (red dots) of the 2nd stage permeate flow. The measured flow is done with a clamp-on flowmeter and flow changes induced by altering the PV opening.

The numerical values of the new model coefficients and the flow correction ratio that corrects the model from 385 to 417 m³/h permeate production are presented in table 5.1.

Table 5.1: Equation coefficients and flow correction ratio used in the new model given in Eqn. (5.1)

Parameter	New model
C_v	69.2
C_f	11.6
C_c	91
Δp_{max}^1	9 barg
Flow correction ratio ²	$\frac{-0.0133u_{\%}^2 + 2.6815u_{\%} + 147.89}{-0.0007u_{\%}^2 + 0.7907u_{\%} + 193.72}$
<p><u>Note:</u></p> <ol style="list-style-type: none"> 1. The design shut-in pressure from the datasheet of the valve. 2. This is the measured flow as function of PV position ratio between 365 and 417 m³/h mode. This ratio is factored to the entire expression (new model, Eqn. 5.1) when the production mode is 417 m³/h. 	

Due to SRU A and B being identical systems the new model should be able to predict permeate flows equally well for both SRU's. This depends on its ability to handle changes to the membrane fouling. It should be mentioned that these parameters probably could be better fitted as only a certain amount of time was devoted to working with this mass balance model in this thesis.

Model error is not calculated due to not knowing the exact timestamps for each clamp-on measurement. The measured data are given with minute accuracy as shown in Appendix G.

Permeate split – stage recoveries

Figure 5.4 and 5.5 visualizes how the 1st stage recovery in SRU B balances with Δp across the PV for each of clamp-on flow measurement runs discussed above. Due to that SRU A and B are identical in geometry, dimensions, and equipment type this should be equally relevant for SRU A.

These plots indicates that the Δp across the PV should have been ~ 3.3 and 4 barg to achieve 50 % recovery in both SRU stages for 385 and 417 m³/h production mode, respectively. A 50 % recovery in the initial stage gives 50 % recovery in the second, which gives a split ratio of 0.667 for the 1st stage. This statement somewhat inaccurate as the stage recoveries is not constant with time. They will shift between the stages with membrane increased membrane fouling. However, these plots are assumed as a coarse reference to achieve 50 % stage recoveries.

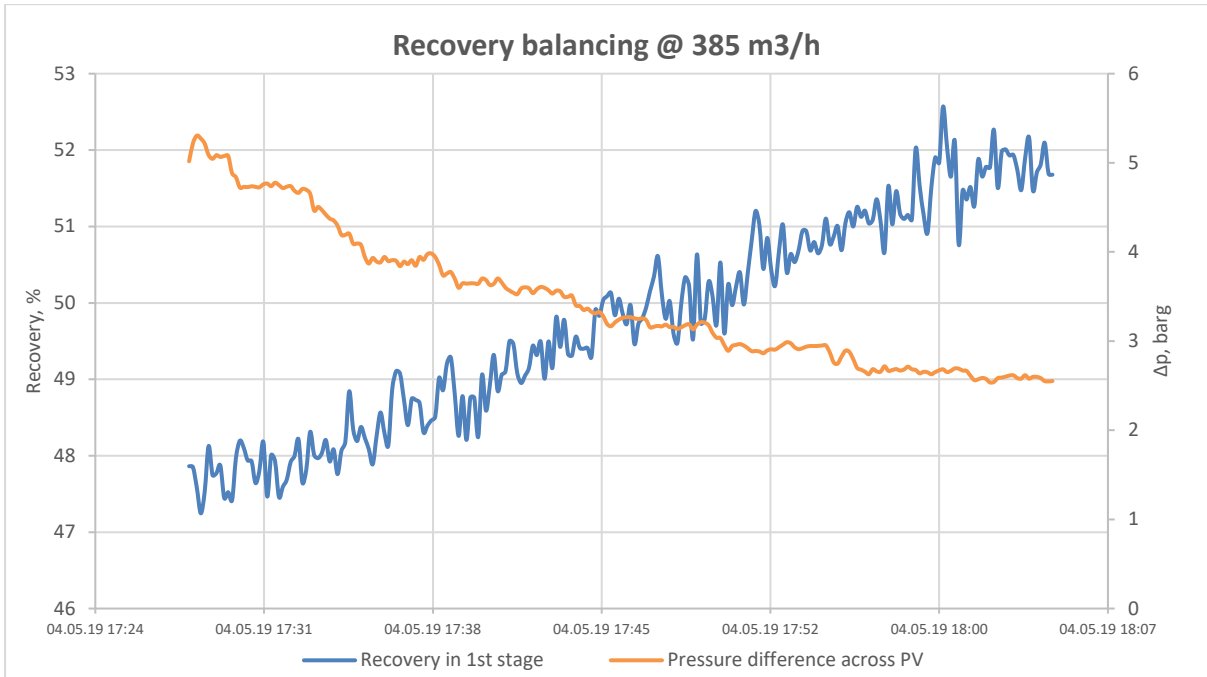


Figure 5.4: Recovery balancing with Δp across the PV on the 1st stage permeate outlet for SRU B during 385 m³/h production mode.

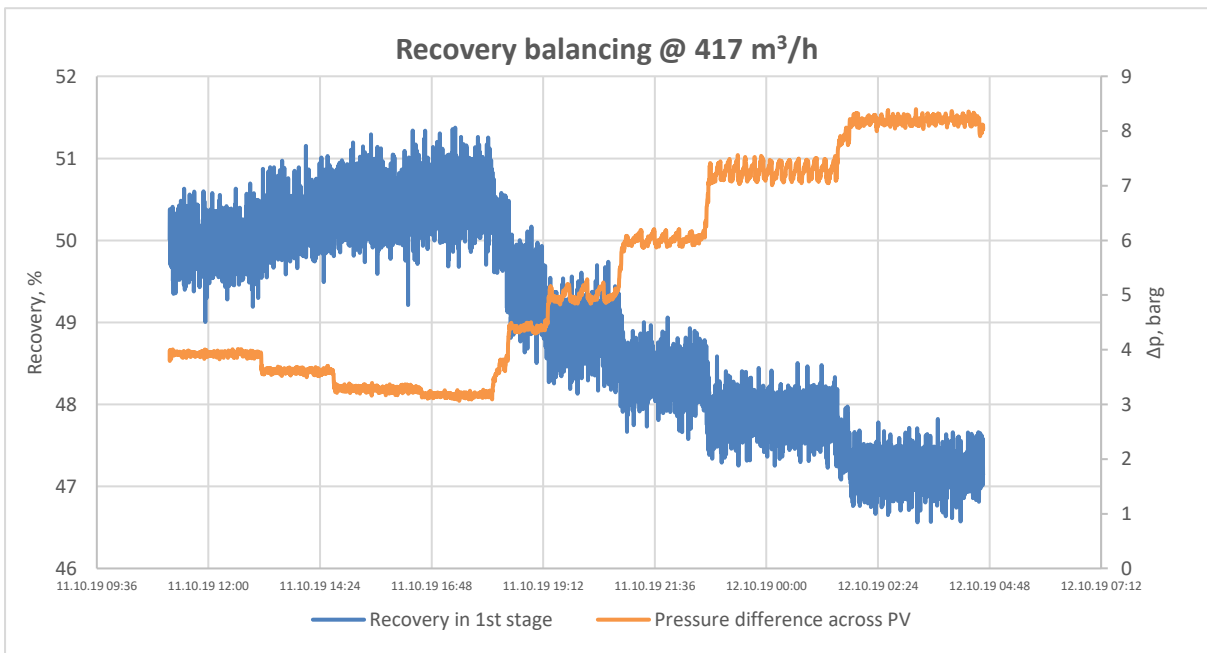


Figure 5.5: Recovery balancing with Δp across the PV on the 1st stage permeate outlet for SRU B during 417 m³/h production mode.

It should be emphasized that most of the work presented in this sub-chapter was already done by Aker BP. This projects part in it has been to assess the data and to (seemingly) improve the flow model in addition to presenting a visual reference relation between stage recoveries and pressure differences across the PV on the 1st stage outlets.

5.1.2 Theoretical mechanical deaeration performance versus the Eta Process Plant performance model

This sub-chapter assesses the theoretical performance model established in Ch. 4.1.3 against the performance plot generated by the manufacturer, Eta Process Plant. The theoretical model is also compared to the deaerator behavior during plant tests with increased seawater temperature later in this chapter.

The performance curves shown in Fig. 4.5 indicates that the increase in pressure in the 2nd stage overcomes how increased temperature reduces the solubility of oxygen in seawater when the seawater exceeds ~ 8 °C. This probably happens as the release of dissolved gases and water vapor increases with temperature. This increased amount of gas must be conveyed by the vacuum pump running at fixed speed. Thus, more gas therefore means higher pressure. It also indicates that increasing the seawater temperature above 18 to 21 °C, depending on production mode, will deteriorate the mechanical deaeration to a level of dissolved oxygen above the performance guarantee of 50 ppb mol.

It is evident that the theoretical performance curves in Fig. 4.5 do not resemble the performance estimated by Eta Process Plant given in Fig. 2.22. The plot in Figure 5.6 compares these performance curves at 840 m³/h seawater production. The theoretical performance curve is recalculated from 833 to 840 m³/h to correlate the seawater production in the comparison. Again, little similarity between the curves in addition to that the 50 ppb mol design guarantee differs with 2 °C. The comparison shows that the performance curve derived in this thesis is the least dependent on the seawater temperature of the two. The theoretical model seems to be a non-linear scaled inversion of the Eta curve.

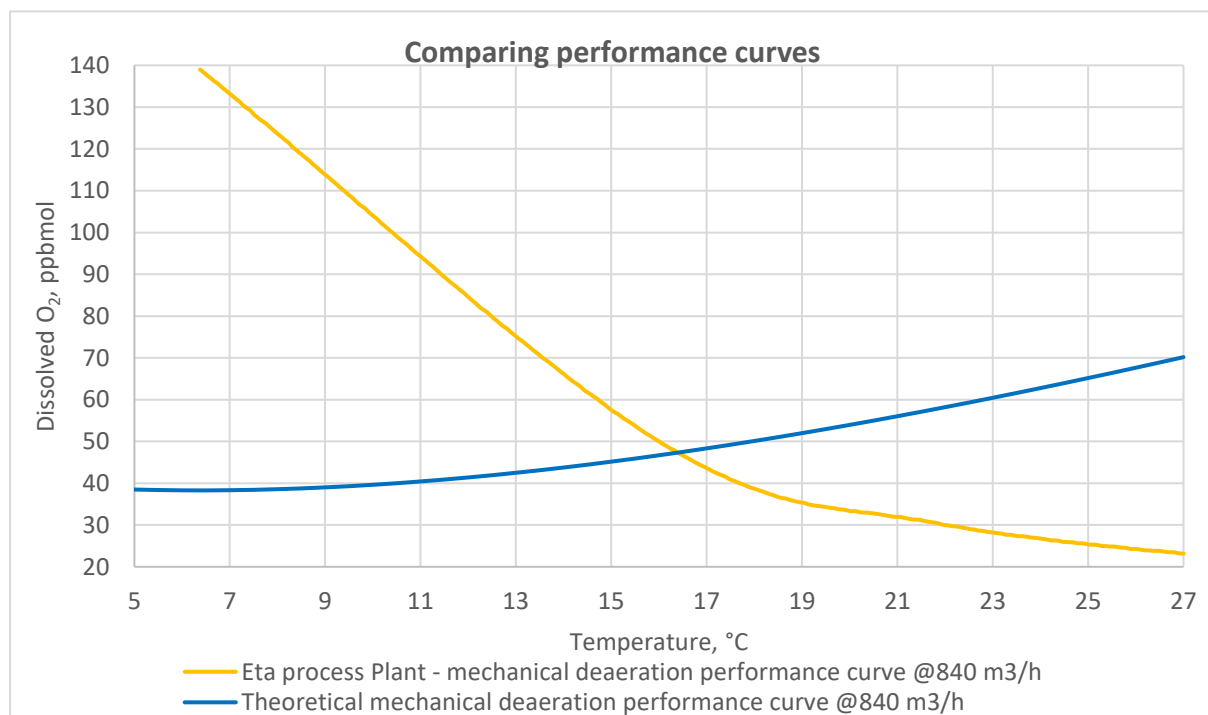


Figure 5.6: Comparison of the derived theoretical- and the manufacturers (Eta Process Plant) mechanical performance curves as function of seawater temperature. Both curves are based on a seawater production of 840 m³/h.

The reason for the difference in functional dependence to seawater temperature between the derived model and that from Eta Process Plant is probably caused due to one or more of the following explanations.

- An error in the established theoretical model derived in Ch. 4.1.3 not identified by the author.
- The mol fraction of oxygen in the gas phase is not constant with increasing temperature as assumed. If the release of water vapor, dissolved- nitrogen and carbon dioxide increases more than that of dissolved oxygen its mol fraction in gas phase will be inversely dependent on temperature.
- Eta's performance curve neglects how the deaerator stage pressures changes with temperature. An indication of this is that Eta's performance curve can be approached by assuming a constant pressure in the deaerator while increasing the temperature. This is done in Fig. 5.7 where pressures are averaged across the temperature interval assessed. These curves do not match the absolute values relative to Eta's performance curve, but the functional dependence to temperature is more similar.

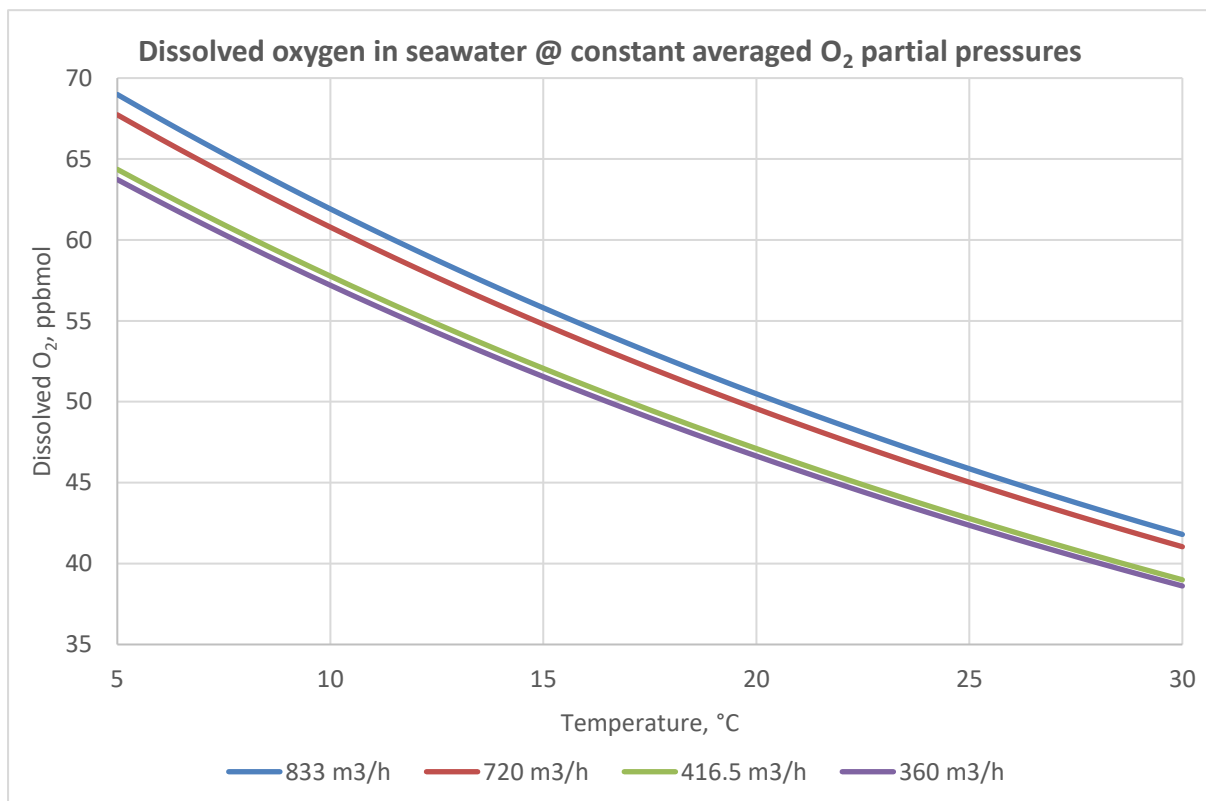


Figure 5.7: . Theoretical dissolved oxygen content in seawater after mechanical deaeration as function of seawater flow and temperature when partial pressure of oxygen is constant at its average pressure via Fig. 4.4 converted to partial pressure of oxygen.

5.2 Plant tests

This chapter evaluates the different plant test that was performed during the project period.

5.2.1 Test 1 – Increasing feedwater temperature

The ideal performance indicator to evaluate in this test, with respect to SRU optimization, would have been the CIP frequency and how it changes with increased temperature. However, the CIP frequency is too long relative to the project period to be able to assess it. Only 3 CIP washes have been done during the project. In addition, since the temperature depends on the gas export rate, when operating at increased temperatures, the feed-to-concentrate pressure difference fluctuates with the gas export. This makes it difficult to assess changes to the derivative of this pressure difference build-up that triggers the CIP washes. This is visualized and explained later in the sub-chapter.

Another challenge regarding analysis of data in an operational plant is that changes occur from time to time. Figure 5.8 shows flow adjustments, start and stop of SRUs and how this affects the seawater temperature. The smaller fluctuations in seawater temperature are likely caused by variations in the gas export rate through the amount of heat discarded in the gas compression coolers. With flow variations comes other variations like changes in pressure differences across the membranes, pressure changes in the deaerator and need of more oxygen scavenger in the deaerator. The combination of a short test duration and process alterations like these makes it difficult to assess the effects of the temperature change alone.

Test 1 was initiated the 26th of February and ended abruptly the 21st of March due to a breakdown of the main power deliverance from Edvard Grieg to Ivar Aasen. This disabled the gas export for the remainder of this project so that there was no new opportunity to test the system with elevated seawater temperatures. Due to this, the part of Test 1 where the seawater temperature was to be alternated during stable production conditions was never done. This means that the only significant and controlled temperature induced dynamic response in the plant happened during test start. The variations in gas export flow rate also makes some changes to the seawater temperature but typically not enough to evaluate the system response. The other temperature changes during the test occurs due to changes in the total seawater flow (total permeate production) due to that the compression coolers have no temperature control on the coolant (seawater) side.

There are many elements to be assessed and discussed relative to how the system responds to the increased seawater temperature. For that reason the assessment is subdivided into three sections to make the evaluation structured. The evaluation of Test 1 is sub-divided and analyzed with respect to temperature dependence as follows:

Instantaneous SRU effects

- The permeate sulfate concentration
- Membrane pressure drop and the
- Potential pumping power savings.

Long term SRU effects

- Biofouling
- General fouling

Deaerator response and performance model validation

- Design performance guarantee
- System behavior comparison between normal- and increased seawater temperatures.
- Evaluation of the theoretical mechanical performance model.

The evaluation of the theoretical mechanical performance model should have been done in a separate test. This was not possible due to the mentioned power loss on Ivar Aasen. For that reason was this model evaluated with data from Test 1. To clarify, this model evaluation has nothing to do with the assessment of if increased seawater can optimize the system.

Some elements discussed in the instantaneous membrane effects section relates to the long-term effects and vice versa. - and long-term membrane effects. It is still done this way as this sectioning is believed to give the reader a more structured discussion of a test with many elements to consider. And since there are so many elements to be assessed an overall summary and conclusion of the test is given at the end of this sub-chapter.

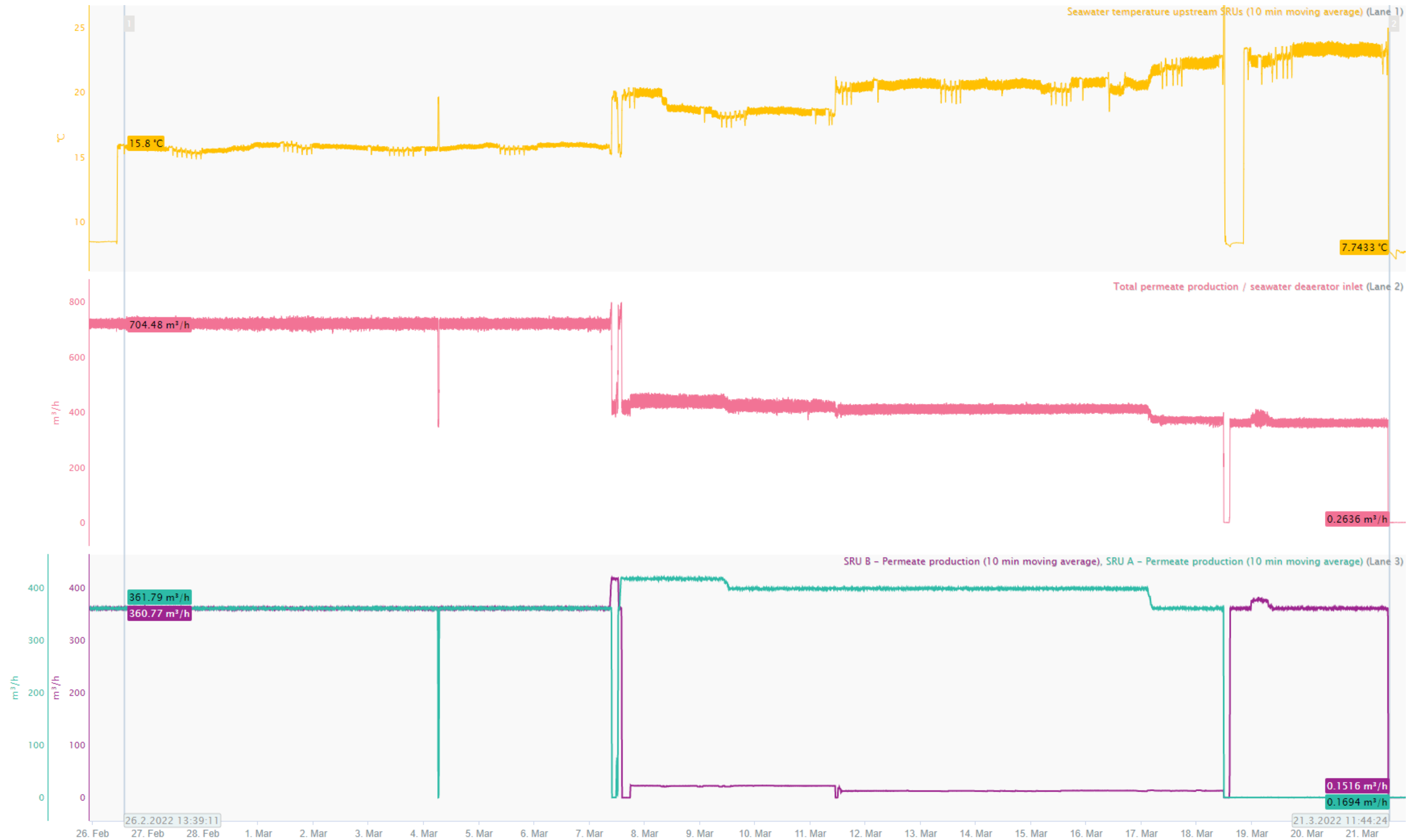


Figure 5.8: Process variations and plant changes during Test 1 from 26th of February to 21st of March. The upper lane shows the seawater temperature upstream the ultrafiltration which is later introduced to the SRUs and deaerator. The rate of gas export affects the heat discarded to the seawater in the transfer gas coolers. The middle lane shows total permeate production from the SRUs, i.e. seawater feed to the vacuum deaerator. The lower lane shows the separate permeate production from each SRU.

5.2.1.1 Instantaneous SRU effects

Elevating the seawater temperature will increase the membrane permeability for all species in addition to reducing the water viscosity. This should increase the permeate sulfate concentration and reduce the feed-to-concentrate pressure and feed-to-permeate pressure difference across the membranes. Less membrane pressure drop means less wear and tear for the membranes so that operating close to the 30 mg/L sulfate target should be positive with respect to SRU optimization.

Permeate sulfate concentration:

Figure 5.9 shows a plot of the sulfate content in the permeate streams of both SRUs relative to the seawater temperature introduced to the SRUs. A period of ~2 months prior to the test is also presented to show the sulfate content behavior during a period with stable and low seawater temperature. The jump in sulfate content from SRU B the 31st of January is taken shortly after startup after a CIP wash. There will typically be somewhat higher sulfate content initially after startup until it creeps down to a steady state.

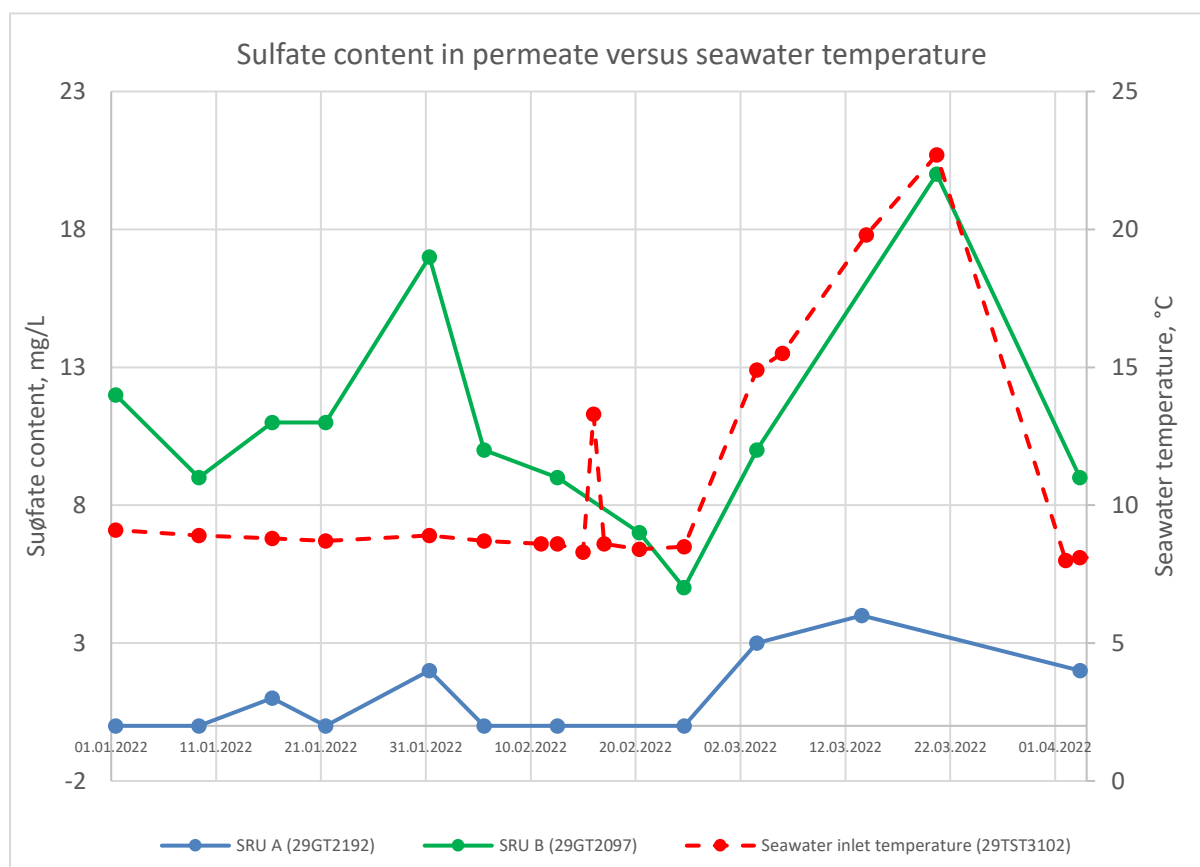


Figure 5.9: Lab measured sulfate content in permeate versus seawater temperature measured upstream the ultrafiltration package. Temperature data is retrieved from SeeQ and manually plotted. Test 1 is performed from 26th of February to 21st of March. Two months prior to test is also presented to show sulfate fluctuations during stable temperature conditions.

Even though there are few datapoints during the actual test there seems to be a strong correlation between the sulfate content and seawater temperature. This was as expected but the extent of it was unknown. The test indicates that the sulfate content in the permeate from both SRUs is well within the 30 mg/L criterion when the temperature reaches its highest value of ~ 23 °C during the test.

It is not known if the SRUs are able to produce within the target value of 30 mg/L at the highest possible temperature for the seawater. This maximum temperature is not calculated with an energy balance in this project and is not known. The main reason for neglecting this calculation is the combination of project time constraint and that the SRDP system is monitored and protected. The sulfate content is monitored and gives an alarm if the values get too high. This means that the operator can act if necessary and reduce the temperature. In addition the membranes are protected with a temperature safety transmitter that shuts down the system if the temperatures get ≥ 34 °C.

Membrane pressure drop

Membrane pressure drop or membrane pressure difference is in this thesis used as a general term for both feed-to-concentrate and feed-to-permeate pressure difference or pressure drop. The feed-to-concentrate pressure difference is the pressure drop axially along the feed spacer, while feed-to-permeate pressure difference is the pressure drop across the active membrane layer. It will be shown that these are coupled and behave proportionally but scaled. For the membrane pressure drop is often visualized with only one of them. It is often the feed-to-concentrate pressure difference that is used since this is the measured parameter triggering the need of CIP washes at Ivar Aasen.

The plot given in Fig. 5.10 visualizes how the membrane feed-to-concentrate and feed-to-permeate pressure differences decrease significantly with increased seawater temperature. The upper lane presents these pressure drops for both stages in SRU A, while the middle lane those of SRU B. The bottom lane shows seawater temperature and total permeate production which is stable besides the controlled temperature change.

A decrease in pressure drops along the feed spacer (feed-to-concentrate) and across the active membrane layer (feed-to-permeate) should be favorable for the system in that elements are subjected to less axial and radial stress. This should make the membranes less prone to damages like compaction, intrusion and telescoping in the long run. Thus, increasing the seawater temperature should reduce the rate of normal membrane degradation through less wear and tear.

From this test it is evident that the feed-to-permeate and feed-to-concentrate decreases with several bars and millibars when seawater temperature is increased with approximately 7 °C. The largest relative change happens to the pressure drop across the active membrane layer. This is likely so as it is affected through both increased permeability and decreased viscosity. The feed spacer pressure drop on the other hand is only affected by the decreased viscosity.

To sum up, lower membrane pressure drops in the SRU stages should be positive as it will reduce the rate of normal wear and tear. In addition, it might reduce biofouling through reduced concentration polarization due to increased degree of turbulence via reduced viscosity and higher diffusion coefficients increasing the laminar boundary layer back-diffusion. The latter will also depend on how the rate of bio growth increase with increased temperatures. Biofouling is assessed separately later in this sub-chapter.

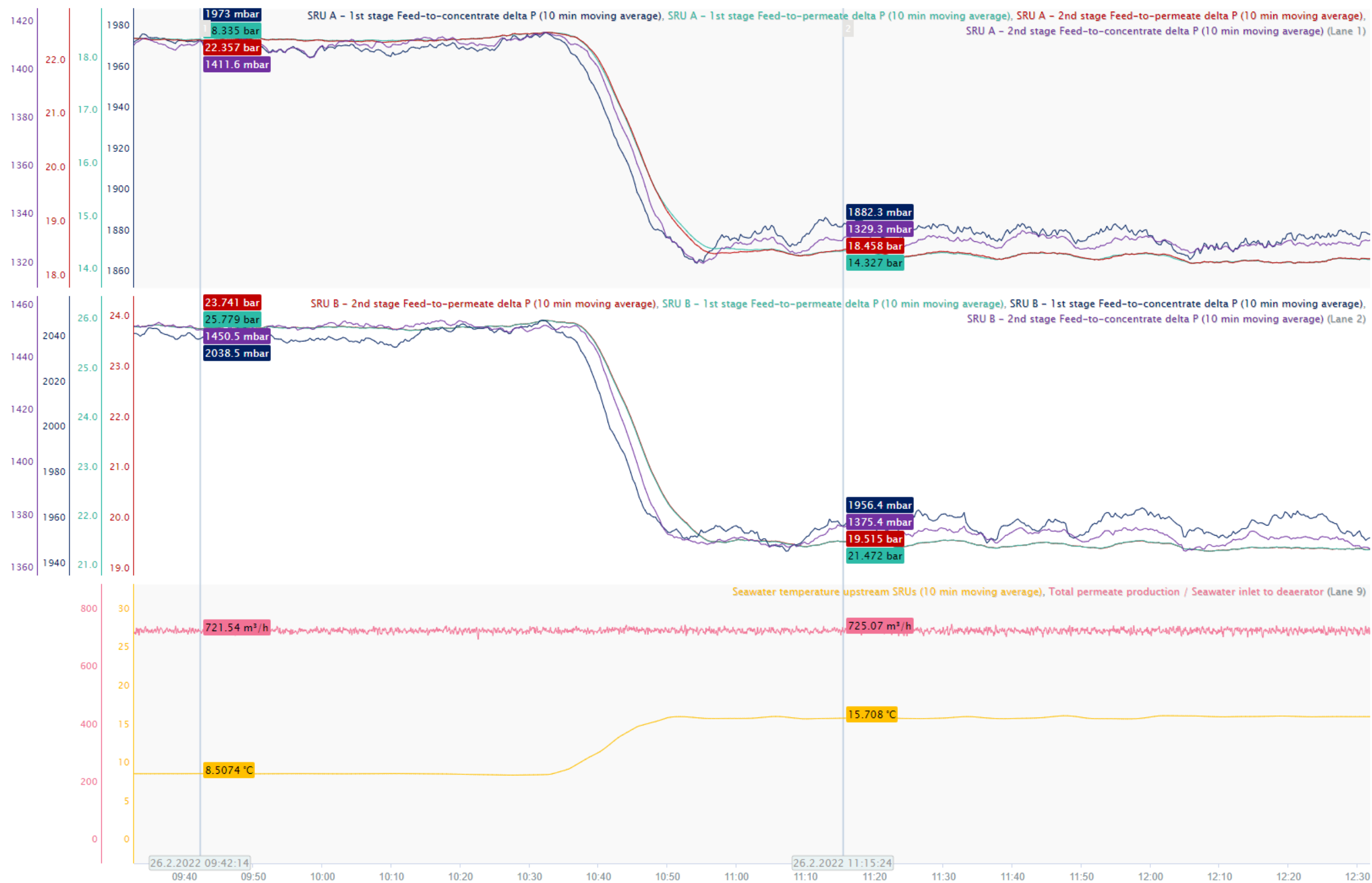


Figure 5.10: Change in feed-to-concentrate and feed-to-permeate pressure differences with increased seawater temperature. The upper lane shows the pressure drops for both stages in SRU A, while the middle lane those of SRU B. The lower lane shows the seawater temperature and total permeate production.

Another interesting observation regarding the membrane pressure drops, shown in Fig. 5.11, is that the differential pressure across the stages fluctuates more after that the temperature is increased. These fluctuations are shown through the feed-to-concentrate pressure differences in this plot. The feed-to-permeate pressure differences are coupled to these and add no new information in this particular plot. The red circles in this figure indicates, from left to right, start of Test 1, temperature fluctuations connected to the pressure control of the seawater to the ultrafiltration package, and a short trip of the SRUs. The temperature irregularities are not assessed in this project due since they are very small and do not seem to cause issues for the system.

The pressure fluctuations are likely to be positive for mitigation of biofouling as it will add dynamics to the fluid and thus alter laminar boundary layer thickness so that the concentration polarization fluctuates. DuPont states that the permeate backpressure should not remain constant which is yet another reason to why these fluctuations could be positive [57].

The explanation for why they occur is not easy to read from the plots. The main reasons are that the fluctuations have a different period than the seawater temperature fluctuations and that the fluctuations between SRU A and B seems synchronous but inverted. This is somewhat surprising as it was expected synchronous proportional behavior between the SRUs differential pressures. However, the main reason for any fluctuations is probably caused by fluctuation in the gas export rate and that this induces variations in the seawater temperature through the gas compression coolers. How the temperature fluctuations manifests through the pressure drops and why the SRUs seems to be inverted can probably be explained by a higher degree of instability in the pressure control for the stages. The inlet to both SRU is coupled to the same seawater manifold supplied from the SRU pumps which enables pressure coupling effects between the stages as observed.

The presence of these pressure difference fluctuations in combination with short duration of time with constant permeate production during Test 1 makes it very hard to evaluate the change in pressure difference build-up across the membranes. Assessing the time derivatives of these pressure curves would have been a good indicator on how the temperature affects the CIP wash frequency.



Figure 5.11: Feed-to-concentrate pressure difference for each stage in the SRUs versus seawater temperature. The upper lane shows seawater temperature and total permeate production. The latter is presented to show that the temperature fluctuations are not induced by permeate production. The middle lanes show the stage pressure differences for both SRUs while the lower lane show the total gas flow rate through the gas compression coolers via total gas export to Edvard Grieg. Circles in the upper lane indicates from left to right start of Test 1, temperature fluctuations due to the seawater pressure control to the ultrafiltration packager, and a short trip of the SRUs.

Pumping power consumption

The reduction in pressure differences across the SRUs should also affect the pumping power consume in a positive way. Fig. 5.12 shows a simple calculation of the power consumption potential based on the how the SRU pump power changes the first 14 hours after test initiation, indicated by the red circle. In this plot twelve randomly picked data points are selected to average the power consume before and after the seawater temperature is increased. This indicates that the SRU power drops with 4.9 kW. Relative to the normal power load of about 19 MW for Ivar Aasen this is a marginal effect. However, In light of resource and energy optimization this is a positive outcome even though it is a relatively small contribution.



Figure 5.12: Power consumption [kW] for the SRU pumps upstream the SRUs correlated to the increased seawater temperature upon initiation of Test 1 marked with the red circle. The upper lane shows total permeate production and seawater temperature upstream the ultrafiltration. The lower lane shows the SRU pumps power consumption in kW.

5.2.1.2 Long term SRU effects

Biofouling is likely the dominating factor inducing the need for CIP washes and is for that reason very important when considering SRU optimization. As stated in the introduction of this test assessment the CIP wash frequency cannot be assessed explicitly. For that reason it is necessary to assess other parameters that can indicate the bio growth rate dependence on seawater temperature. The elements used to assess the biofouling to temperature dependence are a chlorine filter wash frequency and bacterial count samples on the injection water after the seawater and produced water is mixed.

A separate section assessing general fouling is also given in this sub-chapter. The intent is to check how the pretreatment, or ultrafiltration package, is affected by the increased temperature. If the Silt Density Index (SDI) increases significantly with temperature this could induce more fouling in the SRU membranes.

Biofouling

The chlorine concentration in the seawater upstream the SRUs is monitored by two online sensors. This is to protect the membranes from halogen damage due to free available chlorine. These transmitters are fitted with filters to protect the sensors. When the filter fouls the sample flow drops and gives too high readings for the sensors which indicates the need of sensor flushing. Each time the sensor is flushed the filter upstream the cell is also replaced with a new filter.

In dialogue with the Aker BP supervisor he mentioned that this flushing frequency might be an indicator on the degree of biofouling in which I agree. If the flushing frequency increase with increased seawater temperature it could indicate an increased rate of bio growth. This in turn could indicate that increased membrane biofouling should be expected. However, to conclude that increased rate of bio growth in the seawater increases biofouling one must also consider the competing effects in the membranes. This is the potential reduction in concentration polarization through increased turbulence and increased species diffusion in water. The only way to truly understand the outcome is to evaluate the system over time.

Figure 5.13 shows the sensor flushing frequency during Test 1. In this plot the initial red circle indicates test start and the second test stop. The filter flushing is indicated with abrupt changes in the measured mV and sample flow from/to the chlorine cells. This is shown in the middle- and lower lanes. The upper lane shows seawater temperature and total permeate production. The latter is included in the plots as changes to it affects the seawater temperature significantly. The seawater flow itself should not affect the sensor flushing frequency significantly since the sample flow to the sensors is controlled. But to be on the safe side this should also be considered in when comparing flushing frequencies during the test to normal operations. Normal operation means operation without using the heated seawater from the compression coolers in the SRUs.

The intent with the plot in Fig. 5.13 is to establish the flushing interval time at different seawater temperatures and permeate production during Test 1. Due to a short test period with several permeate flow changes there are only a few flushing intervals available for assessment. The first two flush intervals at ~16 °C and ~720 m³/h permeate production is 72.5 and 72.8 hours. The last two intervals at ~20 °C and ~420 m³/h permeate production is 58.4 and 61.5 hours. These time intervals averages to flushing periods of 72.65 and 60 hours at the different

seawater temperatures and permeate flows. This is obviously a very coarse estimate as far more intervals should be assessed to have representative selections.

The plots shown in Fig. 5.14 and 5.15 shows flushing frequencies at normal seawater temperatures of about ~ 8.5 °C and ~ 720 m³/h permeate production. This normal temperature will fluctuate seasonally. The permeate production is correlated to ensure that any effect from this is accounted for in the comparisons. Averaging all flushing intervals, except of one, from these two plots yields an average of 73.8 hours. The excluded interval is the one marked with a red circle in Fig. 5.14 where the permeate production is reduces for a short period. By assessing the flushing time intervals used to calculate this average it is evident that there is a significant spread. The longest interval is 99.7 hours while the shortest is 39.3 hours.

When it comes to normal seawater temperatures at ~ 420 m³/h permeate production there are little consistency to find. Neither are there any long enough periods to assess historically. For that reason it the comparison is not done for this mode of production.

By assessing the averages at ~ 16 °C and ~ 720 m³/h permeate production it seems to indicate that the temperature does not affect the flushing frequency significantly. This in turn seems positive relative bio growth in the system at elevated temperatures. For the 20 °C situation the normal average flushing period is longer than that during the test. This could indicate that the increase from 16 to 20 °C increases the rate of bio growth.

However, this assessment cannot be trusted as is. The duration should be much longer to yield better flushing frequency averages during the test. In addition, the flushing frequency is a manual operation in that the control room gets an alarm and informs an offshore technician to perform flushing and change the filter. This means that there is a time uncertainty in the assessed time intervals as the response time from the alarm given to flushing is depends on this human interaction. This is yet another argument for longer test duration to yield better averages for the comparison.

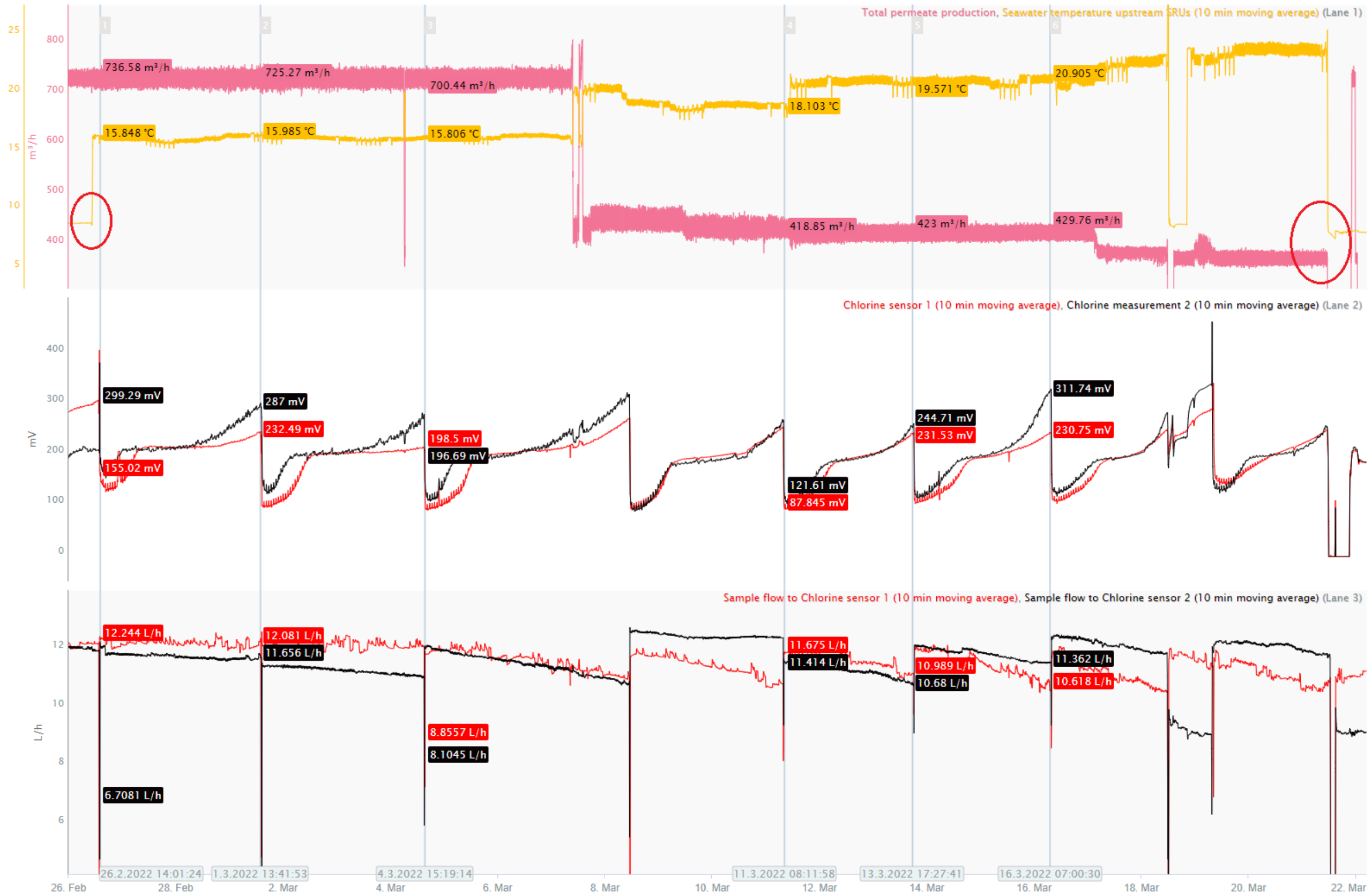


Figure 5.13: Flushing frequency during test period of Test 1 indicated with red circles. The upper lane shows total permeate production and seawater temperature. The middle and lower lane shows chlorine measurements (in mV) and sample flowrate to the two chlorine sensors. The production modes of ~16 °C at ~720 m³/h permeate production and ~20°C at ~420 m³/h permeate production is assessed and is indicated with rulers.



Figure 5.14: Flushing frequency during normal operation when ~8.5 °C seawater temperature and 720 m³/h permeate production. The upper lane shows total permeate production and seawater temperature. The middle and lower lane shows chlorine measurements (in mV) and sample flowrate to the sensors. The red circle indicates a change in total permeate production which excludes that particular flushing time interval from the assessment.

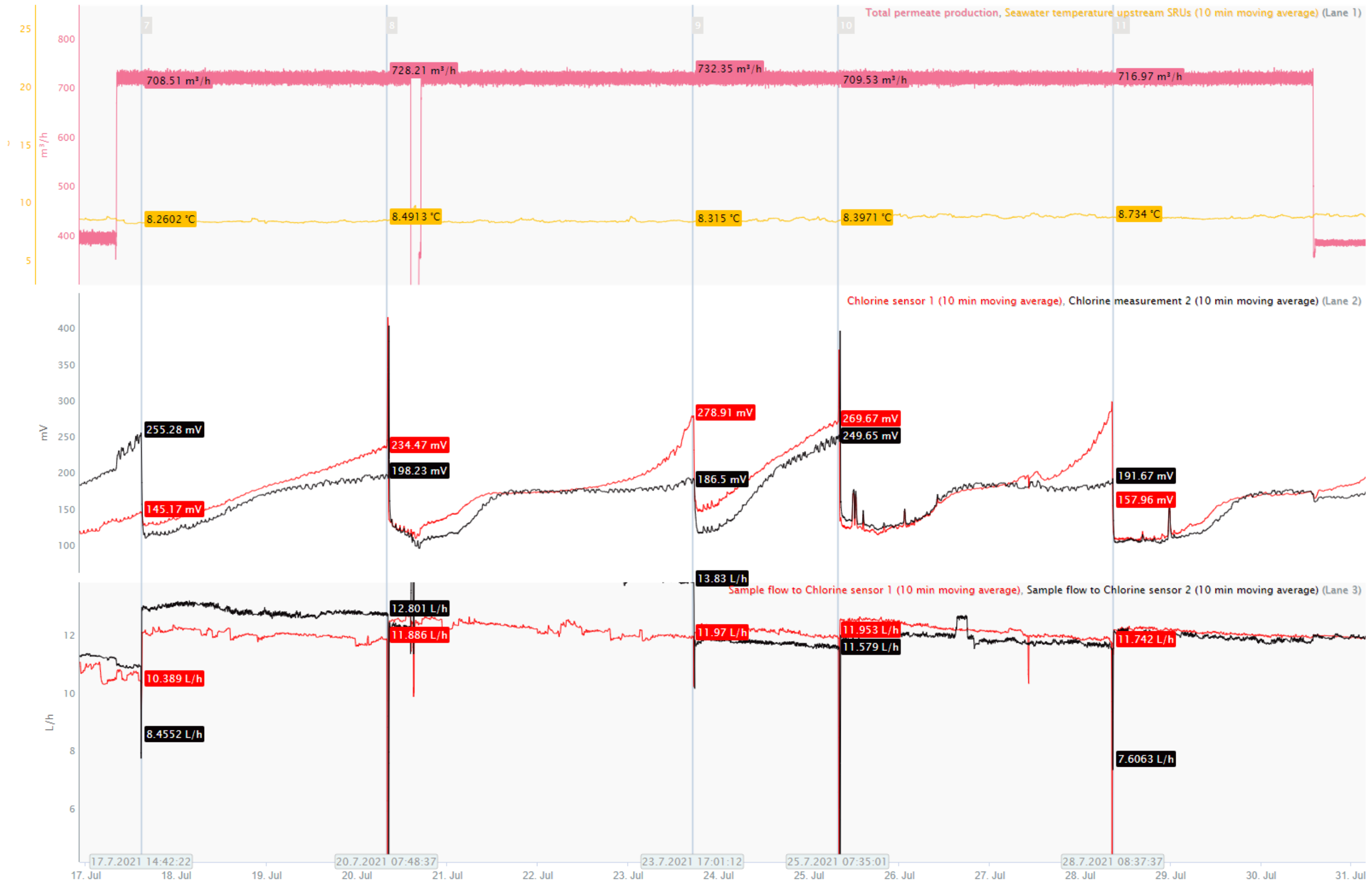


Figure 5.15: Flushing frequency during normal operation when ~8.5 °C seawater temperature and 720 m³/h permeate production. The upper lane shows total permeate production and seawater temperature. The middle and lower lane shows chlorine measurements (in mV) and sample flowrate to the sensors.

Bacteria samples are taken on a 6 monthly basis upstream the water injection pump. The sample is then a mix of produced water from the oil separators and treated seawater from the SRDP. These samples can indicate changes in bio growth if the produced water is assumed to be constant relative to the bacteria growth and the seawater to produced water flow ratio in the injection water is constant.

The analysis method for the bacteria samples is cATP QGO-M which is not assessed in this thesis. The data for this analysis is trusted as they are distributed from the production chemist responsible for Ivar Aasen.

There are only 3 samples available for the bacteria analysis of the injection water upstream the injection pump. All of which are sampled at a fairly equal seawater to produced water flow ratio. The last of these were taken the 13th of March, which is during the high temperature test, Test 1. Table 5.2 shows the sample data and flow ratio where the unit ME/mL is microbial equivalents per milliliter of sample where the spec is < 10⁵ ME/mL. The higher the number the more bacterial activity.

Table 5.2: Bacteria samples upstream the water injection pump compared to seawater temperatures and seawater to produced water flow ratios.

Sample date	Sample time	Sample point	Seawater to produced water ratio	Seawater temperature upstream SRUs, [°C]	Result, [ME/mL]
15.03.2021	10:30	29PDT1055	0.88	8.6	31584.6
01.12.2021	14:30	29PDT1055	0.68	10.7	14911.0
10.03.2022	13:00	29PDT1055	0.81	18.1	2838.2

The data in Table 5.2 seems favorable as it does not indicate increased bacterial activity upon increased seawater temperature. The highest bacterial activity is measured at the lowest temperature. Here, as for the chlorine sensor flushing assessment, there are too few datapoints to be able to conclude with how bio growth behaves with increased seawater temperature.

General fouling

The SDI is measured downstream of each ultrafiltration pair (or twin) on a monthly interval. Water from the UFs is introduced to the SRUs and SDI is thus an important parameter regarding fouling due to particulate matter and colloids.

Figures 5.16 and 5.17 show the lab measured SDI plotted against seawater temperature upstream the ultrafiltration package. The initial figure focuses on the test period while the next plot includes a 10-month period prior to test initiation to address the normal SDI variations with normal and relatively constant temperatures. The temperature spike on the 15th of March, just before Test 1, was a short temperature test before a CIP wash. This is not evaluated in this thesis due to its short duration.

The SDI profiles in Fig. 5.16 shows little correlation between temperature and SDI. It is important to consider that only twin A, B, and D are measured during the actual test. Due to a staggered test interval between the UF twins this is what is available during the short test period of Test 1. Of these, twin D is the only one that increases slightly with temperature relative to its previous sample one month before.

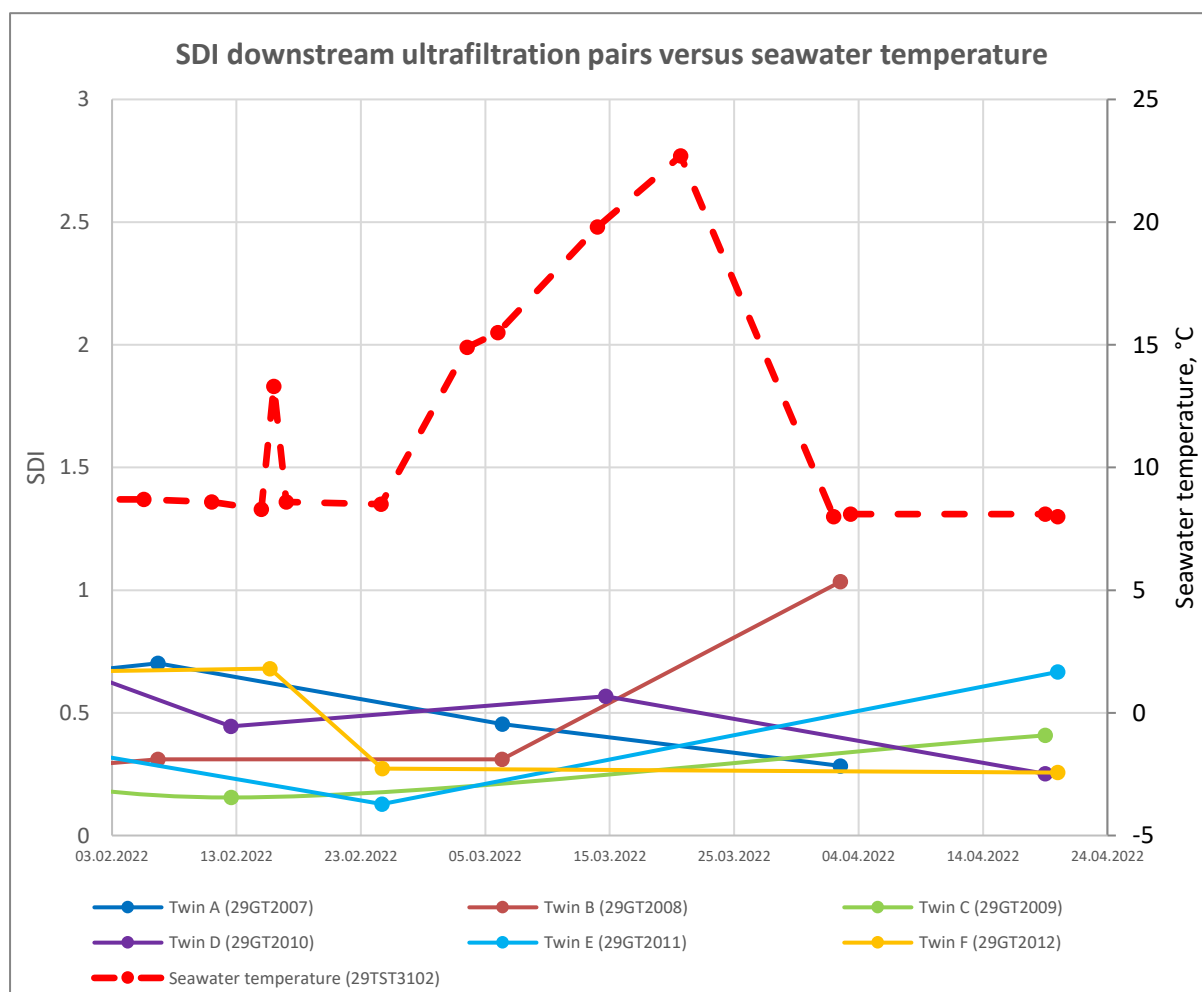


Figure 5.16: Lab measured SDI of the seawater downstream each UF pair versus seawater temperature measured upstream the ultrafiltration package. Temperature data is retrieved from SeeQ and manually plotted. This plot is based around Test 1 performed from 26th of February to 21st of March indicated with the large spike in temperature.

Comparing SDI to temperature over a 10-month period prior to the test, as done in Fig. 5.17, makes it evident that the SDI fluctuates even when there are no significant temperature variations. These fluctuations seem to correlate with the SDI measured upstream the ultrafiltration package as shown in Fig. 5.18 which presents data from the same time period as in Fig. 5.17. The SDI in the water upstream the UFs only affected by the seawater coarse filters. This means that it is independent the seawater temperature evaluated here since the compressor coolers are positioned downstream these coarse filters.

The plots assessed regarding SDI to seawater temperature correlation indicates that there are little to no correlation over the temperature range assessed, ~8 to 23 °C. It also shows how the SDI in the feedwater introduced to the SRUs are well within the recommended and maximum SDI level of 3 and 5, shown in Tab. 2.2, even during the high temperature test. For that reason the general fouling due to particulate matter and colloids should not be affected by temperature, at least within the assessed temperature range

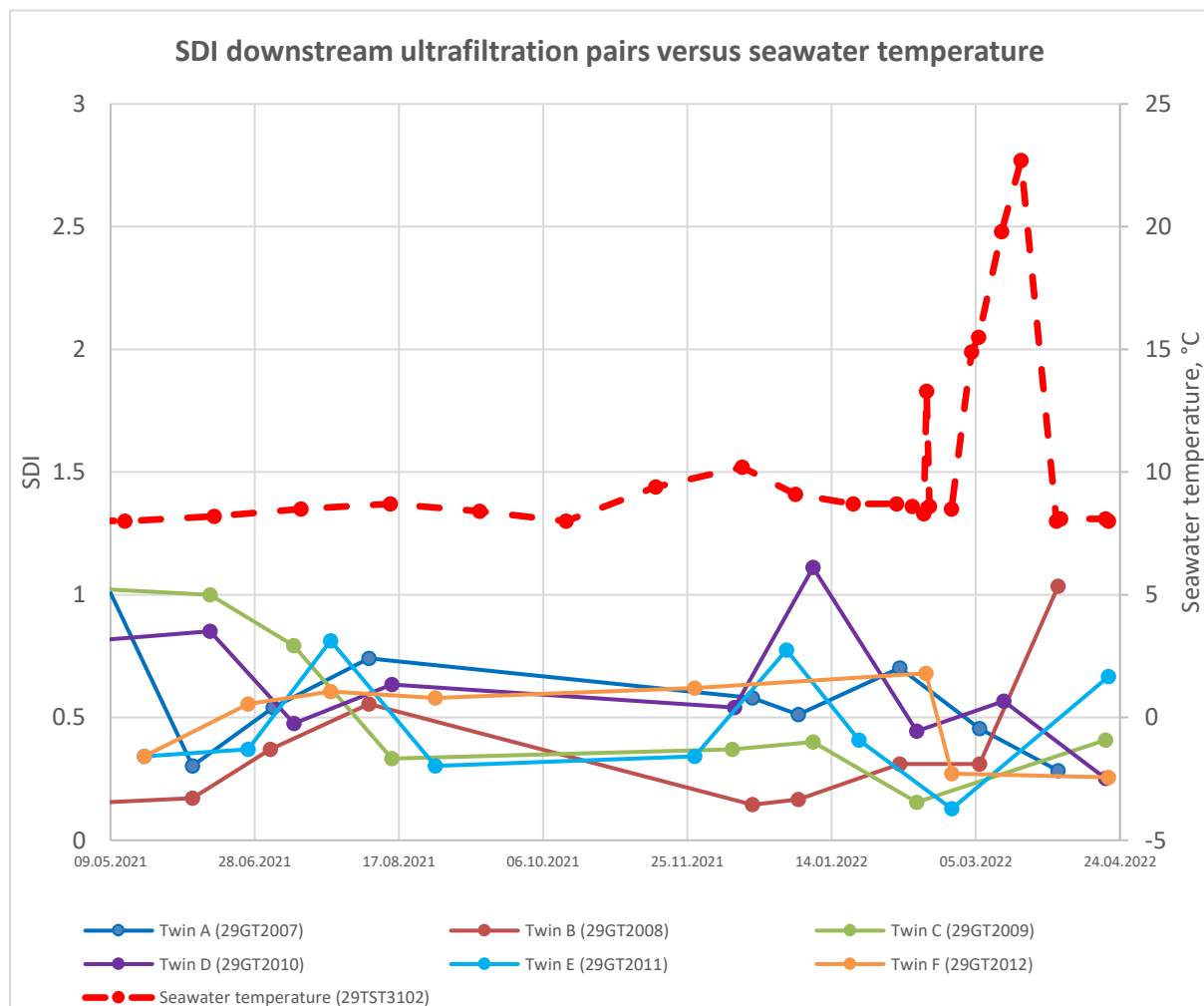


Figure 5.17: Lab measured SDI of the seawater downstream each UF pair versus seawater temperature measured upstream the ultrafiltration package over a one-year period including Test 1. This plot shows the SDI variations during normal operation with relatively stable seawater temperatures prior- and during Test 1.

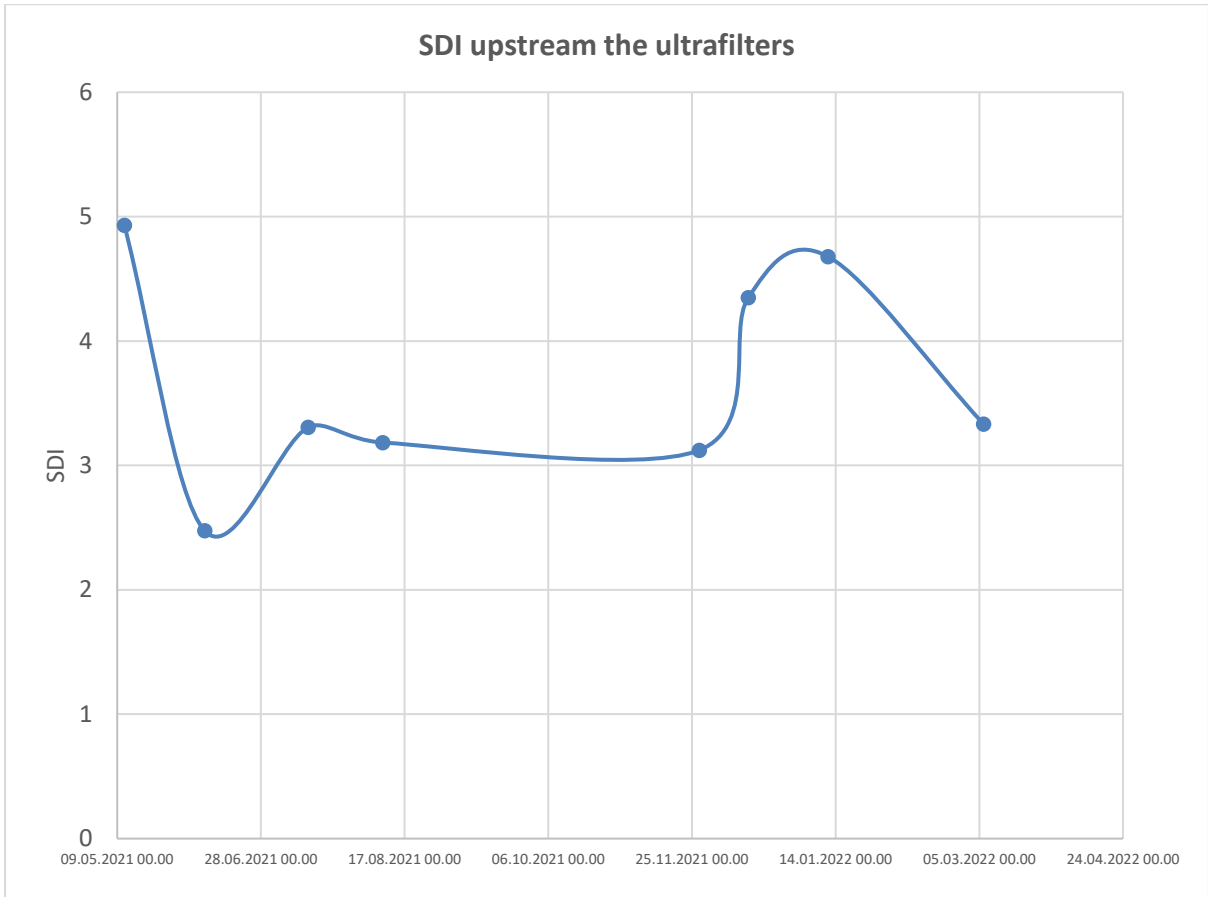


Figure 5.18: Lab measured SDI of the seawater upstream the ultrafiltration package prior to- and during Test 1. The x-axis is equal to that in Fig. 5.17 to better visualize how these data correlates to the SDI measurements downstream the ultrafiltration package.

5.2.1.3 Deaerator response and performance model validation

To consider the deaerator system response to increased seawater temperatures an assessment of the design performance guarantee is done. Such an assessment is also done in the “historical performance” section of Chapter 2.4 which indicates that the ejector underperforms. The intent with a new such performance assessment is to consider if increasing the seawater temperature brings the system closer to its performance guarantee. In addition a trend comparison between normal- and high temperature operation is performed.

At the end of this sub-chapter is an assessment of the theoretical mechanical performance model given in Fig. 4.5. The procedure is to see if the system responds to increased temperatures as the model predicts. It is also evaluated against the equivalent predictions by use of the manufacturer’s performance model for mechanical deaeration.

Design performance guarantee

The simple analysis done in Ch. 2.4.4 assesses the historical mechanical deaeration performance based on the deaerator stage pressures. The historical data evaluated here indicates that the vacuum ejector underperforms. Data from Test 1 is used to see if this issue is related to the seawater temperature. Eta Process Plant, the system manufacturer, guarantees that the mechanical deaeration will be able to deliver seawater with an oxygen content of 50 ppb mol at seawater temperatures above 16 °C (see Fig. 2.22). This 16 °C limit makes Test 1 a good reference to evaluate if the system delivers as guaranteed.

The deaerator operates with both mechanical and chemical deaeration. The residual oxygen content, after mechanical deaeration, will be chemically deaerated to a level of 10 ppb mol or less by use of an oxygen scavenger. To be able to assess the mechanical deaerator performance it is necessary to know how much oxygen scavenger that should be dosed to remove the residual dissolved oxygen per design. This knowledge enables the possibility to assess the performance by evaluating the oxygen scavenger dosage rate. By doing so it is assumed that there are no issues with the chemical reaction between oxygen scavenger and dissolved oxygen.

When operating at 720 m³/h seawater production the oxygen scavenger dosage should be approximately 2.4 L/h. This is if the mechanical deaeration delivers on its 50 ppb mol dissolved oxygen performance guarantee. At a seawater flow in the range of 373 to 440 m³/h this dosage rate should be from ~1.25 to 1.47 L/h. These dosage rates are according to Eta’s performance calculations converted to the seawater flow in question and the concentration of the oxygen scavenger used at Ivar Aasen. These performance calculations are not shared here due to confidentiality reasons.

It is important to know that the oxygen scavenger dosage rate is manually adjusted by the control room operators based on how they assess the measured dissolved oxygen content downstream the deaerator booster pumps. The instruction is that the dissolved oxygen content must be lower than 200 ppb mol but should be beneath 20 ppb mol and to adjust the dosage rate of oxygen scavenger accordingly. This means that there is a human factor to this parameter which is used in this assessment. For that reason the oxygen scavenger dosage rate should be considered in combination with the dissolved oxygen content.

The plot shown in Fig. 5.19 presents a section from Test 1 when the deaerator operates at ~720 m³/h seawater flow at ~15.6 °C. The initial part of Test 1 is not considered in this analysis as it was recently started after a trip. During this startup the system was not in steady state so that the data has no value relative to assessing the deaerator performance. At this temperature, 15.6 °C, the mechanical deaeration should be very close on delivering the performance guarantee of 50 ppbmol dissolved oxygen. It is evident that the use of ~15.4 – 17 L/h of oxygen scavenger is much higher than what should be needed if the mechanical deaeration is functioning as intended.

The mechanical deaeration is governed by the lowest pressure in the deaerator, thus the 2nd stage. According to Eta's stage pressure plots given in Fig. 2.23 the pressures should be approximately 53.5 and 20 mbara in the 1st and 2nd stages at these operational conditions. This means that the 2nd stage underperforms by delivering a vacuum of only ~27 mbara. This is likely the reason for the need of excess oxygen scavenger as the pressure is not low enough to mechanically remove enough oxygen. On the other hand, the 1st stage over performs which indicates that the deterioration in performance is caused by the ejector.

The data points assessed in Fig. 5.19 are selected during the stable sections of the plot. The fluctuating parts are not considered as they are assumed to not represent the “average behavior” of the system. The spikes in stage pressures and dissolved oxygen might be induced by manual flushing of the ejector and/or the oxygen sensor or batching of biocide to mitigate system bio growth. The online measurement for dissolved oxygen downstream the deaerator booster pumps is checked against the weekly lab tests sampled at the same position, and these correlates well.



Figure 5.19: Evaluation of the deaerator performance guarantee by assessing dosage rate of oxygen scavenger and dissolved oxygen during a section of Test 1. The upper lane shows the seawater temperature and flow entering the deaerator which is approximately 15.5 °C and 720 m³/h during this section of Test 1. The middle lane presents the deaerator stage pressures where the top packing is the 1st stage while the lower packing is the 2nd stage. The lower lane shows the dissolved oxygen and oxygen scavenger dosage rate.

The next plot shown in Fig. 5.20 evaluates another section of Test 1. This plot shows the deaerator behavior with seawater temperature and flow in the ranges of 18.5 to 21.8 °C and 374 to 440 m³/h, approximately. This plot tells the same story as what is found in Fig. 5.19 with respect to the dosage rates of oxygen scavenger. The oxygen scavenger is dosed in the range of 1.86 to 9.4 L/h which is higher than the targeted rate from ~1.25 to 1.47 L/h for the flows assessed in the plot. These target oxygen scavenger rates should be even lower since the seawater temperatures are even higher than the 16 °C needed to deliver on mechanical deaeration. I.e., the mechanical deaeration should bring the dissolved oxygen content below 50 ppb mol leaving less residual dissolved oxygen content in need of chemical deaeration.

The pressure in the stages cannot be correlated to Eta's plots directly since the flow range in Fig. 5.20 is lower than what is valid in their estimates. By using the 2nd stage pressure turndown curves for seawater flows below 720 m³/h presented in Fig. 4.4 the 2nd stage pressures should lie in the range of ~22 to 27 mbara with these temperatures and flows. This is very close to the pressure in the 2nd stage shown in the plot. This indicates that the need of excess oxygen scavenger is not caused by the mechanical deaeration performance. That is if Eta's predicted performance curves are correct.

The best way to assess whether the mechanical deaeration is according to the performance guarantee is to operate the system with no chemical deaeration. This cannot be done unless the mechanical deaerator alone manages to deliver on spec which is less than 200 ppb mol but should be less than 20 ppb mol. The red circles in Fig. 5.20 indicate data that reveal how the mechanical deaeration perform when the oxygen scavenger is significantly reduced/stopped. The first circle, from the left-hand side, shows that the dissolved oxygen reaches almost 100 ppb mol when the oxygen scavenger is reduced from 4.5 to 0 L/h. The second circle shows how the dissolved oxygen content crosses 85 ppb mol when reducing the dosage rate from approximately 2.1 to 0.5 L/h. During both these periods the seawater temperature, seawater flow and stage pressures are very stable. Thus, this are both strong indications of that the mechanical deaeration is not delivering according to the performance guarantee. More detailed plots of these incidents are presented in Appendix K.



Figure 5.20: Evaluation of the deaerator performance guarantee by assessing dosage rate of oxygen scavenger and dissolved oxygen during Test 1. The upper lane shows the seawater temperature and flow entering the deaerator which is in the range of 18.5 to 21.8 °C and 374 to 440 m³/h during this section of Test 1. The middle lane presents the deaerator stage pressures where the top packing is the 1st stage while the lower packing is the 2nd stage. The lower lane shows the dissolved oxygen and oxygen scavenger dosage rate.

System behavior comparison between normal- and high seawater temperatures

To assess if it is favorable to operate at elevated seawater temperatures the deaerator behavior during Test 1 is compared to behavior during normal operation at similar seawater flows. The plots shown in Figures 5.21 and 5.22 show a period of operation at $\sim 720 \text{ m}^3/\text{h}$ seawater production, while Figures 5.23 and 5.24 shows seawater flows of 380 to 440 m^3/h . All four plots consider normal operations with respect to seawater temperatures.

By comparing the normal temperature cases in Fig 5.21 and 5.22 to the high temperature case in Fig. 5.19, all of which represent 720 m^3/h production mode, the following differences can be seen:

- The 2nd stage pressure increases with temperature which is in line with the form of the functional dependence reported by Eta Process plant. But the pressures at normal seawater temperature ($\sim 9 \text{ }^\circ\text{C}$ in Fig. 5.21 and 5.22) are still higher than what is estimated by Eta Process Plant in Fig. 2.23 which suggests a 2nd stage pressure close to 15 mbara at 9°C .
- The dosage rate of oxygen scavenger and dissolved oxygen content is similar between the high- and normal temperature cases. The average dissolved oxygen content is somewhat higher in Fig. 5.22, but the oxygen scavenger is somewhat lower at the same time.

To evaluate production modes in the range of 380 to 440 m^3/h a comparison between Fig. 5.23 to 5.24 and 5.20 is done. This comparison shows the following differences:

- Increased 2nd stage pressure with temperature. But at temperatures of 8.5 to 10 $^\circ\text{C}$ the pressure in this stage should be in the range of approximately 13.5 to 14.5 mbara. These pressures are based on the 2nd stage pressure turndown curves for seawater flows below 720 m^3/h presented in Fig. 4.4.
- Similar oxygen scavenger dosage and dissolved oxygen content between the high- and normal temperature cases. At 440 m^3/h the low temperature operation seems slightly favorable in that the dosage rate of oxygen scavenger is somewhat lower while the dissolved oxygen content is almost similar. On the other hand, at 380 m^3/h production the high temperature test seems favorable with less oxygen scavenger and relatively equal dissolved oxygen content. But the time span of these comparisons was very short and therefore not reliable.

Based on these comparisons it cannot be seen a distinctive improvement in deaerator performance with increased temperature. At the same time the mechanical deaeration performance is likely not according to the design through that the 2nd stage pressure is higher than Eta Process Plant's estimate in Fig. 2.23. The high temperature test should have been longer to better optimize the oxygen scavenger dosage rate. And more data should be assessed for the lower production rates (380 to 440 m^3/h) in this comparison but there are few periods of time with stable production to assess at these production levels. In addition, the seawater temperature should have been altered manually during constant seawater flow to isolate the effects on temperature on the system. These isolated effects should have been induced upon initiation of Test 1, but the system was at the time unsteady due to start up after a system trip.

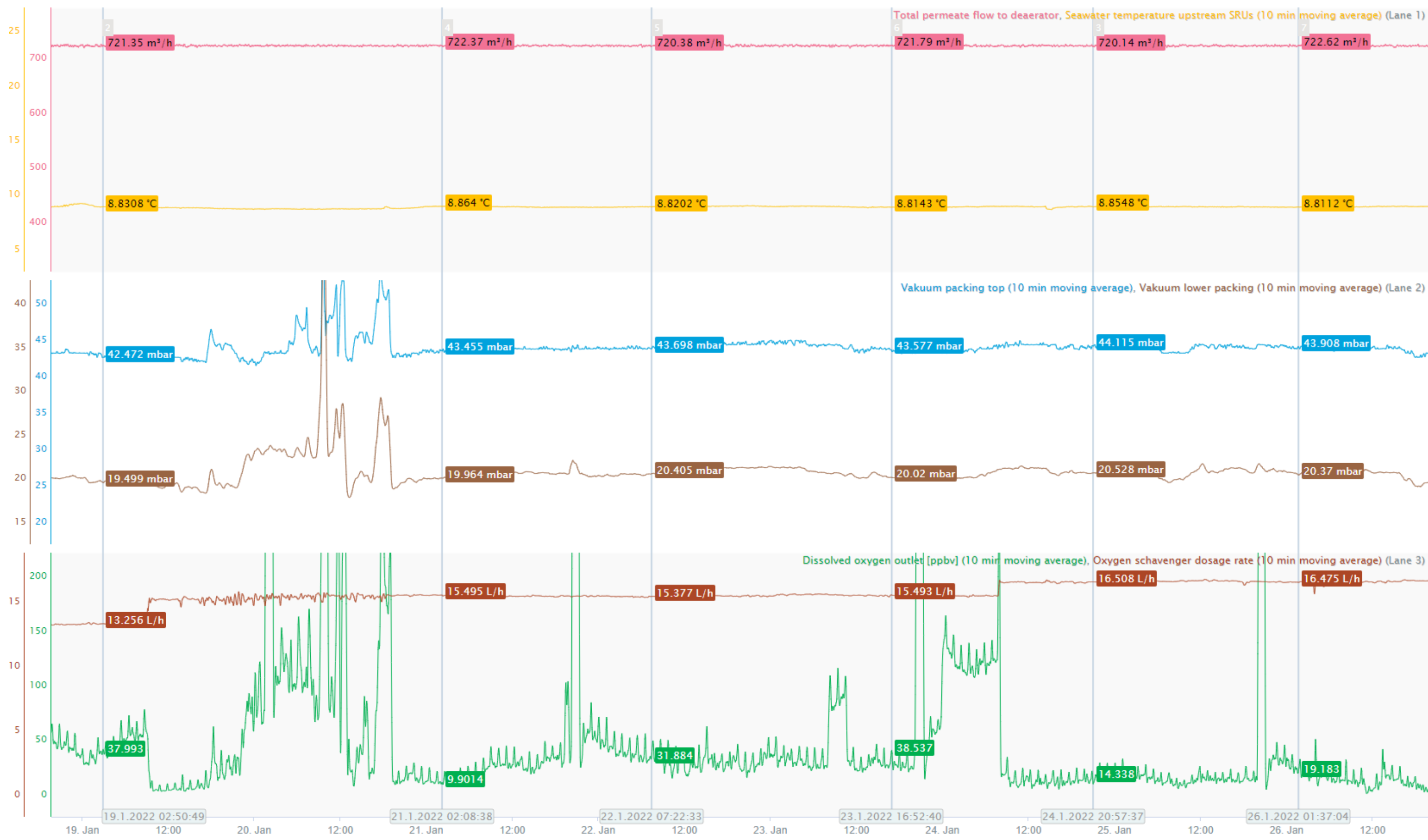


Figure 5.21: Deaerator parameters during normal operation at a seawater production and temperature of ~720 m³/h and 8.8 °C. The upper lane shows the seawater temperature and flow entering the deaerator. The middle lane presents the deaerator stage pressures where the top packing is the 1st stage while the lower packing is the 2nd stage. The lower lane shows the dissolved oxygen and oxygen scavenger dosage rate.



Figure 5.22: Deaerator parameters during normal operation at a seawater production and temperature of ~720 m³/h and 9.1 °C. The upper lane shows the seawater temperature and flow entering the deaerator. The middle lane presents the deaerator stage pressures where the top packing is the 1st stage while the lower packing is the 2nd stage. The lower lane shows the dissolved oxygen and oxygen scavenger dosage rate.



Figure 5.23: Deaerator parameters during normal operation at a seawater production and temperature of ~380 m³/h and 10.3 °C. The upper lane shows the seawater temperature and flow entering the deaerator. The middle lane presents the deaerator stage pressures where the top packing is the 1st stage while the lower packing is the 2nd stage. The lower lane shows the dissolved oxygen and oxygen scavenger dosage rate.

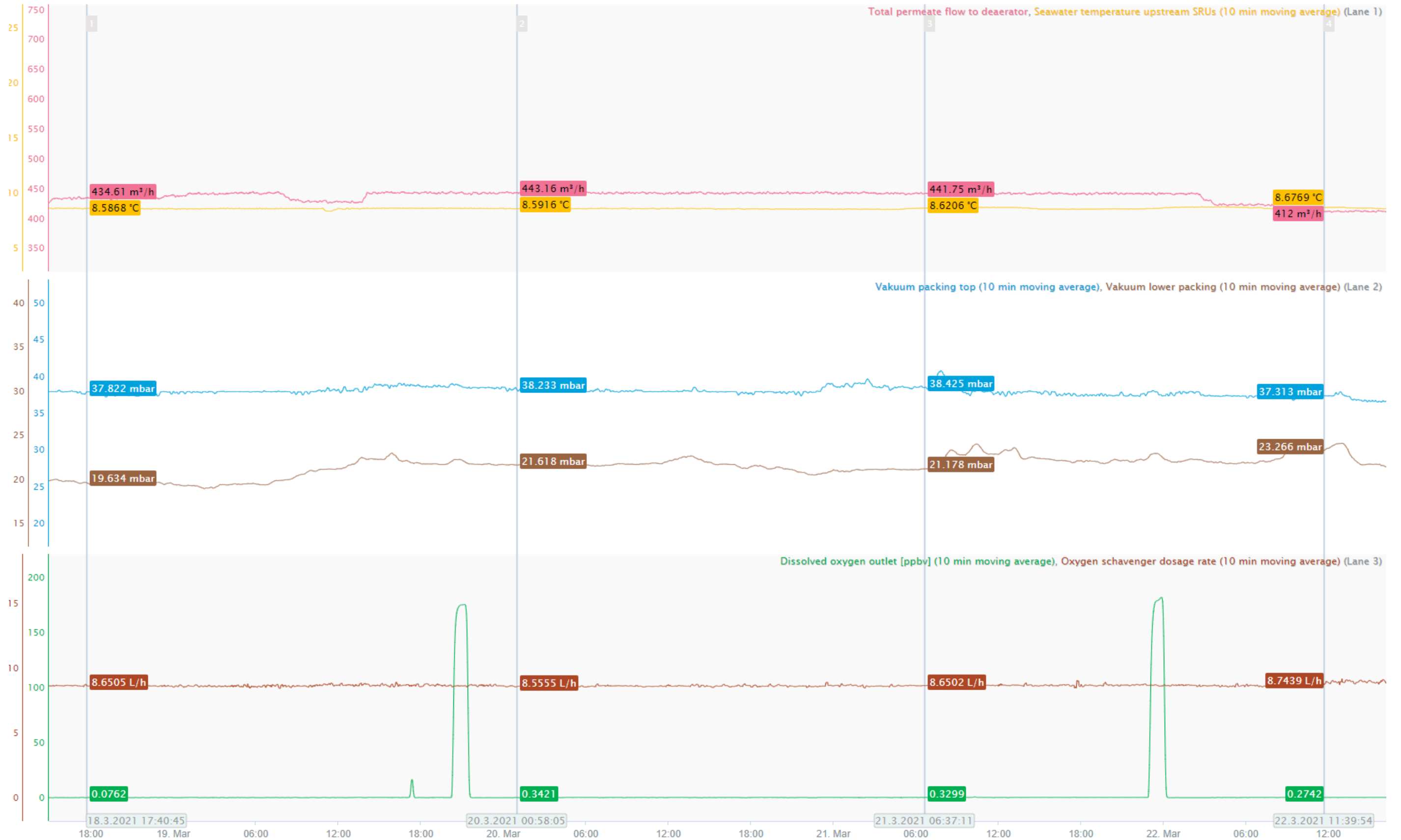


Figure 5.24: Deaerator parameters during normal operation at a seawater production and temperature of ~440 m³/h and 8.6 °C. The upper lane shows the seawater temperature and flow entering the deaerator. The middle lane presents the deaerator stage pressures where the top packing is the 1st stage while the lower packing is the 2nd stage. The lower lane shows the dissolved oxygen and oxygen scavenger dosage rate.

Evaluation of the theoretical mechanical deaeration performance model

It is not easy to evaluate the theoretical mechanical deaeration performance without operating the deaerator with no chemical deaeration. This is obviously not feasible due to causing damage to the downstream process equipment and reservoir. Alternatively the oxygen scavenger feed could be kept constant while changing the temperature and keeping the seawater flow constant. Doing so should show how the mechanical deaeration alters with temperature if the chemical deaeration is assumed constant. This will induce an error through that the chemical oxygen removal reaction will have a functional dependence on temperature. This can likely be estimated with a suitable model for the reaction rate constant, e.g. Arrhenius equation. This is not done in this project.

Considering all above plots and evaluations it cannot be proven that the oxygen content after mechanical deaeration increases with increased temperature as is indicated in the theoretical model established in Fig. 4.5 On the other hand, neither can it be shown that increased temperatures significantly improve the performance as indicated by Eta Process Plant in Fig. 2.22. In that the deaerator performance behaves seemingly stable, performance wise, the model derived in this thesis seems the most feasible of the two. That since it predicts the least dissolved oxygen to temperature dependence of the two.

The seawater flow dependence on dissolved oxygen cannot be evaluated as the changes in seawater flow also induces temperature changes. For instance, the theoretical model predicts that by moving from 720 m³/h seawater flow at 15 °C (as in Fig. 5.19) to ~400 m³/h at around 20 °C (in Fig. 5.20) the oxygen content should increase from approximately 44 to 48 ppbmol. The only plant parameter that can be used to control if this is in fact the actual dissolved oxygen content after mechanical deaeration is the dosage rate of oxygen scavenger. This cannot be done due to not knowing the exact amount of chemical necessary to bring the dissolved oxygen content from these levels of dissolved oxygen to below 10 ppbmol.

5.2.1.4 Test 1 - Summary

Based on most of the parameters assessed the test indicates a positive outcome for the SRUs from elevating the seawater temperature, but the test cannot conclude whether to expect increased membrane biofouling with increased temperature. This must be considered over a longer period of time to enable a more statistical approach on the CIP frequency and membrane pressure differences. This might enable the possibility of assessing the time derivatives of the membrane pressure difference curves which would be a strong tool to predict the changes in CIP frequency.

Regarding the vacuum deaerator there are strong indications that the mechanical deaeration does not perform according to the performance guarantee. The assessed parameters point towards the gas ejector being the reason for this. However, the data collected during this test cannot be used to conclude if it was favorable or not to increase temperature with respect to the deaerator performance. The data produced in the test seem to indicate that the performance is not very affected by the changes in seawater temperature. Neither can the test be used to properly evaluate the validity of the theoretical mechanical deaeration model. The deaerator was under start-up and out of balance when the temperature was increased, and the test period was too short. To be able to conclude a new and longer test should be performed where the seawater temperature is adjusted manually by altering seawater routing from the compression coolers to the SRDP at constant seawater production.

Based on this the temperature test should be reassumed when possible. The test was too short, and the temperature was not adjusted during stable periods to isolate the system dynamics response upon changing it. In addition, after the temperature changes, the system should be kept at highest possible level by routing all seawater from the compression coolers to the ultrafilters while monitoring sulfate content as usual. Over time this will enable the possibility for a statistical comparison of CIP wash frequency and membrane stage pressure differences between high- and normal temperature modes for the SRUs. This will also make it possible to do a new and proper evaluation on the deaerator performance at higher seawater temperature. Confirming the mechanical deaeration performance model will likely need an effort to estimate the chemical deaeration reaction rate and its dependence to temperature to be able to distinguish the mechanical deaeration part from the overall deaeration.

Another aspect to consider is that the maximum seawater temperature was not reached during this test. This means that whenever passing ~ 23 °C, the highest temperature reading in Test 1, it is unknown if the system will be able to deliver on target. However, the system is monitored on both sulfate content and dissolved oxygen in addition to being protected against too high temperature. For that reason it is the risk of tripping the system rather than damaging it that is present.

5.2.2 Test 2 – Validate permeate flow model

It was planned to do this flow model validation with data sampled from SRU A, but it was not possible due to issues with the PV positioner on the 1st stage permeate. For that reason this test was carried out on SRU B. But still, these SRUs are identical so the model should perform equally for them both. It was also planned to test with different seawater temperatures to simulate membrane fouling. This was not possible due to gas export constraints on Edvard Grieg.

It was intended to do several measurements at different flows and temperatures as a part of Test 2. Only one measurement run was done due to time constraints. The discussion below refers to “the initial measurement run” based on that there are more to come after the project period. In Test 2 of this thesis this initial measurement run is the only one performed.

Data sampling

A Fluxus G608 flowmeter was mounted on the permeate stream out of the 2nd stage of SRU B by an instrument technician at Ivar Aasen. This flowmeter was used to measure the permeate flow from this stage during the test. This is a portable ultrasonic flowmeter applicable for measuring both liquid and gas flows. It was setup to log data each 10th second and the timestamp on the device was synchronized with the control system time with 1 minute uncertainty. This is important since the measured data is correlated with data from the control system in validation part of the test. Detailed info about this flowmeter can be found in [58].

The test was done during stable conditions with respect to permeate production and seawater temperature. And the total recovery was checked to be constant during the test. Both of which is shown in the plot in Fig. 5.25. The rulers indicate the start and stop of data recording with the clamp-on flowmeter. The upper lane shows the PV position and Δp across it on the permeate outlet of the 1st stage of SRU B. The black curve in this lane shows how the PV was manually adjusted by the control room technician. The middle lane shows the feed-to-concentrate pressure difference for both stages in the SRU. And the bottom lane shows seawater temperature, total permeate production and concentrate flow from SRU B. The lower lane shows how the temperature is relatively stable and how the total recovery is unaffected by the manual PV steps. The permeate flow production was $\sim 405 \text{ m}^3/\text{h}$ during the initial measurement run of Test 2.

After the measurement run the instrument technician stopped the data logging and sent the file to be analyzed. This data was converted to Excel from FluxDiag Reader 2.10.1 for evaluation against the calculated flows estimated by the new model presented in Ch. 5.1.1.

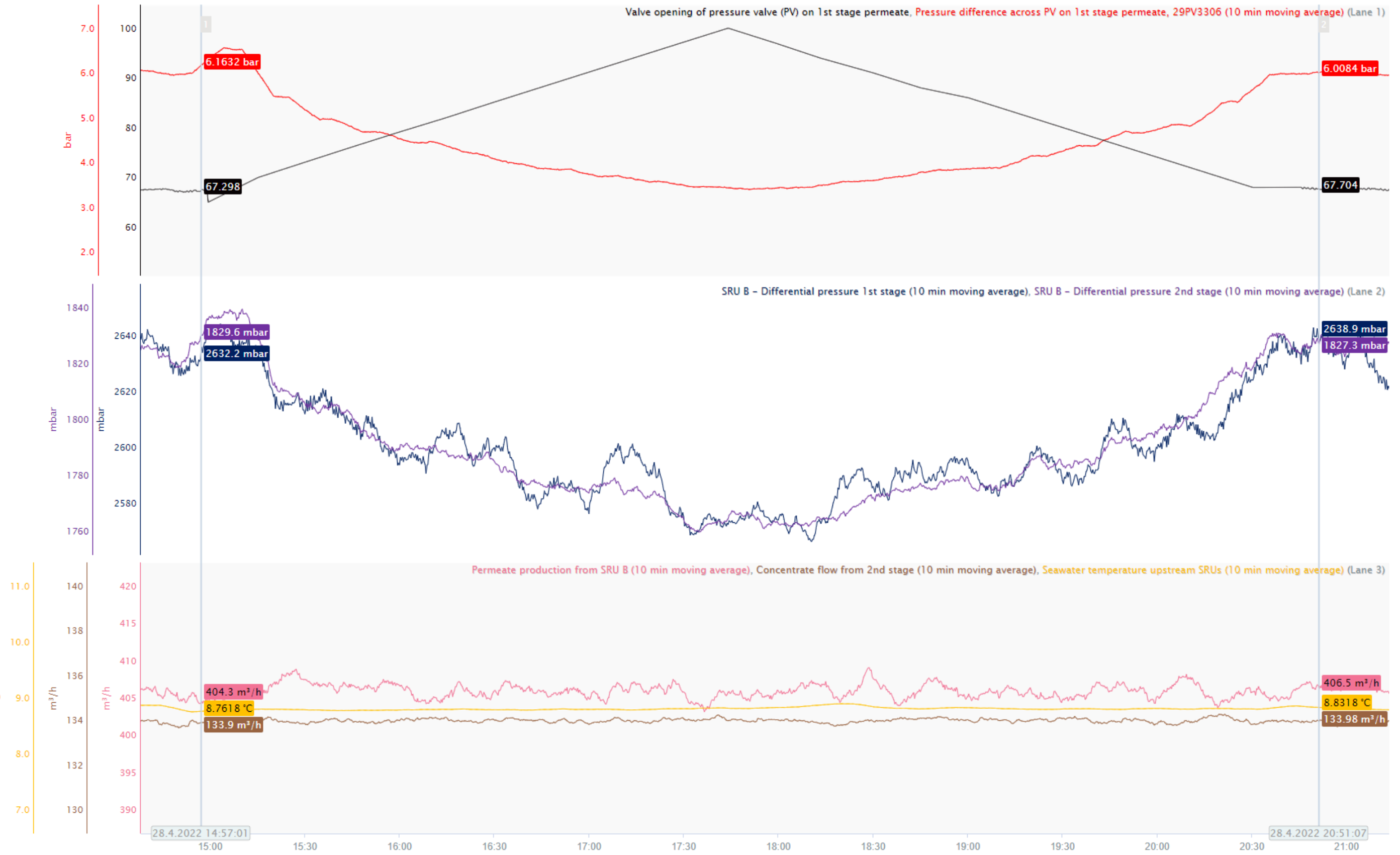


Figure 5.25: Overview of Test 2. The upper lane shows the PV position and Δp across it. The middle lane presents the feed-to-concentrate pressure difference in both stages of SRU B. The lower lane shows the seawater temperature, permeate and concentrate flows. The test is recorded with a clamp-on flowmeter in the period of time between the rulers in the plot. The PV stepping sequence performed by the control room technician is shown with the black curve in the upper lane.

Model validation

The new model estimates the 1st stage permeate flow with use of pressure drop across the PV and the valve position data from the control system. The total permeate production from SRU B is used to complete the system mass balance so that the permeate flow out of the 2nd stage can be modelled.

The plot in Fig. 5.26 shows how the new model predicts the 2nd stage permeate flow during the test. In this plot the flow correction ratio is neglected to show that the model needs correction between different permeate flows. It is evident that the model fails to predict separate permeate flows during the test. This is likely due to that the flow through the PV is higher in this test compared to what the flow the model is fitted against originally, 385 m³/h. In addition, the degree of fouling in the 1st stage membranes can also affect the result. The latter must be tested by altering the seawater temperature while keeping the permeate flow constant.

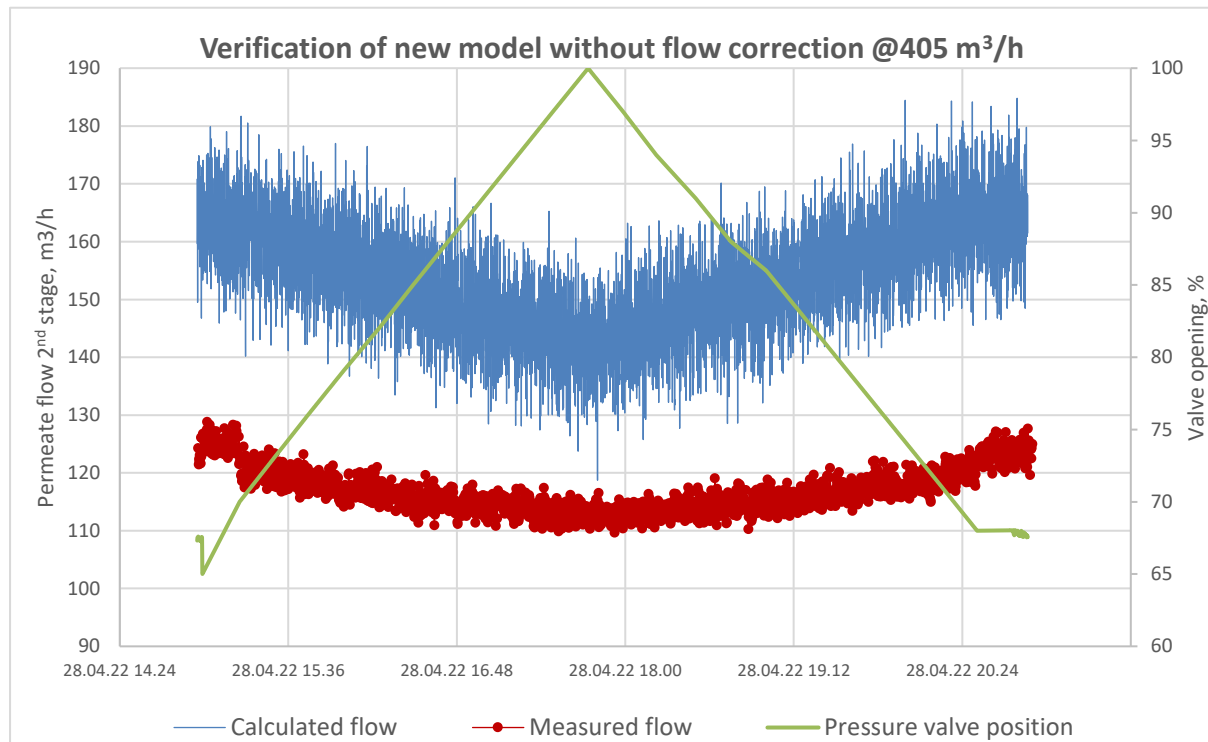


Figure 5.26: Verification of the new model (with no flow correction from 385 m³/h flow) on SRU B during 405 m³/h production mode by comparing model estimation against measured flow (red dots) of the 2nd stage permeate flow. The measured flow is done with a clamp-on flowmeter and flow changes induced by altering the PV opening.

To compensate for the error induced by the production level a new 2nd order polynomial regression was done for measured flow versus valve opening at the permeate production during Test 2 of 405 m³/h. This regression line was in turn used in the flow correction ratio to adjust the new model from 385 to 405 m³/h of permeate production as shown in Eqn. (5.2).

$$\frac{-0.0108u_{\%}^2 + 2.1159u_{\%} + 189.45}{-0.0007u_{\%}^2 + 0.7907u_{\%} + 193.72} \quad (5.2)$$

In this equation the denominator contains the flow to valve opening polynomial regression at 385 m³/h permeate production. Equation (5.2) is then used to correct the flow model presented in Eqn. (5.1) and Tab. (5.1) from 385 to 405 m³/h. This yields the flow estimation shown in Fig. 5.27 which fits the measured flow relatively well. This initial measurement run shows that the new flow model can be corrected in the same way that was done with the 417-mode model based on Aker BP's test as presented in Ch. 5.1.1.

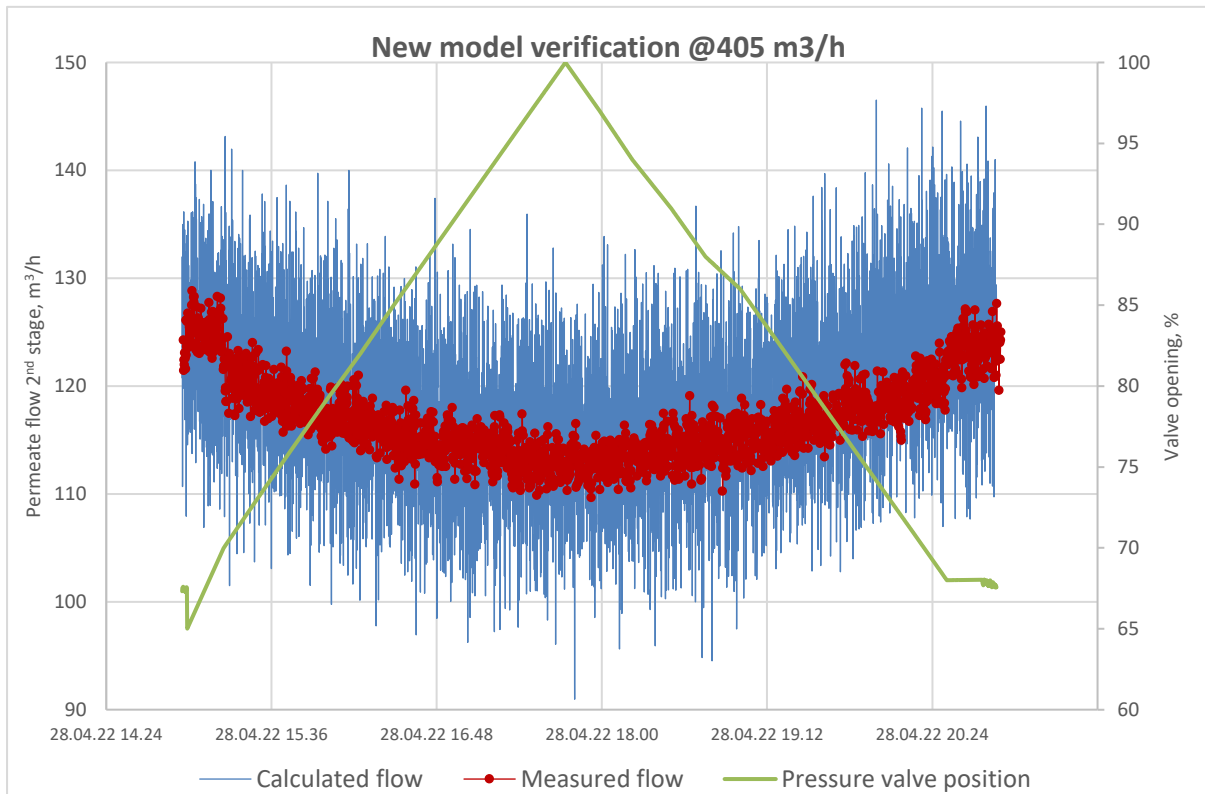


Figure 5.27: Verification of the new model on SRU B during 405 m³/h production mode by comparing model estimation against measured flow (red dots) of the 2nd stage permeate flow. The measured flow is done with a clamp-on flowmeter and flow changes induced by altering the PV opening.

There are still errors in the calculated flow relative to the clamp-on measurement, but it seems to be induced to a large extent by signal variations on the inputs to the new flow model. This is shown by comparing the error curves in Fig. 5.28 where the calculated error with and without signal smoothing (10 minutes moving averages) is presented. The signal smoothing is done to the model inputs that fluctuates. That is, the measured pressures on both sides of the PV (used to calculate Δp) and the total permeate production used in the mass balance. The valve position does not need any signal smoothing during the test as the valve is in manual mode. During auto mode it fluctuates somewhat but not to the extent of the other inputs mentioned above. There is also a degree of accuracy on the clamp-on flowmeter that should be assessed. This is not done in this project, but it should be assessed during fine-tuning of the model if it proves applicable.

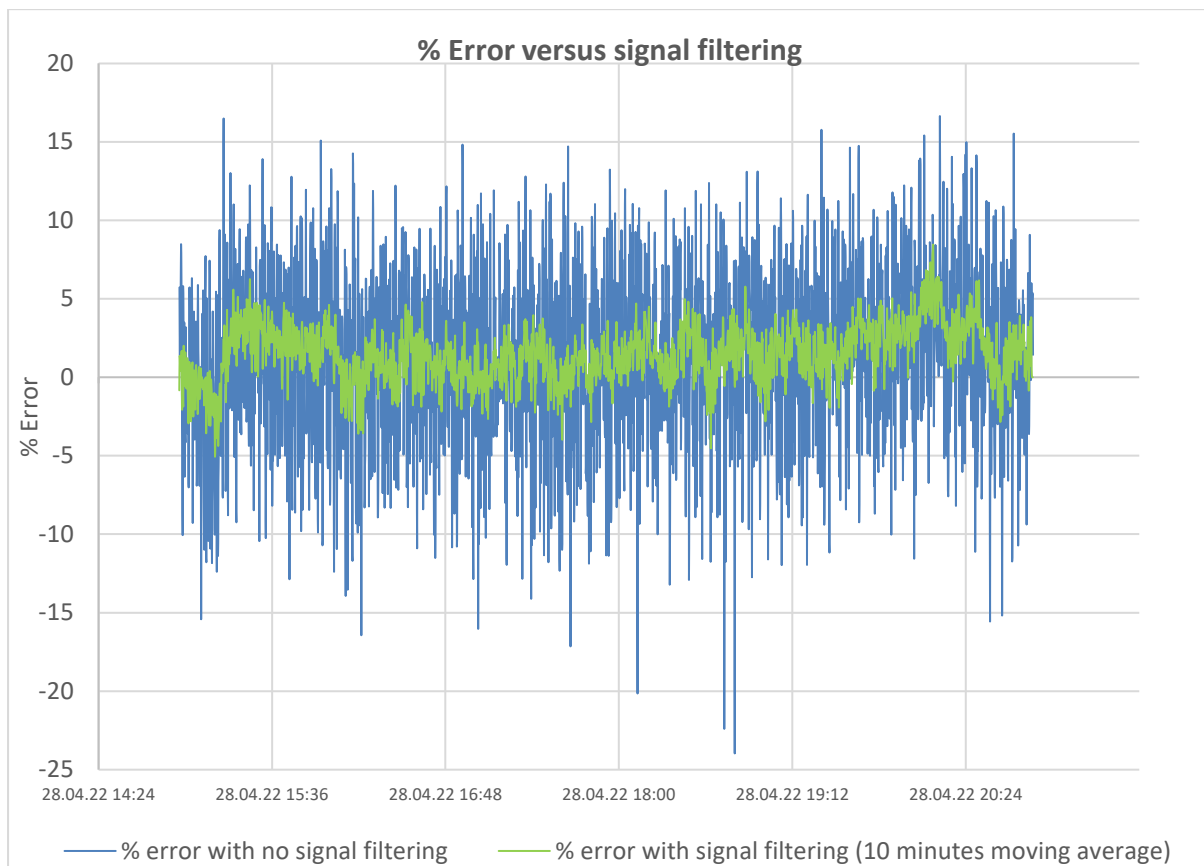


Figure 5.28: Percentage error between flow calculation and measurements done with the clamp-on flowmeter. The blue curve shows the errors when no signal filtering is applied. The orange line presents the error when the input parameters from the control system is smoothed with a 10-minutes moving average.

Due to time constraints and no heat available to increase the seawater temperature to the SRUs no further measurement runs at other permeate temperatures and flows was carried out during this project. In a discussion with the Aker BP supervisor it was agreed that new measurements are to be done after 23rd of May when the ability to change the seawater temperature is back. This data will be used to evaluate if the model can deal with different degrees of fouling.

An effort to assess the question regarding if the model can handle different degrees of membrane fouling is done in Fig. 5.29. The flow correction regression lines of the three clamp-on measurements are plotted for a comparison in this figure. These are based on Aker BP's measurements during 385 and 417 m³/h, and the measurement done at 405 m³/h during Test 2. The idea with this comparison is to see if the regression line defined at 405 m³/h is placed between the regression lines at 385 and 417 m³/h. If so, this can indicate that the flow correction is in fact only a flow correction and that the variations in membrane fouling is dealt with by the valve equation- and/or flow orifice correction terms in the new flow model, Eqn. (5.1).

Based on the plot in Fig. 5.29 the constant term for the 405-mode line places itself between the other two. It is closer to the 385-mode which is somewhat suspect. It is evident that the 405-mode line does not stay between these lines with increasing % valve opening. Another interesting feature is that the 405- and 417-mode lines seems to correlate nicely while the 385-mode line does not. The dotted curve denoted $f_{expected-385}$ shows an approximation on how the 385-mode line should be relative to the other two. This plot indicates that the flow

correction regression lines, if all are correct, might be affected by the degree of fouling. Another explanation might be that the 385-mode regression line is wrong as it is based on only 6 measured values compared to 9 and 2000+ datapoints for the 417 and 405 modes, respectively.

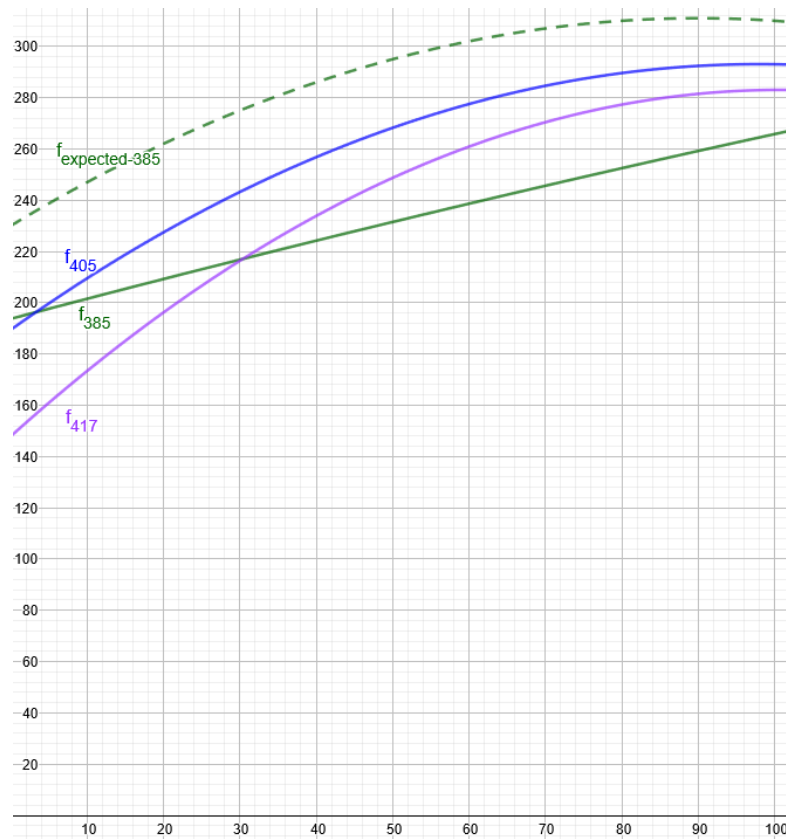


Figure 5.29: Comparison of the 2nd order polynomial regression curves of clamp-on measurements to the PV position. The y-axis is flow in m³/h while the x-axis is in % valve opening. The function subscripts in the plot indicate the flow modes, e.g. f_{385} is the regression line defined with measurements at 385 m³/h permeate production from the SRU. The polynomial expressions in this plot are presented in Tab. 5.1 and Eqn. 5.2.

Test 2 -Summary

Test 2 is not finished and for that reason no conclusion can be drawn. The test shows that the new flow model can be corrected in the same way that was done with the 417-mode model as done in Ch. 5.1.1. The data from Test 2 in combination with data from Aker BP's measurements indicates that the new model will fail to estimate stage permeate flows upon changed membrane fouling. This should be checked by altering temperatures while keeping constant permeate production in the SRU. If the model turns out to be able to deal with fouling it is still a demanding task to make it functional in the control system. That is since the new model needs to be corrected for each permeate production level that the system can/will be operated at. Due to that the SRUs can be operated in free flow mode it becomes a significant task to define flow correction ratios and to structure the control system to schedule these as function of actual permeate production. For that reason this model is not recommended as is even if it is proven valid. Instead it should be investigated further with more data which might lead to simpler expressions or a logic relation between permeate production and model correction.

5.2.3 Test 3 – Recovery and backpressure adjustments

This test was kept relatively short due to not having control over the actual stage recoveries in the SRUs. The overview of Test 3 is shown in Fig. 5.30 with seawater temperature, PV position and Δp across it is presented in the upper lane. The middle lane shows the feed-to-permeate pressure drop of both stages, while the lower lane shows the 2nd stage concentrate and permeate production. The middle lane showing membrane pressure differences is scaled to show small variations in pressure differences across the membranes. The red circles with black rulers indicate start and stop of the test. The other rulers show some arbitrary data values before and after the test in addition to values after each of the changes during the test.

Based on this plot it is evident that the seawater temperature was relatively stable during the test. Thus, the changes to the feed-to-concentrate pressure difference should be induced by the changes in permeate backpressure on the 1st stage through the PV adjustments. The permeate and concentrate flows in the lower lane shows that the total recovery remains constant and is unaffected by the PV alterations during the recovery shifting between the stages. The permeate production during the test was approximately 360 m³/h.

It should be mentioned that one day prior to this test, when the backpressure was reduced, SRU B was started up after 24 hours downtime. Based on the plot presented in the overview, Fig. 5.30, it seems that the system is in steady state prior to initiation of Test 3. That is as feed-to-concentrate pressure differences, permeate production and concentrate flow are stable.

Initially the pressure difference across the PV is reduced from 6 to about 3.2 barg, which was based on the findings from Fig. 5.4. This backpressure reduction lowered both 1st and 2nd stage feed-to-concentrate pressure differences. After 38 hours the new flow model in Eqn. 5.1 was applied to estimate the 1st stage recovery which was calculated to ~ 53.5 %. It should be mentioned that this model is not validated neither is it flow adjusted to the permeate production present during this test. Based on this seemingly high 1st stage recovery the pressure difference across the PV was elevated to 5 barg where the new model estimated a recovery of ~50.7 % in the 1st stage. The system was operated at this setting for about one day before the test was ended.

To evaluate the system behavior to recovery shifting and backpressure changes the slopes of the feed-to-concentrate pressure difference curves in both stages are assessed in Fig. 5.31 and 5.32. These slopes, or time derivative estimates, are of interest as they can indicate changes in membrane fouling. The slopes are defined by use of linear regression on the different data sections during the test. That is, the pressure difference before test start, during the test and every change within it, and after the test. The basis data used for each regression analysis is highlighted with the same color as the regression line it produces. The regression line equations are also presented for each line to show the exact estimated slopes. It has been a focus to select regression analysis data that are stable after changes and without spikes/variations that are assumed random (cannot be tied to other parameters). Between the 1st and 2nd stage analysis all time equivalent regression lines are defined with exactly the same time intervals.

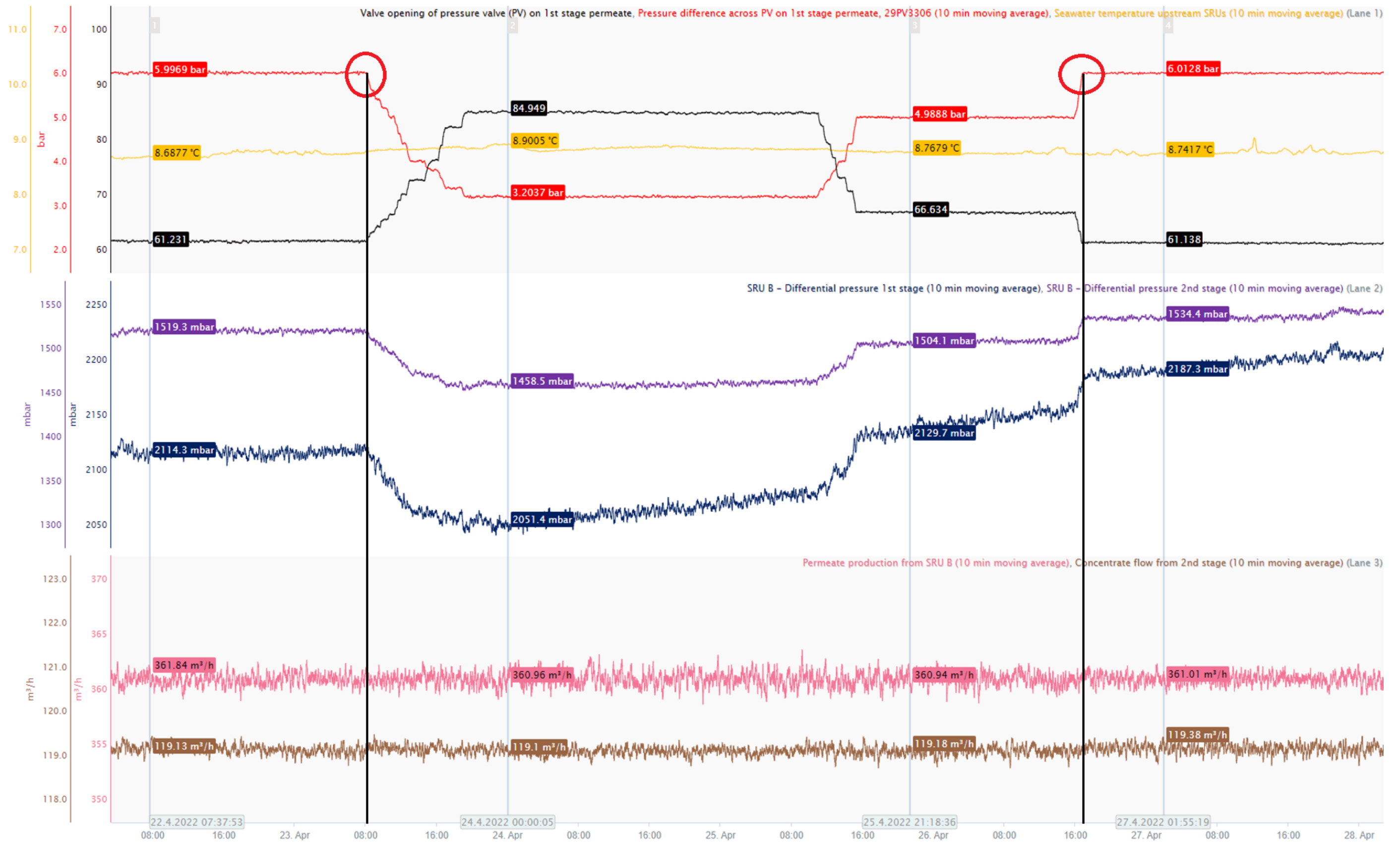


Figure 5.30: Feed-to-concentrate pressure difference (middle lane) during adjustments of the differential pressure across the PV on the 1st stage permeate (upper lane). Seawater temperature introduced to the SRUs are shown and the valve opening of the PV in also shown in the upper lane. The lower lane shows the permeate production- and concentrate flow from the 2nd stage of SRU B during the test. The red circles and black rulers indicate start and stop of the test.

1st stage membrane pressure difference slopes, Fig. 5.31

The estimated feed-to-concentrate slopes for the 1st stage of SRU B is shown in Fig. 5.31. This plot shows only the feed-to-concentrate pressure difference across the stage to keep the information level reasonable. However, the period of time presented is almost identical to what is shown in the overview plot given in Fig. 5.30. Thus, it should be easy to correlate the parameter changes between the two.

Initially there are two slopes defined and the reason is that the feed-to-concentrate pressure difference starts to increase 11 hours before the start of Test 2s. There are no other parameters that can be used to explain why this happens. It might be a random fluctuation or maybe the system reaching a steady state after the start-up of the SRU. Either way, two slopes are defined to evaluate both cases.

Comparing all slopes for the 1st stage in Fig. 5.31 reveals that the slope is at its steepest in the period after that the backpressure is increased during the test. This was unexpected as it should be at its highest when the recovery is at its highest, which is when the backpressure is at its lowest. In other words, the yellow slope should have been steeper than the purple. It can be that this had been the other way around if the duration of these test sections had been increased.

By comparing the initial- and end slopes (red outline/green highlight and orange highlight) it is evident that the slope is higher after the test is finished independently of which initial slope is true. If the green and orange slope had been the same line this could have been explained by normal fouling with time. As they are not it seems to indicate the rate of fouling was higher during the test. They are very close to be shifted parallel lines as the slopes are almost the same, 13.45 to 15.90. This reasoning depends on which of the initial slopes are true, green or red. Based on the pressure development pre- and post-test it seems reasonable that the green slope is the most correct of the two. Either way, the fact that the slope is steeper after the test can be explained by the increased concentration polarization in the stage during the test. If the red regression line is the true initial slope then the test shows that it was not a good idea to increase the 1st stage recovery. That is, by looking at the isolated effects on the 1st stage.

It should be mentioned that the plot given in Fig. 5.31 is scaled to show small variations in pressure differences. The absolute values of the overall changes pre- and post-test can be seen by evaluating the data on the initial and last of the grey rulers in the Fig. 5.30. The 1st stage pressure difference increases with approximately 70 mbara, and the PV position is close to identical pre and post-test. , ~61.2 versus ~61.1 %.

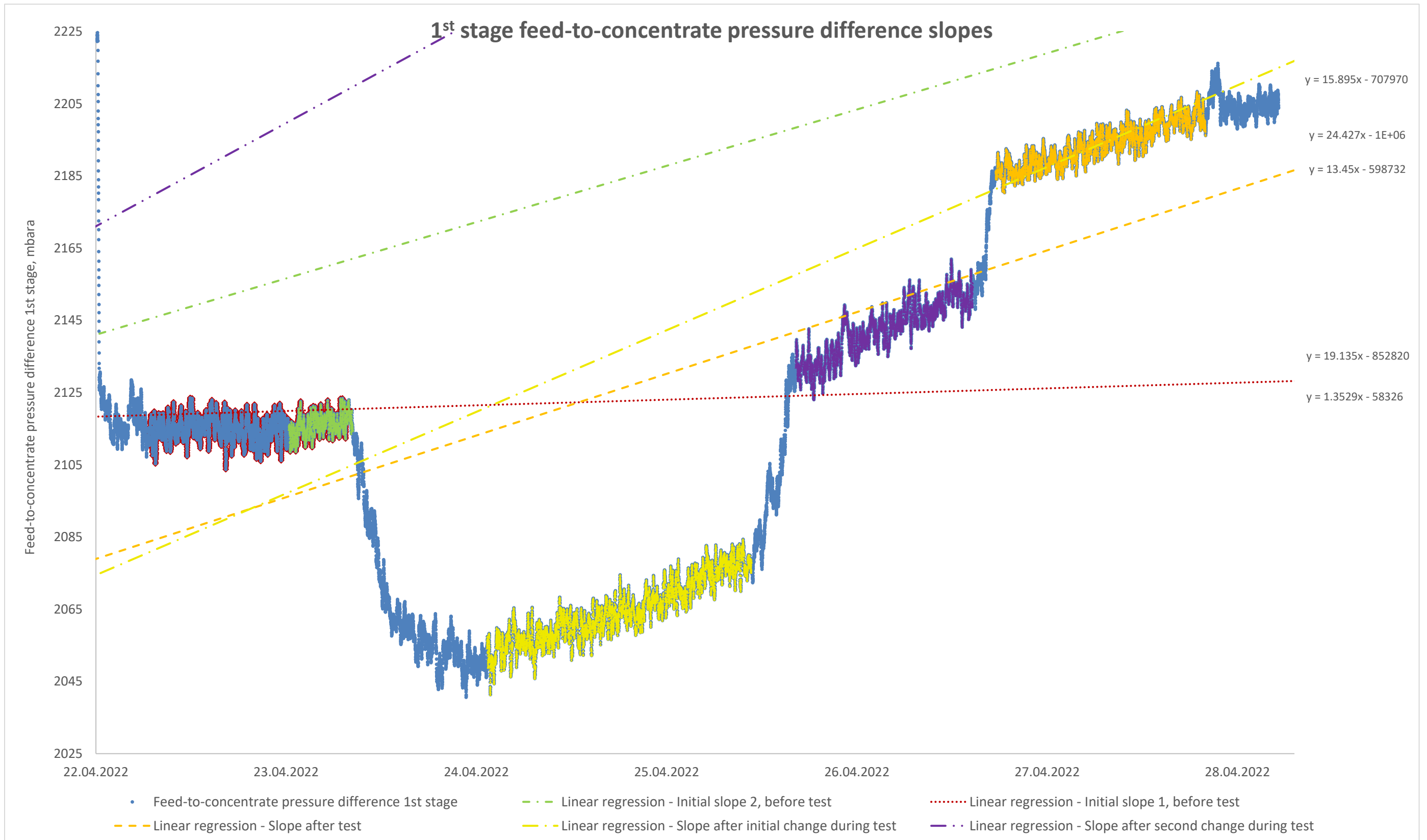


Figure 5.31: Estimating slopes of the 1st stage differential pressure (feed-to-concentrate) with linear regression to evaluate how it is affected by adjusting the 1st stage permeate backpressure (shifting recovery between the stages). Highlighted data indicates and corresponds with the basis and color of the regression lines. The initial slope is defined twice due to an increase in the feed-to-concentrate pressure difference some hours prior to test initiation.

2nd stage membrane pressure difference slopes, Fig. 5.32

The plot in Fig. 5.32 presenting the estimated feed-to-concentrate pressure difference slopes in the 2nd stage is built identically as the plot evaluating the 1st stage. And this plot shows very similar behavior as was the case for the 1st stage. That is, the slope is higher after the test, and the highest slope occurs after the second adjustment during the test. However, the slopes are in general not as steep and the relative changes between them are smaller compared to that of the 1st stage.

It is important to consider that the 2nd stage experiences the opposite of the 1st stage with respect to recovery. This means that the recovery is decreased after the initial change and increased in the second change and upon test stop. It is for that reason odd that the slope increases with decreased recovery by comparing the green and yellow slopes. While on the other hand reasonable that the slope increases when the recovery increases in the change mid-test shown by comparing the purple and yellow slopes. And again, counterintuitive that the slope decreases with increased recovery when the test is ended by resuming to the initial 1st stage permeate backpressure. The latter is shown by comparing the orange to the purple slope.

These effects are likely induced by what is happening in the 1st stage as these stages are coupled and regulated to constant total recovery. This through that the 1st stage the PV is chocking back slightly during the test and after, probably due to fouling build-up on the active membrane layer. As this PV closes the recovery shifts towards the 2nd through a slightly increasing feed flow which increases feed-to-concentrate pressure difference gradually.

It is not possible to see this PV valve chocking in Fig. 5.30 without scaling the y-axis to a very narrow range. It can be shown that the PV closes from ~84.95 % (shown in ruler two from the left) to ~84.73 % before the PV Δp is altered mid-test. This is a marginal change but so is it for the changes in feed-to-concentrate pressure difference that are in the order of 10^0 to 10^1 millibars for the different stages during the mid-test slopes.

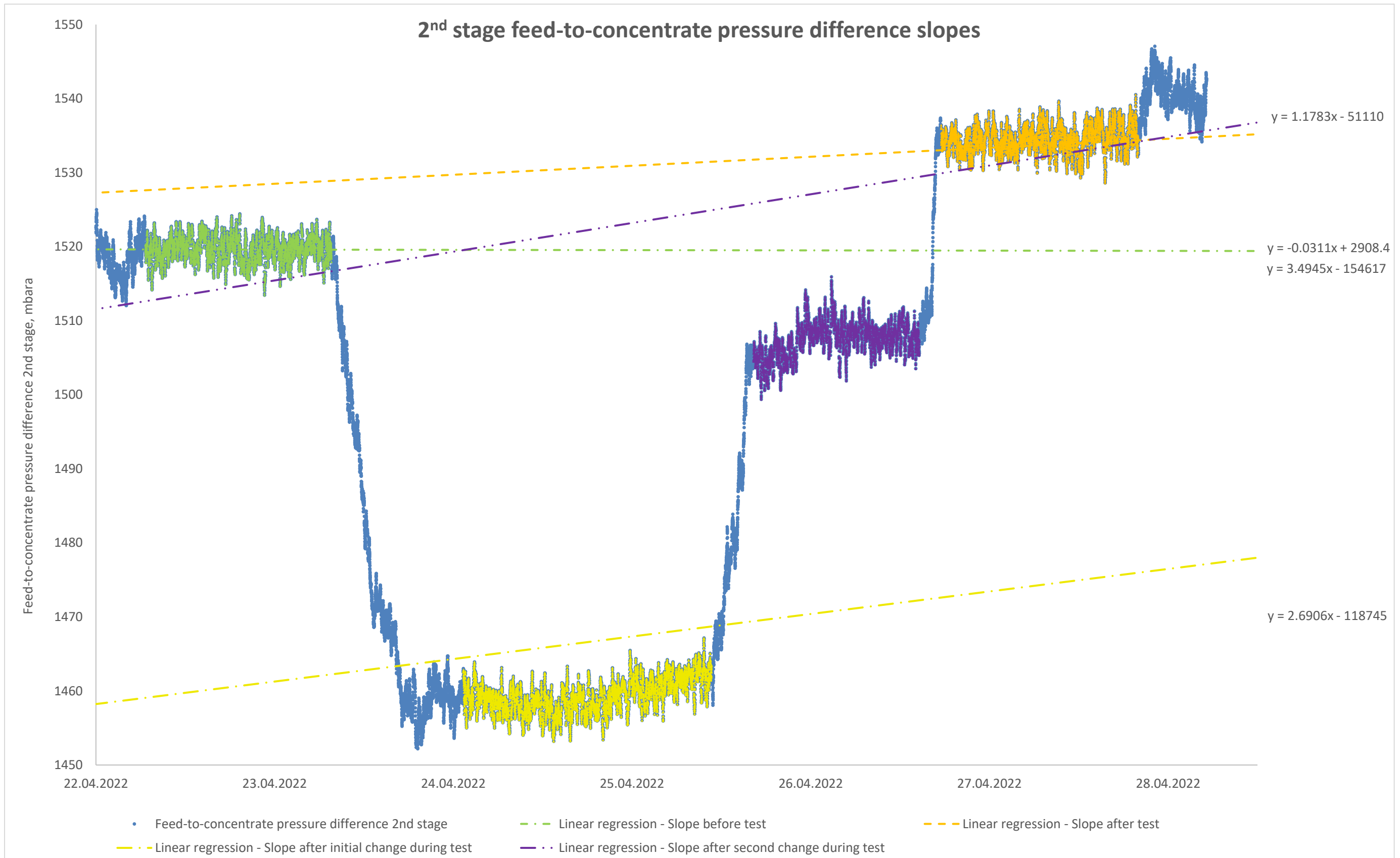


Figure 5.32: Estimating slopes of the 2nd stage differential pressure (feed-to-concentrate) with linear regression to evaluate how it is affected by adjusting the 1st stage permeate backpressure (shifting recovery between the stages). Highlighted data indicates and corresponds with the basis and color of the regression lines.

Test 3 – summary

Based on the test data it seems that the system was better off before the test. The hypothesis to why this happens is that the recovery was pushed too high initially in the 1st stage. The new model estimated it as high as 53.5 %. If this figure is correct then the concentrate flow out of the 1st stage would have been ~226 m³/h which is well within the minimum criterion to keep the concentration polarization modulus below 1.2. But since the model is not validated it is not sure that this was the actual stage recovery. Maybe the 1st stage recovery was even higher so that the modulus increased beyond 1.2. This could explain the jump in pressure differences and slopes for both stages after the test was finished.

The test seems to indicate that increasing the 1st stage recovery to a certain (unknown) extent can increase the fouling rate, which is line with the theory.

The ideal test would have been to optimize the system with full control over the stage recoveries. This cannot be done until the separate permeate flows from each stage is known. This means that it is necessary with a rigid flow model or flow measurement of one of the permeate streams in each SRU. The latter can be done with a clamp-on flowmeter. Based on this test a new recovery adjustment should not be done before this is in place. Knowing the separate stage recoveries means also knowing all system flows. This knowledge gives good control of any tests on altering stage recoveries as it can be restricted to operate within the recommended minimum concentrate flows out of each stage. Thus, the system can be optimized with respect to recovery split over a much longer period of time than what was the case for Test 3.

The other parameters that should be affected by this test are not evaluated. The sulfate rejection cannot be controlled since the online sensor was not functioning during the test. The test was too short to be checked against the weekly sulfate lab measurements. The changes in cartridge loading can probably be controlled with salt probing in the 1st stage, but this equipment is not available. And lastly, how the scale potentials changes demand manual samples of the 2nd stage concentrate in addition to a model to estimate the salt concentration in the laminar boundary layer which is somewhat complex.

6 Conclusion

This project has studied the Sulphate Removal Units (SRU) and Oxygen Deaerator at Ivar Aasen during the last five months. The project phase has been two folded with an initial plant study and literature review and a following practical test period. The theoretical study was mainly intended to build detailed understanding of the systems to be able to theoretically evaluate- and potentially optimize the plant performance. The practical part of this project suffered from too little time for proper testing, mainly caused by an unforeseen main power loss to Ivar Aasen. For that reason the performed tests need to be reassumed and some additional tests are suggested for further work.

The theoretical study showed that it would not be possible to establish a good theoretical performance model for the SRUs. The reason was lack of public information regarding the membranes used in the SRUs. As a compromise an overview on the theoretically expected SRU system response upon parameter changes was constructed. For the deaerator on the other hand, a theoretical performance model for mechanical deaeration was derived. The model is a combination of Henry's law, the Henry-Setchenov model, and process calculations done by the system manufacturer (Eta Process Plant). This model, relative to the model made by the manufacturer, shows a different dependence of the seawater temperature for the mechanical deaeration. The specific plant study yielded some interesting findings regarding operational issues at Ivar Aasen. It was found that the SRUs operate with a total recovery that exceeds the manufacturers recommendation of 55-60 %. Reducing total recovery could potentially reduce the chemical membrane wash frequency due to decreasing the concentration polarization in the SRUs. This was not tested during this project due to plant issues. For the deaerator the historical performance assessment indicates that the ejector is underperforming.

The practical phase of the project gave no explicit findings of that the plant has been operated poorly historically. However, there are signs of optimization potential that likely can be achieved through minor changes of parameters or way of operation. The practical phase strengthened the indications that the vacuum ejector is causing the deaerator to underperform

Increasing the seawater temperature indicates promising results with respect to the SRUs, but it failed to conclude if the biofouling increased to a noticeable extent. The vacuum deaerator did not respond significantly to the increased temperature, but it gave strong indications of that the mechanical deaeration is not according to the design guarantee. Validation of the theoretical deaeration model was inconclusive but it seems to be the best estimate on deaerator temperature dependence compared to the manufacturer's performance model. To be able to validate the theoretical deaeration model it is necessary to know the contribution of the chemical deaeration of oxygen. To do so it is either necessary to operate the deaerator with no chemical deaeration or to model the chemical deaeration as function of temperature and dosage rate of oxygen scavenger. This test is not finished due to the power loss.

The permeate flow model (new model) validation planned proved possible to correct the new model to a new permeate production level such as done to correct the new model during evaluation/derivation of it. The data retrieved from the test indicates that the model will fail to compensate for different degrees of fouling. This should be tested by altering the seawater temperature as initially planned. Changing the seawater temperature is believed to simulate

fouling through viscosity and pressure drop alterations. This work will continue after the project period.

Testing the SRU system behavior to recovery shifting and changes to the backpressure showed that recovery shifting should be done with care when not having full control stage recoveries. The test indicates that increasing the 1st stage recovery to a certain level can increase the rate of fouling and pressure buildup in the entire system. At which point of stage recovery this occurs is not concluded. It should be performed a proper recovery balancing to optimize the SRU when the recoveries are known. This depends on either an accurate flow model or a flowmeter is in place on one of the permeate stream stages.

6.1 Further work

The elements suggested for further work are mainly based on tests that was not conducted in the practical phase of the project in addition to performance issues found through both testing and the theoretical plant study. There is also a suggestion on replacing to a new type of membrane that shows potential.

- Consider the FilmTec™ Fortilife™ SR90i membranes upon the next replacement of membranes in one or both SRUs. This membrane should be more resistant to biofouling due to an improved feed spacer which also reduces the feed-to-concentrate pressure drop relative to the SR90-440i. This recommendation is not explicitly elaborated in the thesis, but is based on:
 - Literature findings suggesting biofouling to dominate fouling for sulfate removal systems.
 - Avista autopsy of Ivar Aasen membranes indicating that bio growth is the dominating type of fouling.
 - Dialogue with both NOV and DuPont, recommending the Fortilife membrane.
 - The Fortilife series should fit both the mechanical setup and the operational process conditions of the SRUs at Ivar Aasen.

Based on this it is recommended to get membrane projections on this Fortilife series for the SRUs at Ivar Aasen and to initiate a MOC if the projections show promise.

- Consider installing a permanent flow transmitter to gain control over the separate stage recoveries if it proves not possible to accurately model the separate permeate flows from each stage of the SRUs.
- Due to indications of underperformance for the vacuum ejector it should be dismantled, and its internals investigated. If there is no sign of malfunction or fouling consider performing a capacity study to assess if its dimensioning is sufficient.

The following suggestions are valid for the membranes in use today, the SR90-440i. They need to be reconsidered if it is decided to replace the SR90-440i with the FilmTec™ Fortilife™ SR90i as suggested above:

- Consider reducing the total system recovery to 60 % in one of the SRUs for a couple of months. This is according to the recommendations from DuPont and should decrease CIP frequency through operation at lower concentration polarization in the system. The downsides of this are reduced system capacity and increased the specific power consume (power per permeate volume).
- Consider testing volume flux pulsing through a sinusoidal function on the 1st stage permeate pressure difference controller on one of the SRUs. This could improve the CIP wash frequency. A proposed test scheme is appended in Appendix J.
- Consider acquiring salt probing equipment for the SRUs. This can be a good troubleshooting tool which makes it possible to find local system issues like a defect membrane cartridge. In addition it can be used to optimize the backpressure profile in the initial stages by assessing the conductivity profiles.

References

- [1] Aker BP, *Vår virksomhet*, 2022. Available: <https://akerbp.com/var-virksomhet/#vare-felt>. Accessed: 11.01.2022
- [2] Aker BP, *Hvem er vi*, 2022. Available: <https://akerbp.com/om-oss/#hvem-vi-er>. Accessed: 11.01.2022
- [3] Aker BP, *Ivar Aasen*, 2022. Available: <https://akerbp.com/asset/ivar-aasen/>. Accessed: 11.01.2022.
- [4] A. K. Fard, G. Mckay, R. Chamoun, T. Rhadfi, H. Preud'Homme and M.A. Atieh, "Barium removal from synthetic natural and produced water using MXene as two dimensional (2-D) nanosheet adsorbent," *Chemical Engineering Journal*, vol. 317, no.1, pp. 331-342, Jun. 2017. [Online]. Available: doi: <https://doi.org/10.1016/j.cej.2017.02.090>
- [5] R. J. Johnson, B. D. Folwell, A. Wirekoh, M. Frenzel and T. L. Skovhus, "Reservoir Souring – Latest developments for application and mitigation," *Journal of Biotechnology*, vol. 256, pp. 57-67, Apr. 2017. [Online]. Available: doi: <https://doi.org/10.1016/j.jbiotec.2017.04.003>
- [6] PetroWiki, *Surface water treatment for injection*, 2018. Available: https://petrowiki.spe.org/Surface_water_treatment_for_injection. Accessed: 12.01.2022
- [7] *FilmTec™ Reverse Osmosis Membranes Technical Manual*, 9th ver., DuPont, Wilmington, DE, USA, 2021. [Online]. Available: <https://www.dupont.com/content/dam/dupont/amer/us/en/water-solutions/public/documents/en/45-D01504-en.pdf>. Accessed: 18.01.2022.
- [8] H. B. Shukor, Lecture, Topic: "Membrane Separation Process", ERT 313, Bioprocess Engineering, Universiti Malaysia Perlis, Malaysia, 2010. [Online]. Available: <https://cupdf.com/document/ert-313-bioseparation-engineering-membrane-separation-process-by-mrs.html>. Accessed on: 28.01.2022
- [9] H. Takabatake, M. Taniguchi and M. Kurihara, «Advanced Technologies for Stabilization and High Performance of Seawater RO Membrane Desalination Plants," *MDPI*, vol. 11, no. 2, p. 138, Feb. 2021. [Online]. Available: doi: <https://doi.org/10.3390/membranes11020138>
- [10] Koch-Glitsch, *PLASTIC Packing and Column Internals*, 2019. Available: <https://koch-glitsch.com/technical-documents/brochures/plastic-packing-and-column-internals>. Accessed: 09.03.2022
- [11] Made-in-China, *Pipe Liquid Distributor*, 2016. Available: <https://www.made-in-china.com/showroom/max4230781/product-detailQMVJUeMpoNpn/China-Pipe-Liquid-Distributor.html>. Accessed: 09.03.2022
- [12] Koch-Glitsch, *Deaeration for water injection*, 2021. Available: <https://koch-glitsch.com/technical-documents/brochures/deaeration-water-injection>. Accessed: 10.03.2022
- [13] Busch, *Installation and Operating Instructions*, NA. Available: https://www.buschvacuum.com/documents/10180/404813/Busch_Instruction_Manual_D

[olphin LA 0053-1111 A LB 0063-1011 A en 0870150638.pdf](#). Accessed: 11.03.2022

- [14] L. Boumaraf, A Lallemand and P. Haberschill, *Ejectors and Their Usefulness in the Energy Savings*, New York: Nova Science Publishers, Incorporated, 2010. [Online]. Available: <https://ebookcentral-proquest-com.ezproxy1.usn.no/lib/ucsn-ebooks/detail.action?docID=3018862>
- [15] R. Smith, *Chemical Process – Design and Integration*, 2nd ed. Chichester: Wiley, 2016.
- [16] H. Dach, “Comparison of nanofiltration and reverse osmosis processes for a selective desalination of brackish water feeds” Doctoral thesis, Engineering Science - Physics, Université d’Angers, Angers, 2008. [Online]. Available: <https://tel.archives-ouvertes.fr/tel-00433513>
- [17] Membrane Specialists, *Membrane Solutions*, 2022. Available: <https://membranespecialists.com/membrane-solutions/>. Accessed on: 26.01.2022.
- [18] “Terminology for Membranes and Membrane Processes (IUPAC Recommendation 1996),” *Journal of Membrane Science*, vol. 120, no. 2, pp. 149–159, 1996. [Online]. Available: doi: [https://doi.org/10.1016/0376-7388\(96\)82861-4](https://doi.org/10.1016/0376-7388(96)82861-4)
- [19] R. W. Baker, *Membrane Technology and Applications*, 3rd ed. Chichester: Wiley, 2012. [Online]. Available: <https://ebookcentral-proquest-com.ezproxy1.usn.no/lib/ucsn-ebooks/detail.action?docID=977928>
- [20] T. Uragami, *Science and Technology of Separation Membranes*, 1.st ed. Chichester: Wiley, 2017. [Online]. Available: <https://ebookcentral-proquest-com.ezproxy1.usn.no/lib/ucsn-ebooks/detail.action?docID=4816161#>
- [21] R. Wang and S. Lin, “Pore model for nanofiltration: History, theoretical framework, key predictions, limitations, and prospects,” *Journal of Membrane Science*, vol. 620, pp. 1-20, Oct. 2020. [Online]. Available: doi: <https://doi.org/10.1016/j.memsci.2020.118809>
- [22] A. Yaroshchuk, X. Martínez-Lladó, L. Llenas, M. Rovira and J. Pablo, “Solution-diffusion-film model for the description of pressure-driven trans-membrane transfer of electrolyte mixtures: One dominant salt and trace ions,” *Journal of Membrane Science*, vol. 368, no. 1-2, pp. 192-201, Nov. 2010. [Online]. Available: doi: <https://doi.org/10.1016/j.memsci.2010.11.037>
- [23] S. Bason, O. Kedem and V. Freger, “Determination of concentration-dependent transport coefficients in nanofiltration: Experimental evaluation of coefficients,” *Journal of Membrane Science*, vol. 326, no. 1, pp. 197-204, Oct. 2008. [Online]. Available: doi: <https://doi.org/10.1016/j.memsci.2008.09.054>
- [24] S. Bason, Y. Kaufman and V. Freger, “Analysis of Ion Transport in Nanofiltration Using Phenomenological Coefficients and Structural Characteristics,” *The Journal of Physical Chemistry*, vol. 114, no. 10, pp. 3510-3517, Jan. 2010. [Online]. Available: doi: <https://doi.org/10.1021/jp911615n>
- [25] A. Yaroshchuk, M. L. Bruening and E. E. L. Bernal, “A Solution-Diffusion–Electro-Migration model and its uses for analysis of nanofiltration, pressure-retarded osmosis and forward osmosis in multi-ionic solutions,” *Journal of Membrane Science*, vol. 447, pp. 463-476 Jul. 2013. [Online]. Available: doi: <http://dx.doi.org/10.1016/j.memsci.2013.07.047>

- [26] P. Atkins and J. Paula, *Atkins' Physical Chemistry*, 10th ed. Oxford: Oxford University Press, 2014.
- [27] M. Helbæk and S. Kjelstrup, *Fysikalsk kjemi*, 2nd ed. Bergen: Fagbokforlaget, 2009.
- [28] S. C. Moldoveanu and V. David, *Selection of the HPLC Method in Chemical Analysis*, 1st ed. Amsterdam: Elsevier, 2016. [Online]. Available: <https://ebookcentral-proquest-com.ezproxy2.usn.no/lib/ucsn-ebooks/detail.action?docID=4731681>
- [29] YouTube – Physical Chemistry, *Partial Molar Volume*, 2020. Available: <https://www.youtube.com/watch?v=IRvi3AHTHE8>. Accessed: 09.02.2020
- [30] Engineering ToolBox, *Water - Density, Specific Weight and Thermal Expansion Coefficients*, 2003. Available: https://www.engineeringtoolbox.com/water-density-specific-weight-d_595.html. Accessed: 09.02.2022
- [31] A. Poisson and J. Chanu, “Partial Molal Volumes of Some Major Ions in Seawater,” *Limnology and Oceanography*, vol. 21, no. 6, pp. 853-861, Nov. 1976. [Online]. Available: <http://www.jstor.org/stable/2835050>
- [32] C. Yang, X. Xing, Z. Li and S. Zhang, “A Comprehensive Review on Water Diffusion in Polymers Focusing on the Polymer–Metal Interface Combination,” *Polymers*, vol. 12, no. 1, pp. 1-27. Jan. 2020 [Online]. Available: doi: <https://doi.org/10.3390/polym12010138>
- [33] T. Bauer, P. Lunkenheimer and A. Loidl, “Cooperativity and the Freezing of Molecular Motion at the Glass Transition,” *Physical Review Letters*, vol. 111, no. 22, pp. 225702, Nov. 2013. [Online]. Available: doi: <https://doi.org/10.1103/PhysRevLett.111.225702>
- [34] Y. Marcus, “Ionic Radii in Aqueous Solutions,” *Chemical Reviews*, vol. 88, no. 8, pp. 1475-1498, Apr. 1988. [Online]. Available: doi: <https://doi.org/10.1021/cr00090a003>
- [35] Engineering ToolBox, *Water – Dynamic (Absolute) and Kinetic Viscosity vs. Temperature and Pressure*, 2004. Available: https://www.engineeringtoolbox.com/water-dynamic-kinematic-viscosity-d_596.html. Accessed: 15.02.2022
- [36] Engineering ToolBox, *Seawater - Properties*, 2005. Available: https://www.engineeringtoolbox.com/sea-water-properties-d_840.html. Accessed: 16.02.2022
- [37] S. Ilias and R. Govind, “Potential Applications of Pulsed Flow for Minimizing Concentration Polarization in Ultrafiltration,” *Separatio Science and Technology*, vol. 25, no. 13-15, pp. 1307-1324, Oct. 2006. [Online]. Available: doi: <https://doi.org/10.1080/01496399008050393>
- [38] N. AlSawaftah, W. Abuwatfa, N. Darwish and G. Husseini, “A Comprehensive Review on Membrane Fouling: Mathematical Modelling, Prediction, Diagnosis, and Mitigation,” *Water (Basel)*, vol.13, no. 9, 2021. p. 1327, May 2021. [Online]. Available: doi: <https://doi.org/10.3390/w13091327>
- [39] J. S. Vrouwenvelder, D. A. Graf von der Schulenburg, J. C. Kruithof, M. L. Johns and M. C. M. van Loosdrecht, “Biofouling of spiral-wound nanofiltration and reverse osmosis membranes: A feed spacer problem,” *Water Research*, vol. 43, no. 3, pp. 583-594, Nov. 2008. [Online] Available: doi: <https://doi.org/10.1016/j.watres.2008.11.019>

- [40] N. M. Farhat, J. S. Vrouwenvelder, M. C. M. van Loosdrecht, S. S. Bucs and M. Staal, "Effect of water temperature on biofouling development in reverse osmosis membrane systems," *Water research*, vol. 103, pp. 149-159, Jul. 2016. [Online] Available: doi: <https://doi.org/10.1016/j.watres.2016.07.015>
- [41] J. E. Brady, *Generell kjemi – Grunnlag og prinsipper*, 2nd ed. Trondheim: Tapir Akademisk Forlag, 2008.
- [42] T. Solomon, "The Definition and Unit of Ionic Strength," *Journal of Chemical Education*, vol. 78, no. 12, pp. 1691-1692, Dec. 2001. [Online]. Available: doi: <https://doi.org/10.1021/ed078p1691>
- [43] W. M. Haynes, D. R. Lide and T. J. Bruno, Eds. *Handbook of Chemistry and Physics*. Boca Raton, USA: CRC press, 2016.
- [44] I. G. Zenkevich, "Recurrent Approximation of the Temperature Dependence of the Solubility of Inorganic Salts in Water," *Russian Journal of Physical Chemistry A*, vol. 95, no. 7, pp.1358-1371, Sept. 2020. [Online]. Available: doi: <https://doi.org/10.1134/S0036024421060315>
- [45] DuPont, "FilmTec™ Reverse Osmosis / Nanofiltration Element(s) Three-Year Limited Prorated Element Warranty," 45-D00903, 2019. [Online]. Available: <https://www.dupont.com/content/dam/dupont/amer/us/en/water-solutions/public/documents/en/45-D00903-en.pdf>. Accessed: 21.03.2022
- [46] R. Sander, W. E. Acree, A. D. Visscher, S. E. Schwartz and T. J. Wallington, "Henry's law constants (IUPAC Recommendation 2021)," *Pure and Applied Chemistry*, vol. 94, no. 1, pp. 71-85, Oct. 2022. [Online]. Available: doi: <https://doi.org/10.1515/pac-2020-0302>
- [47] Engineering ToolBox, *Oxygen – Solubility in Fresh and Sea Water vs. temperature*, 2005. Available: https://www.engineeringtoolbox.com/oxygen-solubility-water-d_841.html. Accessed: 22.03.2022
- [48] J. M. Prausnitz, R. N. Lichtenthaler and E. G. Azevedo, *Molecular Thermodynamics of Fluid-Phase Equilibria*, 3rd ed. Upper Saddle River, N. J.: Prentice Hall PTR, 1999.
- [49] R. Sander, "Compilation of Henry's law constants (version 4.0) for water as solvent," *Atmospheric Chemistry and Physics*, vol. 15, no. 8, pp. 4399-4981, Apr. 2015. [Online]. Available: doi: <https://doi.org/10.5194/acp-15-4399-2015>
- [50] J. O. Valderrama, R. A. Campusano and L. A. Forero, "A new generalized Henry-Setchenov equation for predicting the solubility of air gases (oxygen, nitrogen and argon) in seawater and saline solutions," *Journal of Molecular Liquids*, vol. 222, pp. 1218-1227, Jul. 2016. [Online]. Available: doi: <https://doi.org/10.1016/j.molliq.2016.07.110>
- [51] G. Saville. "Acentric factor." Thermopedia. <https://www.thermopedia.com/content/287/>. Accessed: 30.03.2022
- [52] J. M. Smith, H. C. Van Ness and M. M. Abbott, *Introduction to Chemical Engineering Thermodynamics*, 7th ed. New York: McGraw-Hill Education, 2005
- [53] V. Alexiades and J. Kosny, "Melting and Freezing," in *CRC Handbook of Thermal Engineering*, 2nd ed. Boca Raton, USA: CRC press, 2017, pp.393-416

- [54] S. B. Reddy. «Inherent vs Installed Control Valve Flow Characteristics.” Inst Tools. <https://instrumentationtools.com/inherent-versus-installed-valve-characteristics/> Accessed: 12.04.2022
- [55] Wikipedia, *Orifice plate*, 2022. Available: https://en.wikipedia.org/wiki/Orifice_plate. Accessed: 12.04.2022
- [56] S. B. Reddy. «Difference between Quick Opening, Linear & Equal Percentage Control Valve characteristics.” Inst Tools. <https://instrumentationtools.com/difference-between-quick-opening-linear-equal-percentage-control-valve-characteristics/> Accessed: 12.04.2022
- [57] DuPont, “Usage Guidelines for FilmTec™ 8” Elements,” 45-D01706, Jan. 2020. [Online]. Available: <https://www.dupont.com/content/dam/dupont/amer/us/en/water-solutions/public/documents/en/45-D01706-en.pdf>. Accessed: 13.04.2022
- [58] Flow-Teknikk, *Fluxus F/G608*, 2020. Available: <https://flow.no/produkt/flow/clamp-on-ultralyd-flowmetere/portabel/fluxus-f608/>. Accessed: 03.05.2022
- [59] Engineering ToolBox, *Water – Saturation Pressure vs. Temperature*, 2004. Available: https://www.engineeringtoolbox.com/water-vapor-saturation-pressure-d_599.html. Accessed: 11.04.2022
- [60] University of California, *Salinity measurement and unit conversion*, 2022. Available: https://ucanr.edu/sites/Salinity/Salinity_Management/Salinity_Basics/Salinity_measurement_and_unit_conversions. Accessed: 20.04.2022

Appendices

Appendix A - Task description



Faculty of Technology, Natural Sciences and Maritime Sciences, Campus Porsgrunn

FMH606 Master's Thesis

Title: Enhanced sulphate removal and deaeration package performance at Ivar Aasen

USN supervisor: Prof. Britt M. E. Moldestad

External partner: AkerBP – Ivar Aasen Asset (Halvor Igland Damslora)

Task background:

Water injection is the primary method of pressure maintenance for the Ivar Aasen reservoir. The injected water consists of produced water commingled with treated seawater from a Sulphate Removal Deaeration Package (SRDP).

The availability of the SRDP is crucial to achieve the required reservoir pressure by voided replacement. Increased performance can be achieved by optimising mass balance between SRU stages and elevated temperature of the seawater feed. Increased performance results in increased availability and reduced CIP (Clean in Place) frequency which again gives reduced chemical consumption and discharge to sea. Deaeration efficiency is important to avoid degradation of piping material and reservoir management.

Task description:

The main tasks of the project are:

1. Literature study of SRU design and which parameters affecting SRU performance
2. Evaluate SRU performance with respect to mass balance, seawater temperature, algae season, chemical treatment and CIP frequency based on available data.
3. Elaborate and test means of enhanced SRU performance (e.g. mass distribution with existing instrumentation, elevated seawater temperature).
4. Theoretical assessment of deaerator efficiency, i.e. expected dissolved O₂-content as function of pressure, flow and temperature on the incoming seawater.
5. Recommend further work for SRDP optimisation

Student category: Reserved for Espen Nilsen (online student and AkerBP employee)

Is the task suitable for online students (not present at the campus)? No

Practical arrangements:

The project requires a deep dive into SRDP design, operating procedures and control narratives. As part of the work the student will have to collaborate with control room operators, chemical specialists and onshore support functions within various disciplines.

The thesis work will be primarily performed from the student's home office, with video conference calls to the supervisor at USN and external partners when necessary.

The student has access to all the necessary data systems from home as he is a fulltime employee with the external partner. Some work and testing will be done on-site or at AkerBP's simulator in Trondheim. The project might involve some modeling and simulations.

Supervision:

As a general rule, the student is entitled to 15-20 hours of supervision. This includes necessary time for the supervisor to prepare for supervision meetings (reading material to be discussed, etc).

Signatures:

Supervisor (date and signature):

Budd Middelstad

Student (write clearly in all capitalized letters):

ESPEN NILSEN

Student (date and signature):

20.01.2022



Appendix B – Seawater analysis Ivar Aasen

Laboratorierapport

Prøvested Ivar Aasen
 Prøve­merking 50JX0001 D/S Seawater lift pumps.
 Prøve tatt 11.apr.2019 17:23:00
 Prøvetype Sjøvann
 Prøve tatt av (id): Finn Haakonsen
 Original Prøve ID: IA-28576

Prøvested. ID IVAR_AASEN
 Preservering Scalefiks 50

Resultater for prøve 2019-03291-001

Parameter	Resultat	Enhet	PKG		Usikkerhet Rel Abs
			Nedre	Øvre	
<i>Klorid i vann, titrering</i>			<i>Metode/standard: Mod. NS 4756</i>		
Klorid, Cl-	20100	mg/l	1000	300000	10%
<i>9-ion, Na,Ca,Mg,Ba,Fe,Sr,K,Cl,S</i>			<i>Metode/standard: a-v-026</i>		
Natrium, Na	11100	mg/l	100	75000	10% ±25
Kalsium, Ca	413	mg/l	5	35000	10% ±5
Magnesium, Mg	1330	mg/l	0,1	3000	10% ±0,1
Barium, Ba	0,19	mg/l	0,05	1500	10% ±0,05
Jern, Fe	<0.1	mg/l	0,1	2000	15% ±0,2
Strontium, Sr	8,05	mg/l	0,05	1600	10% ±0,1
Kalium, K	408	mg/l	10	26000	15% ±10
Bor, B	4,2	mg/l	1	180	15% ±1
Svovel, S	893	mg/l	1	1100	10% ±1
Fosfor, P	<0.6	mg/l	0,6	670	10% ±0,6
<i>Sulfat i vann, beregnet fra svovel på ICP</i>			<i>Metode/standard: ICP-OES</i>		
Sulfat fra svovel, ICP	2700	mg/l	2		
<i>Enkelt element, ICP</i>			<i>Metode/standard: I-1-32</i>		
Bly, Pb	<0.05	mg/l	0,01	20000	15% ±0,02
Sink, Zn	<0.025	mg/l	0,005	20000	30% ±0,020
<i>Bestemmelse av ione­balanse.</i>			<i>Metode/standard: -</i>		
ione­balanse (kation/anion)	-0,4	%	-5	5	
<i>Spesifikk tetthet i vann, Anton Paar</i>			<i>Metode/standard: Mod. ASTM D-4052</i>		
Spesifikk tetthet 15°C	1,027	-			0,2% ±0,002
<i>Suspendert materiale i vann, gravimetrisk</i>			<i>Metode/standard: NACE TM01-73</i>		
Suspendert materiale	<15	mg/l	15		40% ±15
<i>Alkalitet i vann, titrering til pH 4,5</i>			<i>Metode/standard: NS-EN ISO 9963-1/NS 4754</i>		
Bikarbonat, HCO ₃ ⁻	144	mg/l	5		15% ±3
<i>pH i vann</i>			<i>Metode/standard: NS 4720 (Mod.)</i>		
pH v/20°C	8,0	pH	0	14	±0,3
<i>Resistivitet i vann, 25°C</i>			<i>Metode/standard: NS-ISO 7888</i>		
Resistivitet	0,199	ohm-m			10%
Resistivitet ved temperatur	21,5	°C			
<i>TDS (Sum ioner)</i>			<i>Metode/standard: -</i>		
Total oppløst salt	36200	mg/l			
<i># TOC i vann (ALS Scandinavia)</i>			<i>Metode/standard: -</i>		
Totalt Organisk Karbon (TOC)	1,5	mg/l			

Tegn­forklaring: PKG = Praktisk kvantifiseringsgrense, kan avvike p.g.a forbehandling av prøven. # = Analysen er utført av underleverandør.

Usikkerheten er angitt med 95% konfidensintervall. Der det er oppgitt både relativ og absolutt usikkerhet gjelder det argumentet som til enhver tid representerer størst usikkerhet.

Appendix C – Boiling analysis in deaerator

To assess if boiling occurs inside the deaerator the gas phase pressures must be compared to the saturation pressure of the seawater inside the tower. The salinity of the seawater in the tower depends somewhat on the SRU performance but is approximately 2.8 %.

The plot given in Fig. C.1 shows 2nd stage gas phase pressures versus saturation pressure curves of fresh water and seawater of 3.5 % salinity. These plots indicate that there should not be any boiling inside the deaerator tower. The 1st stage will not induce boiling as it has higher gas phase pressure than the 2nd stage. The pressure curves, in Fig. C.1, for the different flow modes of seawater are derived from Eta's pressure plot shown in Fig. 2.23, while the saturation pressure curves are constructed from [36][59]. Saturation pressure of seawater with ~2.8 % salinity will be very close to that of the normal seawater saturation pressure curve.

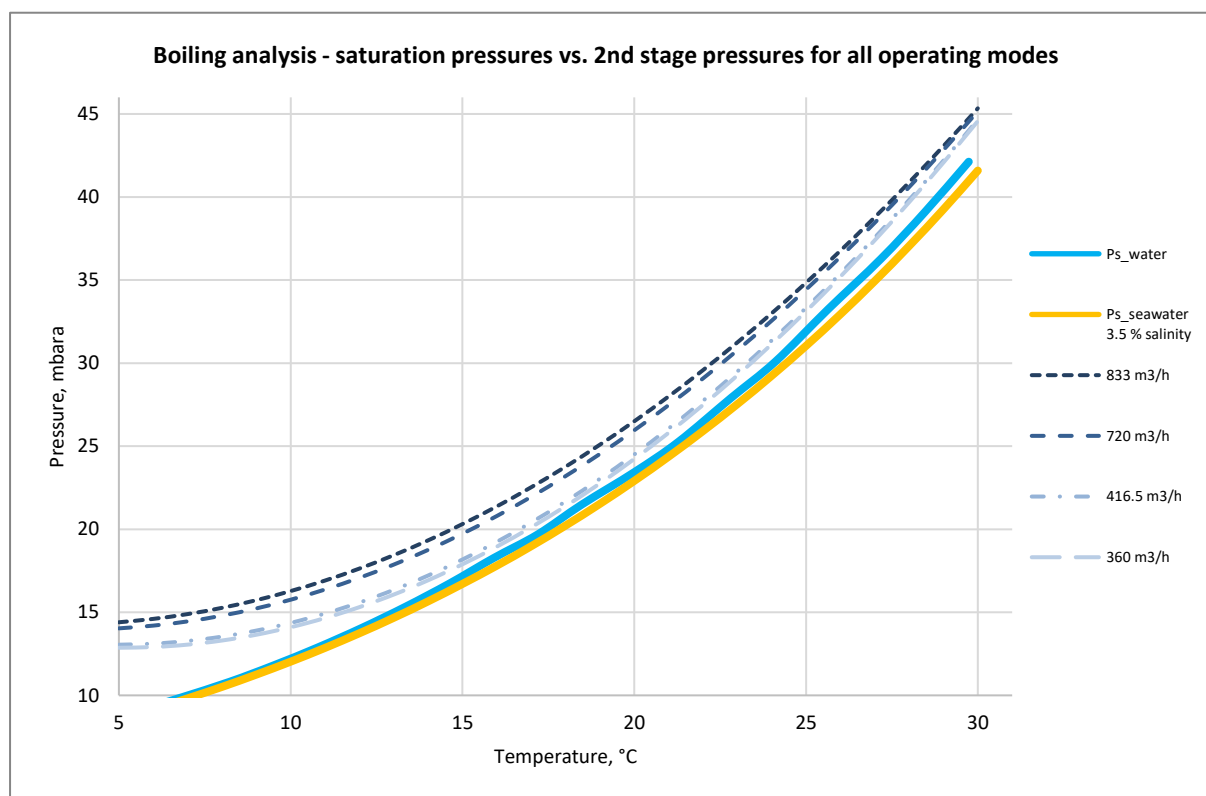


Figure C.1: Boiling analysis inside vacuum deaerator across operational temperature and flow range.

Appendix D – Vacuum pump performance vs. seal water flow to vacuum pumps

A series of seal water adjustments have been done historically at Ivar Aasen, these are presented in Fig. D.1 – D.5 in this appendix. The y axes are on auto scaling in each plot, thus do not compare the plots without considering the scales. The last figure in the series (Fig. D.6) shows a five-year time span of the same data as the other figures intended to give a comparison between the different seal water flows. That since it will even out the effect of other variables such as changes in seawater feed and temperature, and ejector flushing.

Fig. D.1 shows a series of seal water reductions from ~10 to 6.6 m³/h done the 17th of August 2018. The data visualized with the rulers shows no significant improvement after steady state is reached. The stage pressures seem to increase after this adjustment. The increasing pressure in the lower packed bed, or 2nd stage, (lane 3) between 2nd and 3rd ruler seems to be caused by a drop in seawater feed, and not by the adjustments of seal water flow. Regarding the more instantaneous response the stage pressures seems to increase and decrease upon seal water reductions. Also, there is little consistency in duration between change and response. That is since the two initial reductions give an initial reduction in vacuum performance through increased pressures. Then after some time the vacuum improves in the lower packer but worsens in the upper, without any alterations in seal water flow. The last two adjustments give no response.

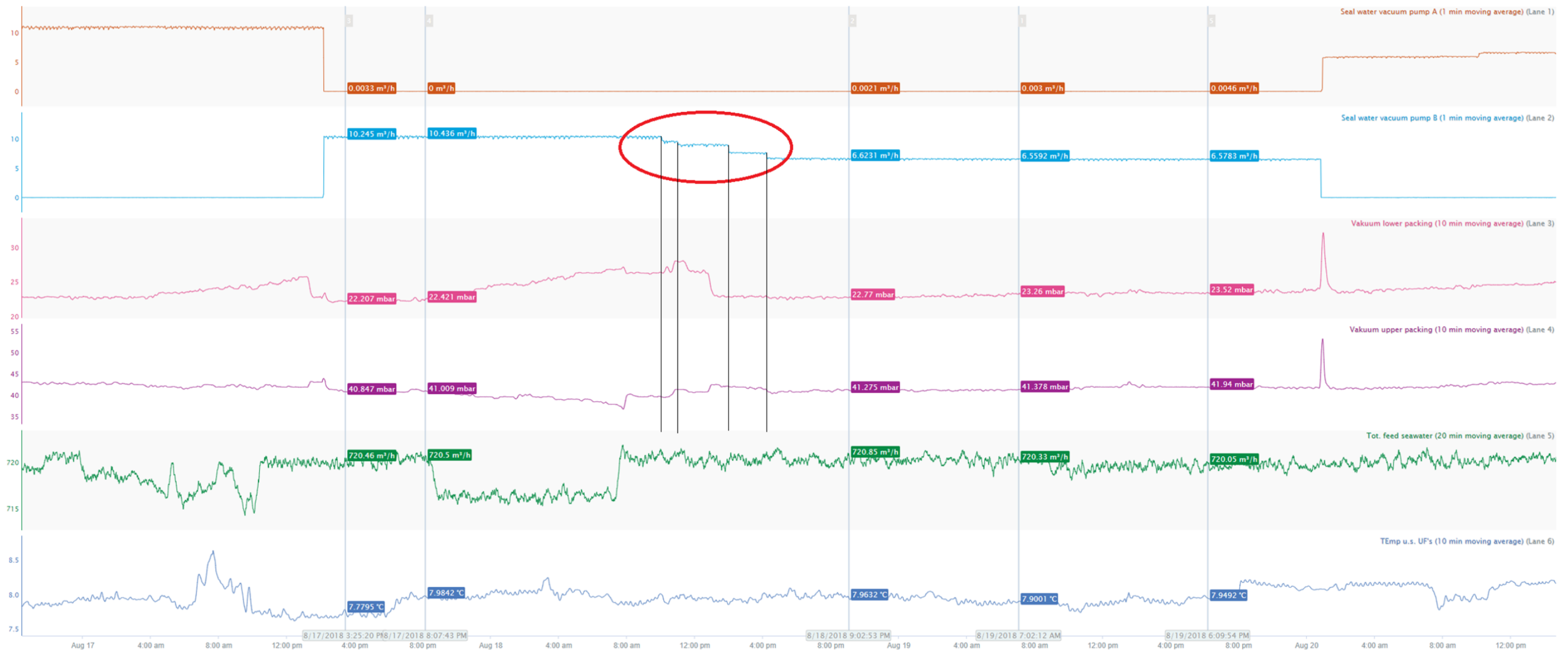


Figure D.1: Adjustment of seal water flow the 17th of August 2018 with response in packed bed pressures. From the top: The two upper lanes present seal water flows, one for each of the vacuum pumps. The middle two lanes present the parameter of interest, namely the lower- and upper packing (packed beds) respectively. While the last two lanes show seawater feed flowrate (liquid loading in deaerator) and temperature, respectively. These are included since both can affect the packed bed pressure. The seal water changes are marked with a red circle in each plot. Rulers are drawn from adjustments of seal water to better visualize instantaneous effects.

Fig. D.2 shows a reduction of seal water flow from ~ 6.5 to 4.8 m³/h done the 18th of May 2020. An instantons improvement is seen for the vacuum in the upper packed bed. The pressure in this bed drops with ~1 mbar when the seal water is reduced. However, it is evident that during the time after the alteration the upper packed bed pressure returns to its original state, and that the pressure in the lower packing increases. Thus the overall vacuum performance seems to be reduced during the sub sequent days after the alteration while seawater parameters are fairly “constant” relative to before adjusting the seal water.

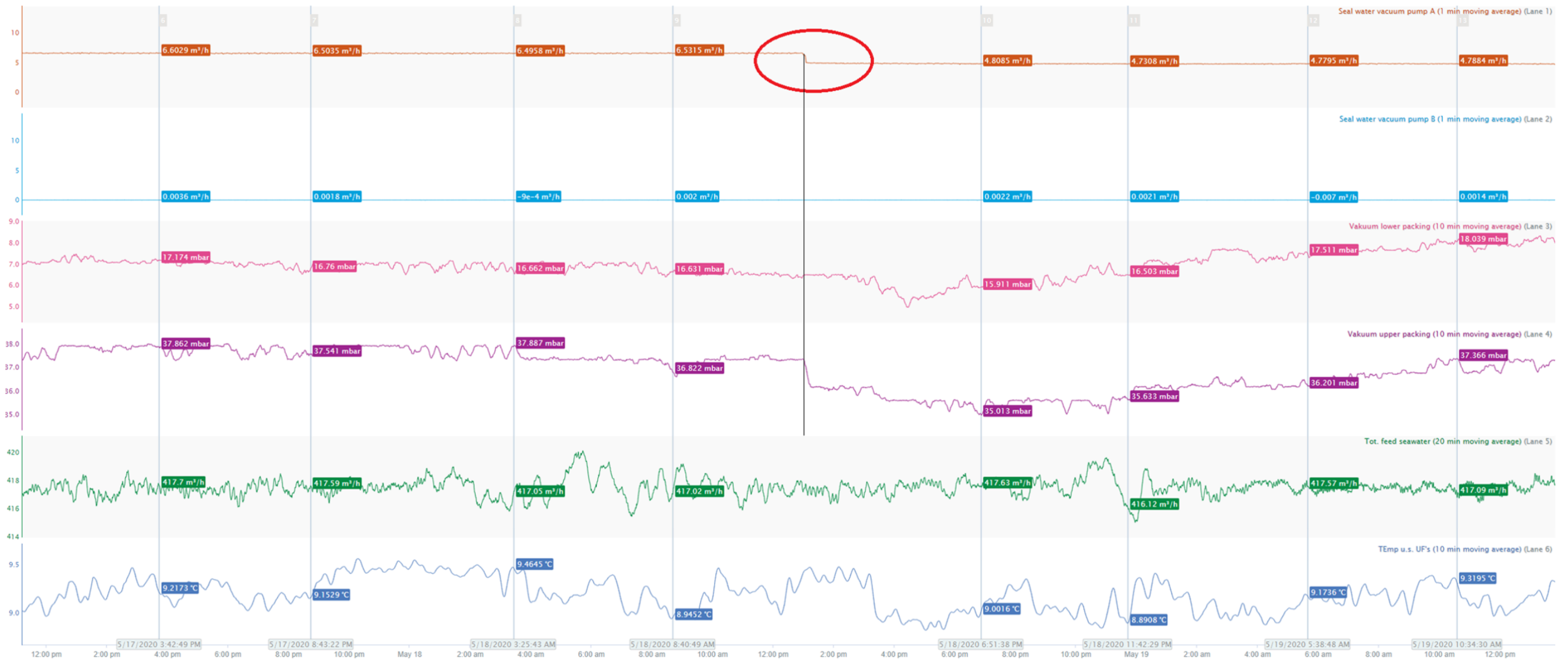


Figure D.2: Adjustment of seal water flow the 18th of May 2020 with response in packed bed pressures. From the top: The two upper lanes present seal water flows, one for each of the vacuum pumps. The middle two lanes present the parameter of interest, namely the lower- and upper packing (packed beds) respectively. While the last two lanes show seawater feed flowrate (liquid loading in deaerator) and temperature, respectively. These are included since both can affect the packed bed pressure. The seal water changes are marked with a red circle in each plot. Rulers are drawn from adjustments of seal water to better visualize instantaneous effects.

Fig. D.3 shows a series of seal water alterations inside the two red circles. From the left the first alteration is an increase of seal water flow from ~ 6.3 to 9.1 m³/h before returning to the initial flow. The second change is a gradual reduction from ~6.3 to 3.7 m³/h. Both alterations are done the 9th of August 2020.

No significant improvement after steady state is reached as the pressures in both packed beds are almost equal. There seems to be an instantaneous negative effect during seal water reductions in the right most red circle as both stage pressures increases with decreased flow. Also the increase in seal flow indicated by the two last rulers inside this red circle seems to reestablish some of the lost vacuum performance. However, it is also a negative effect in increased pressure when increasing the seal flow to 9.1 m³/h indicated in the left red circle, this is also reestablished by returning to the initial seal flow of 6.3 m³/h. A comparison of the two tests shows that the reduction in seal flow (right circle) yields a larger negative response compared to the reduction in seal flow in the left circle.

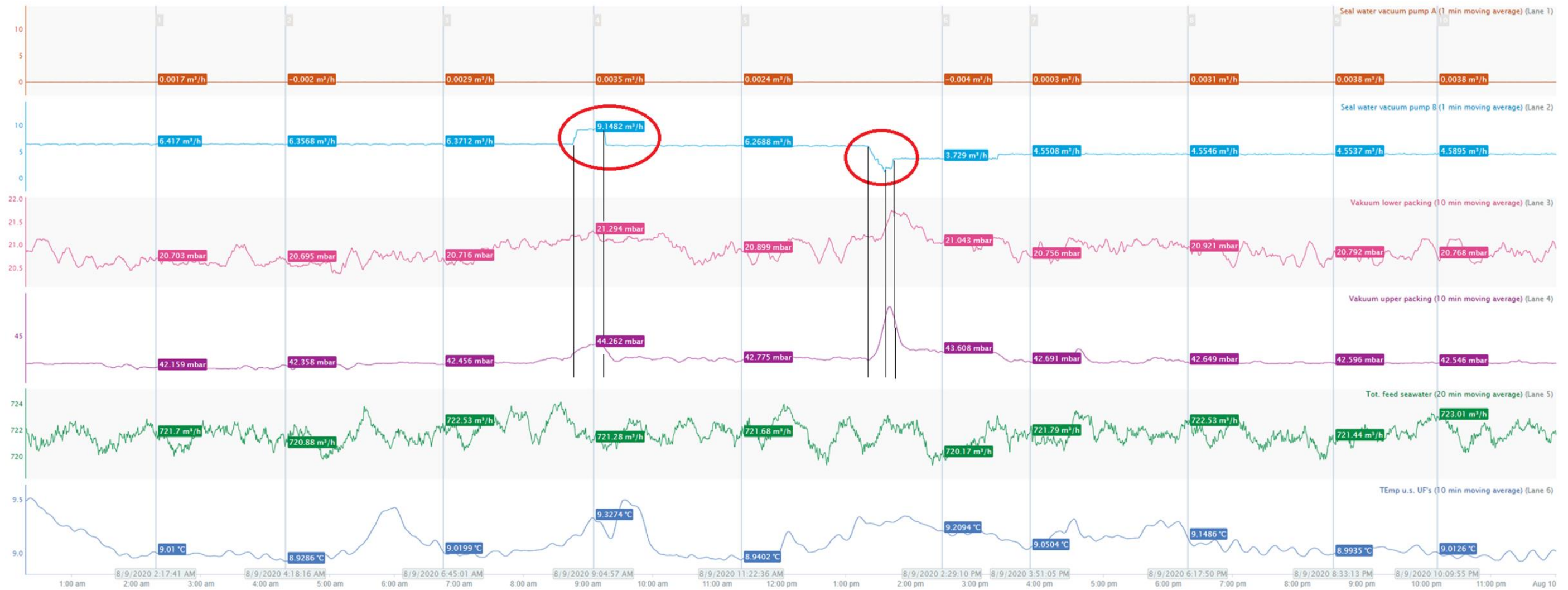


Figure D.3: Adjustments of seal water flow the 9th of August 2020 with response in packed bed pressures. From the top: The two upper lanes present seal water flows, one for each of the vacuum pumps. The middle two lanes present the parameter of interest, namely the lower- and upper packing (packed beds) respectively. While the last two lanes show seawater feed flowrate (liquid loading in deaerator) and temperature, respectively. These are included since both can affect the packed bed pressure. The seal water changes are marked with a red circle in each plot. Rulers are drawn from adjustments of seal water to better visualize instantaneous effects.

Fig. D.4 shows an increase of seal water flow from ~ 3.6 to 6.6 m³/h done the 11th of September 2020. An instantons small improvement is seen for the vacuum in the upper packed bed as its pressure falls with ~1 mbara (higher vacuum). However, as the vacuum increases slightly before the seal water adjustment some of this is probably due to the drop in seawater flow and/or temperature occurring at the same time. But still, there is a more distinct change in the upper packing here relative to the other fluctuations with the seawater before and after the alteration. Thus, an indication on improved vacuum pump performance with increased seal water flow. In a more long-term perspective the pressure in the upper bed seems relatively stable, while the lower packed bed pressure increases somewhat in pressure. The latter also occurs in the same degree prior to the adjustment.

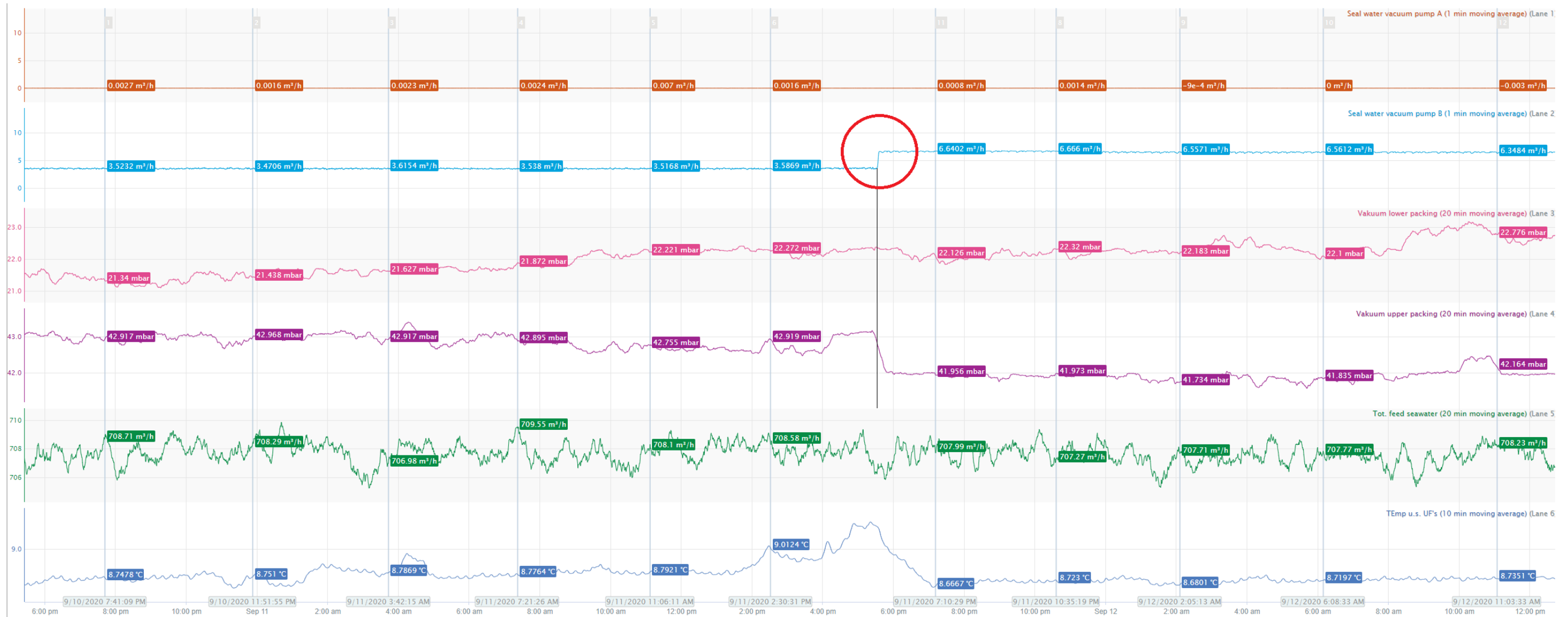


Figure D.4: Adjustments of seal water flow the 11th of September 2020 with response in packed bed pressures. From the top: The two upper lanes present seal water flows, one for each of the vacuum pumps. The middle two lanes present the parameter of interest, namely the lower- and upper packing (packed beds) respectively. While the last two lanes show seawater feed flowrate (liquid loading in deaerator) and temperature, respectively. These are included since both can affect the packed bed pressure. The seal water changes are marked with a red circle in each plot. Rulers are drawn from adjustments of seal water to better visualize instantaneous effects.

Fig. D.5 shows a reduction of seal water flow from ~ 6.5 to $3.6 \text{ m}^3/\text{h}$ done the 16th of October 2020. This seal water reduction seems to work in favor of reducing pressure in the upper packed bed both instantaneously and in quasi steady state. I.e. seemingly steady with respect to the alteration done but not relative to other variations like seawater and temperature fluctuations.

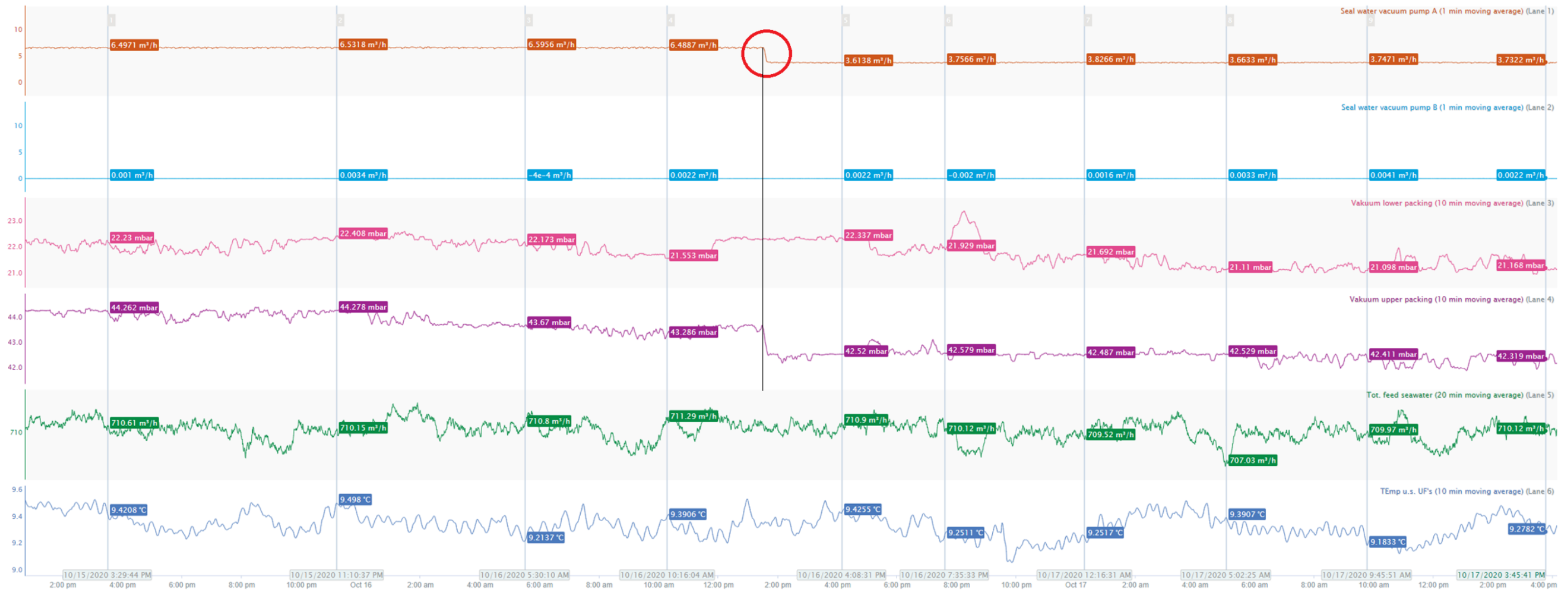


Figure D.5: Adjustments of seal water flow the 16th of October 2020 with response in packed bed pressures. From the top: The two upper lanes present seal water flows, one for each of the vacuum pumps. The middle two lanes present the parameter of interest, namely the lower- and upper packing (packed beds) respectively. While the last two lanes show seawater feed flowrate (liquid loading in deaerator) and temperature, respectively. These are included since both can affect the packed bed pressure. The seal water changes are marked with a red circle in each plot. Rulers are drawn from adjustments of seal water to better visualize instantaneous effects.

Fig. D.6 shows a 5-year trend with the same data as presented in the previous figures. The only alteration is that both seal flows are combined in the upper lane, and seawater flow and temp are combined in the lane below. The two lower lanes show the lower- and upper packed bed pressures, respectively. The four red circles (from left to right) indicate the seal water changes done in Fig. D.1 – D.5, respectively. Horizontal rulers are placed to better visualize the vacuum alterations over the years. These rulers are intended to be based in the average vacuums **before** starting to reduce the seal water flow. Thus, averages in vacuums to the left of the initial red circle. All the spikes have been neglected as they correlate to a large extent with the large variations in production and stops (green plot, lane 2). Examining the stage pressures during the last 5 years the seal water reductions seems not particularly favorable for the vacuum package performance relative to the original ~10 m³/h. Especially not when considering the 2nd bed (lower packing).

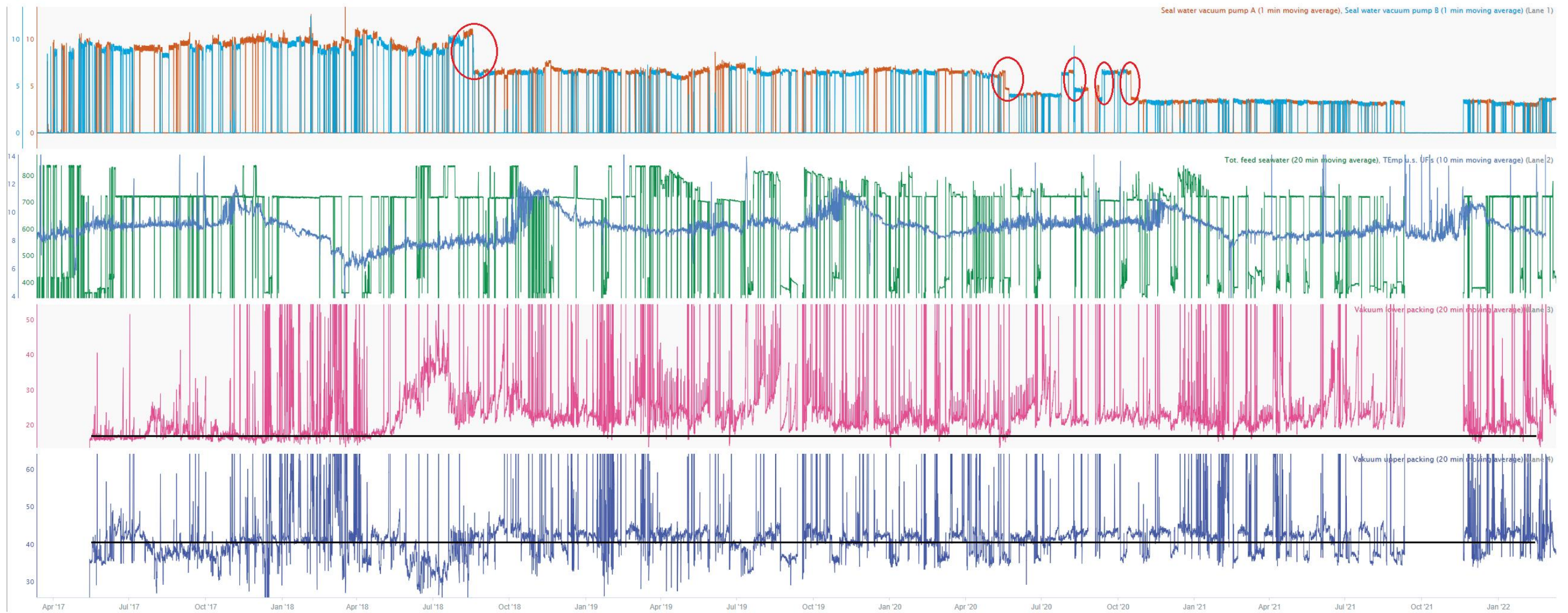


Figure D.6: Historical data comparing packed bed vacuums over a 5-year period vs. seal water flow, seawater flow and temperature. The upper lane shows seal water flow to both vacuum pumps. The second lane shows both seawater- flow and temperature. The lower lanes show the lower- and upper packed bed pressures, respectively. The four red circles (from left to right) indicate the seal water changes done in Fig. D.1 – D.5, respectively.

Appendix E – Mechanical deaeration performance – historical data on packed bed vacuum

Below in Fig. (E.1) to (E.3) three plots are given with several datapoints for packed bed vacuums. Each plot is based on a specific production mode, starting with above 800 m³/h seawater introduced to the vacuum tower. The middle plot presents several data points when the seawater flow is ~720 m³/h. While the last plot present data points when the seawater flow is between 350 - 400 m³/h. The points are picked arbitrarily only based on the production mode of interest. The intent is to calculate average packed bed pressures at different liquid loadings of the deaerator system as this is assumed related to the mechanical deaeration performance. It should be noted that the plant has been operated at ~720 m³/h to a much higher degree compared to the other modes. This means that the statistical data on the ~720 m³/h mode is more random and thus representative than the others. The other two modes data points are forced to be selected in much narrower time windows. Seawater temperatures are also plotted and averaged as it affects the vacuums assessed. But as the temperature has not been actively controlled historically it is only intended to show natural variation.

Based on Fig. E.1 the average pressures for the upper and lower packed beds, during an inlet flow of above 800 m³/h to the vacuum tower, have been calculated to 39.4 mbara and 27.2 mbar, respectively. Using temperature data from the same timestamps as used in the vacuum average gives a sea water temperature average of 9.2 °C during this operation mode.

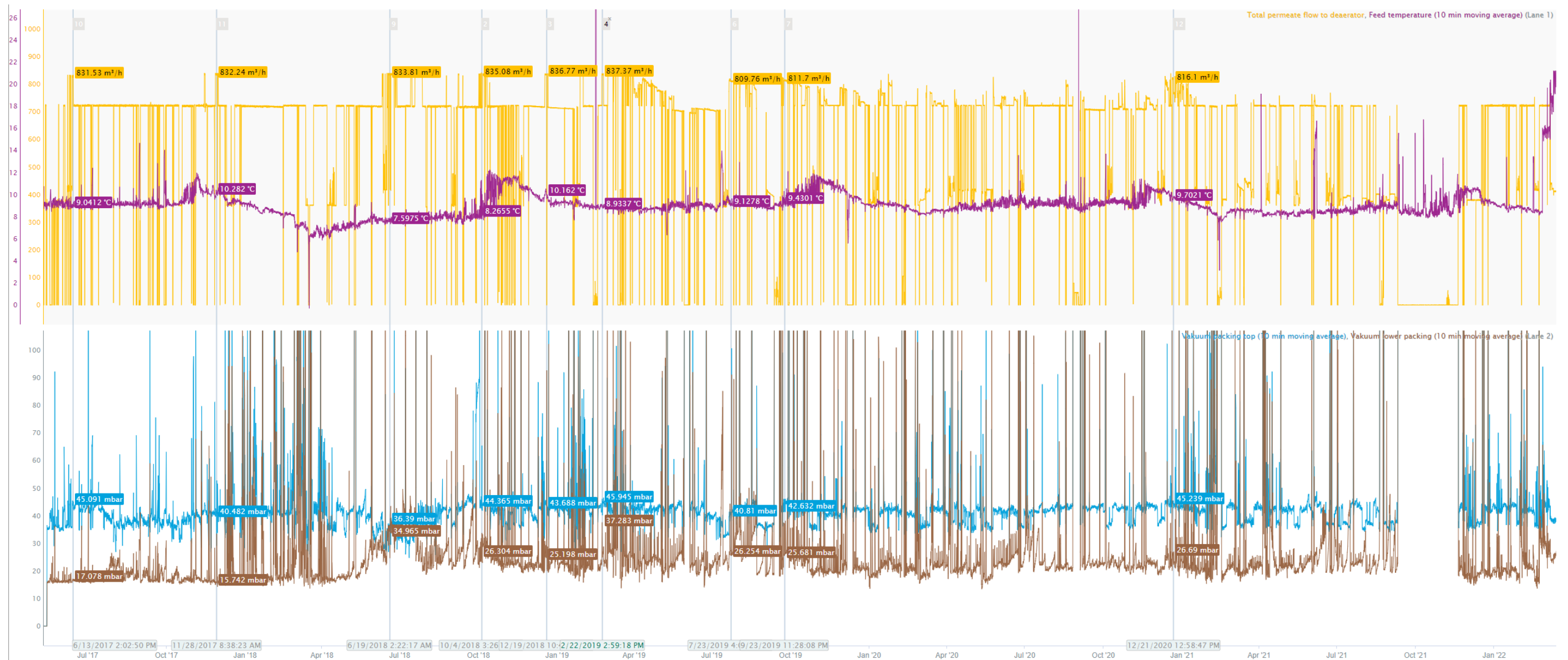


Figure E.1: Several datapoints for packed bed vacuum at production of above 800 m³/h of deaerated seawater. Upper plot shows seawater flow and temperature introduced to the vacuum tower in orange and purple, respectively. Lower plot shows upper- and lower packed bed absolute pressures in blue and brown, respectively.

Based on Fig. E.2 the average pressures for the upper and lower packed beds, during an inlet flow of $\sim 720 \text{ m}^3/\text{h}$ to the vacuum tower, have been calculated to 41.8 mbara and 22.2 mbar, respectively. Using temperature data from the same timestamps as used in the vacuum average gives a sea water temperature average of $8.9 \text{ }^\circ\text{C}$ during this operation mode.

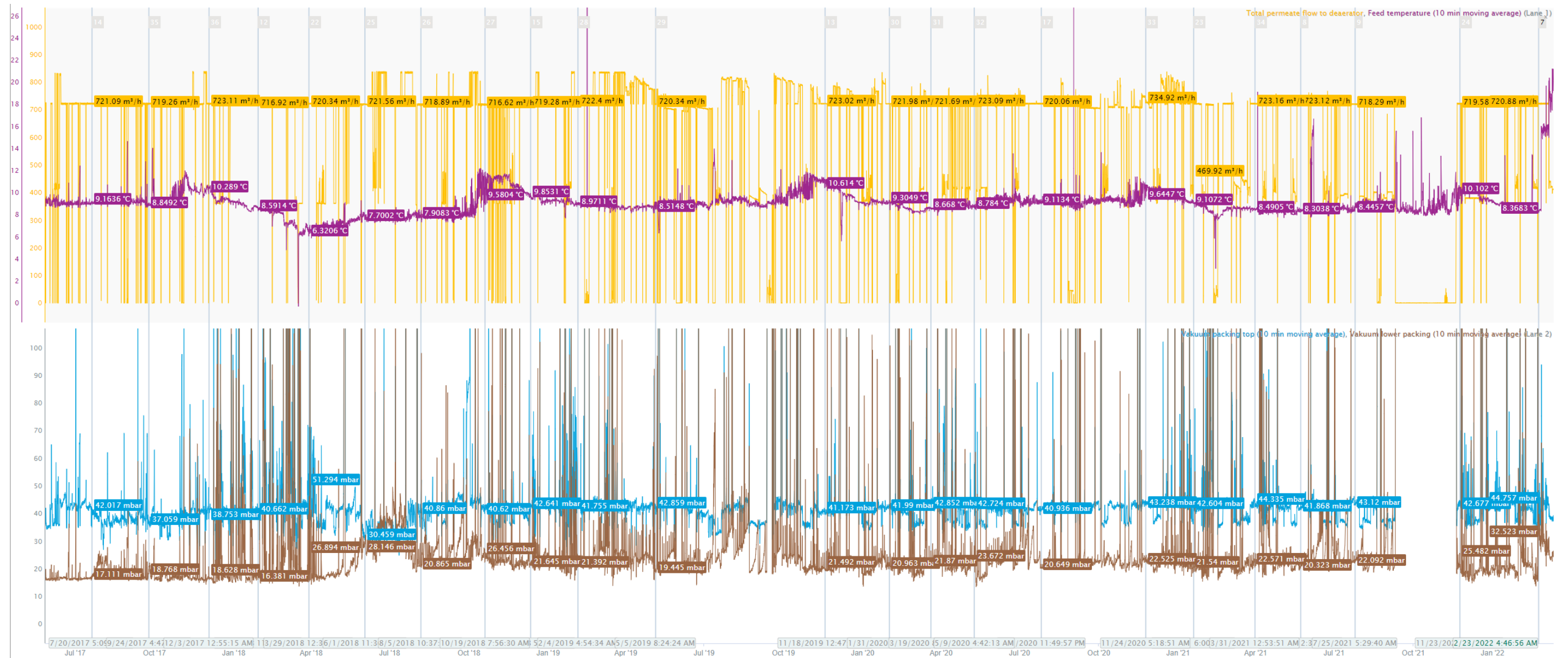


Figure E.2: Several datapoints for packed bed vacuum at production of $\sim 720 \text{ m}^3/\text{h}$ of deaerated seawater. Upper plot shows seawater flow and temperature introduced to the vacuum tower in orange and purple, respectively. Lower plot shows upper- and lower packed bed absolute pressures in blue and brown, respectively.

Based on Fig. E.3 the average pressures for the upper and lower packed beds, during an inlet flow of 350 - 400 m³/h to the vacuum tower, have been calculated to 36.0 mbara and 19.5 mbar, respectively. Using temperature data from the same timestamps as used in the vacuum average gives a sea water temperature average of 9.0 °C during this operation mode.

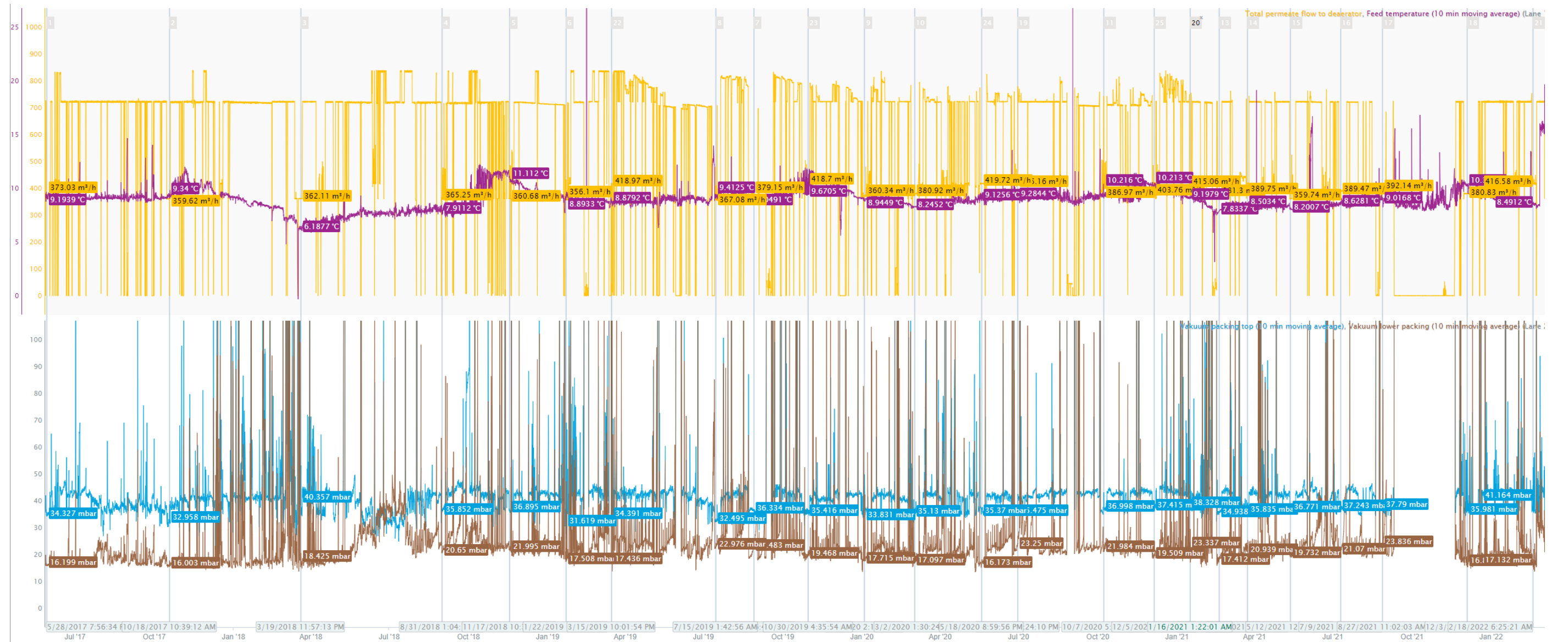


Figure E.3: Several datapoints for packed bed vacuum at production between 350 to 400 m³/h of deaerated seawater. Upper plot shows seawater flow and temperature introduced to the vacuum tower in orange and purple, respectively. Lower plot shows upper- and lower packed bed absolute pressures in blue and brown, respectively.

Appendix F – Solution-diffusion operational dependencies and scaling through molar volumes.

If the permeability and molar volumes are considered independent of pressure and temperature the mathematical expressions for flux of solvent and solutes through the Solution-diffusion model, shown in Eqn. (3.14) and (3.15), indicates that: [19]

1. Both solvent and solutes respond in the same direction to changes in temperature and pressures. The degree in response and the magnitude of fluxes will however be different and scaled against the absolute values of permeability, molar volume, and feed concentration for each species.
2. Increasing feed pressure, p_0 , increases fluxes through that the concentration gradient increases. Flux asymptotically reaches a maximum as the interface concentrations reaches zero on the permeate side, thus yielding the highest possible concentration gradients inside the membrane.
3. Increasing permeate pressure, p_l , reduces flux through reducing the concentration gradient in the membrane. I.e., concentrations on the permeate interface increases and equals the feed side concentration when Δp across the membrane reaches zero.
4. Elevating the system temperature, T , reduces the fluxes as the concentration gradient is inversely proportional to the negative exponent of it.

To give a visual representation of variable changes and scaling of molar volumes the solution-diffusion equations are plotted in three different plots given in Fig. F.1 to F.3. One plot for each variable in p_0 , p_l and T . In each of these figures two curves are plotted where the difference between them is a molar volume with a ratio of 5:1. The symbol v_h and v_l indicates high and low molar volume, respectively. Between water and sulfate it is sulfate that has the highest molar volume, $\sim 3 \cdot 10^{-5}$ relative to $\sim 1.8 \cdot 10^{-5}$ kg/m³.

To isolate the effects of pressure and temperature on the permeate concentration, the factor $\frac{P_i c_0}{l}$ and initial permeate concentration c_l are set to unity, while arbitrary constant values are selected for the two variables kept constant in each plot. The permeabilities will typically vary greatly between solutes and solvent. Hence, equal fluxes of solute and solvent will not occur such as shown in the plots below. Changes in permeability will simply shift the entire plot on the y-axis, i.e. doubling the permeability doubles the flux.

Through Fig. F.1 it is evident that as the feed pressure increases the specie with the highest molar volume is more responsive in that its permeation (or flux) increases faster and reaches the threshold value sooner compared to the specie with lowest molar volume.

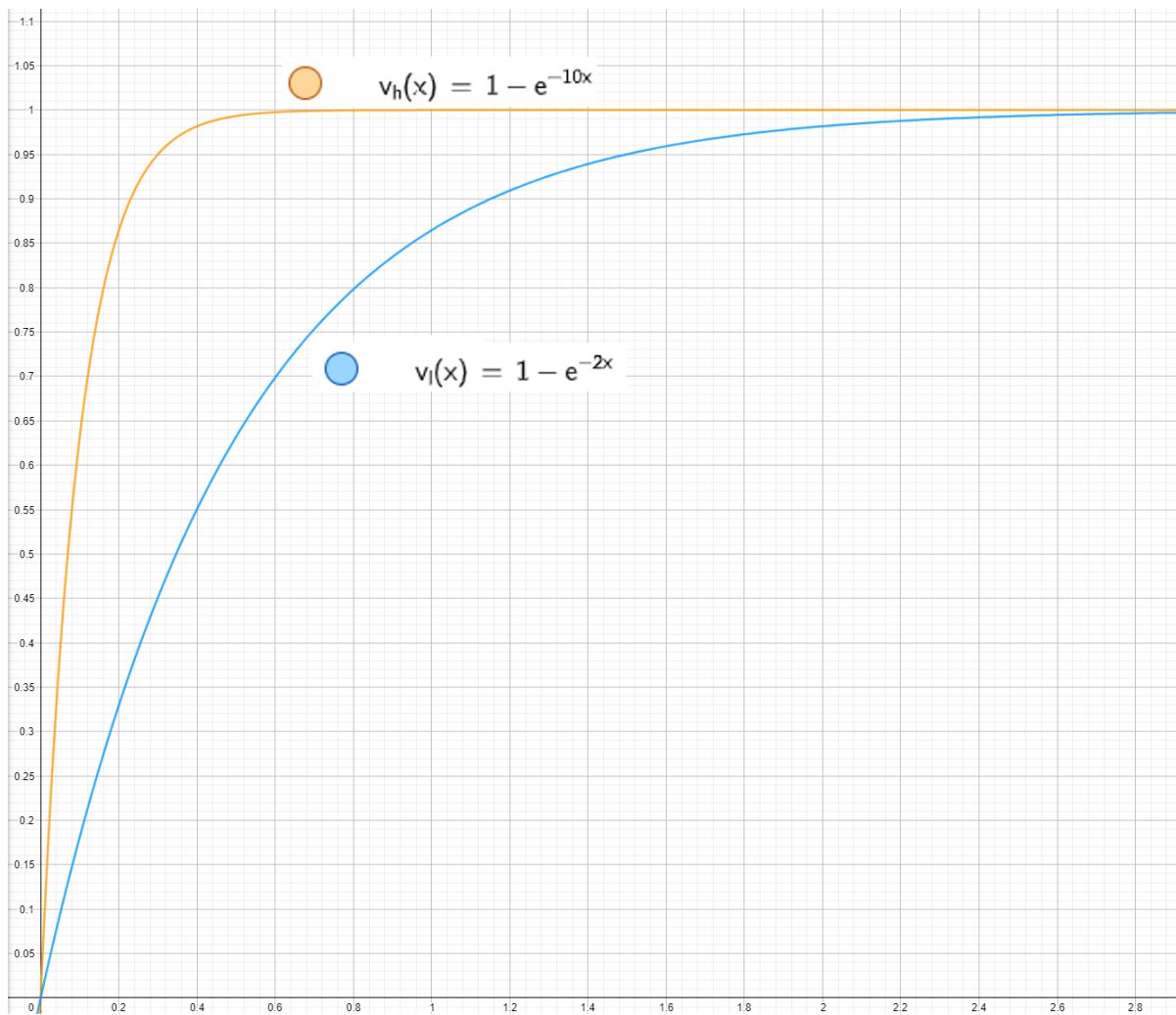


Figure F.1: Flux as function of feed pressure, p_0 . All other variables are kept constant at arbitrarily selected values. The plot is only intended to study the effects of p_0 on flux and to do a comparison of a high and low molar volume indicated with v_h and v_l . The x-axis is mass fluxes in $[\text{kg}/(\text{m}^2\text{s})]$ while the y-axis is feed pressure in pascals.

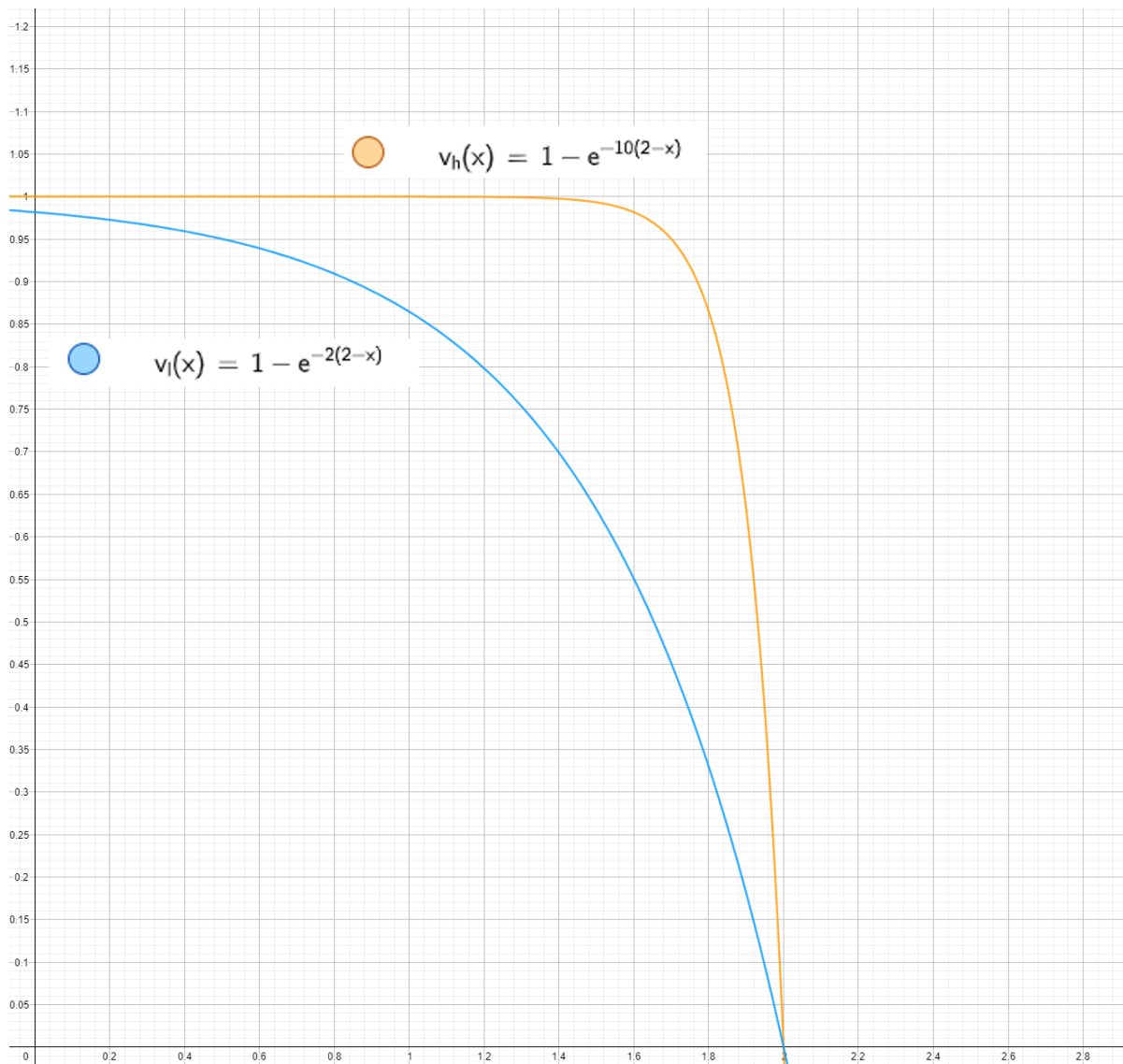


Figure F.2: Flux as function of permeate pressure, p_l . All other variables are kept constant at arbitrarily selected values. The plot is only intended to study the effects of p_l on flux and to do a comparison of a high and low molar volume indicated with v_h and v_l . The x-axis is mass fluxes in [kg/(m²s)] while the y-axis is permeate pressure in pascals.

Figure F.2 illustrates that as permeate pressure increases fluxes drops and it is most responsive for the specie with the lowest molar volume. The species with the highest molar volume has more buffer in that it is seemingly unaffected initially as the permeate pressure increases. However, when the pressure difference, $p_0 - p_l$, gets sufficiently small the flux drops fast to zero as the pressure difference reaches zero.

In the last plot, Fig. F.3, it is evident that flux drops with increased temperature. Regarding scaling effect of molar volumes both cases respond almost alike, where the specie with the highest molar volume is slightly more responsive.

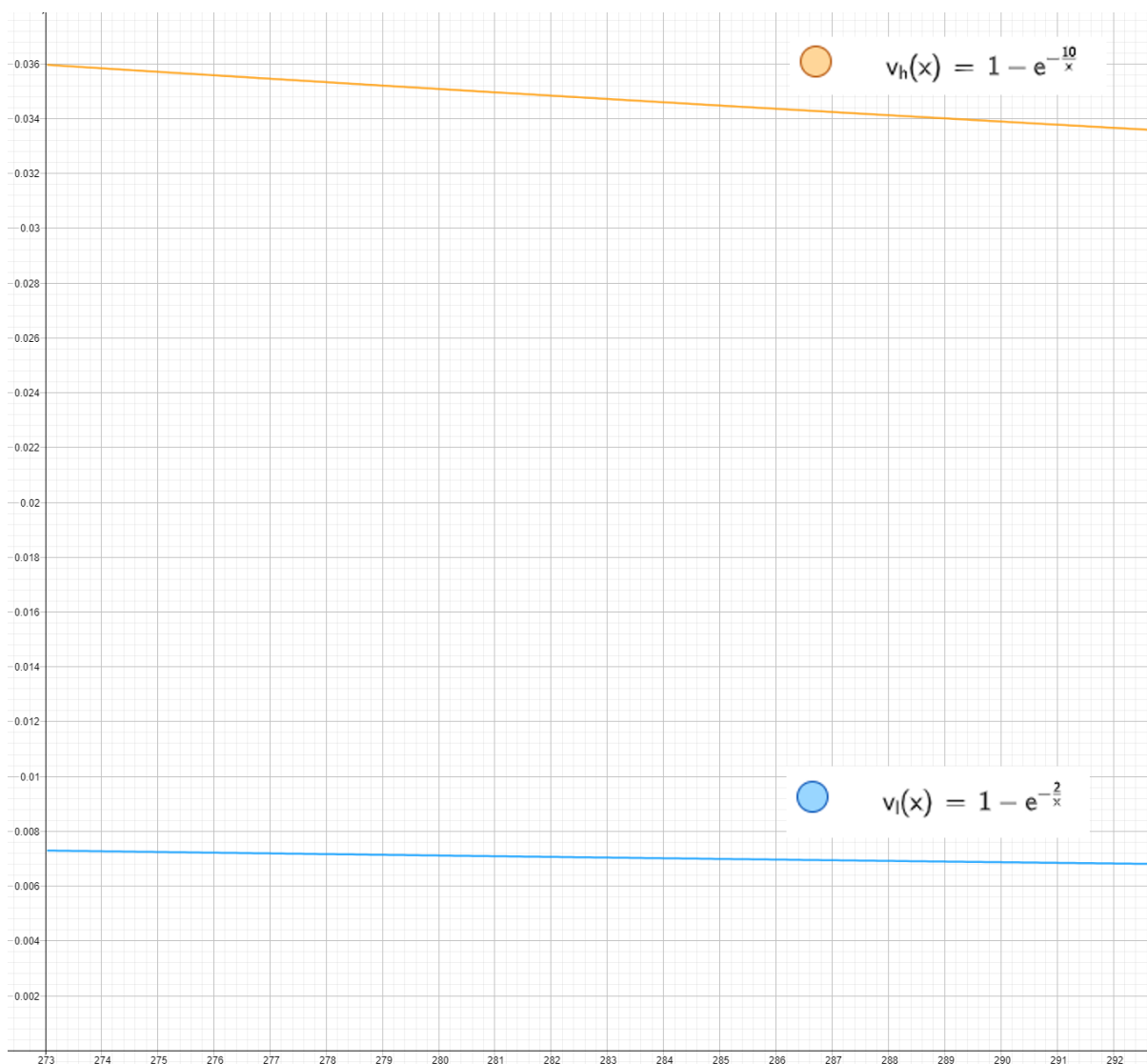


Figure F.3: Flux as function of temperature, T . All other variables are kept constant at arbitrarily selected values. The plot is only intended to study the effects of T on flux and to do a comparison of a high and low molar volume indicated with v_h and v_l . The x-axis is mass fluxes in $[\text{kg}/(\text{m}^2\text{s})]$ while the y-axis is solvent/solute temperature in absolute temperature, $[\text{K}]$.

Appendix G – Mass balance – test of permeate split versus pressure valve position

Note: two of the logged datapoints are suspected to be erroneous. The reason is that the permeate flow out of the 2nd stage increases as the PV is opened above 90 % valve opening. This flow should decrease with increased PV opening throughout the entire valve opening range.

LØRDAG

Test av permeat flow splitt SRU B vs 29PV3306 ventilåpning

Hensikt:

- 1) Bestemme om permeatflow gjennom trinn 1 og 2 er skjevfordelt
- 2) Undersøke hvordan justering av PV påvirker innløpstrykk og DP over trinn 1.
- 3) Verifisere teoretisk beregning av flowfordeling mellom peremetat 1. og 2. trinn, og om denne kan brukes til å opprette soft-tag i SAS.

Utførelse:

Trinn	Beskrivelse	Informasjon	SKR	Felt
1	Monter clamp-on måler på 29L1072B	Permeat fra 2. trinn SRU B		X
2	Sett 29PV3306 i manuell			
3	Juster 29PV3306 gradvis opp til 100%. For hver 5% åpning, noter klokkeslett og tilhørende flowmåling fra felt	Fyll inn i tabell under	X	X
4	Juster gradvis ned til 65%. For hver 5% åpning som ikke allerede har blitt notert, noter klokkeslett og tilhørende flowmåling fra felt	Fyll inn i tabell under	X	X
5	Juster gradvis opp til startpunkt og sett i PV i kontroll		X	

Klokkeslett	29PV3306 [%]	Clamp-on 29L1072B
1733 1733	70	137 140
1736 1738	75	137 134,5
1741 1744	80	132 132,5
1746 1750	85	130 131
1749 1755	90	125 125
1800	95	131
1805	100	129 129
1728	65	143

Appendix H – Estimating salinity change with temperature.

The salinity in the permeate from the SRU will change with seawater temperature. In this appendix data from Test 1, discussed in Ch. 5.2.1, is utilized to make a functional relation between salinity and temperature. This example relates specifically to this test as the relation is based on the test data. This function is in turn implemented into the Henry-Setchenov model used to estimate the solubility of oxygen.

The measured conductivities of the SRU permeate streams show in Fig. H.1 with dotted lines. For simplicity it is assumed that the average of these is approximately the seawater conductivity fed to the deaerator. This will be correct when the SRUs are operated in parallel at equal permeate production. When one SRU is operational the estimate will be somewhat erroneous. The assumption is made since the SRUs produce relatively similar permeate quality relative to conductivity in the assessed period.

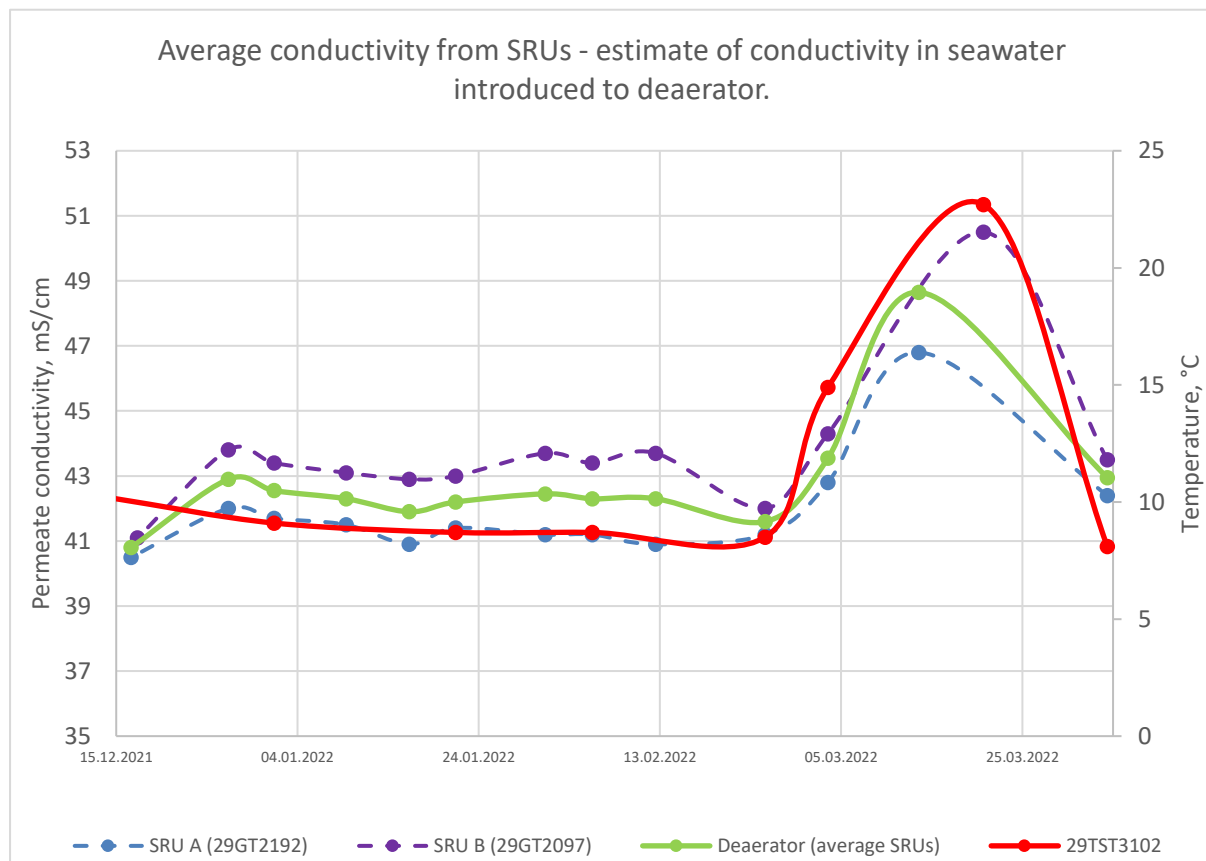


Figure H.1: Estimate of conductivity of seawater introduced to deaerator by taking the average permeate conductivity of both SRUs. The green line is the average conductivity assumed to be introduced to the deaerator. It is plotted against seawater temperature introduced to the SRUs.

To predict the salinity behavior with seawater temperature the $\Delta\bar{\varphi} / \Delta T$ was defined from the measured conductivities during the test. This is the change in average conductivity ($\bar{\varphi}$) per change in temperature. By using the average conductivity and temperature plotted in Fig. H.1 a factor of 0.4964 mS/(cm·°C) can be calculated by use of sample data from test start to the highest temperature measured. This factor is assumed to be linear across the relevant

temperature interval (5 to 30 °C) and multiplied to the temperature change from a reference point as shown in Eqn. (H.1). In this equation the conductivity is converted to salinity in mg/L by using a factor of 800 (mg · cm)/(L · mS) [60].

$$S(T) = (S^{\circ} + 0.218T) * 800 \quad (\text{H.1})$$

Salinity is fixed at a reference of 29000 mg/L at 9 °C which is based on a TDS measurement done by Aker BP on the permeate the 19th of august 2017 at 14:31 when the seawater temperature to the SRUs was ~9 °C. This salinity estimate is converted to g/kg with use of a water density of 1.025 kg/m³ to fit the Henry-Setchenov model. This model has a validity range to approximately 27 °C as it estimates higher salinity than what is present in the seawater lifted to the platform from the sea, 32600 mg/L (from Tab. 2.1).

Figure H.2 compares the performance curves predicted by use of Henry's law and Henry-Setchenov modelling of Henry solubilities with constant salinity of 2.9 % to use of the salinity-temperature relation expressed in Eqn. (H.1). Dotted curves are performance curves where Eqn. (H.1) is implemented into the model.

The constant salinity model overestimates the dissolved oxygen with 0.3 % at 10 °C. The error is independent on seawater flow rate. The error increases with the temperature and is at a level of 4.2 % error at 25 °C and at the maximum of 4.6 % at 27 °C.

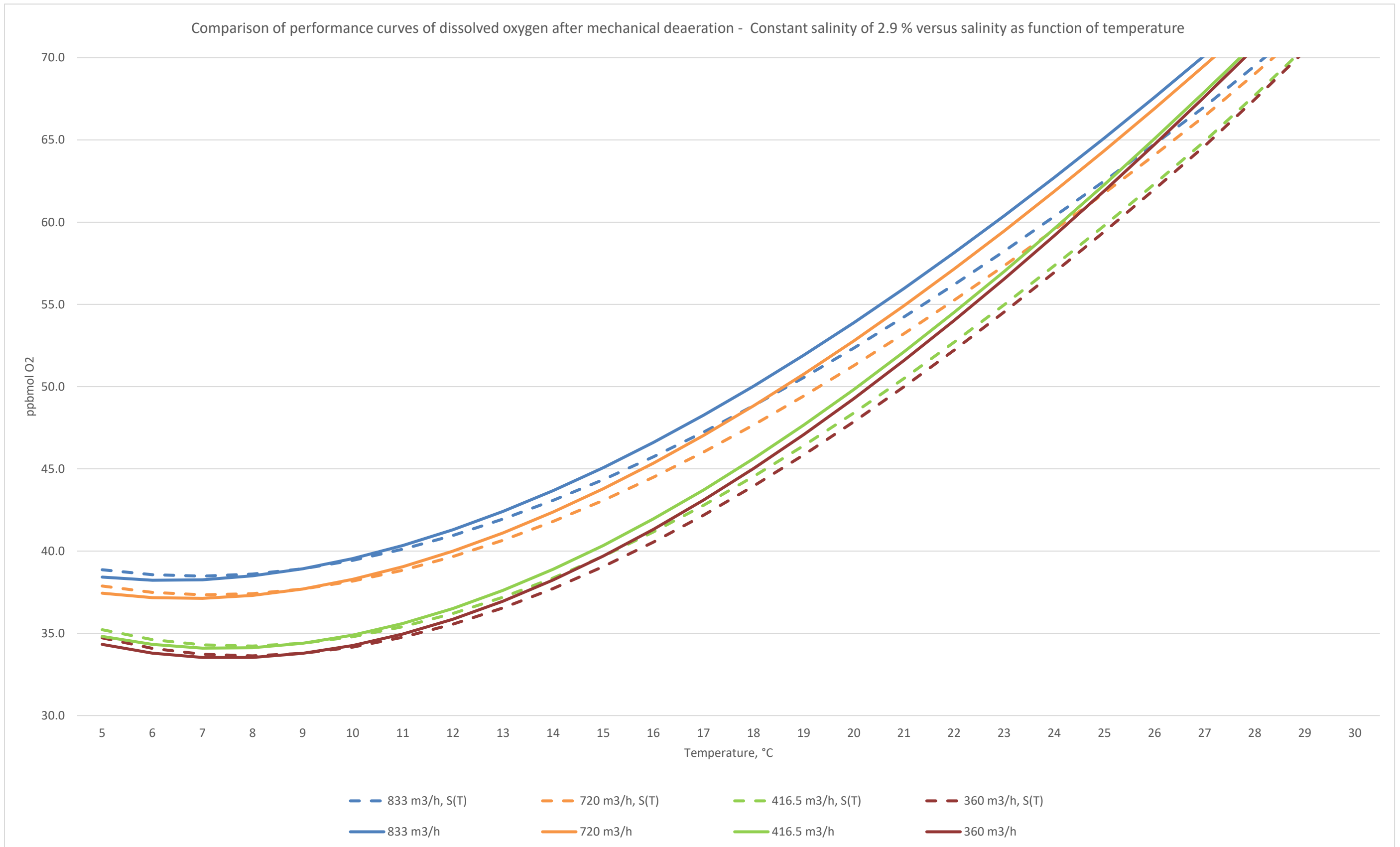


Figure H.2: Comparison of performance curves for dissolved oxygen after mechanical deaeration with constant salinity of 2.9 % versus salinity as function of temperature though Eqn. (H.1). Dotted curves present the dissolved oxygen when the salinity depends on the seawater temperature through Eqn. (H.1).

Appendix I – Test procedure for Test 2 – Validate permeate flow model

Verifisere strømnings modell

Hensikten med denne testen er å verifisere en matematisk flow beregning av permeat gjennom PV på utløpet av permeatet fra første trinnet i SRU B. Ifølge FA automasjon skal det være ca. 1 times jobb og montere selve måleren. Når loggingen er startet tar en test ca. 5 timer, dvs. at SKR må steppe etter prosedyre i ca. 5 timer. Det er ønskelig med 3 slike tester, men en av dem bortfaller høyst antakelig pga. problemene med gasskompresjonen på EG.

1. Montere clamp-on måler på permeat løpet ut av andre trinnet på SRU B. Denne bør plasseres på et rettstrekk lengst mulig nedstrøms eventuelle innsnevninger og rørbend. Dette slik at rørbend/innsnevninger oppstrøms forstyrrer strømningsprofilen der clamp-on måler plasseres. Den bør heller ikke plasseres direkte oppstrøms rørbend eller innsnevninger da dette også kan påvirke strømningsprofilen. Dere må også vurdere plassering ift. hva som er hensiktsmessig for dere.
 2. Start logging av data på clamp-on måler
 3. Sett PV ut av 1. trinn i manuell og juster til nærmeste hele 5'er i % ventil åpning.
 4. Stepp opp 5 %_{poeng} ventilåpning av gangen til 100 % med 15 minutters tidsintervall. Når 100 % er oppnådd steppes det ned til minimum ventilåpning med samme prosedyre.
 5. Når minimum ventilåpning er oppnådd steppes det med samme tidsintervall tilbake til utgangspunktet i punkt 2.
 6. Sett PDIC tilbake i auto etter 15 minutter
 7. Stopp logging, lagre fil og send den til Espen Nilsen
 8. Juster permeat produksjon i SRU B til ett høyere nivå enn hva den var i forrige loggerunde. Dette gjøres ifm. CIP vask av SRU A som er planlagt for denne uken når det er behov for mere vann.
 9. Repeter punkt 2 til 7 og hopp deretter til punkt 10.
- Neste steg i prosedyren er kun aktuelt dersom det kan leveres varme fra kompressor kjølerne til sjøvanns systemet. Hvis det fortsatt er problemer på EG hopper dere til punkt 12 og avslutter testen.
10. Juster temperaturen på sjøvannet til det motsatte av utgangspunktet. Dvs. dersom maksimalt med sjøvann er rutet fra kompressor kjølerne til UF skal man nå rute alt sjøvann fra disse kjølerne mot dump for å minimere temperaturen.
 11. Repeter punkt 2 til 7. Hopp deretter til punkt 12.
 12. Etter endt test tilbakestilles alt til slik det var før test. PV settes i auto, balansering av kompressor kjølerne tilbakestilles og clamp-on måler demonteres.

Appendix J - Volume flux pulsing

Test 4 - Volume flux pulsing

Introduce slow changing pulses in the volume fluxes.

Theoretical basis and predicted outcomes:

Pulsing in the volume flux will induce pulsing in the feed/concentrate flows for both stages. This will introduce dynamic that affects the laminar boundary layer and concentration polarization modulus. This can retard the rate of bio growth which in turn can result in reduce CIP frequency. If the CIP frequency is reduced the power consumption for the SRU pumps will also be lowered. DuPont recommend not keeping permeate pressures static for their 8” FilmTec elements in [57].

The amplitude and frequency of the sinusoidal pressure curve are only a suggestion. This should be altered to find the optimum parameters with respect to the CIP frequency. It should also be performed a literature review on the topic to see if there are some guidance to what amplitude and frequency that should be employed.

Limitations:

- Do not introduce flow variations in the seawater inlet to the SRU. From Aker BP’s experience such flow variation can deteriorate SRU performance through shearing off- and introducing particles and growth from the upstream pipe walls. Altering internal recoveries should not affect upstream or downstream pipe flow since the SRUs are controlled to a fixed total recovery of 75 %. A check of the total feed flow (permeate + concentrate) during the clamp-on tests performed back in 2018 shows that it remained unchanged during increments done in the 1st stage permeate pressure valve. The feed pressure changes but not the flow.
- Feed pressure changes should not be altered too rapid. The SR90-440i datasheet states that upon startup it should take at least 30 seconds to pressurize the feed side. The suggested PDIC function introduces a period of 10 minutes between ± 0.5 barg of the differential pressure set point.

Implementation:

Introduce a sinusoidal function with to the setpoint of the pressure difference controller so that it fluctuates $\pm 0,5$ barg with a 10-minute period (600 seconds) about the setpoint.

For a second counting system and sinus degree function this setpoint function will have the following form where SP is the Δp setpoint:

$$f_{SP} = SP + 0.5\sin(seconds/1.667) \quad (J.1)$$

The control system probably has in-built functions for this purpose.

Appendix K – Testing the mechanical deaeration by stopping/significantly reducing the oxygen scavenger dosage rate.

The plot shown in Fig. K.1 below shows how the mechanical deaeration performs during periods with very low or no chemical deaeration occurring. The plot on the left-hand-side is from the same period of time as indicated in the red circle to the left in Fig. 5.20 while the one to the right correlates with the second circle in Fig. 5.20.

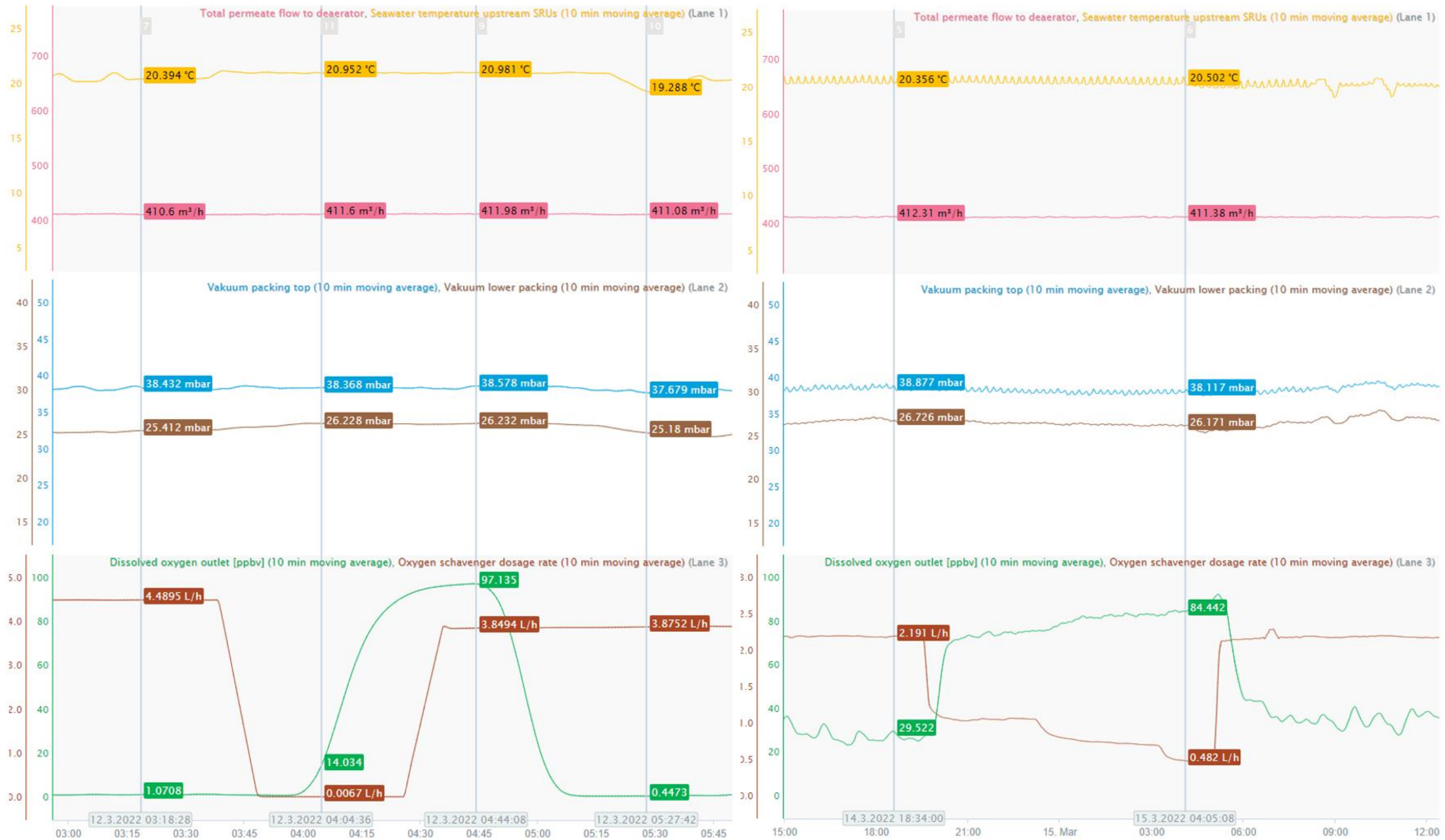


Figure K.1: Testing the mechanical deaeration by stopping/significantly reducing the oxygen scavenger dosage rate.